
ENVIRONMENTAL MONITORING USING ELECTROMAGNETIC AND ACOUSTIC RADIATIONS OF OBJECTS, EXISTING GROUND AND SPACE RADIO SYSTEMS

NATIONAL ACADEMY OF SCIENCES OF UKRAINE
O.Ya. USIKOV INSTITUTE FOR RADIOPHYSICS
AND ELECTRONICS OF THE NAS OF UKRAINE

НАЦІОНАЛЬНА АКАДЕМІЯ НАУК УКРАЇНИ
ІНСТИТУТ РАДІОФІЗИКИ ТА ЕЛЕКТРОНІКИ
ім. О.Я. УСИКОВА НАН УКРАЇНИ

В.І. ЛУЦЕНКО
І.В. ЛУЦЕНКО
І.В. ПОПОВ
О.В. СОБОЛЯК

МОНІТОРИНГ ДОВКІЛЛЯ З ВИКОРИСТАННЯМ ЕЛЕКТРОМАГНІТНИХ І АКУСТИЧНИХ ВИПРОМІНЮВАНЬ ОБ'ЄКТІВ, ІСНУЮЧИХ НАЗЕМНИХ ТА КОСМІЧНИХ РАДІОСИСТЕМ

ПРОЄКТ
«УКРАЇНСЬКА НАУКОВА КНИГА
ІНОЗЕМНОЮ МОВОЮ»

КИЇВ
АКАДЕМПЕРІОДИКА
2024

V.I. LUTSENKO
I.V. LUTSENKO
I.V. POPOV
O.V. SOBOLIAK

ENVIRONMENTAL MONITORING USING ELECTROMAGNETIC AND ACOUSTIC RADIATIONS OF OBJECTS, EXISTING GROUND AND SPACE RADIO SYSTEMS

PROJECT
«UKRAINIAN SCIENTIFIC BOOK
IN A FOREIGN LANGUAGE»

KYIV
AKADEMPERIODYKA
2024

https://doi.org/10.15407/akademperiodyka.525.268
UDC 504.064.3:528.8
L97

Reviewers:

Yu.F. LOHVINOV, Acting Director of the O.Ya. Usikov Institute for Radiophysics and Electronics of the NAS of Ukraine, Doctor of Physical and Mathematical Sciences, Senior Staff Scientist

V.V. PAVLIKOV, Vice-Rector for Scientific Work of the National Aerospace University "Kharkiv Aviation Institute" (KhAI), Doctor of Technical Sciences, Professor

S.M. SHULGA, Dean of Radiophysics, Biomedical Electronics, and Computer Systems School, V.N. Karazin Kharkiv National University, Doctor of Physical and Mathematical Sciences, Professor

Approved for publication by the O.Ya. Usikov Institute for Radiophysics and Electronics of the National Academy of Sciences of Ukraine (29.07.2023, Protocol No. 5)

The publication was funded within the framework of the Targeted Complex Program of the NAS of Ukraine "Scientific Bases of Functioning and Providing for Conditions for the Development of the Scientific and Publishing Complex of the NAS of Ukraine"

Lutsenko V.I.

L97 Environmental Monitoring using Electromagnetic and Acoustic Radiations of Objects, Existing Ground and Space Radio Systems / V.I. Lutsenko, I.V. Lutsenko, I.V. Popov, O.V. Soboliak; O.Ya. Usikov Institute for Radiophysics and Electronics of the NAS of Ukraine. — Kyiv: Akademperiodyka, 2024. — 268 p.

ISBN 978-966-360-525-8

The monograph considers the solution to the problem of using the own acoustic and secondary electromagnetic radiations of objects of anthropogenic origin in active-passive monitoring systems. Techniques for estimating the range of detection of acoustic radiation sources, a method for determining radar signatures of objects based on optical and acoustic portraits and the selection of a useful signal against the background of noise, methods for estimating the range and RCS of aerial objects, methods for the sea surface state remote diagnostics, the troposphere of the Earth by the radiation of TV and radio broadcasting stations and global navigation systems, a model of non-stationary disturbances are proposed. New methods are considered to describe non-stationary processes and signals using Kravchenko-Rvachev distribution functions and nested semi-Markov processes.

UDC 504.064.3:528.8

ISBN 978-966-360-525-8

Contents

CHAPTER 4

Environmental monitoring and solving the tasks of radio location using radiation of broadcasting and TV stations of HF and VHF bands and GNSS systems

CHAPTER 5

Interferences for active-passive monitoring systems

CHAPTER 6

Kravchenko-Rvachev distribution functions describing some non-stationary non-Gaussian processes

CHAPTER 7

Non-equidistant two-dimensional antenna arrays based on magic squares

CHAPTER 8

Smart Grid technology for increasing the efficiency of ground equipment facilities

List of abbreviations and acronyms

AA	—	antenna array
ADGE	—	air defense
AGD	—	automatic gain adjustment
AGW	—	atmospheric gravity waves
ASE	—	an artificial satellite of the Earth
ASM	—	anti-ship missile
AT	—	air targets
CDS	—	cyclic difference set
CMSC	—	correlation matrix of spectral components
dB	—	decibel
DP	—	directional pattern
EHF	—	extremely high frequencies
ESA	—	effective scattering area
GLONASS	—	global navigation satellite system
GNSS	—	global navigation satellite system
GPS	—	global positioning system
GTE	—	gas turbine engine
HP	—	horizontal polarization
LAF	—	lowest applicable frequencies
MAF	—	maximum applicable frequencies
MGA	—	manual gain adjustment
MLS	—	method of least squares
MTS	—	moving targets selection
OBDC	—	on-board digital computer
OES	—	optoelectronic system
OOF	—	operating frequencies
PE	—	propeller engine
PP	—	power plant
RCS	—	radar cross-section
RS	—	radar systems
RV	—	reconnaissance vehicle
SESA	—	specific effective scattering area
SIR	—	signal-interference ratio
SW	—	short waves

TJE — turbojet engine
TJTCE — turbojet two-circuit engine
TPE — turboprop engine
UAV — an unmanned aerial vehicle
UHF — ultra-high frequencies
UMS — unified management system
USW — ultra-short waves
VP — vertical polarization
A_f — the amplitude of the spectral component
$c_s(q)$ — cepstrum
c — speed of light in vacuum
c, c_1 — speed of propagation in environments
d — the distance from the noise source to the receiver
d_B — screw diameter
$E(l)$ — distribution of intensity of the irradiating field along the length of the propeller blade
f_D — Doppler frequency shift
$f_{ij}(t)$ — distribution density
Δf — spectrum width
F — reflection coefficient
G_{Tr}, G_R — gain coefficients of transmitting and receiving antennas
$H_i \in \nu_1 \ldots \nu_K$ — phase states
h_{Tr} — transmitter height
h_T — the height of the noise source
h_R — height of the receiver
k — wave number
$K(f)$ — suppression ratio
$L(\bullet)$ — attenuation factor
$L_{div}(R)$ — attenuation due to geometric divergence
$L_{atm}(R)$ — attenuation due to sound absorption by the atmosphere
L_{bar} — attenuation due to shielding
L_{TrT}, L_{TR} — losses during the propagation of radio waves from the transmitter to the target and from the target to the receiver, respectively
Γ_Σ, L_Σ — integral coefficients of reflection and attenuation by foliage
Dl — amplitude of body vibrations
M_{im} — m moment for the i^{th} state
$n_B \cdot n_{HR}$ — the number of blades and the number of screws
P_i — the final probability of the existence of the process in the i^{th} state
P_R — the strength of the received signal from the transmitting station
P_{Tr}, P_T — power of the received signal emitted and reflected from the target
$\overrightarrow{\|P(S)\|}$ — density matrix of the distribution of values
R_{TrT}, R_{TR} — range between transmitter and target, target and receiver

S_0 — values of spectral density at zero frequencies
S_{ij} — values of the elements of the square
$S_r(f, R, h_r, h_T)$ — spectrum of the sound source
$S(F)$ — spectrum of amplitude fluctuations
$S(F_i)$, $S(F_j)$ — spectral density at F_i and F_j frequencies
$\overrightarrow{S(t)}$ — continuous component of the process
$[S_i(t)]$ — statistical scatter matrix
T_{ij} — waiting time in state n_i before transition to state n_j
V — attenuation factor
V_0 — flight speed
V_{max} — the maximum permissible speed of movement of the end of the blade
$V_{gr}(R, h_r, h_T)$ — attenuation due to ground influence
Z, Z_1 — impedance of the incident wave and the wave that passed into the second medium
$\|Z\|$ — complex matrix
$\|\hat{Z}\|$ — inverse matrix
wav — Waveform Audio File Format
$\alpha\%$ — a fraction of the total noise power
β — redundancy factor
γ — linear decay
l — blade length
l_x, l_y — horizontal and vertical dimensions of the structure
$\theta(t) = \nu_i$ — discrete process component
θ_{Tr}, θ_R — directions from the target to the transmitter and receiver
λ — the wavelength of the signal at the carrier frequency
μ — signal-to-noise ratio
μ_{TR} — by the ratio of the target signal to the illumination signal
μ_{SN} — by the ratio of the carrier spectral line level to the noise spectral density
ε — dielectric constant
π_{ij} — element of the transition probability matrix
ρ — air density
ρ, ρ_1 — density of environments
ρ_S — the reflection coefficient determines the rms value of the field
$\rho(t)$ — correlation function
$\rho(F_i, F_j)$ — mutual correlation coefficient at F_i and F_j frequencies
$\sigma(\theta_{Tr}, \theta_R)$ — bistatic RCS of targets in the direction of the transmitter and receiver
σ, σ_W — RCS of the spectral line due to vibration and TDU bodies
σ_h — root mean square value of the heights of surface irregularities
σ^0_{lmi} — specific RCS of the i^{th} cluster of the land surface (phase state) with l irradiation polarization and m reception of a scattered signal
$\sigma_{x(y)}$ — RCS on horizontal and vertical polarizations
τ_{05} — correlation interval
ψ — angle of reflection

Foreword

The presented work is devoted to the creation of active-passive environmental monitoring systems using secondary electromagnetic and own acoustic radiations of anthropogenic and natural objects. The urgency of creating active-passive monitoring systems is due to the high requirements level for such systems in terms of cost, impact on the environment, visibility, and reliability. Unlike active monitoring systems, active-passive ones do not require their own source of illumination, which determines their economy, low visibility, and versatility. The development of high-performance computing equipment and element base in the part of sensor systems, which allow receiving and processing electromagnetic and acoustic radiation in a wide range of wavelengths, determine the availability of building active-passive monitoring systems with high sensitivity and resolution.

The main issues considered in the work include the analysis of the propagation characteristics of acoustic and electromagnetic waves in the atmosphere, the determination of the own acoustic and secondary electromagnetic waves parameters of anthropogenic and natural objects, the determination of the possibility of using ground and space-based electromagnetic radiation sources as illumination stations, the development of methods of obtaining signatures, evaluation of the resolution and range of monitoring systems, development of mathematical models of acoustic radiation of heterogeneous objects of anthropogenic and natural origin, development of methods for remote monitoring of the state of the sea surface, the Earth's troposphere, development of a mathematical model of non-stationary disturbances using semi-Markov nested processes, synthesis of non-equidistant two-dimensional antennas based on magic squares; creation of intelligent monitoring systems based on a multi-channel sensor complex.

The work may be of interest to scientists and experts involved in the development of methods and technologies of environment remote sensing, as well as students of radiophysics specialties.

The first chapter of the monograph reviews the history of the development of acoustic and radar detection systems, features of electromagnetic and acoustic wave propagation in the Earth's atmosphere, features of secondary electromagnetic radiation from anthropogenic and natural objects in the optical and short wavelength range radio range, possibilities of active-passive monitoring systems, application of smart devices in detection systems.

In the second chapter, the characteristics of the acoustic radiation attenuation from various sources in the atmosphere are described based on experimental data, taking into account the state of the subsurface and the range, the method of obtaining acoustic portraits and determining the range of detection of acoustic signal sources is proposed, the possibilities and methods of detecting acoustic signals against the background of natural noise interference from rain and wind are considered.

In the third section, the possibility of detecting and recognizing air objects of various types based on the frequency of modulation of the signal of the illumination station by the propellers is substantiated based on experimental and calculated data, the possibility of creating electromagnetic signatures of air objects based on their acoustic radiation and optical images is determined, the possibility of detecting helicopters in the mode of spectral density hovering in the high-frequency region, the characteristics of radar reflection from vegetation under wind influence were investigated.

In the fourth chapter, the refraction properties of the troposphere are investigated, and methods of diagnostics based on the amplitude of VHF signals on the over-the-horizon (OTH) path are proposed; the analysis of the characteristics of inversion layers in the propagation channel based on fluctuations of the received signal is given, RCS estimates of aerial objects at frequencies corresponding to radar illumination through the ionosphere are given, considered the possibility of using signals of GNSS to determine the state of the sea surface.

In the fifth chapter, interference for active-passive monitoring systems is considered, the results of an experimental study of the characteristics of non-stationary interference for active-passive acoustic and radio systems are given, a model for describing non-stationary interference based on semi-Markov nested processes with two-phase states is proposed, the main parameters contained in the model.

In the sixth chapter, the possibility of using Kravchenko-Rvachev atomic functions to describe the laws of distribution of various non-stationary processes, the apparatus of correlation matrices of spectral components (CMSC) for describing the statistical relationships of various spectral components of a signal scattered by objects, subsoil surfaces, and hydrometeors, experimentally — passive systems of the decameter range from the radiation of broadcasting stations in the HF band are considered.

In the seventh chapter, the possibility of synthesizing two-dimensional non-equidistant antenna arrays for environmental monitoring systems, ac-

tive-passive radar, and radio astronomy based on magic squares is considered, and their properties are investigated, algorithms for obtaining the maximum coverage of spatial frequencies of sparse antenna arrays by adding magic elements are proposed. Square, the deceleration of the electromagnetic wave, the distribution of the surface current, and the input impedance of a symmetric vibrator, whose arms consist of cylindrical spirals with a diameter and pitch small compared to the length of the vibrator, were experimentally investigated, and the external calibration of radars and radar targets with them on the database of structures is proposed.

In the eighth chapter, the basics of building intelligent networks from ground equipment objects, the integration of sensors of various types and wavelength ranges, and methods of evaluating the effectiveness of the proposed approaches are considered.

The authors express their deep gratitude for the cooperation and discussion of the results to Doctors of Physical and Mathematical Sciences S.O. Masalov and I.M. Mytsenko. We are also grateful to all other participants of the Remote Sensing scientific seminar and, especially, the Acting Director of the O.Ya. Usikov Institute for Radiophysics and Electronics of the NAS of Ukraine, Doctor of Physical and Mathematical Sciences Yu.F. Lohvinov for constructive comments and useful advice.

Introduction

In modern conditions, the creation of active-passive monitoring systems is becoming increasingly urgent. It is necessary to have complete and reliable data on the state of the surrounding environment to make decisions and develop management influences in a wide range of activities. This applies to both natural and anthropogenic objects. At the same time, the use of active radioacoustic sounding and radar surveillance systems, which have developed significantly in recent decades, may be limited based on considerations of economic feasibility, limitations of the radio frequency range resource, environmental friendliness, and visibility.

The means of recording acoustic radiation, bistatic radar with an external source of illumination, and optical devices can be engaged in solving the problems of active-passive monitoring. The problems that arise during the implementation of active-passive monitoring, regardless of the nature of the physical fields used, are generally of a general nature, namely, the selection of a useful signal coming from the object against the background of obstacles, taking into account the influence of the radiation propagation medium on the parameters of the received signal, determination of characteristic features in the structure of the useful signal scattered (radiated) by the object and compilation of the library of signatures of monitoring objects. Increasing the effectiveness of active-passive monitoring systems requires the use of smart technologies and the integration of heterogeneous systems. Reviewing the ways to solve these problems is the main task of this monograph.

The following issues are considered in the monograph to achieve the set goal:

- the regularities of the distribution of acoustic radiation from ground and air objects in the atmosphere are determined on the basis of the conducted experimental studies, taking into account the condition of the underlying surface; the possibility of describing the spectra of noise sources by fractal dependencies is shown; the method of estimating the detection range of sources of acoustic radiation under the influence of attenuation

in the atmosphere and interference attenuation by the Earth's surface is given; the principles of building acoustic systems are outlined;

• the characteristic features of the spectra of acoustic radiation and reradiated electromagnetic waves of ground and air objects are selected and classified; the possibility of determining the electromagnetic signatures of objects based on their optical images and acoustic signatures is shown;

• the use of a two-channel equipment complex for measuring the level of signals on spatially separated antennas in the frequency band of television signals for the purpose of monitoring tropospheric refraction by signal attenuation factors on the over-the-horizon route is considered; experimental data on interference phenomena in the propagation channel on over-the-horizon routes in the mid-latitudes due to changes in the signal level from television centers that occur in the presence of inversion layers are given; a methodology for estimating the detection range and RCS of aerial objects for active-passive monitoring systems is given; the possibility of using signals from navigation satellites for remote monitoring and diagnosis of the state of the sea surface is shown;

• a simulated model of non-stationary acoustic noises of natural (wind, leaves), anthropogenic (human steps, automatic weapon shots), and signal scattered from sea and land using semi-Markov nested processes with two-phase states is proposed; a modified correlation function is proposed, which allows taking into account the deformation of the spectra

• it is shown that the finiteness of the Kravchenko-Rvachev functions is the physical reason for their use to describe the statistics of many types of non-stationary processes; it was established that the use of the apparatus of correlation matrices of spectral components allows establishing the synchronicity of the appearance of individual spectral components in signal spectra and can be used to create spectral-polarization portraits of scattered signals, which can be used in solving recognition problems and synthesizing multi-channel detection systems;

• solving the problem of optimizing antenna systems, which is especially relevant when creating antenna systems of the decameter wave band, a technique for the synthesis of non-equidistant antenna arrays was developed based on the use of the properties of magic squares; a reflector-calibrator created on the basis of a decelerating structure in the form of a spiral half-wave symmetric vibrator operating in the mode of transverse radiation is proposed for external calibration of the radar and simulation of the RCS of a moving radar target

• the scientific foundations of building intelligent cloud networks from ground technology objects, the integration of sensors of various types and wavelength ranges are considered, and the methods of evaluating the effectiveness of the proposed approaches are proposed.

The material presented in the monograph will be useful for scientists and experts involved in the development of methods and technologies for remote sensing of the environment using the radiation of existing terrestrial and space radio engineering systems.

CHAPTER 1

Electromagnetic and acoustic radiation and their use in monitoring systems

1.1. Acoustic noises of natural and anthropogenic origin

With the development of computer systems, means of storing, processing and transmitting information, it became possible to build monitoring systems based on the use of secondary electromagnetic and own acoustic radiation of objects of natural and artificial origin [1—4]. It is necessary to know the acoustic properties of the atmosphere, the noise characteristics of both natural processes and noises associated with human activity, the functioning of technical objects, and industrial and infrastructure objects to solve this problem [5—13]. Broadband acoustic pulses are of particular interest [6].

The acoustic field of any complex technical object is formed as a superposition of the acoustic fields of individual radiation sources [10]. At the same time, it is possible to shield the radiation of individual sources by elements of the object itself. The propagation of noise in the atmosphere and near the Earth's surface is accompanied by a number of effects that lead to a change in the intensity and spectral composition of the radiation. Thus, the main sources of noise for an airplane are its engines (propellers — for airplanes with a turboprop engine (TPE) and a propeller engine (PE), jets of a power plant (JP) — for airplanes with a turbojet engine (TJE) and a turbojet two-circuit engine (TJTCE), blade machines (fan, compressor, turbine) of a gas turbine engine (GTE), elements of an aircraft airframe (landing gear, wing mechanization). Blade machines of a GTE generate radiation with discrete and continuous frequency spectra. The intensity is dominated by radiation with a discrete spectrum on the harmonics of the frequency of the blades of the impellers (frequencies 1,000...4,000 Hz) and on the harmonics of the rotor frequency (supersonic fans, frequency range 500...2,000 Hz). The jet generates frequency-continuous radiation with maximum power spectral density in the low-frequency region (f_{max} = Sh U_0/d,

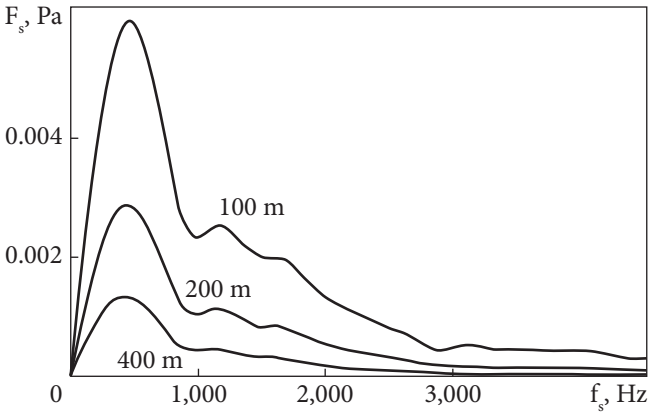

Fig. 1.1. Change in the spectrum of the acoustic pulse of a shot from the distance to the source in the frequency range of 1...4,600 Hz [6]

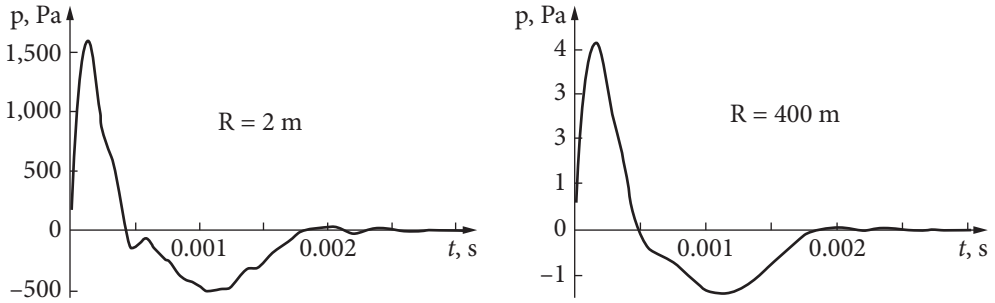

Fig. 1.2. Change in the shape of the pulse with increasing distance from the source [6]

where Sh = 0.2...0.3 is the Strouhal number, U_0 is the outflow velocity of the jet, d is the diameter of the jet nozzle). The aircraft glider is a source of broadband noise with maximum spectral density in the mid-frequency range. Such considerations are also valid for helicopters. In wheeled and tracked ground vehicles, the main sources of noise are the power plant, transmission elements, chassis elements (for tracked machines), and elements of the exhaust system. Different directional diagrams are characteristic of different components of the acoustic field of ground equipment. The spread of power plant noise is usually related to the direction of the exhaust system emission.

The noises of the chassis and transmission systems have a circular diagram. The level of external noise can reach values of 90 dB. The main energy of the acoustic signal is in the band of rotation frequencies of the crankshaft of the power plant. A volley of a rifle or cannon is a broadband acoustic pulse, which is a superposition of a large number of harmonics [6]. When modeling the propagation of such a signal in the atmosphere, it is necessary to take energy losses into account. Since the sound absorption coefficient depends on its frequency, the amplitude of each of the components of a harmonics broadband signal will change with distance according to its own law. Thus, during the propagation of a

broadband acoustic pulse in the atmosphere, in addition to a general decrease in amplitude, a change in its shape will occur. A broadband acoustic pulse can be considered as an aperiodic function of sound pressure as a function of time, which turns to zero at infinity and can be represented as a Fourier integral. To simplify calculations, it is assumed that sound propagates in a homogeneous volume of air, in which normal conditions have been established: temperature — 293.15 K, pressure — 1,013 mbar, humidity — 80%. In this case, the vertical gradient of the sound absorption coefficient is a linear dependence on distance. According to the simulation results [6], the spectrum and the shape dependences of the acoustic pulse on the distance were obtained and are presented in Fig. 1.1 and Fig. 1.2, respectively.

In the assumption of homogeneity of the atmosphere and the absence of side wind, the front of the acoustic pulse will be a segment of the sphere. Table 1.1 gives the RCS values of the acoustic pulse and turbulent inhomogeneities.

Acoustic waves during explosions of chemical explosives have been studied for a long time [5]. As a result of these studies, it was established that air waves at distances of 1...10 km, even with a small depth of charge, are acoustic because with the distance, the waves kept their phase characteristics, and their amplitudes decreased inversely proportional to the distance. The speed of propagation of waves coincided with the speed of sound. At the same time, the amplitudes of acoustic waves depend on the cube root of the mass of explosives, and the main energy of sound vibrations is in the infrasound zone at a frequency of up to 1 Hz [5].

The maximum spectral sound components in thunder strikes are in the frequency range of 50...500 Hz [14]. The sound level of thunder rolls is up to 100 dB. Rain noise is up to 70 dB.

The volume of a human voice at a distance of 1 m in the band 0.1...10 kHz relative to the hearing threshold ($2 \cdot 10^{-5}$ Pa) is — a quiet conversation, whispering — 20 dB, loud conversation — 40 dB, shouting — 60 dB [8].

At night, a whisper can be discovered at a distance of 150 m, a loud conversation — 600 m, and an emotional one — at a distance of up to 1.5 km. The sound of precipitation helps to reduce the range of discovering a whisper to 90 m, a loud conversation to 500 m, and a shout to 1,300 m. If there are cars between the sound source and the receiver — a whisper will not be discovered, a loud conversation

Table 1.1. **RCS value of acoustic pulse and turbulent inhomogeneities [6]**

Distance from the source *R*, m	Acoustic pulse RCS, m^2	RCS of turbulent inhomogeneities, m^2
50	$1.7 \cdot 10^{-8}$	$1.2 \cdot 10^{-10}$
100	$1.0 \cdot 10^{-8}$	$6.7 \cdot 10^{-10}$
150	$7.1 \cdot 10^{-9}$	$1.6 \cdot 10^{-9}$
200	$4.8 \cdot 10^{-9}$	$3.1 \cdot 10^{-9}$
250	$3.4 \cdot 10^{-9}$	$5.1 \cdot 10^{-9}$

will be discovered at a distance of 150 m, and an emotional one at 600 m. In the case of a passing train, only an emotional conversation will be discovered at a distance of up to 90 m. Thus, the determining factor in the detection of acoustic targets is the interfering environment, which is caused by the presence of other noise sources, so the target detection range can vary from dozens of meters to some kilometers.

1.2. Features of the propagation of radio waves in the Earth's atmosphere

When propagating in the Earth's atmosphere, radio waves are affected both by the atmosphere and objects that are in the path of electromagnetic wave propagation. The nature of the propagation of radio waves is determined by the atmosphere state, as well as by the physical processes occurring along the propagation path.

There are daily and seasonal features in the atmosphere that affect the propagation of radio waves. When the Earth's surface is heated and cooled, moisture evaporates, water vapor condenses and falls as precipitation, and both horizontal and vertical shifts of air masses occur. Air masses can undergo both laminar shifts and turbulent mixing. The uneven heating of the Earth's surface leads to the formation, movement, and disappearance of local inhomogeneities. The processes taking place in the atmosphere lead to scattering of radio waves on inhomogeneities, weakening and deviation of the direction of propagation from the straight line.

The influence of the atmosphere has a complex character, which is determined by the very structure of the atmosphere and the variety of processes occurring in it. The Earth's atmosphere has a layered nature and consists of an electrically neutral region, as well as an ionosphere, strongly ionized due to the influence of solar and cosmic radiation, located at altitudes of approximately 50 to 300 km. Although the influence of each area on the propagation of radio waves is considered independently of each other, there is a relation between the ionosphere and the neutral atmosphere [15]; the geomagnetic field and phenomena occurring on the Sun affect the processes occurring both in the Earth's ionosphere and in the neutral atmosphere. In the papers [16, 17], observations were made, and the existence of a strong relation between the state of the ionosphere F layer and the meteorological parameters of the lower atmosphere was shown. Variations of the total electron concentration of the F layer have a dependence of up to 30% on the meteorological parameters of the stratosphere under the condition of a calm geomagnetic state.

The state of the ionosphere as an electrically charged environment depends on many natural and anthropogenic factors. The impact on the ionosphere can be both cyclical and random. The main influence appears "from above" — in the form of radiation and corpuscular energy flows spreading from the Sun. Earthquakes, explosions, rocket launches, volcanic eruptions, cyclonic activity, which generate in-

ternal atmospheric gravity waves (AGW) [18—20], which act as a carrier of disturbances from the troposphere to the ionosphere, have an influence "from below".

Along with the regular altitude dependence of the electron concentration, the ionospheric layer can contain many heterogeneous formations of various sizes that are in constant motion, appearing and disappearing. Scattering on these inhomogeneities leads to the appearance of multipath propagation. The existence of heterogeneous formations leads to the possibility of propagation of radio waves at frequencies that significantly exceed the maximum acceptable ones.

The main feature of of high-frequency (HF) signals use is multipath propagation, which occurs when radio waves are reflected from layers and even during single-hop propagation within the conditions of a calm ionosphere. Multipath propagation leads to fading signals at the receiving point. Similarly, the interference of ordinary and unusual components of a magnetically split wave and the rotation of the polarization plane of the wave during propagation in the direction of the lines of force of the Earth's magnetic field lead to fading. The main method of protection from fading is spatial selection using antennas with a narrow directional pattern, as well as the diversity of antennas by polarization, simultaneous reception on vertical and horizontal antennas with subsequent summing of signals.

Disturbances of the ionosphere caused by the influence of high-power radio waves lead to the appearance of nonlinearity, which can manifest itself in the form of cross-modulation of Luxembourg-Gorky effect signals, as well as to distortions and attenuation of the signal reflected from the ionosphere of the disturbing wave itself.

When predicting the spread of HF radio waves, it is necessary to determine the daily course of the maximum applicable frequencies (MAF), the optimal operating frequencies (OOF), the strength of the electric field at the place of reception or the determination of the daily course of the lowest applicable frequencies (LAF).

For the ionosphere, which is a dispersive medium, the refractive index in the radio range is less than unity, depends on the frequency and increase in the signal propagation path, and leads to group delay and phase advance of radio signals [21].

In the general case, the refractive index for the atmosphere is described by the expression [22, 23]:

$$N = \frac{c_1 p}{T} + \frac{c_2 p_w}{T} + \frac{c_3 p_w}{T^2} + \frac{c_4 10^6 N_e}{f^2}, \qquad (1.1)$$

where c_1 = 77.6 °K/mbar, c_2 = 71.6 °K/mbar, c_3 = 3.747 · 10^5 °K^2/mbar, c_4 = = 40.308 m^3/c^2; p — partial pressure of dry air, p_w — partial pressure of water vapor, N_e — electron concentration.

For the heights where the ionosphere is located, the last term (1.1) prevails, while for the troposphere, the second and third terms are essential.

1.3. Secondary electromagnetic radiation of objects in the optical, VHF, and HF ranges

The rapid development of intelligence tools that work in different ranges of electromagnetic wavelengths began in the late 1970s. Today, there are many detection systems that use various ranges of electromagnetic waves and allow to detect and identify ground objects with high probability [24]. The advantages of visual search for objects include the high resolution of the eye, the ability to work in a wide range of brightness and a wide range of wavelengths, high sensitivity, as well as the logic of the operator, and the ability to recognize the object by movement, shape, silhouette and individual elements. The disadvantages include the dependence of the search efficiency on the training, fatigue, and attentiveness of the operator, as well as the relatively low reaction speed to the appearance of a signal (from 0.1 to 1 sec.). When performing a visual search in the optical range, its effectiveness strongly depends on the transparency of the atmosphere, lighting, and meteorological conditions. In cloudy weather, light objects appear dark against the horizon. Light gray objects are hard to see in cloudy weather. It's quite the opposite in sunny weather (but only against the Sun). In clear weather and on the side opposite the Sun, gray objects are the hardest to see (reflection coefficient is 0.25). Maximum visibility is white in clear weather against the Sun and black in fog and under the Sun (striped beacons). The minimum visibility is gray. Visibility range is the distance when the target becomes visible in the haze. The illustrated range of visibility is the range of visibility of a completely black body (coniferous forest, black ships). A black object from a distance appears bright, but it is not its reflected light, but the light scattered by the air. Therefore, the observation range does not depend on the brightness of the object's illumination (because it does not reflect) but only on the transparency of the air. Depending on the lighting conditions, the visibility range of the object is proportional to the visibility range of a completely black object. Visibility depends on the wavelength — the longer the wavelength, the lesser influence weather factors such as haze, fog, rain, etc. have. The haze transmits red (0.61...0.76 μm) well and poorly transmits blue (0.4...0.52 μm) rays of the spectrum. The haze is stronger on the side of the Sun. Therefore, on a sunny day, dark objects (forests) are blue, and light objects (mountain peaks) are pink. To increase the visibility range in conditions of haze and fog, use yellow light filters (from light yellow in light haze to yellow-orange in fog). The limit contrast at which an object can be detected during the search is considered to be 0.04 — so the difference between the brightness of the object and the background varies by no more than 4%. At the same time, dark objects are 20% better than light ones. When the illuminance decreases below the threshold value, the light source ceases to be visible. At night, when observing group lights, the maximum illuminance is 10^{-6} lux, and during the day — 10^{-3} lux [25]. At the same time, in clear weather at night, a fire with a brightness of 1 cd (one candle) is detected at a distance of 750 m, in heavy haze

(visibility range — 1 km) — at 500 m, and in fog (visibility range — 500 m) — at 300 m [24, 25]. The best visibility at night is inherent in red and green lights, and the worst — yellow. Deforming painting is used to distort the image and make it hard to recognize detected objects. Imitation painting is more effective [24, 25, 26] but it is practically not used for moving objects, except for anti-tank guns, on the shield of which elements that imitate the background can be applied. In the visible part of the spectrum, the contrast between the object in a protective monochromatic color and various natural formations changes sign, lies within +0.2...–0.45, and has, mainly, a small value, except for cases when the background is the sky. This is explained by the fact that the maximum radiation of the sky lies in the short-wavelength part of the visible spectrum. The average contrast of the object with protective painting lies in the range –0,2...–0,4 (more for distant backgrounds, less for near ones) except for a few separate cases (when the front projection is observed on a nearby leafy background or objects, or the object is lighter than the background). In the case when the object is observed against the background of a cloudy sky, its contrast can reach –0.6. And only in a separate case of observation against the background of nearby leafy backgrounds its contrast is insignificant and lies in the range of +0.2...–0.2.

Radar has been used since 1939. Radars operating in the 0.8 cm, 1.8 cm, and 3.2 cm wavelength ranges are mainly used to detect ground objects [24]. Modern radars work in the mode of moving targets selection (MTS) and are equipped with a device for suppressing noise, which allows them to detect moving objects at a long distance. Modern aircraft side view radars allow for detecting objects in motion, aircraft at airfields, and all types of water crossings at distances of 200 km or more. Object visibility is characterized by the radar cross section (RCS). RCS is calculated only for simple objects (sphere, cylinder, plane), and for complex ones (car, aircraft, person), it is determined, as a rule, experimentally. According to the results of theoretical studies and field experiments on the effect of the external shape of the object on the amount of secondary radiation and the average specific ESR of various elements obtained at the same time, the basic design principles of creating objects with a small RCS were developed [24, 27, 28, 29]:

- the object shape is streamlined and should form a single geometric whole with a smooth surface;
- the object should not have surfaces intersecting at an angle equal to or close to 90°, as well as vertical surfaces;
- the number of auxiliary elements placed on the outer surface is minimal. The height of the object should be as minimal as possible.

The largest contribution to the overall reflection from the object is made by elements located outside — boxes, spare fuel tanks, attached equipment, as well as two- and three-sided reflectors formed by the walls of boxes and tanks with a case [24, 29]. In order to reduce the radar visibility of the object, it is advisable to cover these elements with inclined metal sheets, which can reduce twice the RCS [24]. To further reduce RCS, it is necessary to cover the elements of the object

with radio-absorbing materials [24, 28] or radio-scattering materials [24, 28]. The issue of visibility reduction (RCS) in the radiometric range of 2.2 and 3.2 mm (passive radars) is the least understood. The scanning radiometer, which operates at a wavelength of 8 mm, detects mainly horizontal and close to them areas of the object. The use of radio-absorbing materials is approximately equally effective for all these ranges [24, 28].

1.4. Means and methods of remote environmental monitoring

1.4.1. HF and VHF radar, acoustic reconnaissance systems and their capabilities for monitoring anthropogenic objects

The use of optical devices and night vision devices allows for detecting 6...8 (out of 10) similar ground objects at a distance of 200—2,500 m during the day in 30 minutes and up to 4 objects at night in 40 minutes [30]. Detection of the firing position and determination of its coordinates is possible after 3...10 shots. As a result, the effectiveness of countermeasures is no more than 25—30%.

The difficulty of identifying the snipers' positions during counter-terrorist operations leads to the fact that the attacking side has a significant advantage, primarily in conducting warning fire. This allows the attacker to inflict significant damage before an organized response is initiated.

The acoustic method of detecting sniper positions has many advantages [30, 31]:

- the ability to determine the coordinates of the target in real time with an accuracy sufficient for its fire damage;
- circular (360°) detection sector; sufficient depth of reconnaissance (not less than the range of attack by small arms);
- determining the caliber and type of weapon, which allows for analyzing the situation and setting priorities for targets;
- passive (standby) mode of operation, which ensures stability and masking of the system;
- detection of several positions from which fire is conducted simultaneously;
- long continuous operation (a month or more) in automated mode without additional maintenance;
- work, both during the day and at night, under different weather conditions and difficult photo-target conditions;
- small weight and size characteristics;
- the possibility of working on the move;
- relatively low cost of equipment.

Increasing the accuracy of location determination by acoustic reconnaissance systems is possible when using the method of acoustic monitoring of the boundary layer of the atmosphere [32].

Today, the development of acoustic detection systems is the most urgent — but it is held back by the lack of data on the characteristics of acoustic noises of objects and natural disturbances, as well as methods of analysis and evaluation of their characteristics. However, at the same time, the impact of the shot and the flight of the bullet on the environment remains unchanged. Known characteristics of the impact of a shot [30, 31] are the angle of the cone of the shock wave, which depends on the speed of the bullet; the length of the generated sound wave is 0.16...0.6 meters; the approximate frequency range of a sound wave is from 0.6 to 2 kHz. Calculations based on these parameters allow you to determine the place of the shot accurately.

The United States of America already successfully used such systems as "PDC", "Boomerang", "Lifeguard" [31]. Great Britain uses the "BDI" system. In France, a system for locating snipers, "METRAVIB", is proposed [31]. In the Russian Federation, there is a system for locating snipers, "SOVA" [33]. This complex has the ability to determine the location of snipers in real time. The system can be connected to automatic countermeasures. Such a complex solution significantly decreases the time to identify and suppress the enemy. Coordination by the system is reduced to the selection by operator of priorities by targets. "SOVA" can facilitate the execution of tasks for scouts, as it identifies targets up to 1 kilometer. It is possible to use data obtained from various sources. The system makes calculations and makes corrections in real time. The system includes a set of special acoustic sensors, a computing unit and software that allows the processing of information received from acoustic sensors in all directions with simultaneous selection of defects.

Semi-active radar systems of the HF and VHF ranges have been successfully manufactured worldwide for many years [34—38]. The scope of their application is mainly limited to the traditional radar tasks performance, such as the detection and assessment of the movement parameters of air targets (AT). The success of using the technology to detect AT is due to many advantages. First of all, this is a higher probability of detecting low-flying targets due to the rather high (up to several hundred meters) location of third-party transmitters. Thus, during the tests, the "Field" system [34, 35] showed the ability to control the airspace at low and extremely low altitudes (from 50 to 1,000 m) and to ensure the detection of targets moving with radial speeds relative to the radar of at least 30 mps, at distances of more than 40 km. The helicopter flying at a height of 25 m was detected at a distance of 37 km, at a height of 600 m — at a distance of 51 km [34, 35]. The systems have a higher probability of detecting targets made using "Stealth" technology since modern aviation stealth technologies were not planned for use against signals of those frequencies involved in the system. In addition, they are aimed at minimizing the monostatic RCS, while the bistatic RCS can be much larger. In connection with the absence of its own transmitter, the complete passivity of the receiving position is ensured, that is, its higher stealth and survivability compared to an active radar. Moreover, since standard signals are emit-

ted into the air, even the very fact of the presence and operation of the system remains unknown, which makes it possible to talk about its potential undetectability and, therefore, the impossibility of organizing countermeasures [39—42]. However, there is a transmitter in the system, and its failure leads to the termination of the system. Modern systems operating with FM, DAB, and DVB-T signals can reliably detect and track air targets at a range of 50...150 km at altitudes of 25—1,000 m [39—42].

The appearance of commercial television and radio broadcasting stations with amplitude and frequency modulation stimulated the use of radiation from TV and radio broadcasting stations as sources of external illumination [43-45] and led to the creation by the Lockheed Martin company of the "silent sentry" passive radar, which uses the signals of television and radio broadcasting as illumination radio stations for detection and tracking of aerial objects [46]. With the development of cellular communication, work was carried out on the use of GSM 900, 1800, and 3G bands [47, 48]. In England, in 2003, the Roke Manor company developed the Celldar passive radar, which uses the signals of cellular stations for illumination. Work is also being conducted on the use of Wi-Fi [49, 50], WiMAX [51, 52], LTE [53, 54] and digital radio broadcasting [55] signals. Thales is developing the Homeland Alerter 100 radar, which uses frequency-modulated signals in the 88—108 MHz range. Radiation from GPS and GLONASS navigation satellites is also used to study propagation conditions [56]. The use of surface and ionospheric waves of radio broadcasting stations in the HF range [56—61] is involved in the location of surface objects and propagation conditions. Further development of ideas for the use of commercial radio broadcasting stations will allow continuous monitoring of processes taking place in the atmosphere, diagnosis of dangerous meteorological phenomena, and performing the tasks of radar location.

The "Arrow" reconnaissance vehicle (RM) by the Tula SPA [62—64] is designed for the reconnaissance of ground, surface, and air objects. The machine includes reconnaissance systems operating on various physical principles: an optoelectronic system (OES) with a thermal imaging channel, the FARA-VR radar, unmanned aerial vehicles (UAVs), reconnaissance and signaling equipment, and an acoustic gunshot detection system. The radar and optical-electronic module are placed on a telescopic mast, which allows you to conduct reconnaissance from the shelter. These systems provide continuous search, detection, and recognition of such targets as tracked and wheeled vehicles, people in groups and alone, watercraft, light aircraft, helicopters and UAVs, and determination of their coordinates with the display of the movement trajectory on the electronic map of the area.

The equipment of the reconnaissance vehicle also provides determination of the vehicle's own position and the coordinates of detected targets with display on an electronic map, automated control of all systems and means using the on-board information and control system, including continuous processing of navigation data, reception and processing of reconnaissance video and photo in-

formation from UAVs, as well as blocking radio-controlled explosive devices. The maximum instrument range of target detection by RM equipment is 10 km; fire can be conducted at them at distances of up to two kilometers.

The "Kolchuga" complex consists of three stations. It is able to determine the coordinates of ground and surface targets with high accuracy, the routes of their movement at a distance of up to 600 km deep into the territory and 150 km along the front, and for air targets flying at an altitude of 10 km — up to 800 km [65, 66].

The sensitivity of the tract is from –110 to –155 dB/W in the panoramic view band [65]. This is provided by five antenna systems designed to work in several wavelength ranges.

"Kolchuga-M" monitors pulsed and continuous radiation at frequencies 135...170, 230...470 and 750...18,000 MHz [65]. The system is equipped with a parallel 36-channel detection receiver and electronics capable of eliminating background signals and tracking signals from 200 targets simultaneously.

"Kolchuga" can detect and recognize ground and air targets working according to the principle of tropospheric distribution. Known samples of targets are recorded in the system memory. The "Kolchuga" system is difficult to detect since it conducts reconnaissance in a passive mode, i.e., it does not emit radio waves itself.

One of the main threats from the enemy is massive assault and sniper fire. Considering the urgency of the operational disclosure of the positions of shooters (snipers), the role of technical means of intelligence, which allows performing this task, is growing many times over [67, 68].

Unique opportunities for monitoring the environment are offered by the joint use of electromagnetic and acoustic fields [69, 70]. The method of radioacoustic sounding allows to determine the height profiles of humidity and temperature, surface pressure, and estimate the value of the refractive index.

1.4.2. Remote methods of monitoring the state of the Earth's atmosphere

Radiometric, radioluminescence, radar, laser, acoustic, and radioacoustic methods are used as non-contact, remote diagnostic methods, which are based on the phenomena of propagation, absorption, and scattering of electromagnetic and sound waves [71—76]. Both active and passive methods are used [77]. In active sensing systems, a signal emitted by a transmitter that interacts with an object or environment and then received by a receiver is used for illumination. In passive sounding systems, the own radiation of the research object is accepted [78].

Acoustic sounding methods allow continuous diagnosis of atmospheric meteorological parameters in real time at low costs. The relevance of the development of acoustic methods is determined by the need to monitor the environment in conditions of increased man-made influence. Acoustic waves are more sensitive to changes in meteorological parameters than electromagnetic waves,

and therefore, quite simple equipment can be used for probing. At the same time, sound waves used in acoustic sounding have a small penetrating ability in the atmosphere compared to electromagnetic waves. The sensing range is limited by molecular absorption, wind and temperature refraction, and turbulent attenuation. Therefore, the natural area of application of acoustic sounding is the lower part of the atmosphere up to heights of one kilometer. Acoustic sounding (AS) is an effective means of monitoring the atmospheric boundary layer (ABL). The emission of sound waves has been used for remote sensing of the atmosphere for a long time [79—83]. The principle of operation is based on the ability of acoustic waves to scatter on inhomogeneities of the refractive index formed by turbulence in the atmosphere [84, 85].

Unique opportunities for monitoring the environment are offered by the joint use of electromagnetic and acoustic fields [69, 70]. The method of radio-acoustic sounding allows to determine the height profiles of humidity and temperature, surface pressure, and estimate the value of the refractive index [86]. The measurement of temperature profiles is based on the use of the dependence of the speed of sound on the temperature and speed of the medium and the partial reflection of electromagnetic waves from periodic density inhomogeneities created by a propagating sound wave [87, 88]. When the Bragg condition is met, the level of the reflected signal in radio acoustic sensing systems becomes sufficient for registration and processing. Since the length of the sound wave depends significantly on the values of the meteorological parameters, there is a need to adjust the acoustic or radio signal frequency depending on the variability of the meteorological state under Bragg conditions. In the process of measurements, short blocks of sound waves are emitted, the speed and direction of which are measured using a Doppler radar. On the path of sound wave propagation, periodic changes in the dielectric constant of air are created, which are capable of scattering electromagnetic waves with a coherent phase composition if the Bragg condition is met. The length of the electromagnetic wave is practically independent of the state of the atmosphere, while the length of the acoustic signal as the sound pulse propagates along the sounding path changes depending on changes in air temperature. A significant impact on the amplitude of the scattered signal and the accuracy of measurements is exerted by a change in meteorological parameters along the sounding route, which leads to the deformation (stretching or compression) of the sound wave along the spatial coordinate, and, therefore, to the movement of the spectrum of the acoustic signal along the frequency axis, as a result of which the maxima of the spatial spectra of the signals that interact do not coincide, and the range of overlapping spectra narrows. The amplitude of the resulting scattered signal decreases. The systematic error that occurs when determining the speed of sound based on the Doppler frequency shift leads to significant errors in determining the temperature [89]. In some cases, under the influence of meteorological parameters, the acoustic signal can be completely transparent to the radio signal [90].

The basis of acousto-optical methods is the diffraction of light on ultrasonic waves. Previously, these methods were used only for very high frequencies. Recently, the possibility of developing acoustic-optical methods for relatively low frequencies (for which the wavelength is comparable to the diameter of the light beam) has been shown [90, 91]. A harmonic acoustic oscillation and an unmodulated optical beam are emitted into the troposphere [92]. When two beams (acoustic or electromagnetic) interfere, a system of interference bands is formed. The characteristics of this system (first of all, the spatial frequency — the period of the bands) are determined, on the one hand, by the wavelength and, on the other hand, by the geometric parameters of the rays: the angle between the wave vectors, the divergence of the rays, etc., i.e., for the given geometric parameters (which are determined by the design of the device) by measuring the period of the bands, the wavelength can also be determined if the frequency of the wave is known, then it is not difficult to find its phase speed. So, in essence, the task comes down to determining the period of the streaks. At the same time, this period is quite easy to find by the difference in the phases of the signals obtained at two points of the interference pattern [93].

Laser sensing of the atmosphere is carried out using an active optical device — a LIDAR, which works in both continuous and pulsed modes, emitting a laser beam into the atmosphere and measuring the radiation scattered by the ABL in the reverse direction. LIDAR can be located both on the ground and on flying objects. The method of studying the atmosphere using LIDAR has been used for several decades and is described in numerous publications [94-96]. LIDARs can use radiation in the ultraviolet, visible, and infrared parts of the electromagnetic spectrum. Radiation of different ranges has its own characteristics when interacting with various physical processes in the atmosphere. Thus, it is possible to obtain information about various processes in the atmosphere, such as temperature, atmospheric composition, and wind parameters [97, 98]. Due to the small divergence of the laser beam, high spatial resolution is ensured [99].

Radiometric research of the atmosphere is based on the reception of the own (thermal) radiation of the studied medium and the relation between the characteristics of this radiation (attenuation, intensity, polarization, the thickness of the skin layer, etc.) with the physical parameters of the medium. Radiometric research is a relatively powerful tool with accuracy and efficiency and allows judging the quantitative ratio of the components emitted in the atmosphere.

Remote methods of estimating refractive effects, based on the measurement of the radioluminescence temperature of the atmosphere in the absorption lines of oxygen and water vapor, allow for restoration of height profiles of temperature and humidity [100], which are used to calculate the height profile of the refractive index. However, the distribution profiles of meteorological parameters, primarily humidity, obtained this way do not have the necessary accuracy and spatial resolution.

Using the dependence of the radio brightness temperature on the length of the beam path, it is possible to estimate the conditions of propagation of radio waves within the atmosphere layer that effectively absorbs [101—103].

At the O.Ya. Usikov Institute for Radiophysics and Electronics of the National Academy of Sciences of Ukraine (IRE NASU), studies of the radiobrightness temperature conducted on the control transect track over the sea at sliding angles made it possible to determine the generalized parameters of its dependence on the vertical polarization angle, which is good correlates with the conditions of propagation of radio waves [78, 104]. The use of the radiometric method for operational diagnosis of propagation conditions is promising for the assessment of propagation conditions by atmospheric radiothermal radiation [78, 104].

A peculiarity of the microwave radiation of the Earth's atmosphere is the sensitivity of its characteristics to a large number of physicochemical parameters: temperature, humidity, water content of clouds, pressure, gas composition, turbulence, etc. At the same time, the sensitivity of these characteristics to changes in individual parameters is significantly different in the spectrum. The use of several (most sensitive) spectral sections of the microwave range makes it possible to determine a number of physical and chemical parameters of the atmosphere. Passive remote sensing methods determine such essential parameters of the atmosphere as altitudinal distributions of temperature and humidity, the integral content of vapor and liquid water, the zones and intensity of precipitation, and the content of some impurity gases.

The use of the radar method is based on the study of backscattering of radio waves by hydrometeors, dielectric inhomogeneities, accompanying atmospheric phenomena, aerosol particles, and others [105—113]. In addition, they use artificial reflectors emitted into the atmosphere, such as metallized needles with a size of $\sim\lambda/2$, where λ is the wavelength, as well as special radar reflectors or active responders are miniature radio transmitters mounted on probe balls.

Reflections of radio pulses from turbulent and inversion layers in the troposphere were first noted back in 1936 by Colwell and A. Freud (USA) at medium and short waves. The first reports of precipitation detection using centimeter-range radars were received on February 20, 1941, on the coast of Great Britain, when an aircraft was observed using a radar station at a distance of 11 km [114]. During the Second World War, it was discovered that the propagation of high-frequency waves strongly depends on meteorological conditions, and their reflection occurs from inversion layers, cloud and dust masses, etc. The engineered special meteorological radars began to be widely used in many countries [22].

With the help of meteorological radars, studies of clouds, precipitation zones, and areas with increased temperature and humidity gradients, as well as ionized traces of lightning discharges, etc., are carried out. Data from radar observations allow us to judge the spatial position, movement, structure, shape and size of detected objects and their physical properties. When scattering radio waves on particles of clouds and precipitation, when the dimensions r of these particles are

small compared to the wavelength λ (Rayleigh scattering), the magnitude of the radar signal is $\sim r^6/\lambda^4$. Due to the strong dependence of the magnitude of the reflected signal on the size of the particles, radar images do not always coincide with the visual dimensions of the object. The intensity of scattered signals decreases sharply with increasing λ, and, for millimeter and shorter waves, the signal is greatly weakened, which limits the frequency range of meteorological radars, which, therefore, as a rule, use centimeter and millimeter wavelength ranges [115].

The average power of the reflected signals and the intensity of precipitation are related by an empirical relation, on the basis of which it is possible to obtain the distribution of the intensity and amount of precipitation falling along the direction of radiation of the radar. Measuring the attenuation of radio waves leads to an increase in the accuracy of measurements of precipitation intensity and cloud water content [116, 117]. Two-wave radars are used to determine the attenuation of radio waves. If λ is comparable to the size of the particles, the scattering law is significantly different from the Rayleigh law — and with the known frequency dependence of the attenuation of radio waves, the measurement of reflected signals at several wavelengths makes it possible to estimate the size of precipitation particles. The movement of the scatterers leads to a shift in the frequency of the reflected signals due to the Doppler effect. Measuring the Doppler frequency shift, as well as other parameters of the spectrum of radar signals reflected from clouds and precipitation, large aerosol particles, and artificial scatterers, makes it possible to study the structure of various movements in the atmosphere (wind, turbulence, ordered vertical flows) [118].

The use of polarization characteristics as informative signs of hydrometeors [119, 120] and the use of coherent processing of reflected signals [121] based on the measurement of spectral characteristics allows to improve the informativeness of radar signals significantly.

The polarization structure and spectral characteristics of the reflected signal serve to determine the microstructure of clouds, estimate the turbulent pulsations of air masses, and the movement of elementary scatterers (raindrops, snowflakes, and hail particles) [122—125]. Polarization and spectral characteristics of signals scattered and absorbed by hydrometeors are used to determine the spatial distribution of rainfall intensity and assess the potential degree of their danger. Distortions of the signal parameters (frequency and level) of the emitted SHSZ during movement in the near-Earth orbit can be used to diagnose dangerous meteorological phenomena [126], refractive properties of the troposphere above the sea surface and land [127], solving radar problems [128], studying the substratum surfaces [129]. This method is based on the relation between the measure of atmospheric refraction and the parameters of the received signal [130].

During the propagation of satellite signals over the sea surface, direct and reflected signals from the sea surface arrive at the receiving antenna, which forms an interference structure of the received signal, which allows restoring the profiles of the refractive index *n(h)* in the above water layer of the atmosphere, com-

paring with a set of similar analytically calculated dependencies for different atmospheric conditions [131, 132]. The solution of the inverse problem of refraction allows restoring the profile of the refractive index using the Doppler method with an accuracy of no worse than 20...30 N-units [133]. Recently, attempts have been made to use GNSS signals (GPS of the USA and GLONASS of Russia) to diagnose atmospheric processes (tropospheric refraction [134—137], detection of precipitation zones [138—142]), determination of the roughness of the Earth's surface [143—147], as well as detection of aerial objects [128, 148—149].

Remote methods based on the scattering of radio waves by free electrons, inhomogeneities, and thermal fluctuations of the ionospheric plasma are used for studies of the ionosphere, forecasting the conditions of radio wave propagation along the propagation paths, and near-surface radar. Such methods include methods of vertical, inclined, reverse-inclined probing, etc.

The method of incoherent scattering of radio waves is complicated but the most informative. Incoherent scattering radars work with high-frequency radio waves that significantly exceed the ionosphere's own frequencies. The electron concentration is determined by the power of the scattered signal; the values of ion and electron temperatures, ion composition, and ion drift velocity can be obtained from the spectrum. Thus, the method of incoherent scattering allows observation of almost all ionospheric parameters, but only over the measuring installation. Unlike the ionosonde, the incoherent scattering radar measures the values of the ionosphere parameters not only below the maximum electron concentration but also at high altitudes. Another advantage of this method of studying the ionosphere is that it does not depend on its state. The most disadvantages of incoherent scattering radars are their high cost and high power consumption. Therefore, such measuring devices are quite rare, and measurements by them are performed only during short periods of time.

The simplest and most common method of observing the state of the ionosphere is the method of vertical sounding, which, to this day, remains the main means of studying the structure of the ionosphere. The examination of the ionosphere by this method is performed with the help of an ionospheric station — a transmit-receive device that allows obtaining experimentally a profile of the height of reflection from a gradually changing frequency of a vertically emitted wave.

The transmitter works in pulse mode with a pulse duration of approximately 50÷70 μs. The operating frequency of the transmitter changes smoothly in the range from 1 to 20 MHz at a time of 20÷30 μs at a pulse frequency of about 50 Hz. The transmitter power in a pulse is about P_i = 1÷20 kW. The maximum radiation of the antenna is directed vertically upwards.

The height of the reflecting layer is determined by the propagation time of the wave that is emitted to the reflection point and back. The frequency of the reflected wave is equal to the plasma frequency at the reflection point, which is related to the electron concentration. Thus, an ionogram is a plot of the dependence of electron concentration on height. The disadvantages of the method in-

clude the fact that the measurement of ionosphere parameters is performed only above the ionosonde, the ionosonde uses only short waves, and the electron concentration can be measured only up to the height of the maximum of the F2 layer.

It is necessary to use powerful transmitters to achieve high resolution and long distances, which in turn leads to an increase in costs, and the problem of electromagnetic compatibility of the probing system arises as a whole. Signals with linear frequency modulation are widely used in studying the ionosphere to increase the energy potential and ensure high time resolution while limiting the transmitter's radiated power.

The method of diagnostics of a decameter radio channel in real time based on the data of reverse sounding of the ionosphere by a LFM-CW-signal is based on the selection of the leading edge of the backscattering signal during the processing and interpretation of experimental ionograms, where the interpretation of the signals on the ionogram is performed according to the results of the calculation of the minimum group path of the leading edge of the backscattering signal [150].

One of the most effective methods of studying the region of the ionosphere at altitudes of 60—100 km is the method of partial reflections, based on the scattering by weak natural inhomogeneities of the plasma concentration of radio waves in the wavelength range of 2—6 MHz [151]. This method is used to monitor the height-time ionospheric parameters of concentration [152—154], frequency of collisions of electrons with neutral particles [152], the magnitude and direction of wind speed [155—157], determination of parameters of wave disturbances [158—160]. Considering the large-scale nature of the appeared disturbances, it is desirable to have spaced or moving points of remote radio sensing.

Active experiments have become widespread when the ionosphere is heated by powerful radio radiation to study large-scale disturbances in the lower ionosphere and the reaction of the ionosphere to energy processes of natural and anthropogenic origin, which are directed from the side of the Earth [161—164]. In this case, both the parameters of the energy source and the place and time of action are known clearly.

When conducting studies of the ionosphere with the help of the oblique sounding method, HF radio stations can be the sources of radiation [165, 166]. In this case, a passive radar scheme is implemented, which can provide round-the-clock, continuous sounding simultaneously on several paths of radio wave propagation.

1.5. Antennas of HF-band radio telescopes

In 1933, the American astronomer Carl Jansky discovered cosmic radiation in the decameter range of wavelengths. Observations in this wave range are of great importance for the study of radio galaxies and quasars, the interstellar and interplanetary medium, remnants of supernova flares, pulsars, the Sun, and the space around it. Observations in this range are characterized by such problems as

the high brightness temperature of the galactic non-thermal background, shielding of cosmic radiation by the ionosphere, intense radio interference of terrestrial origin, as well as the large dimensions, complexity, and cost of building antenna systems that meet the required parameters.

Antenna systems of radio astronomy instruments must meet strict, sometimes contradictory requirements. With large occupied areas of the phased antenna array, more than 105 m^2 have good matching, sensitivity of antenna elements, and high angular resolution. Angular resolution is determined, in turn, by how optimal the configuration and filling of the array with antenna elements is. At the same time, the antenna should have a width of the directional pattern < 1° in a wide frequency range, allow electrical control of the directional pattern in both coordinates, have a large field of view, be resistant to interference, be reliable, with effective phasing, control, control and calibration systems [167].

Currently, the most effective radio telescopes in the decameter wavelength range are the Ukrainian systems UTR-2 (Ukrainian T-shaped Radio Telescope, 2nd model), URAN (Ukrainian Radio Interferometer of the Academy of Sciences), GURT (Giant Ukrainian Radio Telescope), Dutch LOFAR (The Low-Frequency Array) and LWA (The Long Wavelength Array), located in New Mexico. UTR-2 [168, 169] has the largest effective area of 140,000 m^2 and the highest sensitivity in the range of 8÷32 (40) MHz. Based on the UTR-2 radio telescope, a system of decameter radio interferometers was built to observe radio sources in the RULB mode (Radio interferometry with an ultra-long base). URAN [170, 171] includes UTR-2 and four more rather large (with effective areas from 7,000 to 28,000 m^2) radio telescopes — URAN-1, ..., URAN-4, forming from UTR-2 bases with a length of 42 to 950 km provide polarimetric capabilities. These radio telescopes successfully participate in international studies of the Sun, solar connections, solar wind, Saturn, Jupiter, and other astronomical objects. The GURT radio telescope consists of 100 antenna arrays of 25 elementary antennas, which receive in the range of 10—80 MHz. LOFAR [171] is an interferometer consisting of radio telescopes that receive cosmic radiation in the range from 10 MHz to 240 MHz. Coverage of the entire frequency range is provided by two sets of antennas — low-frequency Low Band Antenna (LBA) 10—80 MHz and high-frequency High Band Antenna (HBA) 120—240 MHz. About 20,000 small omnidirectional antennas grouped at 48 sites located in the Netherlands, Germany, Great Britain, France, Sweden, and Ireland were used as antenna elements of the interferometer. The total area of the antenna field is approximately 300,000 m^2. LWA [172] is a radio telescope located in central New Mexico. Its operating wavelength range is from 10 to 88 MHz, and it is used to study relativistic particles, the evolution of space, astrophysical plasma, radio radiation from Jupiter-like planets in the decameter range, and giant flares from magnetars. Currently, it consists of 256 antennas [173], with the prospect of building 53 stations with a total number of 13,000 dipole antennas located in a circle with a diameter of about 400 kilometers.

Changing the direction of radiation reception in these instruments occurs by changing the phase delay of signals coming from individual antennas; synthesis of directional diagrams occurs with the help of software. The problem of optimizing the antenna systems of such unique and expensive measuring instruments is extremely urgent.

1.6. Smart Grid technology in detection systems

The main direction of development of detection systems at the current stage is "intellectualization". Thanks to achievements in the field of technical cybernetics, computing, and a number of other sciences, it became possible to create integrated adaptive systems that quickly and effectively respond to changes in the environment. The most important achievement is that it is now possible to process incoming information and optimally manage all subsystems in real time. This led to the further development of various forms and methods of intelligence, united by one ideology [174—179]. From here, there is a sharp, leap-like change in the requirements for individual samples and the appearance of qualitatively new technical devices. One of the concepts envisages increasing the efficiency of both individual performers and structural formations by distributing individual tasks between several objects, combined by means of an automated control system into a single formation — a "system of systems". The system may include manned ground vehicles, unmanned aerial vehicles (UAVs), automatic systems (separate devices), and ground remotely controlled vehicles.

Conclusions

1. The rapid development of the modern technical base has led to an increase in interest and use of passive and active-passive radio means, as well as acoustic reconnaissance. This is due to the use of existing electromagnetic fields for illumination (active-passive systems) or the objects' own thermal and acoustic radiation (passive systems) for their detection and identification;

2. A significant advantage of active-passive and passive systems, in comparison with active radio- and sound-sonar systems that can unmask themselves, is their significantly greater survivability;

3. Active-passive systems can use the existing electromagnetic fields of both terrestrial and space radio systems, including communication and navigation systems, global satellite navigation, radiation from TV and broadcasting satellites, as well as terrestrial broadcasting systems, to illuminate the environment. This allows, on the one hand, not to spend significant funds to create specialized environmental lighting systems and, on the other hand, not to increase its environmental pollution with additional electromagnetic radiation;

4. Because of the greater stealth and survivability of active-passive complexes, including passive acoustic reconnaissance and targeting systems, their use for detecting tracked and wheeled ground vehicles and aerial objects is promising. Attempts are being made to use them to detect individuals and groups, to find and determine the location of a sniper after a shot has been fired as part of anti-terrorist operations, as well as to analyze the occurrence of extreme situations in places of large crowds;

5. When propagating in the Earth's atmosphere, radio waves are affected by both the atmosphere and objects that are in the path of propagation of radio waves. It is necessary to study the peculiarities of the propagation of radio waves in the Earth's atmosphere, create methods for diagnosing the parameters of the troposphere, monitoring dangerous meteorological phenomena, developing new methods and techniques for monitoring the environment (atmosphere), objects in it, natural (precipitation) and anthropogenic (aircraft) origin, as well as characteristics of the underlying surface (land, sea) to forecast the conditions of propagation;

6. Antenna systems, which are one of the defining components of receiving systems for remote sensing of the HF range, due to their significant dimensions, require further development of optimization algorithms as the location of receiving elements of antennas without deterioration of basic parameters, such as angular resolution, width of the directional pattern, frequency range and the possibility of electrical control of the beam, as well as the reduction of the dimensions of individual elements.

Thus, the use of existing electromagnetic and acoustic radiation is an urgent task within the framework of the creation of a global information field concept. In addition, nowadays, not only the expansion of the types of sensors that use physical fields of various nature but also the rational combination of information obtained with their help, as well as the use of smart grid technologies (cloud networks) to create intelligent spatially distributed networks, are gaining special relevance, which provides, due to this, an increase in the efficiency of the creation and use of information flows for solving the tasks of passive monitoring of mobile equipment objects. In many ways, the solution to these questions is hindered by the lack of experimental data on the statistical characteristics of radiation and reflection of acoustic and electromagnetic fields of natural and anthropogenic objects and the scientific basis of their application for solving the problem of environmental monitoring.

CHAPTER 2

Acoustic fields of ground and air objects

2.1. Acoustic noise levels

The range and resolution of passive acoustic systems depend on the level and spectrum of the acoustic signal, as well as on the properties of the propagation medium and the underlying surface [67, 68, 180—183].

Noise levels are estimated with respect to the threshold level of audibility — 10^{-12} W/m^2 [184]. Typical values of noise levels of some sources according to literature data are given in Table 2.1.

The detection range is affected by the distribution of power by frequency, as well as the height of the location of the sound source relative to the Earth's surface.

Ground vehicles are characterized by two sources of sound — the exhaust system of the internal combustion engine and additional equipment. The placement height is 0.8...1.2 m and 1.4...3.0 m [185], respectively. The height of placement of receiving microphones can be from 1.6 m to 2 m [185].

Data on octave attenuation of the signal in the atmosphere, depending on its parameters, are given in [186]. The dependence of linear attenuation for different frequencies obtained from the presented data is shown in Fig. 2.1 [186, 187].

It can be seen that linear attenuation decreases with increasing temperature and humidity and is well approximated by the dependence:

$$\gamma\left[\frac{dB}{km}\right]=\begin{cases} A+B_1 f+B_2 f^2, \text{ when} \geq 0, \\ 0, \text{ when} \leq 0. \end{cases} \quad (2.1)$$

Approximation coefficients are given in the Table 2.2., where A, B_1, and B_2 are parabolic regression coefficients, R is the correlation coefficient of the regression equation with experimental data, and SD is the root mean square error of approximation.

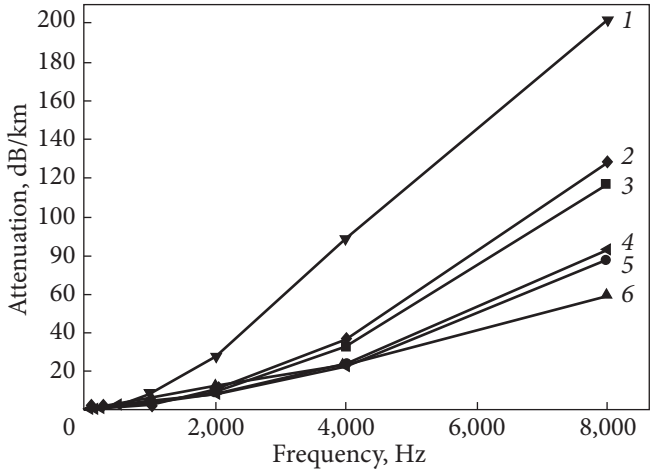

Fig. 2.1. Dependence of linear attenuation during acoustic signal propagation in the atmosphere on temperature t °C and relative humidity η: *1* — t = 15 °C, η = 20%; *2* — = 15 °C, η = 50%; *3* — t = 10 °C, η = 70%; *4* — t = 15 °C, η = 80%; *5* — t = 20 °C, η = 70%; *6* — t = 30 °C, η = 70%

Table 2.1. **Typical values of noise levels**

Source of noise	Sound pressure level, dB	Sound power density, W/m^2	Frequency band, Hz	Note	Source of information
Complete silence 0	0	10^{-12}		It depresses	147
The rustle of leaves	10	10^{-11}		Sound comfort	147
Whisper	20	10^{-10}			147
Rain	50…70		25—1,000		147
Normal conversation	60				147
Human steps	60…65	$10^{-6}…3\cdot10^{-6}$	500—10,000		12
Wind	65—77	$3\cdot10^{-6}…5\cdot10^{-5}$	20—1,000	Max level	12
Stationary machinery:					
caterpillar	65—72	10^{-5}	30—2,000	At a distance of 100 m	12
wheeled	60—65	10^{-6}	30—2,000	At a distance of 100 m	12
Mobile tracked machinery	80—89	$10^{-4}…10^{-3}$	15…1,000	At a distance of 100 m	12
The plane is taking off	140	10^{2}		Near	10
	100	10^{-2}		At a distance of 100 m	10
Aerodynamic objects:					
helicopter	82—89	$10^{-4}…10^{-3}$	100—2,000	During the flight	12
plane	72—74	$10^{-4}…10^{-3}$	100—2,000	During the flight	12
Bullet shock wave	70—100	$10^{-5}…10^{-2}$	~600—2,000	At a distance of 100 m	6

Table 2.2. **Coefficients in regression dependences of linear attenuation**

Temperature, °C	Humidity, %	A	A_1	B_1	B_2	R	SD
10	70	0.314	0.1	0.00161	1.622E-6	0.99996	0.2945
20	70	0.768	0.1	0.00199	9.489E-7	0.9990	0.9793
30	70	0.397	0.1	0.00488	3.060E-7	0.997	1.369
15	20	–4.616	0.3	0.0172	1.097E-6	0.9958	5.47
15	50	0.602	0.1	0.00168	1.796E-6	0.9999	0.390
15	80	0.644	0.1	0.00157	1.086E-6	0.9996	0.672

The value of the constant component, which determines the attenuation of the signal at low frequencies, should be taken from the experimental data — coefficient A_1 given in the Table 2.2.

It is necessary to know both the original radiation spectrum and the dispersion properties of the propagation medium, as well as the influence of the underlying surface, to estimate the spectrum at some distance from the sound source.

2.2. Spectra of acoustic radiation

Ground and air objects emit sound in a rather wide band; however, the spectra contain characteristic spectral components associated with the operation of the engine (frequencies multiples of the rotation frequency of the engine crankshaft — Fig. 2.2, *d*, propeller blades or blades of turbines and compressors — Fig. 2.2, *a*, *b*). The nature of the signal is quasi-stationary.

When a shot is fired, the signal is essentially not stationary. It is necessary to use its description as decomposition by harmonic functions (Fourier spectrum) — Fig. 2.2 with caution.

When calculating the detection range and resolution, it is convenient to use a spectrum approximation model with some fictitious parameter characterizing its effective width [188].

To approximate the spectrum in the high-frequency region, you can use fractal dependences of the form [188]:

$$S(f) = S_0 \left(1 + \left(\frac{f}{\Delta f} \right)^n \right)^{-1}, \tag{2.2}$$

where Δf is the width of the spectrum, S_0 is the value of the spectral density at zero frequencies, and n is the exponent characterizing the rate of its decrease. Table 2.3 shows the results of approximating the spectra of some types of objects depending on the species:

$$\lg S(f) \approx a + b \lg(f). \tag{2.3}$$

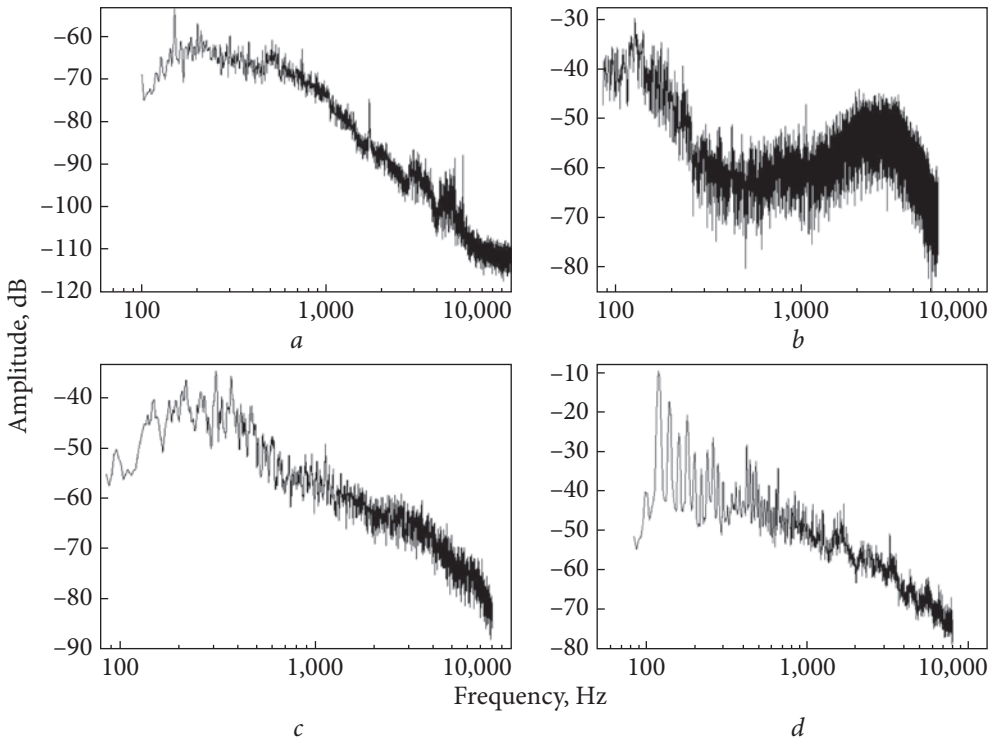

Fig. 2.2. Spectra of acoustic signals: *a* — MI-2 helicopter; *b* — FALCON aircraft; *c* — cannon shot; *d* — diesel 800 rpm

Table 2.3. **Coefficients of approximation of the high frequency part of the spectrum**

Object type	Frequency band, Hz	*a*	*b*	*R*	$n = -\frac{b}{10}$
Mi-24 helicopter	500…8,000	44.0	–39.7	–0.972	3.97
Diesel 800 rpm	500…8,000	22.3	–24.2	–0.941	2.42
Diesel 2,000 rpm	150…2,000	30.34	–26.4	–0.887	2.64
T-34 tank	100…8,000	8.27	–20.29	–0.897	2.03
Shot	150…8,000	2.5	–17.5	–0.922	1.75
Shot 200 mm	150…8,000	45.77	–24.49	–0.944	2.45
Shot	400…6,000	10.5	–22.2	–0.857	2.22
Jet plane (1st hump) from 540 to 2,500 Hz	500…2,500	55.22	–33.24	–0.800	3.32
Jet plane (2nd hump) from 4,5 · 10 Hz	4,500..8,000	183.25	–62.1	0.731	6.21

For most objects (ground equipment, gunshot sound), the spectral density decrease rate of the spectrum is close to $n \approx 2$.

This means that the spectrum, in many cases, can be approximated by the expression:

$$S(f) = S_0 \frac{1}{1 + \left(\frac{f}{\Delta f} \right)^2}, \tag{2.4}$$

and correlation functions:

$$\rho(\tau) = \sigma_S^2 \exp\left(-\left| \frac{\tau}{\tau_{05}} \right| \right), \tag{2.5}$$

where $\sigma_S^2 = S_0 \Delta f$ and $\tau_{05} = \frac{1}{2\pi\Delta f}$.

To estimate the range of the acoustic reconnaissance systems, we introduce the concept of the integral attenuation coefficient $L(\bullet)$ of the acoustic signal and its spectrum $S_r(f, R, h_r, h_T)$ from the sound source located at a height h_T to the receiver located at a height h_r, taking into account the atmosphere $L_0(f, R)$ and the subsoil surface $V(f, R, h_r, h_T)$ when spreading over a distance R, which are determined by the ratio:

$$L(R, h_r, h_T) = \frac{\int_0^\infty S_r(f, R, h_r, h_T) df}{\int_0^\infty S_r(f, R = 0, h_r, h_T) df} = \frac{\int_0^\infty S_T(f)\, L_0(f, R)\, V(f, R, h_r, h_T) df}{\int_0^\infty S_T(f) df}. \tag{2.6}$$

Fig. 2.3 shows radiation spectra calculated at different distances at an air temperature of 15 °C and a humidity of 20%.

The influence of the distribution surface was not taken into account, i.e. $V(f, R, h_r, h_T) \approx 1$. Data on sound attenuation in the atmosphere were used in the calculations [186, 187]. It can be seen that the spectra of wider-band sound sources are more strongly transformed, and with increasing range, the high-frequency components of the spectrum are most strongly attenuated. At the same time, the radiation spectra for all sources narrow (Fig. 2.3, *a*—*d*), and at great distances from the noise source, they become similar (Fig. 2.3, *d*). At the same time, near the radiation source, the differences between them are significantly greater (Fig. 2.3, *a*).

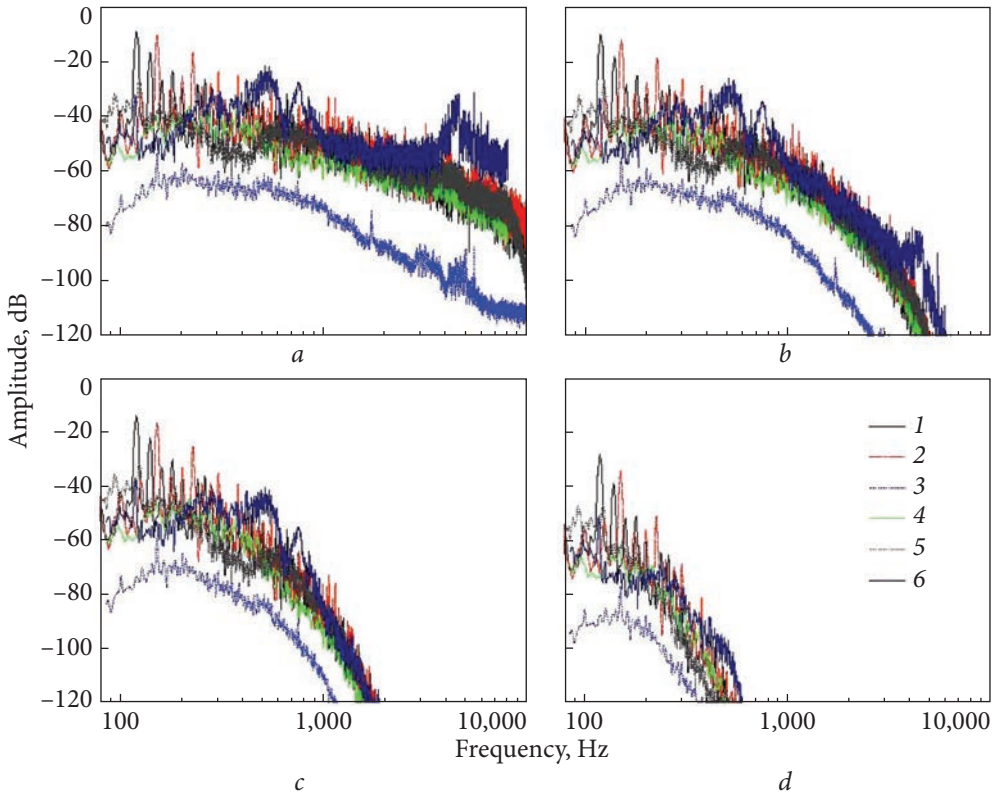

Fig. 2.3. Spectra of acoustic signals at different distances from the sources during propagation in the atmosphere: *a* — near the source; *b* — range of 0.5 km; *c* — range of 2 km; *d* — range of 8 km; *1* — diesel engine 800 rpm; *2* — diesel engine 2,000 rpm; *3* — Mi-24 helicopter; *4* — the sound of a shot; *5* — T-34 tank; *6* — Jet plane

The width of the spectrum $\Delta f_e(R, h_r, h_T, \alpha)$ at the levels from the full power α, taking into account the expression (2.6), can be determined from the ratio:

$$\frac{\int_0^{\Delta f_e} S_r(f, R, h_r, h_T)df}{\int_0^{\infty} S_r(f, R, h_r, h_T)df} = \alpha. \qquad (2.7)$$

Table 2.4 presents the values of the effective width of the radiation spectrum of some noise sources at different power levels α%, and Fig. 2.4 shows changes in the normalized spectrum width at various distances from them during propagation in the atmosphere for the case of the greatest attenuation.

It can be seen that aerial objects and the sound of a shot have the largest spectrum width, which contains half of the radiated power. Fig. 2.4 presents the cal-

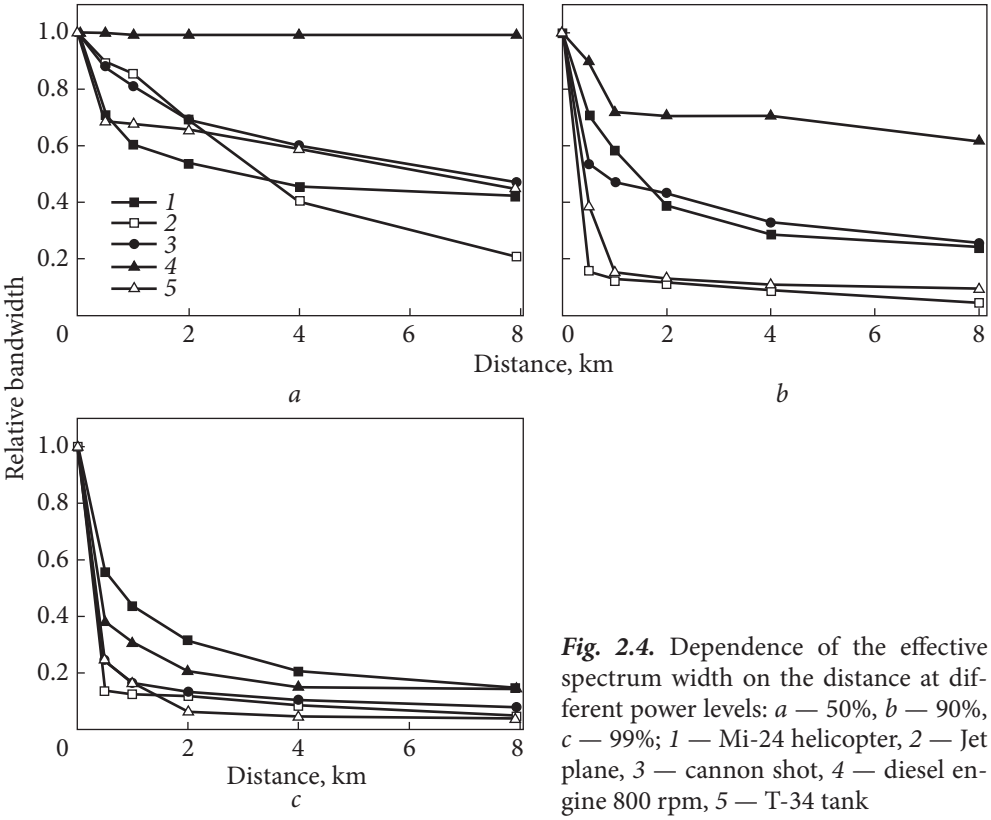

Fig. 2.4. Dependence of the effective spectrum width on the distance at different power levels: *a* — 50%, *b* — 90%, *c* — 99%; *1* — Mi-24 helicopter, *2* — Jet plane, *3* — cannon shot, *4* — diesel engine 800 rpm, *5* — T-34 tank

Table 2.4. **The effective spectrum width of some sources of acoustic noise**

Object type	Full power level, %		
	50	90	99
	Spectrum width, Hz		
Mi-24 helicopter	358	827.7	1,626.7
Jet plane	572	4,666	6,391.3
Diesel engine 800 rpm	121	199,2	1,251
T-34 tank	181.7	1,349.9	4,522.6
Cannon shot	315	834.4	3,658

culated values of the effective width of the radiation spectrum of various sources at different distances. The spectrum of most objects narrows rather quickly due to stronger attenuation of high frequencies, see Fig. 2.4. The narrowing of the effective spectrum width with range will lead to a deterioration in the resolution of acoustic reconnaissance systems.

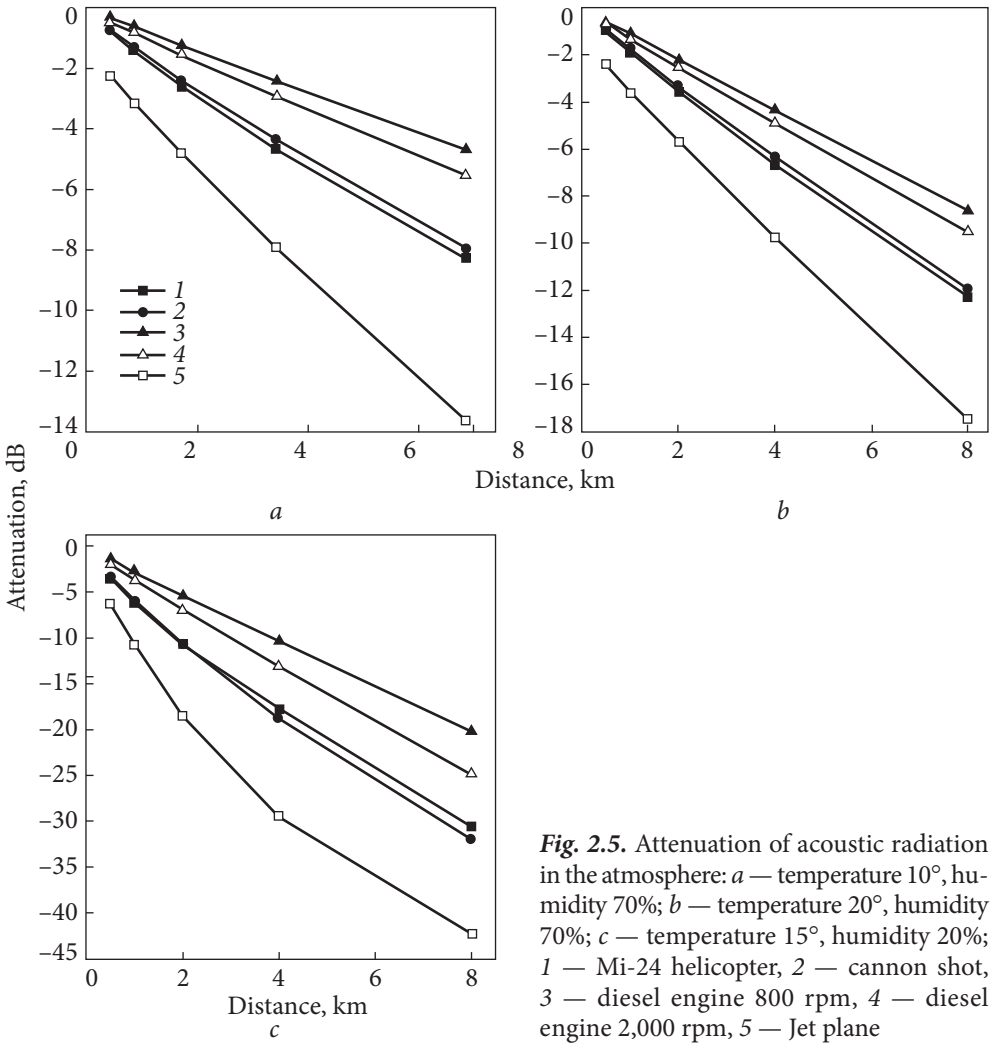

Fig. 2.5. Attenuation of acoustic radiation in the atmosphere: *a* — temperature 10°, humidity 70%; *b* — temperature 20°, humidity 70%; *c* — temperature 15°, humidity 20%; *1* — Mi-24 helicopter, *2* — cannon shot, *3* — diesel engine 800 rpm, *4* — diesel engine 2,000 rpm, *5* — Jet plane

Table 2.5. **Coefficients of linear regression approximation of the dependence of integral attenuation in the atmosphere on range for various noise sources**

Sound source	Coefficients of approximation	Jet plane	Mi-24 helicopter	Shot	Diesel engine 800 rpm.	Diesel engine 2,000 rpm.
Temperature = 10	γ_0	–1.66	–0.43	–0.39	–0.078	–0.17
Humidity = 70%	γ_1	–1.51	–1.00	–0.96	–0.58	–0.68
Temperature = 20	γ_0	–1.60	–0.39	–0.36	–0.073	–0.15
Humidity = 70%	γ_1	–2.00	–1.50	–1.46	–1.069	–1.18
Temperature = 15	γ_0	–6.94	–2.79	–2.40	–0.32	–0.72
Humidity = 20%	γ_1	–4.69	–3.55	–3.78	–2.49	–3.03

The values of integral attenuations of the acoustic field of various radiation sources at different distances shown in Fig. 2.5 are obtained using the real spectra of sound sources [186, 188] based on the relation (2.6).

Integral attenuation for all typical sources, as can be seen from Fig. 2.5, is satisfactorily approximated by a linear dependence:

$$L\left[dB\right] \approx \gamma_0 + \gamma_1 R\left[km\right]. \tag{2.8}$$

Approximation coefficients obtained by the method of least squares (LSM) are given in the Table 2.5.

An increase in the number of revolutions from 800 to 2,000 rpm leads to an increase in the spectral density of high-frequency components (Fig. 2.3 *a*). For modes with many engine revolutions, a greater integrated attenuation of acoustic radiation in the atmosphere will be characteristic. This is manifested in large values of coefficients γ_1 — which characterize the slope of the dependence of attenuation on range. In practical calculations, the γ_0 coefficient should be taken as $\gamma_0 \approx 0$. When propagating an acoustic signal near the Earth's surface, it is necessary to consider the effect of reflection of the signal from the Earth's surface in addition to accounting for absorption in the atmosphere.

2.3. Range of acoustic reconnaissance systems

Influence of the Earth's surface on sound attenuation. Interference of signals coming directly from the noise source to the receiver and after reflection from the Earth's surface can lead to interference weakening of the received sound pressure. When a plane sound wave falls on the plane boundary of the distribution of two media with density ρ, ρ_1 and propagation speed c, c_1, the reflection coefficient F will be determined by the impedance of the incident Z and the one that passed into the second medium Z_1 waves [189, 190]:

$$F_0 = \frac{Z_1 - Z}{Z_1 + Z}, \tag{2.9}$$

where $Z=\rho c/\cos\theta$, $Z_1=\rho_1 c_1/\cos\theta_1$.

In the case when the refractive index is $n = \frac{c_1}{c} \neq 1$, and $\theta \to \pi/2$ (sliding incidence), we get $F_0 \to -1$. If F_0 is the reflection coefficient from a smooth surface, then the specular reflection coefficient for an uneven surface of the same material can be represented as [191, 192]:

$$F = F_0 \rho_S, \tag{2.9a}$$

where ρ_S is the reflection coefficient. Its value can be determined by analogy with the value for electromagnetic fields [191, 192]:

$$\rho_S^2 = \exp\left\{-\left(\frac{4\pi\sigma_h \sin\psi}{\lambda}\right)^2\right\}. \tag{2.10}$$

In this formula, σ_h is the rms value of the height of surface irregularities, ψ is the angle of reflection, and λ is the wavelength.

In cases where the real surface is replaced by a flat surface in calculations, the angle of reflection will be equal to:

$$\psi \approx \frac{h_T + h_r}{R}, \tag{2.11}$$

where h_T is the height of the source, h_r is the height of the receiver, and R is the distance between them.

Then the attenuation coefficient of the surface of the acoustic signal within the framework of the two-beam model is:

$$V = \sqrt{1 + 2F\cos\left(\frac{4\pi h_T h_r}{\lambda R}\right) + F^2}, \tag{2.12}$$

when $\left(\frac{4\pi h_T h_r}{\lambda R}\right) \to 0$. $F_0 \to -1$, and $F \approx -1 + \delta$, then

$$V \approx 2\rho_S \left|\sin\left(\frac{2\pi h_T h_r}{\lambda R}\right)\right| \approx 2\rho_S \left(\frac{2\pi h_T h_r}{\lambda R}\right), \tag{2.13}$$

when

$$\rho_S \approx 1 \tag{2.14}$$

you can write:

$$V^2 \approx 4\sin^2\left(\frac{2\pi h_T h_r}{\lambda R}\right) \approx 4\left(\frac{2\pi h_T h_r}{\lambda R}\right)^2 = 4\left(\frac{2\pi h_T h_r f}{cR}\right)^2. \tag{2.15}$$

Using the expressions (2.9—2.12) to calculate the attenuation factor of the interface, it is possible to determine the signal spectrum of the acoustic radiation source $S_r(f, R, h_r, h_T)$ at a distance R, taking into account losses during propagation in the atmosphere $L(f, R)$ and the influence of the subsoil of the Earth:

$$V(f,R,h_r,h_T):\ \ S_r(f,R,h_r,h_T) = S_T(f)\, L(f,R)\, V(f,R,h_r,h_T). \tag{2.16}$$

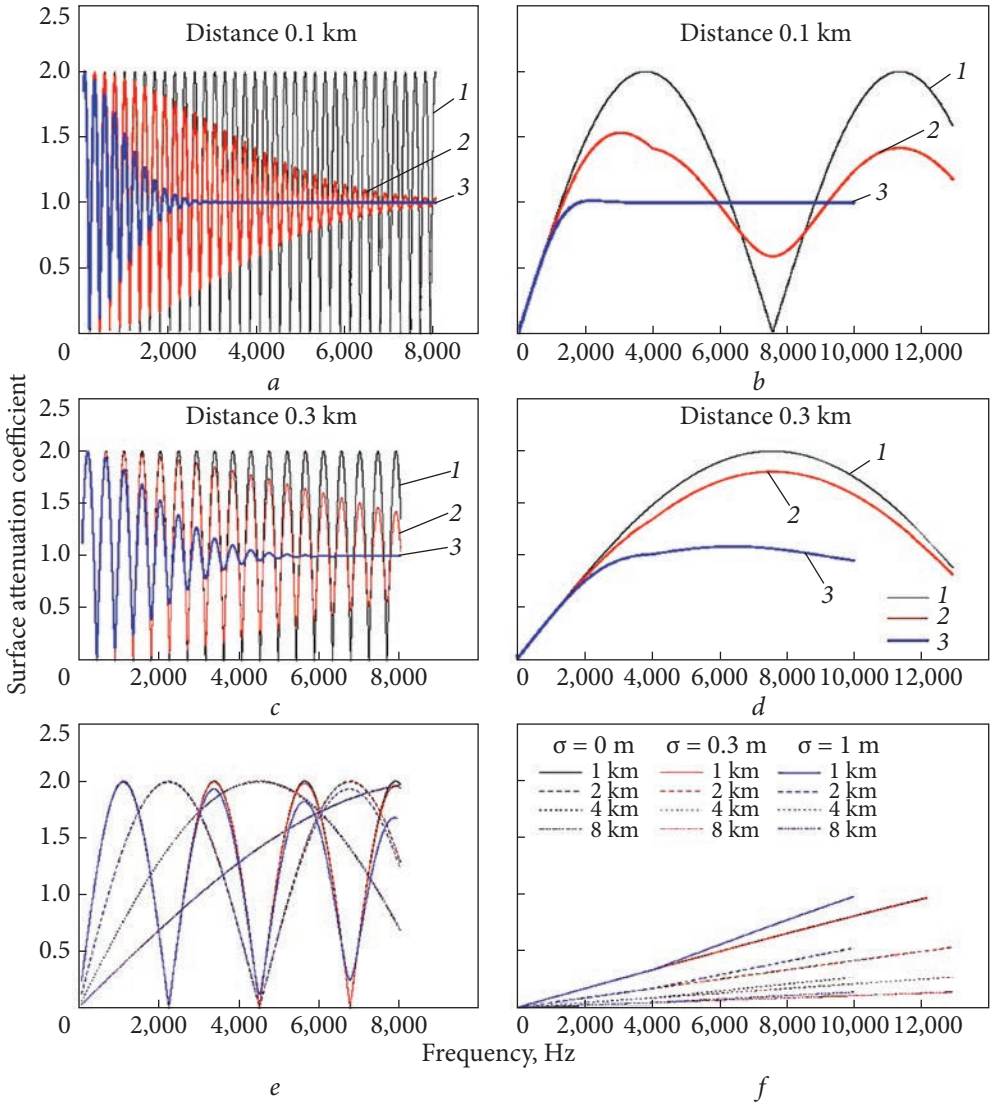

Fig. 2.6. Dependencies of the surface attenuation coefficient at different distances from the sound source for different frequencies depending on the degree of surface roughness: *a*, *c*, *d* — aircraft with a flight height of 50 m, *b*, *d*, *e* — ground equipment; *a*, *b* — distance 0.1 km, *c*, *d* — distance 0.3 km; *d*, *f* — distances of 1...8 km; *1* — σ ≈ 0 m, *2* — σ ≈ 0.3 m, *3* — σ ≈ 1 m

Taking (2.16) and (2.6) into account, it is possible to determine the integral attenuation coefficient $V_1(\bullet)$ of the acoustic signal due to the atmosphere and the underlying surface during propagation over a distance R. The values of the attenuation coefficient of the surface at different frequencies for different degrees of roughness and at various heights of the location of the sound source are shown in Fig. 2.6.

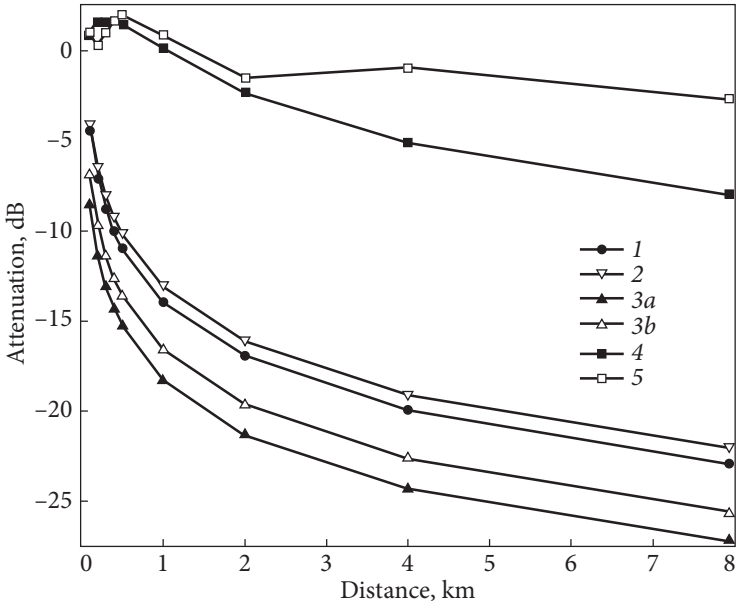

Fig. 2.7. Influence of the distribution surface on sound attenuation: *1* — cannon shot, *2* — T-34 tank, *3* — diesel engine: 2,000 rpm, 800 rpm, *4* — Mi-24 helicopter, *5* — Jet plane

They are calculated using ratios (2.9—2.12). It can be seen that as the degree of surface roughness increases, the depth of interference dips decreases. For higher-frequency sound components, the destruction of the scattering mirror mechanism occurs earlier than for low-frequency components.

It follows from the given data that interference attenuation of sound by the Earth's surface must be taken into account for ground equipment and aircraft at heights of 50...100 m. At higher flight heights, it can be neglected for distances at which acoustic detection can be performed. It can be seen that the growth of the rms height of the irregularities leads to an earlier destruction of the interference structure of the field. For objects of tracked and wheeled equipment (height of the sound source 1...2 m), the interference area begins from distances of several meters for low sound frequencies, dozens of meters for medium, and hundreds of meters for high frequencies.

The surface attenuation coefficient in it decreases quadratically with distance. In this zone, surface roughness does not affect its value. At distances of more than a kilometer, detection of ground equipment objects is performed in the zone of deep interference fading of the signal. Due to the significantly greater bandwidth of acoustic noise sources compared to objects of radar surveillance, the influence of the distribution surface on different parts of the emitted noise spectrum is also significantly different. Due to the surface, low-frequency components are suppressed more strongly, and high-frequency components are suppressed less.

The results of the evaluation of the integral values of the surface attenuation factor for various noise sources are shown in Fig. 2.7.

It can be seen that the attenuation of the signal for air objects is small due to the influence of the interface. At the same time, it can exceed 25 dB for objects of ground equipment and this must be taken into account during calculations.

The equivalent sound pressure level from the leeward side $P_1(R)$ at the receiver in a logarithmic scale can be calculated for each point source, and taking into account the radar equation and ratios (2.6) can be written in the form:

$$P_1(R) = P_0 + G - L, \tag{2.17}$$

where P_0 is the sound power level of a point source of noise in relation to the reference value of sound power equal to 1 pW expressed in dB; G is a correction that takes into account the directionality of a point source of noise and shows how much the equivalent sound pressure level of a point source of noise in a given direction differs from the sound pressure level of a non-directional point source of noise with the same level of sound power P_0, dB. L is attenuation during sound propagation from a point source of noise to the receiver, taking into account the influence of all factors, dB.

The extinction $L(R)$ in formula (2.17) is calculated by formula (2.18)

$$L(R) = L_{div}(R) + L_{atm}(R) + \mathrm{V}_{gr}(R, h_r, h_T) + L_{bar} + L_{misc}, \tag{2.18}$$

where $L_{div}(R)$ is attenuation due to geometric divergence (attenuation in free space due to the difference in sound energy); $L_{atm}(R)$ — attenuation caused by atmospheric sound absorption; V_{gr} — attenuation caused by the influence of the Earth; L_{bar} — attenuation caused by shielding; L_{misc} — damping for other reasons.

Attenuation due to geometric divergence. Attenuation due to geometric divergence (attenuation in free space due to the difference in sound energy) $L_{div}(R)$ [dB], which occurs as a result of the spherical propagation of the sound of a point source of noise in a free sound field, is calculated by the formula:

$$L_{div}(R)\ [\mathrm{dB}] = 20 \lg (d / d_0). \tag{2.19}$$

The detection ranges of objects of acoustic radiation under various weather conditions and external disturbances were estimated using the data on the noise level of various sources (Table 2.1) and the above-calculated values of the integral factors of attenuation of the atmosphere and the underlying surface. They are listed in the Table 2.6. During the calculations, it was considered that an excess of the useful signal over the noise by approximately 10 dB is necessary for detection. The analysis shows that aerial objects can be detected in the absence of obstacles at distances of more than 8 km; at low temperatures and humidity, the range

Table 2.6. **Estimated detection ranges in kilometers for different atmospheric conditions and types of external interference**

Meteorological conditions of the objects' detection range	Without any problems	The rustle of leaves	Wind, rain	Without any problems	The rustle of leaves	Wind, rain	Without any problems	The rustle of leaves	Wind, rain
	Jet plane			Mi-24 helicopter			Shot		
	Influence of the atmosphere and surface								
Temperature = 10, humidity = 70%	>8	>8	1.76	>8	>8	0.9	>8	>8	7.45
Temperature = 20, humidity = 70%	>8	>8	1.7	>8	>8	0.87	>8	>8	6.5
Temperature = 15, humidity = 20%	7.3	5.7	1	7.7	5.93	0.66	>8	>8	3.4
	Influence of the atmosphere								
Temperature = 10, humidity = 70%	>8	>8	1.88	>8	>8	0.89	>8	>8	>8
Temperature = 20, humidity = 70%	>8	>8	1.77	>8	>8	0.86	>8	>8	>8
Temperature = 15, humidity = 20%	>8	>8	0.95	>8	>8	0.63	>8	>8	8,1
Meteorological conditions of the objects' detection range	Without any problems	The rustle of leaves	Wind, rain	Without any problems	The rustle of leaves	Wind, rain	Without any problems	The rustle of leaves	Wind, rain
	Diesel engine 800			Diesel engine 2,000			T-34		
	Influence of the atmosphere and surface								
Temperature = 10, humidity = 70%	>8	7.5	<0.5	>8	7.58	<0.5	>8	7	<0.5
Temperature = 20, humidity = 70%	>8	6.4	<0.5	>8	=6.5	<0.5	>8	6.1	<0.5
Temperature = 15, humidity = 20%	=6.4	4.3	<0.5	=5.9	=4	<0.5	=6.2	4	<0.5
	Influence of the atmosphere								
Temperature = 10, humidity =70%	>8	>8	0.94	>8	>8	0.93	>8	>8	0.88
Temperature = 20, humidity = 70%	>8	>8	0.91	>8	>8	0.9	>8	>8	0.85
Temperature = 15, humidity = 20%	>8	>8	0.8	>8	>8	0.75	>8	>8	0.7

decreases to 5 km. In case of significant interference, the detection range may be less than 1 km.

The sounds of gunshots with weak interference can be detected at distances of more than 8 km, with strong noises at distances of 6...7 km, and in bad weather conditions, it can decrease to 3 km. In the absence of obstacles, objects of ground equipment can be detected at distances of 4...6 km.

It should be noted that during the evaluations, the noise was assumed to be a stationary Gaussian process with a given average intensity. Human and animal movement sounds are a significantly non-stationary process, and this can lead to additional losses in the signal/interference ratio during detection [193, 194].

2.4. Acoustic fields of ground and small air objects

Currently, there is increasing interest in active-passive means of radio [38—41] and acoustic reconnaissance [1, 4, 12, 30, 31]. Works [67, 68, 180] proposed a method for estimating the range of acoustic reconnaissance systems, which takes into account the influence of meteorological factors of the atmosphere and the state of the underlying surface. This section presents the spatio-temporal characteristics of the acoustic radiation of objects of ground equipment and small-sized UAVs obtained experimentally — data that were not available in the literature until now and that are necessary for estimating their detection distances. The goal is an experimental study of the characteristics of acoustic fields (levels, diagrams, and radiation spectra), some types of ground-wheeled vehicles, as well as small-sized aircraft, which are necessary for the evaluation of their detection activities and the development of selection and recognition algorithms.

Levels and spectra of noise emitted by objects. The appearance, technical characteristics of the devices, and the method of noise level research are given in Appendix 1. The noise levels of various sources are evaluated in relative units concerning the threshold level of audibility, which is conventionally accepted as 10^{-12} W/m^2 at a standard (from a point source) distance, usually 1 m. The level of sound (noise) is measured in decibels (dB). The values of the noise levels of some sources obtained experimentally are given in the Table 2.7. The appearance of the UAVs used in the experiments is shown in Fig. 2.8.

The presence of broadband interference (from wind) requires the use of special noise reduction measures. As an example, Fig. 2.9 shows the recording of the noise of the quadcopter at a height of about 10 m from the receiver and its spectrum. During the experiment, the wind speed was about 7...8 mps.

During gusts of wind (moment 1 in Fig. 2.9, *a*), there is an increase in intensity by approximately 10 dB and an expansion of the spectrum at lower frequencies (Fig. 2.9, *b* — curve *1*) in comparison with pauses (moment *2* in Fig. 2.9, *a*, spectrum in Fig. 2.9, *b* — curve *2*). Quadrocopter noise is characterized by stationarity with the presence of periodicity in the spectrum, which is determined

Fig. 2.8. The appearance of the UAV: *a* — aircraft type X-8, wingspan 2.12 m, estimated number of engine revolutions 8,000-11,000 rpm; *b* — quadrocopter, estimated number of engine revolutions 6,000—10,500 rpm

Table 2.7. **Noise levels of different sources**

Engine name/type	Noise level, dB	Range/height/ angle, m	Notes
Ford/diesel	78	1/1.5/0	In the snow, XX
Ford/diesel	80	1/1.5/0	On the asphalt, XX
Gazelle/gasoline	65	1/1.5/0	On the asphalt, XX
UAZ 469	80	1/1.5/180	On the asphalt, XX
UAZ 452	56	1/1.5/0	On the asphalt, XX
Car gasoline (volume 2 liters)	70	5/1/270	On the asphalt
VolkswagenPassat	66	1/1/180	In the snow, XX
UAV-quadrocopter	87	10/1.7/	10 m above the receiver
UAV-quadrocopter	81.5	2/1.7	50% power
UAV-quadrocopter	87	2/1.7	85% power
Aircraft-type UAV	92	2/1/	At the level of the microphone in the room
Aircraft-type UAV	84	4/1/	At the level of the microphone in the room
Steps	73…76	—/1.5/—	Snow crust
»	54…57	—/1.5/—	Virgin snow
»	58…60	—/1.5/—	Concrete
Wind	57…61		7...8 m/s, windward side
»	83…86	/1.5	7...8 m/s, leeward side
Outdoor background	37	1.5	Wind ≤ 1 m/s

XX — idling

by the frequency of rotor rotation (approximately 110 Hz), which corresponds to approximately 7,000 rpm.

The noises of an aircraft UAV look similar — Fig. 2.10. A periodicity with a frequency of approximately 116 Hz, which corresponds to approximately 7,000 rpm, is also observed in the spectrum of an aircraft UAV. Noise during

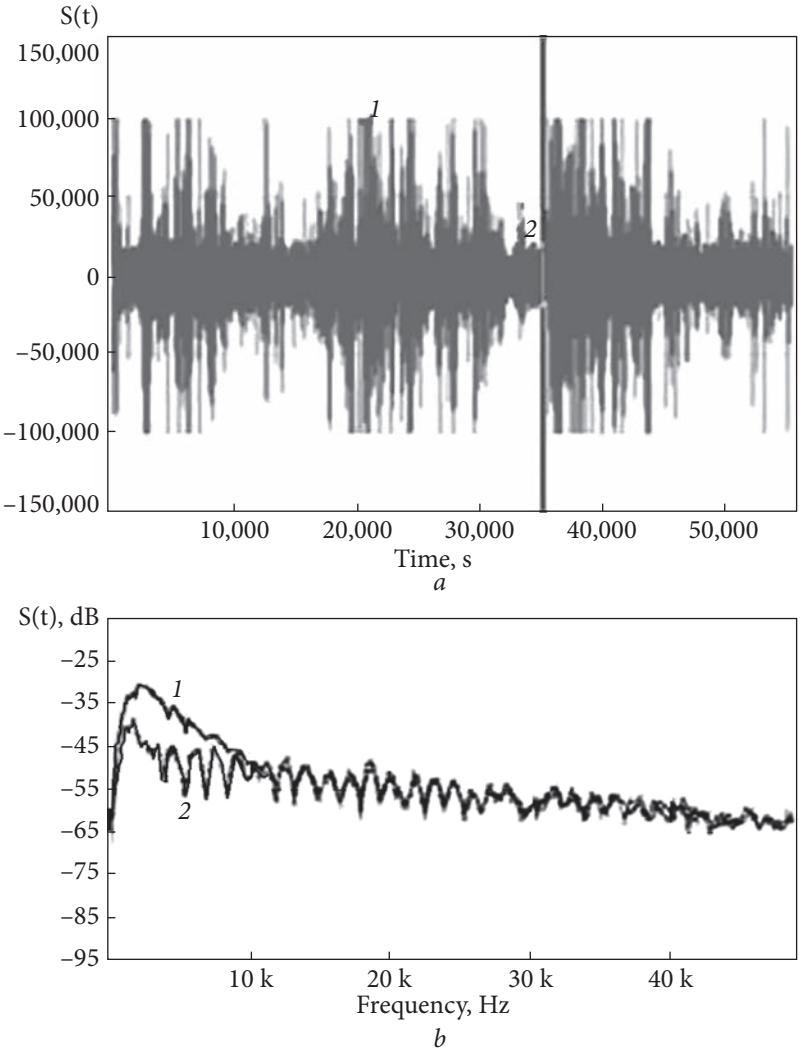

Fig. 2.9. Time realization (*a*) and noise spectra of the quadcopter with a gust of wind (*1*) and its absence (*2*)

gusts of wind (spectrum *3* in Fig. 2.10) can significantly complicate the detection of UAVs. The effect of the number of revolutions of the engine on the level of emitted noise is shown in Table 2.8.

It should be noted that changing the number of engine revolutions from idle to maximum can lead to an increase in the noise level up to 11...18 dB. At the same time, the frequencies of the peaks in the spectrum increase in proportion to the number of engine revolutions. At the same time, the shape of the radiation spectrum practically does not change — Fig. 2.11.

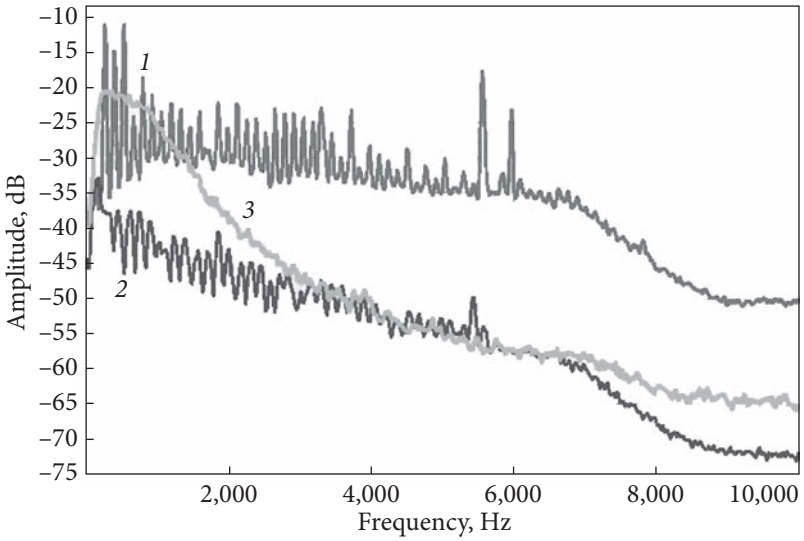

Fig. 2.10. Noise spectra: *1* — aircraft-type UAV, *2* — multi-rotor UAV (quadcopter), *3* — wind gust

The diagram of noise emission in the azimuthal plane is also uneven and is shown in the Table 2.9.

It is worth noting that the maximum values are observed in the direction of the noise source — the exhaust pipe, the engine in front, and the minimum noise when the source is shielded by the body. Differences in noise intensity when changing azimuth and observing at short distances reach 10 dB for a car and 16 dB for a diesel engine.

Based on the distance dependences of the attenuation of radiation $L(R)$ given in Table 2.10 and using the ratio:

$$V(R)[\text{dB}] = P(R = 1\text{m})[\text{dB}] - P(R)[\text{dB}] \tag{2.20a}$$

$$V(R)[\text{dB}] = L(R)[\text{dB}] - 20\lg(R)[\text{dB}], \tag{2.20b}$$

where $P(R = 1\text{m})$ [dB] is the noise level in dB at a distance of 1 m; and $P(R)$ [dB] — at the range R, calculated values of the signal attenuation factor $V(R)$, which are given in the Table 2.11.

The analysis of the obtained data allows us to conclude that due to the surface, noise levels of sources at distances of dozens of meters can be even higher than when they are located in free space; that is, the noise intensity increases due to reflection from the surface. The noise levels of objects of tracked machinery are given in the Table 2.12.

Since the noise of wind, rain, and the engine's own noise can make it difficult to distinguish the noise of other objects of equipment (reconnaissance purposes), the

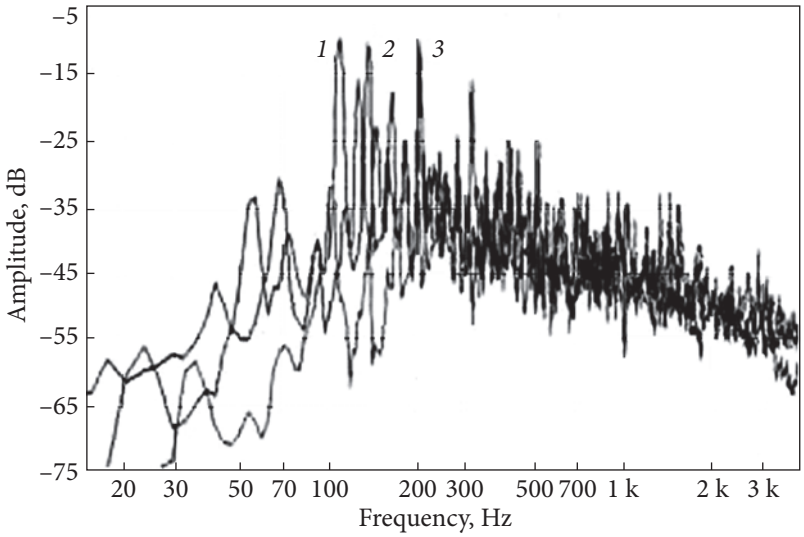

Fig. 2.11. Noise spectra of the 3TD diesel engine at different speeds: *1* — 600 rpm. *2* — 1,800 rpm; *3* — 2,400 rpm

Table 2.8. **An increase in the noise level when the engine speed changes from idling to maximum speed**

Engine name/type	Noise increase, dB	Range/height, angle, m
Ford/diesel	18	50/1.5/0°
Ford/diesel	11	1/1.5/0°
UAZ 469/petrol	12	1/1.5/box
UAZ 452/ petrol	11	1/1.5/box
Volkswagen Passat/petrol	3	1/1/180

Table 2.9. **Dependence of the noise level on the angle of observation of the source when the engine is idling**

Engine name/type	Angle relative to the car, degrees			
	0	90	180	270
Ford/diesel	81—82	74	71	77—78
Gazelle/gasoline	65	60	51	53
UAZ 452	56	54.4	62	56
UAZ 469	—	78.8	80	
Diesel, 500 hp, 1,000 rpm	—	70	82	86
Volkswagen Passat	59	59	64	58

power distribution of noise sources by frequency was studied, as well as the suppression coefficient of the noise source when rejecting low-frequency components:

$$K(f)[\text{dB}] = 10\lg\frac{\int_0^{f_{\max}} s(f)df}{\int_f^{f_{\max}} s(f)df}. \qquad (2.21a)$$

Table 2.10. **Attenuation of radiation**

Object	Range, m					Notes
	10	20	30	50	70	
			Attenuation, dB			
Ford/diesel	14	21.5	23	29	31	0°, snow
Ford/diesel	11.5	18.5				0°, asphalt
Ford/diesel	13	20	23			0°, asphalt

Table 2.11. **The radiation attenuation factor**

Object	Range, m						Notes
	1	10	20	30	50	70	
				Attenuation factor, dB			
Ford/diesel	0	6	4.5	7	5	6	0°, snow
Ford/diesel	0	8.5	7.5				0°, asphalt
Ford/diesel	0	7	6	7			0°, asphalt

Table 2.12. **Noise levels of different sources**

Engine name/type	Noise level, dB	Range/height/angle, m	Notes
Diesel, 500 hp	71	20/1/180	2,500 rpm, speed 0 m/s
Diesel, 500 hp	80	10/1/180	2,500 rpm, speed 0 m/s
Diesel, 500 hp	86	5/1/270 from the exhaust side	1,000 rpm, speed 0 m/s
Diesel, 500 hp	82	5/1/180 behind	1,000 rpm, speed 0 m/s
Diesel, 500 hp	70	5/1/90 from the side	1,000 rpm, speed 0 m/s
Diesel, 500 hp	71	50/1/270	1,000 rpm, speed 0 m/s
Diesel, 750 hp	72	50/1/200/rear and side	1,000 rpm, speed 0 m/s
A column of 2 products with a diesel engine of 500 hp	67	300/30/225	2,500 rpm, diesel 500 l with speed 30 km/h, interval 20

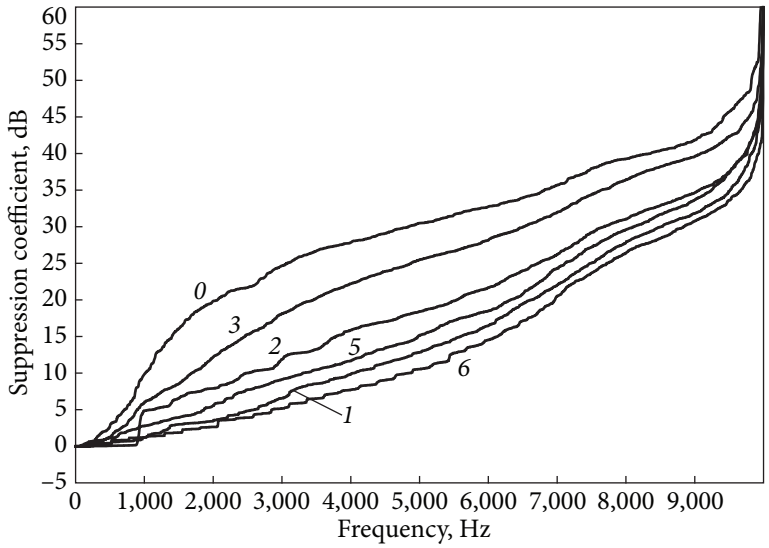

Fig. 2.12. Dependence of the noise suppression coefficient on the rejection band: *0* — wind; *1* — Ford car engine (maximum revolutions, distance 20 m); *2* — BTR-4 engine (idling in the hangar); *3* — a shot from a 30 mm cannon; *4* — multi-rotor UAV (height 50 m, hovering at a point); *5* — Aircraft-type UAV

Table 2.13. **Frequency bands beyond which a given part of the noise power is concentrated**

Object	Hz frequency band, for a given power level		
	–20 dB	–30 dB	–40 dB
Wind	2,064.5	4,842.3	8,357.6
Engine, Ford car (max rev.)	6,624.2	8,516.4	9,821.8
BTR-4 engine (no-load)	5,544.8	7,684.7	9,765.3
Shot, 30 mm cannon	3,458.8	6,513.8	9,087.0
Multirotor UAV	6,325.4	8,120.7	9,730.3
Aircraft-type UAV	6,968.7	8,842.1	9,932.2

The distribution of noise power by frequency, calculated using the ratio (2.21*a*), is shown in Fig. 2.12.

Most surveillance objects have high-frequency components that can be used to detect them and determine their coordinates. Using the data on the interference suppression coefficients of the high-pass filter $K_i(f)$ [dB] for the "i" object of observation, it is possible to estimate the obtained contrasts between A and B objects:

$$\Delta K(f)[\text{dB}] = K_A(f)[\text{dB}] - K_B(f)[\text{dB}]. \qquad (2.21b)$$

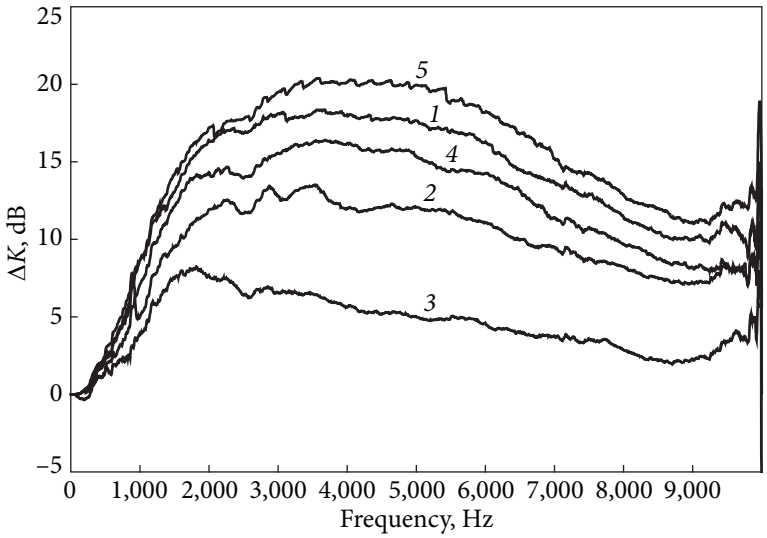

Fig. 2.13. Contrasts of observation of various objects depending on the rejection band: *1* — Ford car engine (maximum revolutions, distance 20 m); *2* — BTR-4 engine (idling in the hangar); *3* — a shot from a 30 mm cannon; *4* — multi-rotor UAV (height 50 m, hovering at a point); *5* — Aircraft-type UAV

The obtained contrasts of observing objects in conditions of wind noise are shown in Fig. 2.12, and intertype contrasts in Fig. 2.13. The frequency bands where a given part of the noise power is concentrated are shown in the Table 2.13.

The analysis shows that the wind noise spectrum lies in a lower frequency region than the noise of technical objects. This means that by rejecting low-frequency components, you can get an additional contrast of about 10...15 dB.

Conclusions

1. Due to the dispersive properties of the atmosphere, the signal spectrum narrows as the distance to the receiver increases. A decrease in humidity and a decrease in temperature lead to an increase in linear damping. These phenomena are most pronounced at high frequencies.

2. Interference phenomena are affected most strongly at low frequencies. The roughness of the surface has a stronger effect at high frequencies, where it leads to a decrease in the reflection coefficient and a decrease in the interference effect of the surface on the signal intensity.

3. The effective spectrum width of acoustic noise sources narrows as the distance to the source increases. Changes in the effective spectrum width at the 90% significance level can reach ten times. This will lead to a decrease in the accuracy of determining its location.

4. A methodology for estimating the detection range of acoustic radiation sources under the influence of attenuation in the atmosphere and interference attenuation by the Earth's surface has been developed. The possibility of detecting objects of ground and air equipment by their acoustic radiation at distances of several kilometers is theoretically demonstrated.

5. The possibility of describing the spectra of noise sources by fractal dependencies is shown. It is shown that, in most cases, the rate of decrease of the spectral density on the wings of the spectrum does not exceed $n \approx 2$.

6. Data on acoustic noise levels of various objects, both ground vehicles and UAVs at different observation distances, were obtained. For example, for cars, the noise level at distances of 1 m is approximately 55...70 dB, objects of armored vehicles at distances of 5...300 m — 67...86 dB, and UAVs at distances of 2...10 m — 92 dB.

7. When the engine speed changes from idling to maximum, the noise level increases, reaching 11 dB for cars.

8. Azimuthal noise anisotropy due to the effect of shielding the source by the housing can reach 16 dB, which is especially strong near the noise source.

9. Natural noises of wind, rain, and one's own engine can significantly (by 1...2 orders of magnitude) reduce the range of acoustic reconnaissance systems.

10. At small distances from the noise source, the separation surface can lead to an increase in the noise level compared to estimates for free space. Distance noise decays somewhat more slowly than theoretical estimates give.

11. The acoustic reconnaissance system should be built as adaptive, ensuring the detection of objects in the gaps between wind gusts.

12. By reducing the low-frequency component of the noise in the band up to 1,000...2,000 Hz, it is possible to increase the contrast of observation of ground objects by approximately 5...13 dB and up to 10...20 dB for UAVs.

13. The noise of the rain is quite spatially homogeneous. To suppress it, you can use spatial methods using noise reception on an auxiliary microphone.

CHAPTER 3

Electromagnetic and acoustic portraits of objects

3.1. Air objects with a propeller engine, such as an airplane, helicopter, UAV

The development of recognition systems is related to solving the problems of choosing the principle of classification and compiling a dictionary of features, which is used both for the a priori description of classes and for the a posteriori description of each unknown object or phenomenon to be recognized.

The most available for analysis are optical images of objects of new technology, as well as acoustic noises. Informative features that can be obtained from optical images and audio recordings and used for the recognition of air and ground objects, as well as their detection technologies, are considered in the section [195—199].

Video recording of equipment objects allows you to estimate their overall dimensions and speed of movement. Overall dimensions can be used to obtain RCS estimates of objects. In the resonant region, the object dimensions are proportional to the wavelength of the irradiating field, and the scattering is resonant in its nature. As was shown in works [200, 201], the RCS of airborne objects in this region can be compared with the RCS of a half-wave (horizontal polarization) or quarter-wave (vertical polarization) grounded dipole. In the high-frequency region, the wavelength is much smaller than the object size, and its RCS is, to a first approximation, determined by the area of the irradiated surface [202]. When solving tasks of radar recognition of aerial targets (AT), spectral components due to reflections from rotating structural elements are often used [203—206]. For example, in [203, 205], a method for recognizing the AT of the "turbojet engine" class was proposed based on the analysis of the ratio of the number of blades on the first two stages of the engine compressor. In the direction of development, it is advisable to consider the possibility of developing an air target recognition algorithm based on the use of a modulation feature.

The spectrum of the signal reflected from the aircraft with a propeller engine is characterized by the presence of spectral components located symmetrically with respect to the planar component in the nodes of the periodic frequency grid. These components have a width that is the inverse of the time of coherent accumulation of the signal t_c, and are characterized by the spectral amplitude A_f and the frequency $F_i = 1, ..., i$, where i is the number of spectral components. Moreover, the modulation components are located on the frequency axis with a period F_0 equal to the product of the number of blades by their rotation frequency. In this case, the task of recognizing a target of a given class can be solved in the form of a task of detecting some compactly located set of signals.

When creating information characteristic spaces for the recognition of helicopter-type ATs, calculation methods and methods of forming polarization-spectral portraits come to the fore. As a rule, the main geometric dimensions and technical characteristics are available from open sources. Accordingly, the method of obtaining informative features should be based on the use of these limited but generally available characteristics.

The maximum flight speed V_0 makes it possible to estimate the maximum value of the Doppler frequency shift of the signal reflected from the helicopter:

$$f_D = \frac{2V_0}{\lambda},$$

where λ is the wavelength of the irradiating helicopter field.

The speed of rotation of the helicopter rotor. The frequency of rotation of the blades of helicopter rotors, as a rule, is not among the given reference data. However, it can be determined based on the fact that the circular speed of the tip of the hovering helicopter blade is approximately 0.75 of the speed of sound. Based on this, it is possible to calculate the frequency of F_{RHR} modulation by the blades of a rotating helicopter rotor [196, 207]:

$$F_{\text{RHR}}[Hz] = \frac{\left(\frac{3}{4}c\right)}{\left(d_{\text{HR}} \cdot \pi\right)} \cdot n_{\text{B}} \cdot n_{\text{HR}}, \tag{3.1}$$

where c is the speed of sound, and d_{HR} is the helicopter rotor diameter; $n_{\text{B}} \cdot n_{\text{HR}}$ — the number of blades and the number of rotors.

At maximum flight speed, the speed of the advancing blade tip should not exceed 96% of the speed of sound [207], the modulation frequency can be written as:

$$F_{\text{RHR}}[Hz] = \frac{V_{\max}}{\left(d_{\text{HR}} \cdot \pi\right)} \cdot n_{\text{B}} \cdot n_{\text{HR}}, \tag{3.1a}$$

where V_{max} is the maximum permissible speed of movement of the end of the blade at the maximum speed of the helicopter $V_{H\,max}$.

You can write:

$$V_{max} + V_{H\,max} \le 0.96c\,, \tag{3.1b}$$

where

$$V_{max} \le \left(0.96 - \frac{V_{H\,max}}{c}\right)c = \alpha c\,, \tag{3.1c}$$

where $\alpha = \left(0.96 - \frac{V_{H\,max}}{c}\right)$.

For known speeds of helicopters, α has a value of 0.75 ± 0.08. This means that (3.1) can be used in approximate calculations. For accurate calculations, use (3.1*b*, 3.1*c*). Comparing (3.1) with (3.1*c*), we can write:

$$0.75 + \delta = \left(0.96 - \frac{V_{H\,max}}{c}\right), \quad \delta = 0.21 - \frac{V_{H\,max}}{c}\,, \tag{3.1d}$$

it can be seen that δ differs from the calculated values (75%) for all types of helicopters by no more than +3% and –6%.

RCS of the helicopter and its individual elements. In the quasi-resonant region, when the wavelength of the irradiating field is comparable to the dimensions of the structure as a whole or its individual elements, resonance growth of RCS is possible [200, 201]. The body of the helicopter can be described by a triaxial ellipsoid, for which the RCS in the resonance region, by analogy with a sphere [208], can be written:

$$\sigma = 3.65\pi ab = 3.65\sigma_m \tag{3.2}$$

at $k\sqrt{ab} \approx 1$ or $\lambda_0 \approx 2\pi\sqrt{ab}$, where $\sigma_m = \pi ab$ is the cross-sectional area of the ellipsoid.

In the case when the shape is close to spherical $a \approx b$,

$$\sigma = 3.65\pi a^2 = 3.65\sigma_m\,. \tag{3.2a}$$

At the same time, the resonant wavelength:

$$\lambda_0 \approx \pi a. \tag{3.2b}$$

On the other hand, the helicopter body can be considered as a quarter-wave vibrator, for which the main rotor acts as a ground. Then, the RCS of such a

design will be approximately 6...7 dB lower than that of a resonant half-wave dipole [200, 201].

Thus, if the helicopter height is $h = \frac{\lambda}{4} \approx b$, then the EPR value for the resonance wavelength is $\lambda_0 = 4h$.

$$\sigma \approx 0.86 \cdot \frac{1}{4}\left(4h\right)^2 = 3.44h^2. \tag{3.2c}$$

Considering the body as a spheroid with axes a, b, at the resonance wavelength for the sphere $\lambda_0 \approx \pi h$ — RCS at resonance $\sigma = 3.65\pi h^2 = 11.46\ h^2$. That is, about 5 dB more than that of a quarter-wave vibrator and about the same as that of a half-wave resonant dipole. At the same time, the resonant frequency at which this RCS is realized is 4 — and π times larger than the vertical size for a quarter-wave grounded dipole and a sphere, respectively.

When the bearing and steering rotors are made of composite materials, it is necessary to introduce the correction coefficient K of reflection from the dielectric [208, 209]. For metal surfaces, $K \approx 1$.

The RCS of rotors made of composite materials, taking into account the data of work [209], is approximately $K = -6...-8$ dB less than that of metal ones. The calculated RCS values are given in Table 3.1.

RCS of blades. Carrier and steering blades can be considered as dipoles rotating with the corresponding frequencies. When the blade length l is equal to half the wavelength of the irradiating field $l \approx \lambda/2$, it will scatter as a resonant half-wave dipole with the maximum RCS value [202]:

$$\sigma_0 \approx 0.86\lambda^2 = 0.86\left(2l^2\right), \tag{3.3}$$

then the RCS of the blades and the body in the resonant region can be estimated [196, 200, 201]:

$$\sigma_{x(y)} \approx 3.44 l_{x(y)}^2, \tag{3.3a}$$

and RCS in the short-wavelength region [202]:

$$\sigma_0 \approx \alpha l_x l_y, \tag{3.3b}$$

where l_x, l_y is the horizontal and vertical size of the structure, $\sigma_{x(y)}$ is the RCS on the horizontal and vertical polarizations, and α is the parameter that depends on the shape of the object. For a sphere and an ellipsoid, it is $\alpha = \pi/4 \approx 0.77$. In practical calculations, usually $\alpha \approx 0{,}5...0{,}3$.

Table 3.1. **RCS of some types of helicopters**

Type of helicopter	Producing country	Product-ion year	Purpose	Horizontal polarization				Vertical polarization		RCS in the VHF range, dB/m²	The rotor rotation speed. Hz F1l* Number of blades	
				RCS Rotor, dB/m²	RCS of the body, dB/m²	Resonance frequency, MHz		RCS of the body, dB/m²	Resonance frequency of the body, MHz			
						Body	Rotor				Main rotor	Tail rotor
Bell 429	USA	2006	MP	26.2	27.7	11.4	13.7	18.6	18.6	14.2	29.6	98.4
Eurocopter UH-72 Lacota	USA	2006	MP	26.2	27.7	11.5	13.6	17.2	21.7	13.5	14.8	82.9
Bell ARH-70 Arapaho	USA	2006	S	25.9	27.2	12.1	14.1	13.7	32.8	11.5	30.4	98.4
Bell 210	USA	2004	MP	28.3	27.4	11.8	10.7	17.3	21.6	13.4	11.6	62.0
Bell, Agusta BA609 Tiltrotor	USA	2003	MP	23.4	27.8	11.3	18.9	19.5	16.7	14.8	30.7	—
Bell UH-1Y Iroquois	USA	2000	MP	28.8	28.0	11.0	10.1	19.4	17.0	14.8	21.9	62.7
Schweizer Model 333	USA	2000	MP	23.8	22.0	22.0	17.9	16.9	22.5	10.6	29.0	124.9
Bell AH-1Z Viper	USA	2000	S	28.7	30.4	8.4	10.3	19.3	17.2	15.9	11.1	54.7
Sikorsky S-92 Helibus	USA	1998	MP	30.3	31.7	7.2	8.5	22.7	11.6	18.3	18.3	97.0
Sikorsky S-92	USA	1998	T	30.3	30.1	8.7	8.5	22.7	11.6	17.5	18.3	94.7
Bell 427	USA	1997	MP	26.4	27.6	11.5	13.4	16.7	23.2	13.2	29.0	93.9
Load Ranger 2000	USA	1997	MP	25.5	26.8	12.7	14.8	17.0	22.4	13.0	16.0	102.2
McD.D. MD 902 Explorer	USA	1997	MP	25.7	26.8	12.7	14.5	17.7	20.5	13.4	39.3	—
Aerocopter ZA-6 (AK-1)	UKR	1999	MP	20.9	23.5	18.5	25.0	13.4	33.8	9.5	40.6	131.0
McDonnell Douglas MD 500E	USA	1982	MP	23.5	22.9	20.0	18.6	15.9	25.3	10.5	40.4	118.6
Aviaimpex Angel	UKR	2003	MP	23.7	22.8	20.1	18.1	14.4	30.2	9.7	29.4	124.9
Mil Mi-34	RUS	1986	MP	25.4	24.2	17.2	15.0	15.3	27.3	10.8	32.5	109.7
Eurocopter EC.120 Colibri	FRA	1995	MP	25.4	26.6	13.0	15.0	17.4	21.4	13.0	24.4	349.3
MBB Bo.108	DEU	1991	MP	25.4	25.9	14.2	15.0	16.0	25.0	12.0	32.5	77.3
Bell ARH-70 Arapaho	USA	2006	S	25.9	27.2	12.1	14.1	13.7	32.8	11.5	30.4	98.4
Bell OH-58D Kiowa Warrior	USA	1982	S	25.9	27.2	12.1	14.1	13.7	32.8	11.5	30.4	98.4
Eurocopter AS.350B-3 Ecureuil	FRA	1997	MP	25.9	27.6	11.6	14.0	14.5	29.6	12.1	22.8	87.3

Eurocopter AS.350B-3 Ecureuil	FRA	1997	MP	25.9	27.6	11.6	14.0	14.5	29.6	12.1	22.8	87.3
Agusta A.119 Koala	ITA	1995	MP	26.0	27.7	11.5	13.9	18.0	19.9	13.9	30.1	81.2
Bell 427	USA	1997	MP	26.4	27.6	11.5	13.4	16.7	23.2	13.2	29.0	93.9
Bell 427	USA	1997	MP	26.4	27.6	11.5	13.4	16.7	23.2	13.2	29.0	93.9
AS.565 Panther	FRA	1984	S	26.9	27.0	12.4	12.6	17.1	22.1	13.1	27.2	738.3
Harbin Z-19	CHN	2010	S	26.9	26.9	12.5	12.6	18.5	18.7	13.8	27.2	481.2
Bell 430	USA	1994	MP	27.5	29.1	9.8	11.7	17.9	20.2	14.5	25.4	77.3
Westland Lynx AH.Mk.7(9)	UK	1985	S	27.6	29.0	9.8	11.6	17.9	20.1	14.5	25.1	137.6
Changhe WZ-10	CHN	2003	S	27.6	28.4	10.6	11.5	18.2	19.5	14.4	25.0	90.2
Sikorsky H-76 Eagle	USA	1984	MP	27.9	27.8	11.3	11.2	19.6	16.6	14.8	18.2	133.1
Bell AH-1F Cobra	USA	1981	S	27.9	29.5	9.3	11.2	18.8	18.2	15.2	12.1	54.7
Bell 210	USA	2004	MP	28.3	27.4	11.8	10.7	17.3	21.6	13.4	11.6	62.0
Kamov Ka-50 Black Shark	RUS	1982	S	28.6	28.0	11.1	10.3	20.3	15.3	15.2	16.8	—
Bell AH-1W Super Cobra	USA	1986	S	28.7	28.2	10.8	10.3	19.2	17.4	14.8	11.1	54.7
McDonnell Douglas AH-64 Apache	USA	1984	S	28.7	30.3	8.5	10.3	19.8	16.2	16.1	16.7	116.4
Bell UH-1Y Iroquois	USA	2000	MP	28.8	28.0	11.0	10.1	19.4	17.0	14.8	21.9	62.7
Eurocopter AS.532UB Cougar 100	FRA	1996	T	29.2	30.8	8.0	9.6	20.3	15.2	16.6	20.8	133.1
Kamov Ka-32	RUS	1980	MP	29.4	26.4	13.3	9.4	21.1	13.9	14.8	15.3	—
Sikorsky HH-60J Jayhawk	USA	1990	MP	29.6	31.3	7.6	9.2	20.8	14.5	17.1	14.9	97.0
Eurocopter EC.725 Cougar Mk.II+	FRA	2000	T	29.6	31.2	7.7	9.3	19.7	16.3	16.5	20.1	103.1
Mil Mi-28	RUS	1982	S	30.1	29.9	8.9	8.7	18.1	19.6	15.1	18.9	84.6
Sikorsky S-92	USA	1998	T	30.3	30.1	8.7	8.5	22.7	11.6	17.5	18.3	94.7
EHI EH.101	UK	1987	T	30.8	32.5	6.6	8.1	19.6	16.5	17.1	17.5	81.2
Changhe Z-8	CHN	1985	MP	30.9	31.1	7.7	7.9	23.1	11.1	18.2	21.5	101.5
Mil Mi-8AMTSh Terminator	RUS	1997	S	31.9	30.6	8.2	7.0	21.5	13.3	17.1	15.3	41.5
Mil Mi-8AMT (Mi-171)	RUS	1991	MP	31.9	30.6	8.3	7.0	21.5	13.3	17.1	19.1	62.3
Mil Mi-18	RUS	1980	MP	31.9	30.7	8.1	7.0	19.8	16.1	16.3	15.3	41.6

* The following designations of helicopters are used in the table: MP — multipurpose, T — transport, S — shock.

If the blades, as well as the body of the helicopter, are not made of metal but of composite materials, then the reflection coefficient R_S from them will be smaller:

$$R_S \approx \left|\frac{n-1}{n+1}\right|^2, \tag{3.4}$$

where $n = \sqrt{\varepsilon}$ is the refractive index of the material, and ε is its dielectric constant, which is ε = 4...7 for composite materials based on multi-walled carbon nanotubes [209].

Table 3.1 shows the RCS for different types of helicopters, as well as the modulation frequencies associated with the rotation of the rotors. When manufacturing a helicopter and its blades from composite materials, listed in the Table 3.1, the RCS value, as can be seen from (3.4), must be reduced by 7...10 dB.

When the blade rotates with a frequency $\Omega = 2\pi f_0$ in the scattered signal, responses will be observed at the frequency of rotation and its harmonics. The first harmonic will be the most important.

The dependence of the intensity of the scattered signal (RCS) on the blade orientation angle with horizontal polarization of the irradiating field is determined by the ratio [210]:

$$\sigma(\Omega t) \approx \sigma_0 \cos^4 \theta, \tag{3.5}$$

where $\theta(t) = \Omega = 2\pi Ft$ is the angle of orientation of the blade with respect to the polarization vector of the irradiating field.

In addition, due to the movement of the blade, the reflection of the signal from its individual elements receives a Doppler shift.

The signal $u(t)$ reflected from the blade can be written as a product of two coefficients: one of which determines the amplitude (3.5), and the other — the reflection phase:

$$u(t) = \sigma(\Omega t)^{1/2} \int_0^{d_B} E(l) \exp\left(2\frac{2\pi l}{\lambda}\sin\Omega t\right) dl, \tag{3.6}$$

where $E(l)$ is the intensity distribution of the irradiating field along the length of the rotor blade.

In the first approximation, we can assume that $E(l) = const$, then from (3.6) we can obtain the expression for the signal scattered by the rotor:

$$u(t) = \sigma_0^{1/2} \cos^2(\Omega t) \int_0^{d_B} E(l) \exp\left(2\frac{2\pi l}{\lambda}\sin\Omega t\right) dl =$$

$$= \sigma_0^{1/2} \cos^2(\Omega t) \frac{\exp(2kl\sin\Omega t) - 1}{2k\sin\Omega t}. \tag{3.6a}$$

Table 3.2. **Typical dimensions and RCS of aircraft**

Type of aircraft	Purpose	Length of the plane, m	Aircraft height, m	Wingspan, m	Wing area, m^2	Horizontal RCS polarization, dB/m^2		Vertical RCS polarization, dB/m^2	Resonance frequency, MHz		
									HP		VP
						Wings	Body	Body	Body	Wings	Body
Russia											
IL-18	P	35.9	10.2	37.4	140	36.82	36.47	25.51	4.18	4.01	7.37
IL-62	P	53.12	12.4	43.2	279	38.08	39.87	27.20	2.82	3.47	6.07
IL-76	MT	46.6	14.7	50.5	300	39.43	38.73	28.71	3.22	2.97	5.10
IL-114T	P	26.88	9.32	30	81.9	34.91	33.95	24.76	5.58	5.00	8.04
Tu-160	B	54.1	13.1	55.7	232	40.3	40.03	27.71	2.77	2.7	5.73
				50.7		39.5				2.96	
				35.6		36.4				4.2	
Tu-22M3	B	42.46	11.1	34.3	183.6	36.07	37.93	26.23	3.53	4.38	6.79
camber angle 20°				34.3	183.6	36.07				4.38	
camber angle 65°				27.7	175.8	34.2				5.4	
MiG-29	F	17.32	4.73	11.4	38.06	26.47	30.14	18.86	8.66	13.20	15.86
MiG -29M	F	17.32	4.73	11.4	38.06	26.47	30.14	18.86	8.66	13.20	15.86
MiG -31	F	22.69	6.15	13.5	61.6	27.95	32.48	21.14	6.61	11.14	12.20
Su-24	B										
camber angle 16°		24.59	6.19	17.6	55.2	30.29	33.18	21.20	6.10	8.50	12.11
camber angle 69°		24.59	6.19	10.4	51	25.68	33.18	21.20	6.10	14.47	12.11
Su-25	A	15.36	4.8	14.4	30.1	28.51	29.09	18.99	9.77	10.45	15.63
Su-27	F	21.95	5.94	14.7	62.04	28.71	32.19	20.84	6.83	10.20	12.63
Su-33	F	21.2	5.9	14.7	67.8	28.71	31.89	20.78	7.08	10.20	12.71
Su-35	F	21.9	5.9	15.3	62.04	29.06	32.17	20.78	6.85	9.80	12.71
Su-47 Golden eagle	F	22.6	6.4	16.7	56	29.82	32.45	21.49	6.64	8.98	11.72
MiG-29M	F	17.32	4.73	11.4	38.06	26.47	30.14	18.86	8.66	13.20	15.86

The End of the Table 3.2

Type of aircraft	Purpose	Length of the plane, m	Aircraft height, m	Wingspan, m	Wing area, m^2	Horizontal RCS polarization, dB/m^2		Vertical RCS polarization, dB/m^2	Resonance frequency, MHz		
									HP		VP
						Wings	Body	Body	Body	Wings	Body
Russia											
Su-57 PAK T-50	F	19.7	4.8	14	82	28.29	31.25	18.99	7.61	10.71	15.63
Ukraine											
An-140	CP	22.6	8.2	25.5		33.50	32.45	23.64	6.64	5.88	9.15
An-24	P	23.53	8.32	29.2	74.98	34.67	32.80	23.77	6.37	5.14	9.01
An-72, An-74	BT	28.07	8.75	31.89	98.6	35.44	34.33	24.21	5.34	4.70	8.57
An-22 «Antei»	T	57.31	12.53	64.4	345	41.54	40.53	27.32	2.62	2.33	5.99
An-124 Ruslan	T	69.1	21.08	73.3	628	42.67	42.16	31.84	2.17	2.05	3.56
Japan + USA											
F-2	F	15.52	4.96	10.8	34.8	26.03	29.18	19.28	9.66	13.89	15.12
USA											
Dassault Mirage F1	F	15.23	4.5	8.4	25	23.85	29.02	18.43	9.85	17.86	16.67
F-22 Raptor	F	18.92	5	13.56	78.04	28.01	30.90	19.34	7.93	11.06	15.00
Northrop B-2 Spirit	SB	20.9	5.1	52.12	460	39.71	31.77	19.52	7.18	2.88	14.71
EMB-145RS	AC	29.87	6.75	20.04	51.2	31.40	34.87	21.95	5.02	7.49	11.11
Boeing B-52 “Stratofortress”	SB	49.05	12.4	56.39	371.6	40.39	39.18	27.23	3.06	2.66	6.05
General Dynamics F-16 Fighting Falcon	F	15.03	5.09	9.45	27.87	24.87	28.90	19.50	9.98	15.87	14.73
with rockets on the wingtips			10		25.37				15.00		
Lockheed Martin F-35 Lightning II	FB	15.57	4.38	10.67	42.7	25.93	29.21	18.20	9.63	14.06	17.12

MT — military transport, P — passenger, B — bomber, F — fighter, A — attack aircraft, AA — amphibious aircraft, T — transport, CP — cargo and passenger, SB — strategic bomber, AC — airborne early warning and control, FB — fighter-bomber.

Table 3.3. **Typical dimensions and RCS of aircraft-type UAVs**

Flight-type UAV	Purpose	UAV length, m	UAV height, m	Wingspan. Rotor/ structure diameter, m	Horizontal polarization				Vertical polarization	
					EPR Wings/rotor/ structures, dB/m²	RCS of the body, dB/m²	Resonant frequency, MHz		RCS of the body, dB/m²	Resonant frequency of the case, MHz
							Body	Wings/Rotor/ structures		
Ukraine										
UAV KHAI	R	0.64	—	2.12	11.9	1.5	234.4	70.75	—	—
"AVIA-JET" electrolyte		0.7	—	1.95	11.2	2.3	214.3	76.92	—	—
Stork		1.2	—	1.8	10.5	6.9	125	83.33	—	—
Snipe		1.6	—	1.9	10.96	9.4	93.75	78.95	—	—
Golden eagle		4	—	6.4	21.5	17.4	37.5	23.44	—	—
Search 2		2.1	—	2.6	13.7	11.8	71.4	57.69	—	—
Khai-112		2.7	—	3.5	16.2	13.9	55.6	42.86	—	—
"Sparrow-M"	UAS		—	1.05	5.8	—	—	142.9	—	—
"ChiZh-L"			—	2	11.4	—	—	75	—	—
A-2 tit	MP	0.95	—	1.8	10.5	4.9	157.9	83.33	—	—
A-3 "Remez"	MP	0.78	—	2	11.4	3.2	192.3	75	—	—
A-4 "Albatross"	MP	1.42	—	2.475	13.2	8.4	105.3	60.60	—	—
Russia										
Delta	R	0.7		1.7	9.9	2.27	214.3	88.24	—	—
Israel										
Hermes 180	MPR	4.43	1.8	6	20.9	18.29	33.86	25	10.47	41.67
Hermes 450S		6.1	1.8	10.5	25.8	21.07	24.59	14.29	10.47	41.67
Hermes 1500		9.4	2.4	18	30.5	24.83	15.96	8.33	12.97	31.25
IAI Heron	R	8.5	2.3	16.6	29.8	23.95	17.65	9.04	12.60	32.61
Skylark		1.83	—	2.74	14.1	10.61	81.97	54.74	—	—
USA										
MQ-1 Predator	MP	8.23	2.21	14.84	28.8	23.67	18.23	10.11	12.25	33.94
European Union										
Barracuda	R	8.25	—	7.22	22.5	23.69	18.18	20.78	—	—

MP — multi-purpose UAV, MPI — multi-purpose reconnaissance UAV, R — reconnaissance UAV, UAS — unmanned aircraft system.

It is obvious that for $m/2$ pairs of blades, there will be frequencies Ωm and $2\Omega m$ in the spectrum; that is, for blades m, the modulation frequencies increase by the corresponding number of times.

The difference in the RCS of the hulls of different helicopters on vertical polarization, as the analysis of the obtained data showed, can reach 10 dB. On horizontal polarization, the differences do not exceed 3 dB. The RCS difference in the resonant and short-wave frequency ranges for most helicopters of different types is less than 6 dB. At the same time, the modulation frequencies of the main rotor for the various types of helicopters can differ by 3...4 times. There are even more differences in tail rotor modulation frequencies. Differences can reach 10...15 times (see Table 3.1).

The ratios given in (3.2—3.4) can also be used to estimate the RCS of aircraft. For airplanes, the data from work [40] are supplemented with the obtained estimates (Table 3.2).

Studies have shown that the resonance frequencies for large aircraft (3...6 MHz) are lower than those of helicopters (10...20 MHz) and fighter jets (10...17 MHz). Since the RCS in the resonant region is determined by the value of the resonance frequency (3.2), the RCS of large aircraft can reach 40 dB/m^2, while for helicopters and small aircraft, it does not exceed 30 dB/m^2.

In a similar way, the RCS is obtained for the UAV — Tables 3.3, 3.4.

The analysis shows that modulation frequencies are more informative than the intensity of the scattered signal for solving the recognition problem. Acoustic noise recordings of helicopters were used to test the proposed methodology for estimating the rotation frequency of rotors and modulation frequencies using

Table 3.4. **Characteristic dimensions and RCS of a multi-rotor UAV**

EPR multi-rotor/ helicopter-type/UAV	The length of the helicopter, m	Rotor/body diameter, m	Construction height, m	Horizontal polarization				Vertical polarization	
				Rotor/structure, dB/m^2	Body, dB/m^2	Resonant frequency, MHz		RCS of the body, dB/m^2	Resonant frequency of the case, MHz
						Body	Rotor		
Electric helicopter “AVIA-EV1”	1.5	0.74		2.8	8.9	100	202.7	—	—
Multirotor “AVIA-Y3”		1.5	0.5	8.9	—	—	100	0.5	150
Multirotor “AVIA-X4”		1.5	0.5	8.9	—	—	100	0.5	150
Multirotor “AVIA-Y6”		1.1	0.5	6.2	—	—	136.4	0.5	150
Multirotor “AVIA-Hybrid”		1.5	1	8.9	—	—	100	6.5	75

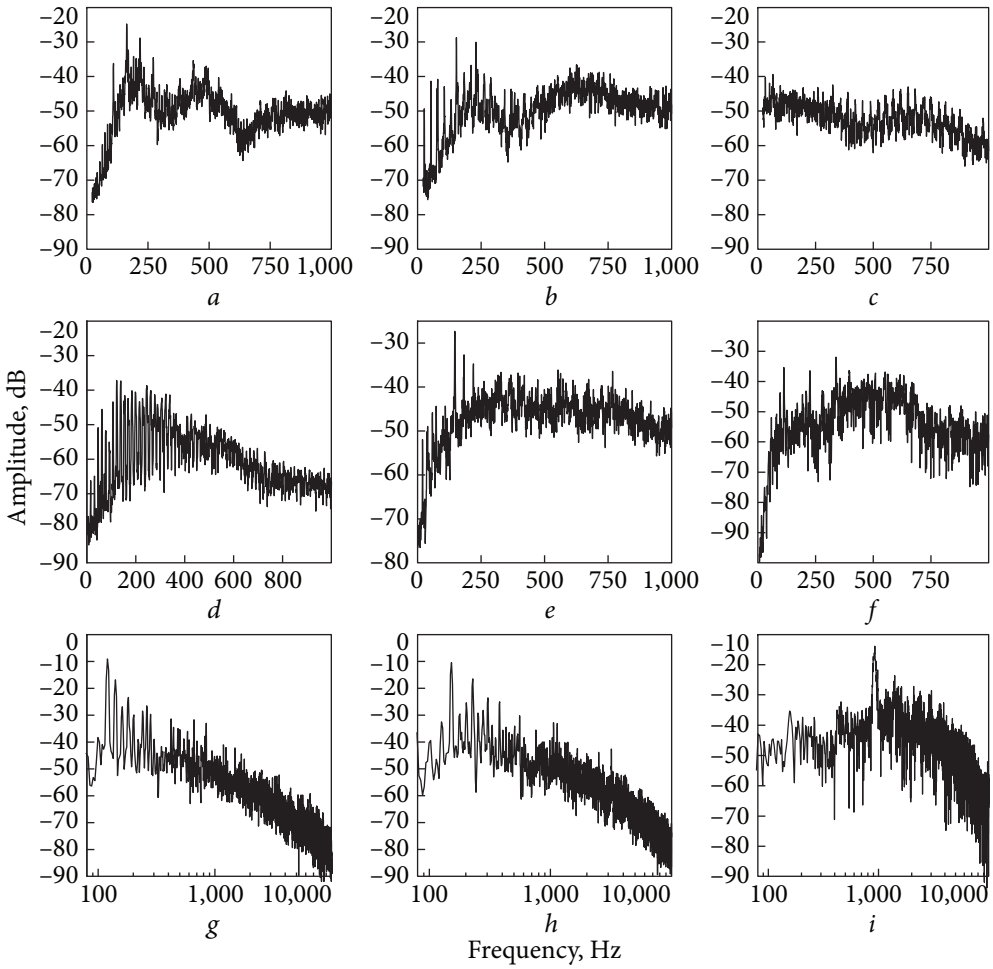

Fig. 3.1. Acoustic noise spectra of of aircraft and ground based objects. Helicopters: *a* — Bell-210 modulation frequency of the main rotor 11 Hz; tail rotor 56 Hz; *b* — Bell-429: modulation frequency of the carrier rotor 26 Hz; *c* — McDonnell Douglas MD 900 Explorer: main rotor modulation frequency 36 Hz; *d* — Kamov Ka-32: main rotor modulation frequency 16 Hz; *e* — Mi-38: main rotor modulation frequency 22 Hz; *f* — Mi-8: main rotor modulation frequency is 16 Hz. Diesel engine, number of revolutions: *g* — 800 rpm, *h* — 2,000 rpm, *i* — idling in the hangar

their optical portraits. Examples of their spectra are shown in Fig. 3.1, *a*—*g*. Comparison of these frequencies with the calculated values given in Table 3.1 shows their satisfactory correspondence; the calculation error does not exceed 10%.

Acoustic and radar spectra of small aerodynamic objects — unmanned aerial vehicles (UAVs) are characterized by the same features associated with the engine speed, which is 7,000...11,000 rpm for them — Fig. 3.2.

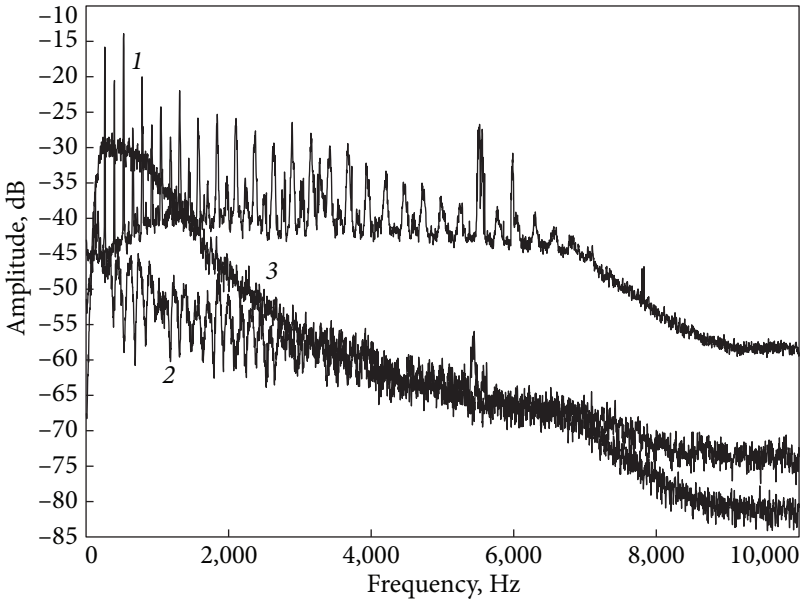

Fig. 3.2 UAV and wind spectra: *1* — aircraft-type UAV, *2* — multi-rotor UAV, *3* — wind gust

A modified Fourier transform can be used to study the dynamics of changes in the characteristics of quasi-periodic sequences.

3.2. Using cepstral processing to determine the modulation frequency

The cepstrum $C_s(q)$ is means the energy spectrum of the function $\ln|S(w)|^2$, which is determined by the expression:

$$C_S(q) = \int_{-\infty}^{\infty} \ln\left|S(w)\right|^2 \exp(-iqw)dw \tag{3.7}$$

In other words, the cepstrum determines the sequence of coefficients of the expansion of the function $\ln|S(w)|^2$ in the Fourier series [211—213].

It was shown in [211] that the logarithm of the power spectrum of the oscillation containing the reflected signal has an additive periodic component created by this signal and, therefore, the Fourier transform of the logarithm of the power spectrum has a peak at the place corresponding to the delay of the reflected signal [212]. Later, in 1969, Shafer introduced the concept of a "complex cepstrum", which is based on the use of information about both the amplitude and phase spectra of the observed signal [214]. The complex cepstrum method is used to restore the original signals from the result of their convolution and

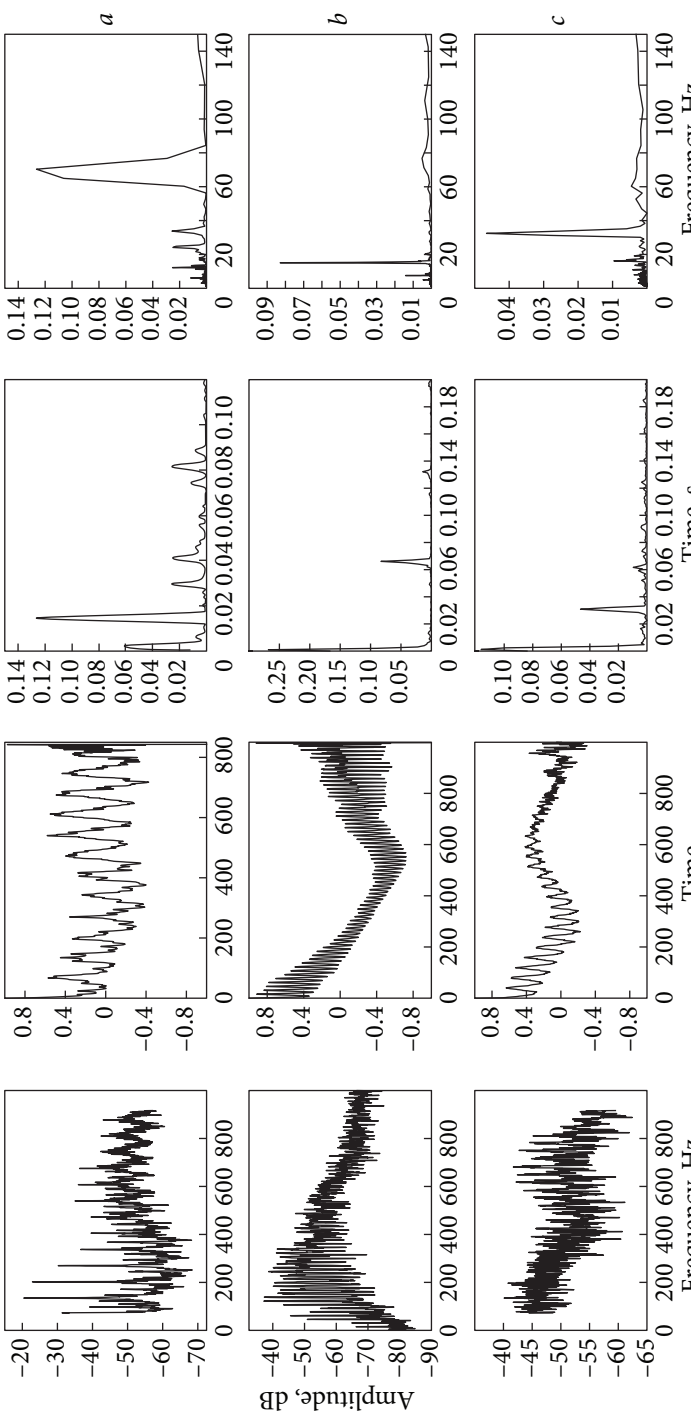

Fig. 3.3. Acoustic noises. Spectra (*1*), autocorrelation functions-ACF (*2*), FFT from ACF-cepstrum (*3*) and periodogram from cepstrum (*4*) for helicopters: *a* — Kazan-Ansat; *b* — Ka-32; *c* — McDonnell Douglas MD 900

was called the method of homomorphic deconvolution or homomorphic filtering [215]. The first mentions of the term "cepstrum" date back to 1978, when Silvia and Robinson in their work [216] used it to denote their proposed method of seismic signal analysis. This approach consists of the fact that for minimum-phase signals, the cepstrum-spectral coefficients can be obtained directly from the estimation of the power spectrum. Both methods agree that they use the inverse FFT of the logarithmic power spectrum. And the difference between them is that the "cepstrum" method is characterized by cepstrum coefficients obtained from Kolmogorov's power series [217].

An example of the use of cepstral processing for the selection of modulation frequencies associated with the rotation of helicopter rotors is shown in Fig. 3.3. From the original recording of the acoustic noise signal using the Fourier transform, we get the spectrum: *iw*

$$S(iw) = F(S(t)). \tag{3.8}$$

Then, the correlation function is calculated from the logarithm of the spectrum modulus:

$$R(\Delta w) = \int_0^\infty \ln(|S(w)|)\ln(|S(iw+\Delta w)|)dw \tag{3.9}$$

and the Fourier transformation $F(*) = \int_0^\infty (*)\exp(-iwt)dt$ is performed, which will be the cepstrum of the original process.

$$C(\tau) = F(R(\Delta w)). \tag{3.10}$$

It can be seen that the harmonics of the modulating frequency of rotation of the rotors can be traced in the acoustic noise spectra of various types of helicopters (Fig. 3.3—1). It should be noted that the selected types of helicopters have only main rotors. This leads to the fact that in the correlation function calculated by the logarithm of the spectrum, the periodicity associated with this can be traced (Fig. 3.3—2). The Fourier transform from the correlation function (caps — Fig. 3.3—3) has a response corresponding to the frequency (mesh) of the period of the modulation function, which, as you can see, has a value of approximately 15 Hz and 30 Hz, respectively (Fig. 3.3—4).

The results of the evaluation of the modulating frequencies of the rotors for several types of helicopters are shown in the Table 3.5. A comparison of the modulation frequencies obtained by the calculation method with the frequencies of the acoustic and radar portraits shows, in most cases, their satisfactory correspondence.

Fig. 3.4 shows the spectrum of the VHF broadcast signal scattered from the helicopter.

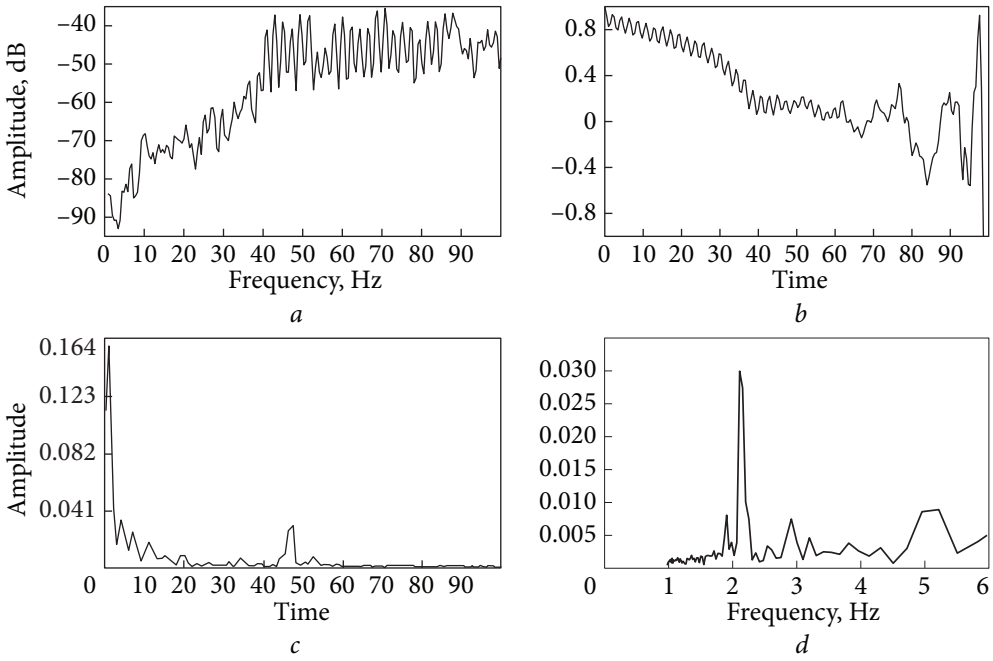

Fig. 3.4. Radar mapping. Spectrum (*a*), its correlation function (*b*), cepstrum abscissa time (*c*), cap frequency abscissa (*d*)

Table 3.5. **Experimental (by spectrum and cepstrum) and calculated values of the modulation frequencies of the carrier and steering rotors**

Type of helicopter	Modulation frequency of the carrier rotor, Hz			Tail rotor modulation frequency, Hz		
	Experiment		Calculation	Experiment		Calculation
	Spectrum	Cepstrum		Spectrum	Cepstrum	
MD 900 Explorer	36	32.4	39.3	—	—	—
Ka-32K	16	15.1	15.3	—	—	—
Kazan-Ansat	—	—	21.1	—	70.3	96.6
Bell-210	11	—	11	56	—	62
Bell-429	26	—	29	—	—	98
Mi-8AMTSh Terminator	—	—	15.3	—	—	41.5
Mi-8AMT (Mi-171)	—	—	19.1	—	—	62.3

It traces the frequencies caused by the presence of rotating elements. They are also observed in the correlation function calculated from the logarithm of the spectrum — Fig. 3.4, *b*, as well as in its Fourier transformation (cepstrum — Fig. 3.4, *c*, *d*).

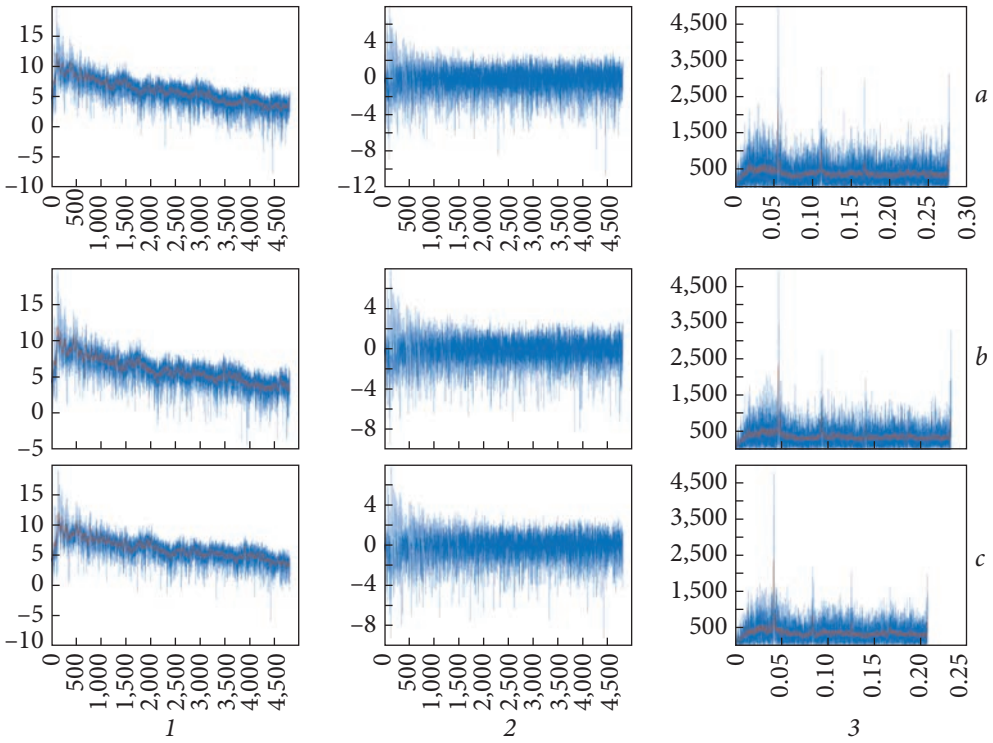

Fig. 3.5. Capturing of acoustic signals of a ground object with a diesel engine at different engine speeds: *a* — 600 rpm; *b* — 900 rpm; *c* — 1100 rpm; *1* — spectrum, *2* — non-viscous, *3* — cepstrum

Another approach of using cepstral processing to determine the rotation period can be proposed. It consists of:

1. Estimates of spectral characteristics of object noise.
2. Definition of the moving average spectrum in the smoothing window.
3. Calculated discrepancies between the spectrum and the smoothed spectrum displayed on a logarithmic scale.
4. Computational Fourier transforms from the spectral incoherence, i.e., cepstrum.

With this approach, it is possible to weaken the influence of trends on the cepstrum, and it is also possible to trace the change in frequencies associated with the modulating effect of the propulsion system (Fig. 3.5).

It shows spectra, sliding spectra — Fig. 3.5, *1*, and their incoherence with the spectra — Fig. 3.5, *2*, as well as Fourier transformations obtained from the incoherence, i.e., cepstrum — Fig. 3.5, *3*. They are obtained from the acoustic noises of a diesel engine at different revolutions. Visible — Fig. 3.5, *3*, that the cepstral processing in this case also allows to distinguish the periodicities associated with engine revolutions, weakening at the same time the influence of low-frequency trends of the spectra.

3.3. Radar and acoustic fields of a turbojet engine

The performed experimental and theoretical studies of radar reflections from turbojet engines (TJE) made it possible to establish the presence of discrete lines in their spectrum. The specified features were noted in the narrow sector of the bow and stern corners. Therefore, it is of interest to study radar reflections in the sector of angles close to the normal when there is no Doppler frequency shift in the reflected signal — and the casing shields the rotating turbine and compressor. In addition, it is advisable to identify the features of the radar and acoustic fields that could be used to detect and recognize objects from the TJE.

Spectral polarization features of radar reflections from TJE and connections of acoustic and radar fields were experimentally investigated. The experiments were carried out using a two-wave (8 mm and 3 cm waves) measuring complex of continuous radiation. The object of research was the TJE of the VK-1 type.

In the second series of experiments, the peculiarities of the acoustic signal created by a working engine were studied. In the spectra of the acoustic signal at all engine operating modes except afterburner (14,000 rpm), discrete lines were observed at frequencies multiples of the engine shaft rotation frequency (curves *1*—*3* in Fig. 3.6). *K* is the value of the estimate of the number of blades.

An increase in engine revolutions led to a displacement of the discrete lines into the high-frequency region and, simultaneously, to an expansion of the continuous part of the acoustic signal spectrum. As research has shown, the continuous part of the acoustic signal spectrum for all engine operating modes can be approximated by Gaussian (at low revolutions) and then exponential (at higher revolutions) curves.

When the engine was operating in the afterburner mode (14,000 rpm), the spectrum became continuous (curve *4* in Fig. 3.6). At the same time, the signal intensity increased by more than two orders of magnitude.

In this case, the dependence of the spectral density on the frequency can be approximated by expressions of the form: $S(F) \sim (F/\Delta F)^{-n}$ if $n \approx 2$.

In the Doppler spectra of the radar reflections from the hull with the engine running, both in the centimeter and millimeter wave ranges, a spectral line is observed at a frequency corresponding to the engine shaft rotation frequency in the aligned (vertical) and cross (horizontal) polarizations. As an example, Fig. 3.7 shows the spectra of reflection from the terrain and TJE, obtained in 0.1 s, at waves of 3 cm (Fig. 3.7) and 8 mm (Fig. 3.7, *b*) on horizontal (curve *1*), vertical (curve *2*) polarizations and the mutual spectrum (curve *3*) normalized to the maximum value of the spectral density. In Fig. 3.7, *2*, the phase characteristics of the scattered signals spectra are shown. The low-frequency part of the spectrum (up to approximately 80—100 Hz) is caused by reflections from the object's body and terrain, and the spectral line at a frequency of about 140 Hz corresponds to the frequency of rotation of the engine shaft (about 8,000 rpm).

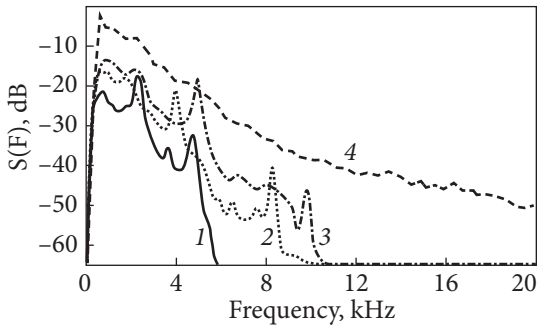

Fig. 3.6. Acoustic noise spectra of the VK-1 engine: *1* — n = 5,000 rpm, 84 Hz, K = 36; *2* — n = 8,000 rpm, 133 Hz, K = 38; *3* — n = 10,000 rpm, 167 Hz, K = 36; *4* — n = 14,000 rpm, 233 Hz

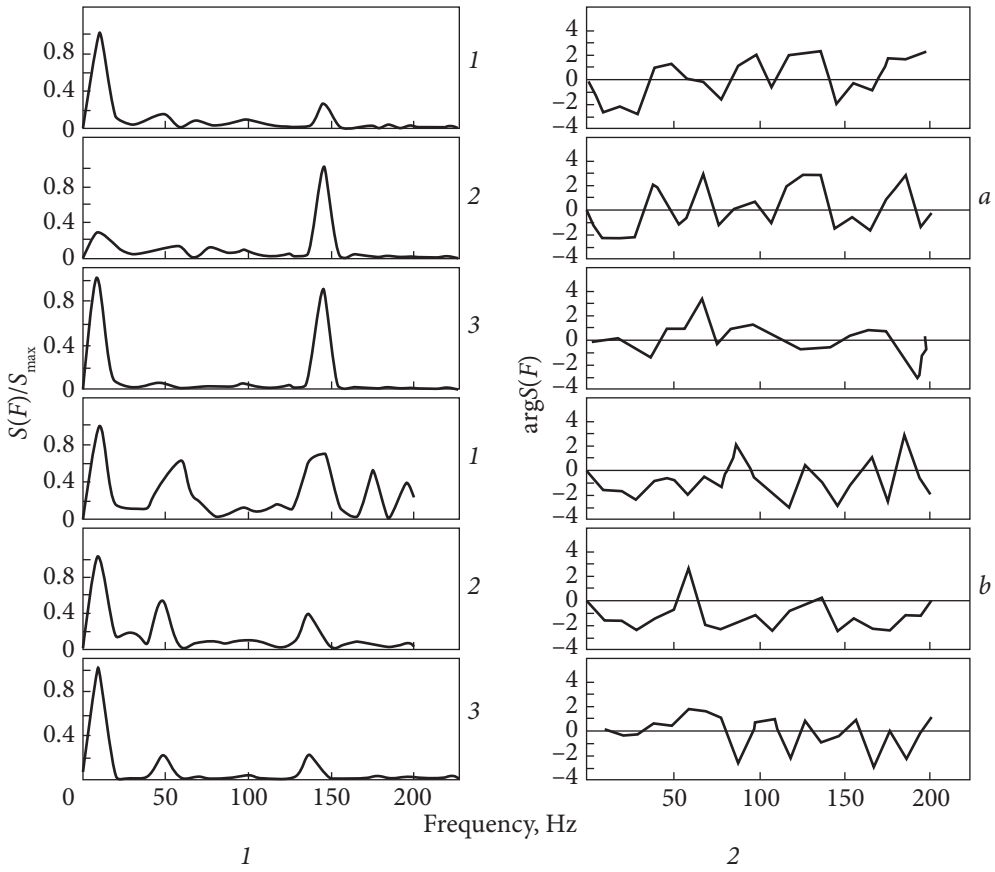

Fig. 3.7. Radar scattering from the VK-1 body during its operation: spectra is on the left *1* and reflection phases is on the right *2* at a wave of 8 mm (*a*) and 3 cm (*b*), *2* is vertical and *1* — horizontal polarization of reception, *3* — mutual spectra

The coincidence of the frequencies of the spectral lines that correspond to the rotation frequency of the motor shaft on horizontal and vertical polarizations in both wave ranges should be noted; while the reflection spectra from

the terrain differ significantly for these wavelengths and signal polarizations. This circumstance can be used for selection by mutual correlation processing of coincident spectral components in a scattered signal at different polarizations or different wave ranges. Presumably, their appearance is related to the phase modulation of the scattered signal caused by the vibration of the TJE housing due to the operation of the engine. The magnitude of the reflected signal at low phase modulation indices:

$$m = K\Delta l << 1, \tag{3.11}$$

where $K = 2\pi/\lambda$ is the wave number, and Δl is the amplitude of vibration of the body, will be proportional:

$$\sigma \sim \sigma_W m^2, \tag{3.12}$$

where σ, σ_W — RCS of the spectral line due to vibration and of the TJE body as a whole.

It is obvious that with the shortening of the wavelength, the effects associated with the modulation of the scattered signal by the body vibrations will increase in proportion to λ^{-2}, which means that for their detection, it is appropriate to use waves of the millimeter and submillimeter ranges.

The study of the reflected TJE signals in the centimeter and millimeter ranges at different polarizations made it possible to establish their correlation. The coefficient of mutual correlation of orthogonally polarized components at a wave of 3 cm was 0.6—0.75, decreasing to 0.25—0.65 at a wave of 8 mm. At the same time, the depolarization coefficient of the scattered signal is 6...10 dB.

The conducted research made it possible to draw the following conclusions:

- in the spectra of signals scattered by objects with a working TJE, both in the centimeter and millimeter ranges on both polarizations (horizontal and vertical), discrete lines at the rotation frequencies of the engine shaft are detected due to the phase modulation of the reflected signal caused by the vibration of the body;
- in the acoustic signal, discrete lines are observed at frequencies that are multiples of the product of the engine shaft rotation frequency and the number of turbine blades.

Correlation of scattered TJE signals in different ranges and polarizations is observed.

3.4. Dynamic spectra of radar and acoustic radiation of objects

To study the dynamics of changes in the spectral composition of the acoustic signal, spectrograms or dynamic Fourier transformation were used. At the same time, expansion in the Fourier series is carried out in a time window limited in duration.

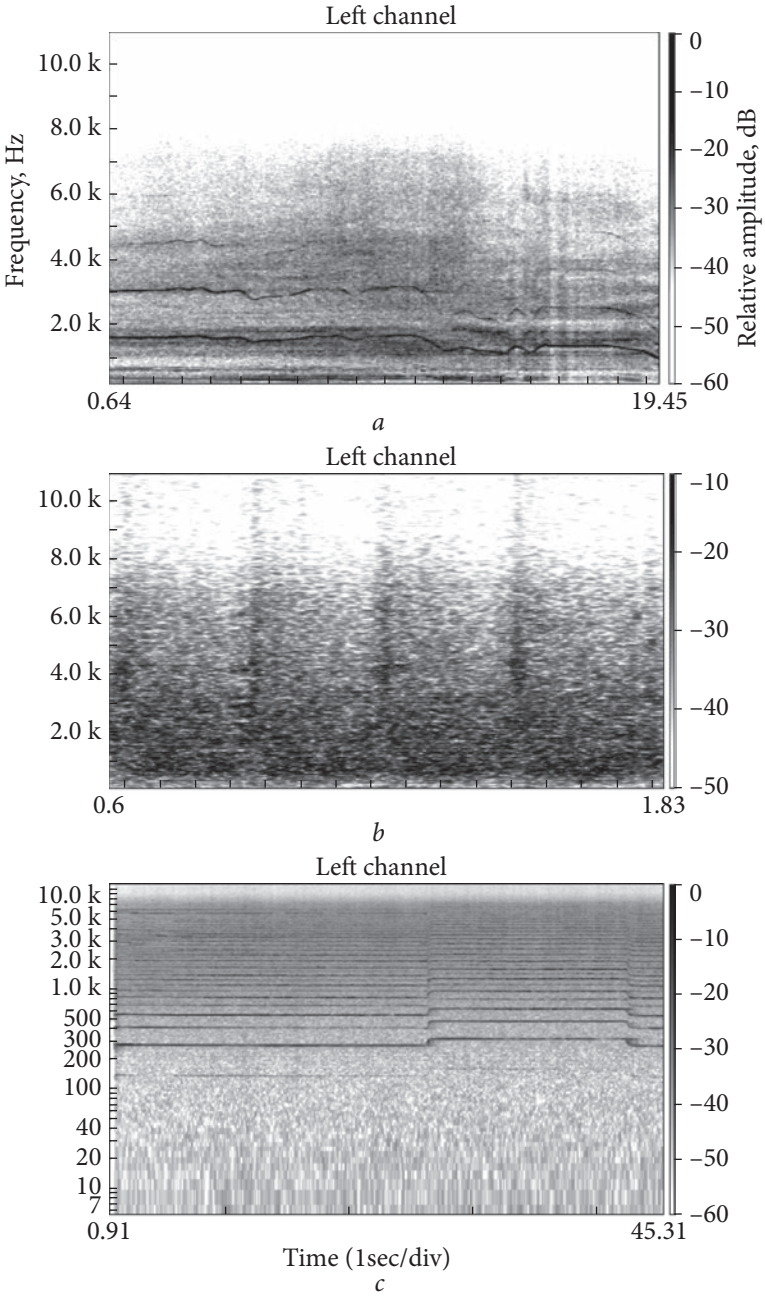
Left channel
Frequency, Hz
10.0 k
8.0 k
6.0 k
4.0 k
2.0 k
0
−10
−20
−30
−40
−50
−60
Relative amplitude, dB
0.64
19.45
a
Left channel
10.0 k
8.0 k
6.0 k
4.0 k
2.0 k
−10
−20
−30
−40
−50
0.6
1.83
b
Left channel
10.0 k
5.0 k
3.0 k
2.0 k
1.0 k
500
300
200
100
40
20
10
7
0
−10
−20
−30
−40
−50
−60
0.91
45.31
Time (1sec/div)
c

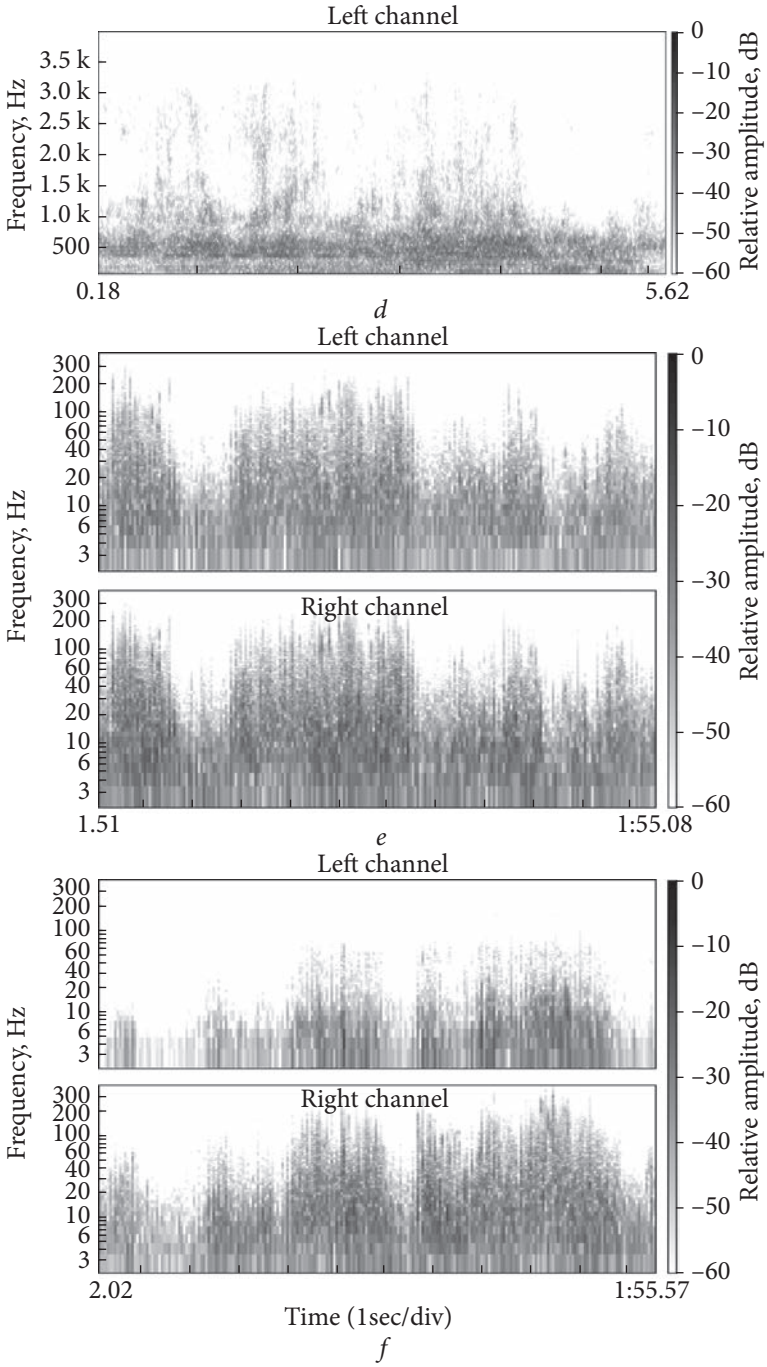

Fig. 3.8. Spectrograms of acoustic noise of technical objects *(a—d)* and radar reflections at 8 mm. and 10 cm. Waves (*e, f*) from reeds: *a* — diesel engine, *b* — several (5) gun shots, *c* — aircraft-type UAV, *d* — MI-8 helicopter. Reflection on the HP (top picture) and VP (bottom picture) from the reed at a wave of 8 mm, *e* — reflection at a wave of 10 cm (top picture) and 8 mm (bottom picture) from reeds on the VP

If this window is moved along the signal implementation, it is possible to study the dynamics of changes in the spectral composition of noise over time. As an example, Fig. 3.8 shows spectrograms of acoustic noises of various objects of technology.

For spectrograms of a diesel engine (Fig. 3.8, *a*) and aircraft-type UAV engine (Fig. 3.8, *c*) you can see the moments of changing engine operating modes — reducing the number of revolutions — Fig. 3.8, *a* and an increase, and then after some time, a decrease to the previous value of the number of revolutions for an aircraft-type UAV — Fig. 3.8, *c*. Spectrograms of the sounds of gunshots (Fig. 3.8, *b*) and the sound caused by the movement of helicopter rotor blades (Fig. 3.8, *d*) are characterized by significant variability in time. Thus, at the moment of the shot, there is a significant expansion of the noise spectrum by 5...10 times within a time of approximately a few milliseconds. The acoustic noise of a helicopter is characterized by periodicity with the period of movement of the rotor blades (Fig. 3.8, *d*). Thus, the use of spectrograms allows studying the dynamics of changes in the spectral characteristics of non-stationary object noises. The same features are characteristic of spectrograms of radar reflections from vegetation under the influence of wind, moving biological objects (people and birds), and helicopters. As an example, Fig. 3.8, *d*, *e* shows the spectra of radar reflections from reeds at 8 mm and 10 cm waves, which fluctuate under the influence of the wind.

The reflection study was performed using a homodyne radar of millimeter (wavelength 8 mm) and centimeter (wavelength 10 cm) ranges of continuous radiation, the appearance and technical characteristics of which are given in Appendix 2.

Spectrograms for reflection from reeds are characterized by bursts of spectral density associated with gusts of wind, and they are observed on both polarizations of reception synchronously — Fig. 3.8, *d*. The same character of reflection from reeds and at waves of centimeter and millimeter ranges Fig. 3.8, *e*. The type of spectrograms of radar reflections from reeds is similar to the spectrograms of acoustic wind noise and sea surf.

3.5. Spectral and polarization structure of reflection from a helicopter

The presence of a discrete structure in the spectrum of the scattered signal of radar reflections from helicopters, the ratio of the levels of spectral components, the distance between them, and their number can be used as a basis for the construction of helicopter recognition algorithms. For this, the length of the implementation must be at least the period of rotation of the rotor, which imposes restrictions on the efficiency of solving recognition tasks. In some cases, the length of the implementation should be less than the rotation period of the rotor. In this case, the spectrum of the signal reflected from the helicopter blades

changes dynamically in time, and it is necessary to use other approaches for analysis. This situation is typical for short-range radar systems.

The polarization and spectral features of the reflection from the helicopter model during the observation times that make up part of the rotor rotation period were experimentally investigated. During experiments with a helicopter model, it was established that in the spectra of scattered signals, on both horizontal and vertical polarizations, with a sample length of 0.4...1 sec, coincident discrete lines with a frequency spread corresponding to the frequency of the rotor shaft rotation are observed. The spectra obtained at short observation intervals (about 40 ms) are significantly different. At the same time, individual spectral lines are no longer separated in the frequency domain. In addition, during observation times shorter than the rotation period of the rotor, in the spectrum of the reflected signal, "flashes" of spectral density are observed in the high-frequency region with the rotation frequency of the rotor shaft. They appear because of the frequency modulation of the signal scattered from the rotor blade due to the change in the projection of the velocity vector of the scattering element in the direction of irradiation. The maximum values of the spectrum width will be when the rotor blade is perpendicular to the direction of irradiation. As an illustration, Fig. 3.9 shows the spectrum of the signal reflected from the helicopter model on vertical polarization, obtained from the implementation, with a length of 40 ms, at the moment when the rotor blade passes through the normal to the direction of irradiation.

Similar values of the width of the reflection spectrum from the helicopter in the high-frequency region will be when using the decimeter wavelength range (wavelength of about 60 cm). A reduction in the operating wavelength will lead to a proportional λ^{-1} broadening of the high-frequency part of the spectrum of the reflected signal. Its width can reach dozens of kilohertz in the UHF and VHF bands. In the pulse mode of probing, the transformation (collapse) of the high-frequency spectral components of the scattered signal is observed in the frequency range up to half the pulse repetition frequency.

The study of the cross-correlation coefficients of various spectral components made it possible to reveal the presence of a highly correlated region in the spectrum of the signal reflected from the helicopter model. Fig. 3.10 shows the dependence of the ρ cross-correlation coefficient on the frequency F_i, F_j of the spectral components, which is calculated using the ratio [44]:

$$\rho(F_i, F_j) = \frac{\left\langle S(F_i)S(F_j)\right\rangle - \left\langle S(F_i)\right\rangle\left\langle S(F_j)\right\rangle}{\sqrt{\left(\left\langle S^2(F_i\right\rangle - \left\langle S(F_i)^2\right\rangle\right)\left(\left\langle S^2(F_j)\right\rangle - \left\langle S(F_j)\right\rangle^2\right)}}, \qquad (3.13)$$

where $S(F_i)$, $S(F_j)$, $\rho(F_i, F_j)$ are the spectral density at F_i and F_j are frequencies and the mutual correlation coefficient, respectively.

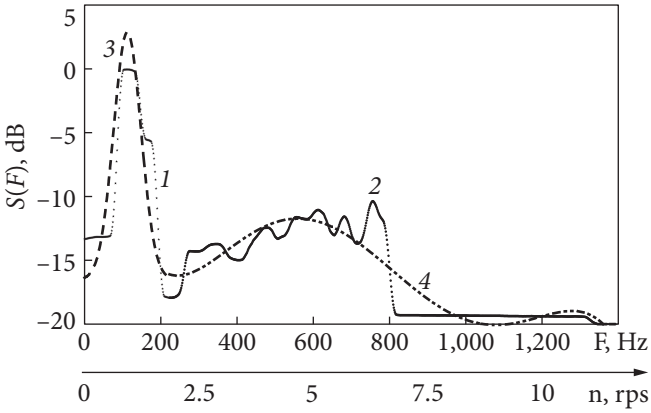

Fig. 3.9. The spectrum of the signal scattered from the helicopter model at an 8mm wavelength and vertical polarization: *1* — body line, *2* — rotor modulation, *3* — approximation by the Gauss function, *4* — approximation by a polynomial of the 5th degree

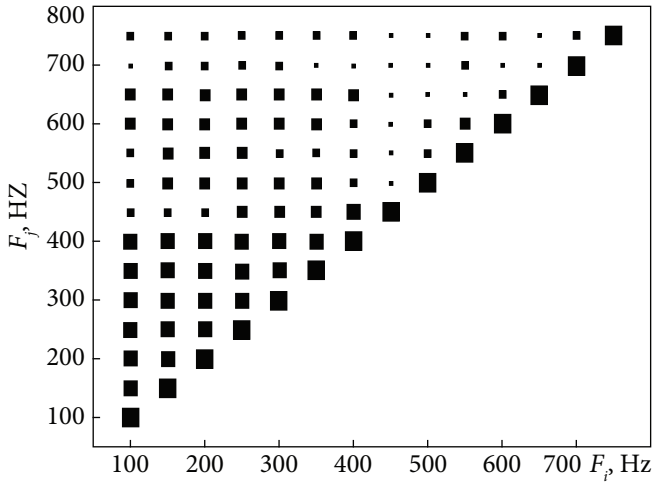

Fig. 3.10. Matrix of cross-correlation coefficients of spectral reflection components from the helicopter model: ■ — $\rho(F_i, F_j) = 1$, ■ — $\rho(F_i, F_j) = 0.8$, ■ — $\rho(F_i, F_j) = 0.6$, ▪ — $\rho(F_i, F_j) = 0.4$, ▪ — $\rho(F_i, F_j) = 0.2$ correlation coefficients

It can be seen that in the frequency range from 100 to 400 Hz, the mutual correlation coefficient of the spectral components of the scattered signal exceeds 0.6. This confirms the conclusion about the synchronicity of the appearance of "flashes" of spectral density in the high-frequency region at different frequencies.

The experiments in natural conditions conducted using pulsed radars of the centimeter range (wavelength 2 cm), the appearance and technical characteristics of which are given in Appendix 2, confirmed the main regularities established during measurements with the model and allowed us to conclude that in the spectra of the reflection from the helicopter, at observation intervals shorter than the rotation period of the rotor blades, bursts of spectral density in the high-frequency region are observed. Their presence can be used to detect and recognize the helicopter.

Conclusions

1. The modulation frequencies of the signal scattered by the rotors of different types of air objects differ significantly, which can be used for their identification.

2. Acoustic portraits of equipment objects make it possible to determine engine revolutions based on the modulation frequency, which also manifests itself in the modulation of reflected radar signals.

3. A sharp increase in the amplitude of the vibration frequency of the body can be a sign of engine operation in the afterburner mode.

4. In the spectrum of reflections from aerodynamic objects with a rotor engine, there are components with frequencies multiples of the rotor rotation frequency.

5. Acoustic portraits and optical images of equipment objects can serve as a basis for determining signatures in radar portraits.

6. In the spectra of signals scattered by objects with a working TJE, both in the centimeter and millimeter ranges, on both polarizations (horizontal and vertical), discrete lines at the engine shaft rotation frequencies were detected due to the phase modulation of the reflected signal caused by the vibration of the body. In the acoustic signal, discrete lines are observed at frequencies that are multiples of the motor shaft rotation frequency by the number of turbine blades.

7. Correlation of scattered TJE signals is observed in different ranges and at different polarizations.

8. Spectral density spikes in the high-frequency region are observed in the spectra of reflections from the helicopter obtained at observation intervals shorter than the rotation period of the rotor blades with a frequency that is a multiple of their rotation frequency. Their presence can be used to detect a helicopter in cases where there is no Doppler frequency shift of the signal reflected from the body, and it is not separated from the background of reflections from the terrain.

9. The high-frequency components of the reflection spectrum are mutually correlated due to the frequency modulation of the scattered signal by the rotating blades. The presence in the high-frequency region of a broadband burst that appears with the frequency of rotation of the rotor can be used as an informative feature for helicopter recognition.

10. Spectrum broadening during wind gusts is observed in radar reflections of vegetation at different polarizations and wavelengths.

CHAPTER 4

Environmental monitoring and solving the tasks of radio location using radiation of broadcasting and TV stations of HF and VHF bands and GNSS systems

The chapter examines the methods of diagnosing the refractive properties of the troposphere based on the amplitude of VHF signals on the over-the-horizon (OTH) paths [218] and analyzes the characteristics of the inversion layers in the propagation channel based on the fluctuations of the received signal.

Estimates of RCS of airborne objects at frequencies corresponding to resonant scattering are given, and RCS of airborne objects are obtained for bistatic radars with illumination through the ionosphere using experimental data on target detection at Doppler frequencies [40].

The possibility of using signals from GNSS to diagnose the state of the sea surface and monitor waves was considered [219].

The main results are published in papers [218—229].

4.1. Estimation of refractive properties of the troposphere by the field attenuation factor of the VHF field over-the-horizon

The papers of A. I. Kalinin [230, 231] were used as a theoretical basis for researching the refractive properties of the troposphere in terms of the VHF signal attenuation factor on OTH paths.

When using a simplified method of approximate estimates of the field strength in the shadow and penumbra zones [230], the errors in the calculation of the attenuation factor for the VHF range do not exceed 2 dB. It is known that the dependence of the attenuation factor on the distance in the shadow zone is close to exponential, and the rate of decrease depends on the wavelength and refraction, which is taken into account through the equivalent radius of the Earth, the polarization of radiation and reception, as well as the electrical parameters of the Earth's surface. Most often, the Vvedenskyi method [231] is used to determine the field strength and, therefore, the attenuation

factor in the shadow region, taking into account the parameters of the underlying surface.

In the VHF range, when the antennas are located not very close to the Earth's surface, the dependence of the attenuation factor V has an exponential character not only for the zone of the geometric shadow but also near it, at the border of the line of sight in the penumbra zone [230] (4.1).

$$V[\text{dB}] = V_0[\text{dB}] = -17.1\sqrt{Y_1}\left(1+\frac{1}{\sqrt{m}}\right)(\xi - 1), \tag{4.1}$$

where $\xi = \dfrac{R}{R_{\text{lsd}}}$, R_{lsd} is the line-of-sight distance (to the radio horizon), $m = \dfrac{Y_1}{Y_2} \le 1$, Y_1, Y_2 are the given altitudes of the receiving and transmitting points. V_0[dB] attenuation factor of the EM field at the line-of-sight range:

$$x_{\text{lsd}} = \frac{R_{\text{lsd}}}{R_0} = \frac{\sqrt{2a_e}\left(\sqrt{h_1}+\sqrt{h_2}\right)}{R_0} = \sqrt{Y_1}+\sqrt{Y_2}\ . \tag{4.2}$$

At the same time, the error in the calculation of the attenuation factor is less than 2 dB, when $x_{\text{lsd}} >> 0.5$. For analytical calculations, a polynomial approximation of the form is used:

$$V_0(\mu) = \sum\nolimits_{i=0}^{n} A_i \mu^i, \tag{4.3}$$

where A_i are the coefficients of the approximating polynomial.

Table 4.1. **The main characteristics of measuring channels**

Path №	Location of the transmitting point	Path length, km	Frequency, MHz	Channel No.	Transmitter power, kW	Height of the transmitting antenna, m	Gain factor of the transmitting antenna, dB	Radius Ist of the Fresnel zone, m
1	B	63	175	6	5.0	175	10	348
1	B	63	223	12	5.0	175	10	308
1	B	63	519	27	1.0	190	5.5	202
1	B	63	655	44	0.5	146	5	180
2	Kr	193	191	8	5.0	250	10	548
3	Kh	207	207	10	40.0	203	10	513

Notes: B — Bilhorod; Kr — Kursk; Kh — Krasnohorivka, Poltava region.

Table 4.2. **Errors of the dependence of V_0 on μ**

Regression order, n	*R*	σ	*N*
2	0.984	2.07	13
3	0.998	0.68	13
4	0.999	0.59	13
5	0.9993	0.52	13
6	0.9994	0.51	13

Three routes were chosen to measure the field attenuation factor and estimate the values of the effective gradient of the refractive index based on experimental data, the main characteristics of which are given in Table 4.1.

The choice of propagation paths was made due to the need to cover both radio wave propagation zones (diffraction and far tropospheric propagation). 1st path (Bilhorod — Kharkiv) covered the transition region of the penumbra — shadow, while 2nd and 3rd paths (Kursk — Kharkiv and Krasnohorivka — Kharkiv) covered the region of deep shadow, which dominates the propagation of radio waves scattering on tropospheric inhomogeneities. Paths 2 and 3 had approximately the same length and mutually orthogonal orientation (angle of about 90 degrees).

This orientation of the tracks made it possible to analyze the influence of the directions of movement of air masses relative to the propagation track on the OTH field attenuation factor. Signals transmitted by TV centers were used for research. The reception point was located in the city of Kharkiv.

For OTH paths, the characteristics of which are presented in Table 4.1, the obtained approximation errors are given in Table 4.2.

In Table 4.2, the following designations are used: *R* — correlation coefficient; σ — residual error of approximation; *N* is the number of points. Based on their analysis using the Fisher criterion [232], a polynomial with $n = 5$ was chosen for further calculations. Errors in estimating the value of the attenuation factor are no more than 2 dB, with errors in measuring the length of the path and the heights of the corresponding points no more than 15%. In papers [233—235],

Table 4.3. **Coefficients of the polynomial approximation of the dependence of the gradient of the refractive index on the attenuation factor for different paths and channels**

Channel	City	Polynomial coefficients					
		A0	A1	A2	A3	A4	A5
6	B	–0.6971	–0.1553	–0.0161	–8.418E-4	–2.114E-5	–2.052E-7
12	B	–0.2728	–0.050	–0.0056	–3.381E-4	–9.594E-6	–1.033E-7
27	B	–0.0950	–0.0049	–1.243E-4	–1.718E-5	–7.619E-7	–1.114E-8
8	Kr	–0.1665	–0.0011	2.049E-6	–2.550E-8	–1.776E-10	–4.012E-13
8	Kh	–0.17223	–0.0012	1.545E-6	–4.411E-8	–3.049E-10	–7.130E-13
10	Kh	–0.16853	–0.0012	1.224E-6	–4.492E-8	–3.115E-10	–7.386E-13

Notes: B — Bilhorod; Kr — Kursk; Kh — Krasnohorivka.

the dependence of the gradient of the refractive index on the values of the attenuation factor $g(V)$ was obtained for the calculated dependence of the attenuation factor $V(g)$ on the gradient of the refractive index g:

$$g(V) = \sum_{i=0}^{n} A_i V_i^n . \tag{4.4}$$

The final equation taking into account (4.4) and Table 4.2 is:

$$g = A_0 + A_1 V + A_2 V^2 + A_3 V^3 + A_4 V^4 + A_5 V^5 . \tag{4.5}$$

The resulting approximation coefficients for all paths are presented in Table 4.3 [218].

It should be noted that Table 4.3 shows the parameters of the polynomial approximation, which are better in terms of the Fisher criterion. The obtained ratios allow us to estimate the value of the effective gradient of the refractive index based on the experimentally obtained values of the field attenuation factor, which can be compared with the data of meteorological measurements.

4.2. Two-channel measurement of amplitude values of VHF signals on over-the-horizon routes

The radiation of the television center located in the city of Bilhorod was used as a source of VHF signal radiation. The receiving point was located in the city of Kharkiv, the height of the center of the two receiving antennas is 30.7 m relative to the Earth's surface, and 207.2 m relative to sea level. The distance between the lower and upper antennas (base) is about 10 m, approximately 15...20 wavelengths depending on the TV channel number.

Fig. 4.1 shows a map of the area with the location of the receiving and transmitting points, as well as the profile of the propagation path, taking into account the heights of the antennas, the curvature of the earth and the profile of the area, obtained using a topographic map. To determine the terrain profile, topographic maps and special software were used, which allowed to determine the relief profile from them [236].

The RMS deviation of the height relative to the average level on the path does not exceed 20 m. Fig. 4.2 shows the diagram of the location of the transmission antennas on the tower of the TV center of the city of Bilhorod.

Also, Fig. 4.2 shows the parameters of the transmitters, such as the radiation power, the value of the carrier frequency, the name of the television channel, and the type of the transmitting device. The distance to the television center of the city of Bilhorod is about 63 km.

The measuring complex should provide the possibility of measuring the level of signals on spatially separated antennas in the frequency band of TV signals, as

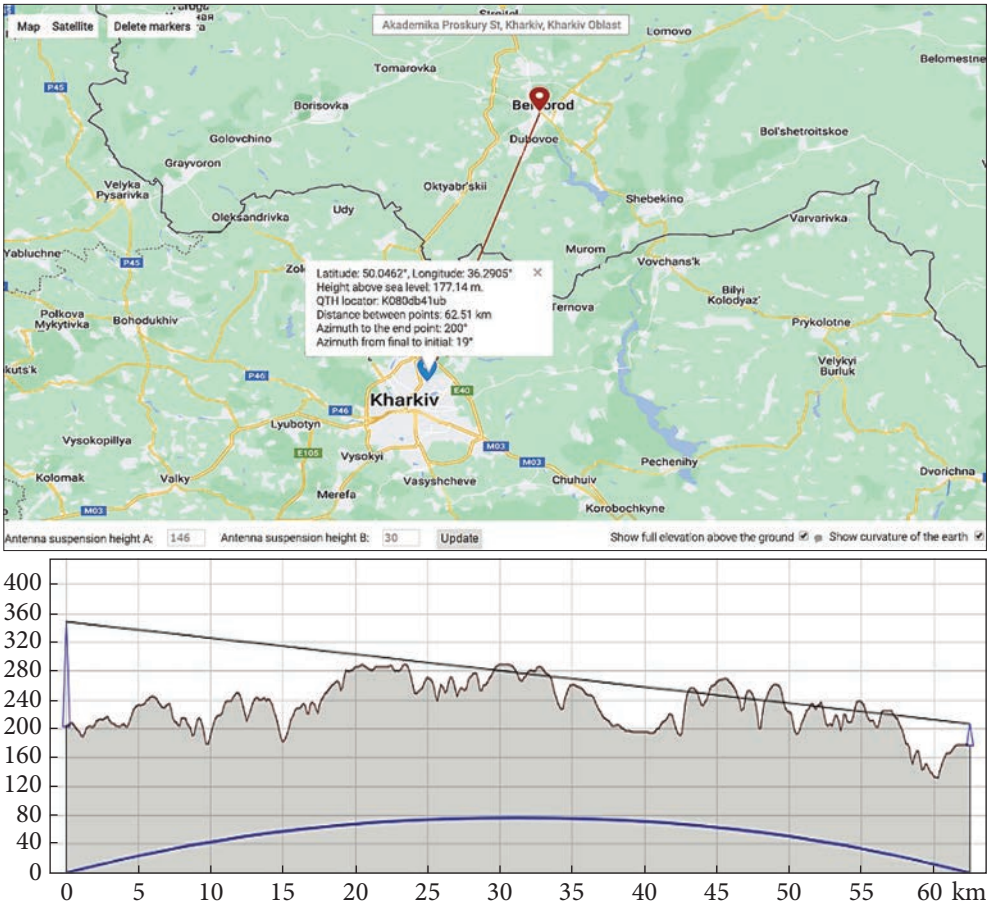

Fig. 4.1. Map of the area with the location of the receiving and transmitting points, the profile of the propagation path taking into account the heights of the antennas and the curvature of the earth and the profile of the area

well as measuring the angles of arrival of the signal, that is, the slope of the phase front arriving at the receiver of the electromagnetic wave. The R820T multifunctional microcircuit was used as a receiving device, which is a receiver with a high degree of integration, the structural diagram of which is shown in Fig. 4.3.

It includes a low-noise amplifier (LNA), a mixer, HF and IF filters, a phase-locking loop (PLL), an output amplifier with a variable gain (VGA), a voltage stabilizer, a tracking filter while eliminating the need for external filters, amplifiers, matching transformers and stabilizers. Fig. 4.4 shows the structural diagram of a two-channel receiver for measuring arrival angles with a common local oscillator based on the R820T microcircuit.

This measuring complex is a software-defined radio system (Software-defined radio, SDR) with a radio receiver that uses technology that allows the use of

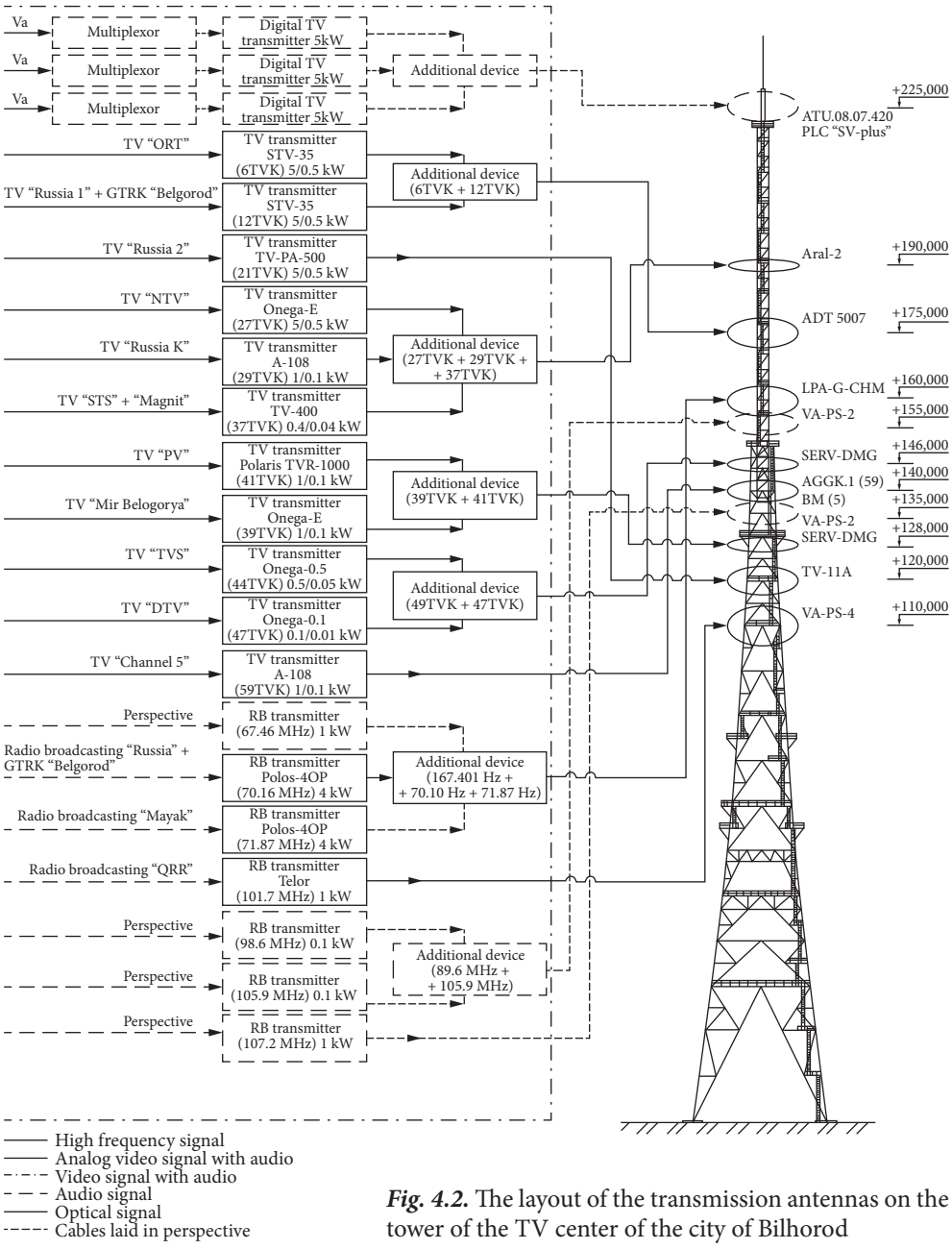

Fig. 4.2. The layout of the transmission antennas on the tower of the TV center of the city of Bilhorod

the software to set or change operating radio frequency parameters, including, in particular, the frequency range, bandwidth, and demodulation type.

A significant part of the digital signal processing is performed on a personal computer, which allows serving a large number of radio protocols. The measuring

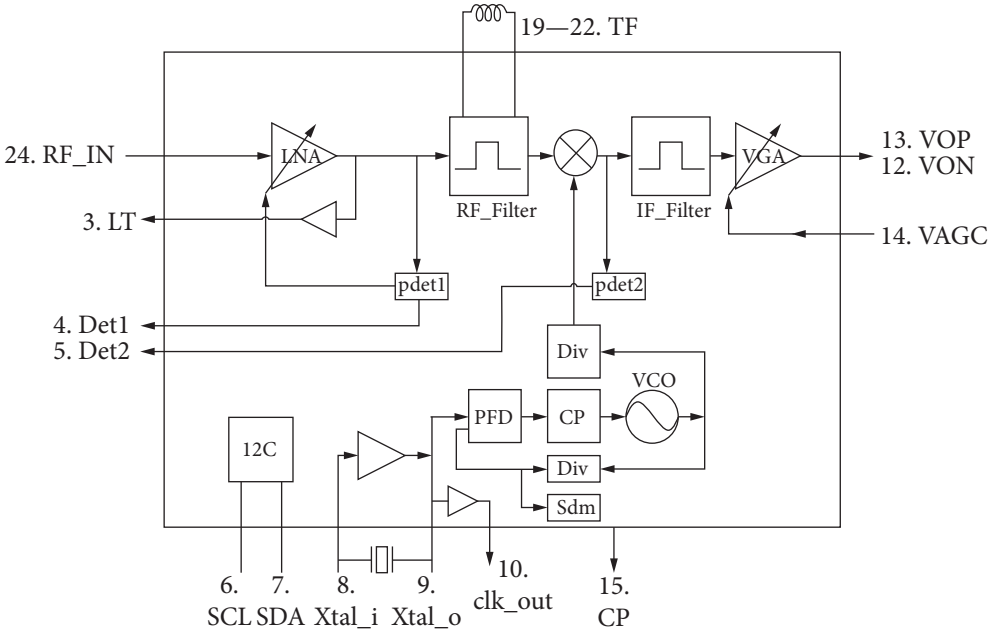

Fig. 4.3. Structure of the R820T measuring receiver

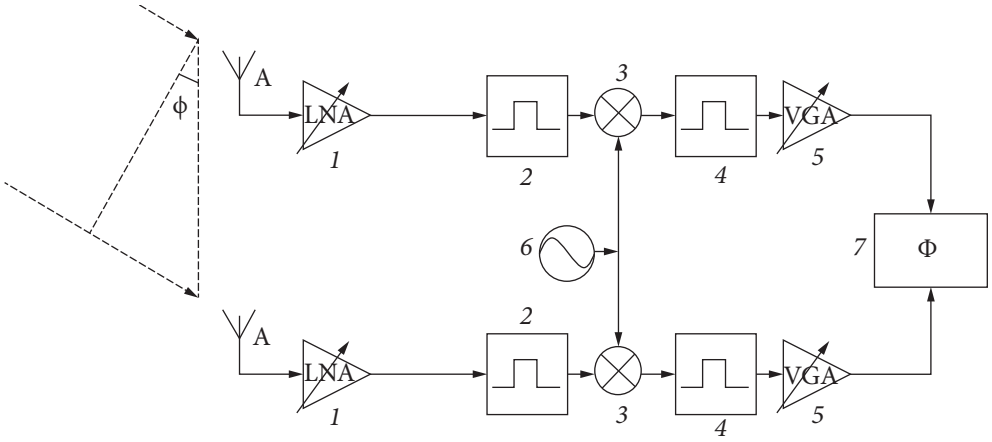

Fig. 4.4. The structure of the receiver for measuring the angles of arrival of television station signals. A — receiving antenna, *1* — low-noise HF signal amplifier, *2* — HF filter, *3* — mixer, *4* — IF filter, *5* — variable IF signal amplifier, *6* — voltage-controlled generator (VCG), *7* — phase difference meter

complex consists of a superheterodyne receiver, which converts the signal from radio frequency to an intermediate frequency, as well as an analog-to-digital converter (ADC). The main parameters of the receiver are the operating frequency range of 42—1,002 MHz, the noise of 3.5 dB, the phase noise level –98 dBm/Hz in the 10 kHz band, the maximum power at the input +10 dBm, the interference

suppression on the mirror channel 65 dBm. The main parameters of the VHF channels of the Bilhorod TV center, which is used in the experiment, are listed in Table 4.4.

Fig. 4.5 shows the examples of signal level recordings (*a*, *b*) and spectra of this signal (*c*, *d*) when receiving 21 channels of the Bilhorod TV Center, frequency 471 MHz from 05/01/18 to 05/08/18 on vertically spaced antennas.

Trend daily changes in the levels received by the upper (*a*) and lower (*b*) antennas are observed, and the signal level of the upper antenna (*a*) is significantly (by more than 6 dB) higher than the level of the lower (*b*), which directly follows from the considered method of field assessment VHF signal over the horizon. With the distances between the upper and lower antennas used in the experiments (about 10 m), both of them were on the slope of the first interference lobe.

These features are also manifested in the spectra of received signals, both in the low-frequency part, where daily trends are manifested and in the high-frequency part, which is caused by the influence of tropospheric inhomogeneities. It can be seen that the frequencies of the most energetic spectral lines (the first 3) coincide in the spectra, although their relative intensities are slightly different.

When the antennas are vertically spread, there is a displacement in the space of the zones essential for propagation. The coefficient of mutual correlation of implementations is quite low — 0.1431.

As an example, Fig. 4.6 shows the recordings of the VHF signals of the Bilhorod TV center for 20 days and the refractive index data for the same period, Fig. 4.7. As well as the combined data, averaged over a day and 3 days, Fig. 4.8.

The signal is characterized by cyclicality associated with the daily behavior of the signal. In addition, it should be noted that apart from inside the daily shifts, slower trend changes are also observed. In general, there is a tendency to decrease the signal level with a decrease in the refractive index of the troposphere, which is consistent with the theoretically expected changes. Thus, at the initial stage of measurements (from 28.03 to approximately 08.04), the average signal level is significantly, approximately 6...7 times higher than in the second period of measurements. An increase in the smoothing interval leads to an increase in the correlation coefficient of the received signal and the refractive index. When the smoothing interval changes from 3 hours to 3 days, the correlation coefficient increases from 0.35 to 0.8. Since the level of the signal received on the OTH path is determined by the value of the effective gradient of the refractive index of the troposphere on the path and the height of the receiving antenna, the signals

Table 4.4. **The parameters of decimeter channels transmitted by the TV center of Bilhorod city were used in the experiment**

The channels	1	2	3
Video carrier frequency, MHz	655.25	615.25	471.25
Antenna height above ground level, m	146	128	120
Transmitter power, W	500	1,000	500

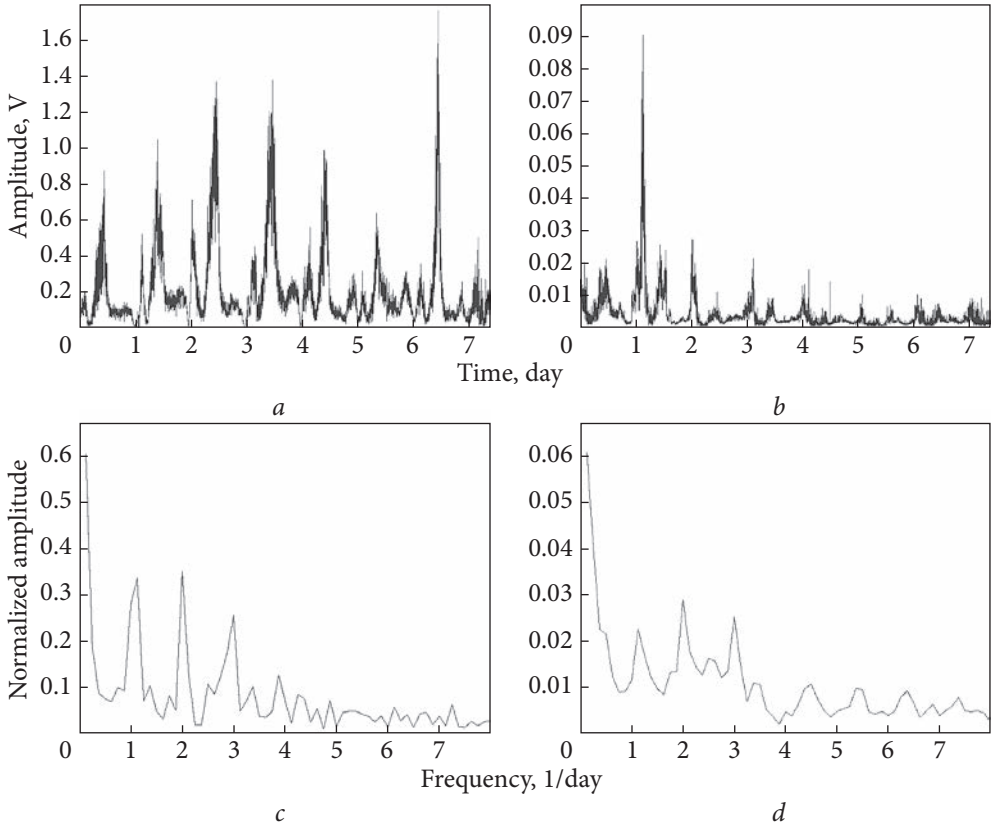

Fig. 4.5. Records of signal levels of 21 channels of the Bilhorod TV Center (*a*, *b*) and their normalized spectra (*c*, *d*) for antennas spaced by height, upper (*a*, *c*) and lower (*b*, *d*) at a frequency of 471 MHz from 01.05.18 to 08.05.18

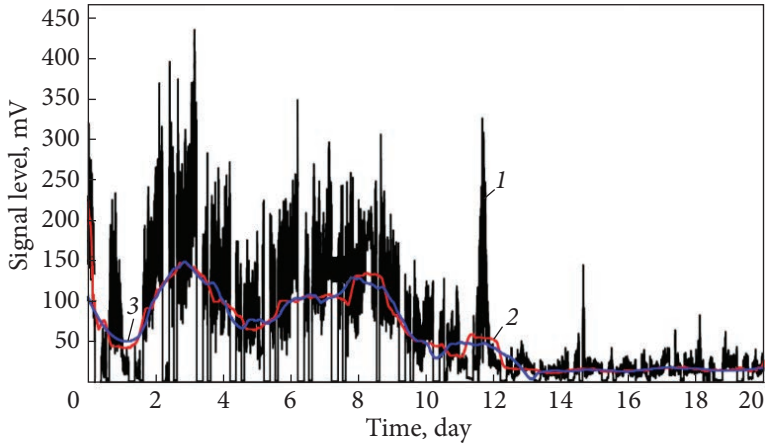

Fig. 4.6. Changes in the signal levels of channel 44 of the Bilhorod TV center, frequency 655 MHz from 03/28/18 to 04/17/18. The signal of the upper channel is initial data and averaged over 1 and 3 days — *1* — signal level, *2* — averaging in a sliding window for a day, *3* — averaging in a sliding window for three days

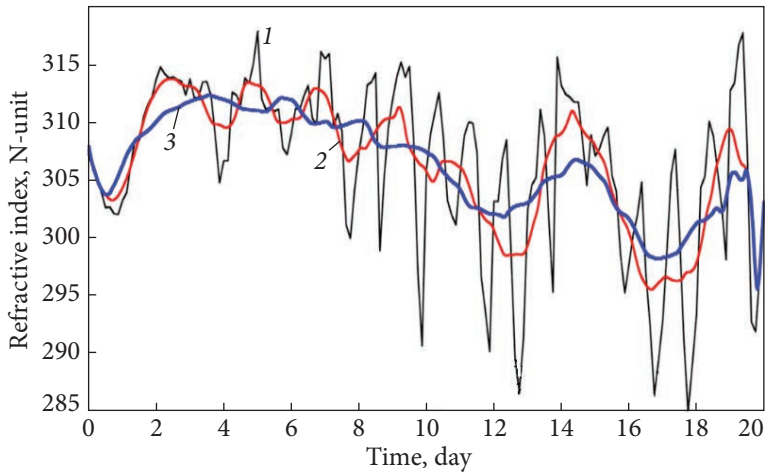

Fig. 4.7. Refractive index data are taken at 3 (1) hour intervals and averaged over *1* (*2*) and *3* (*3*) days — *1* — output data, *2* — averaging in a sliding window for a day, 3 — averaging in a sliding window for three days

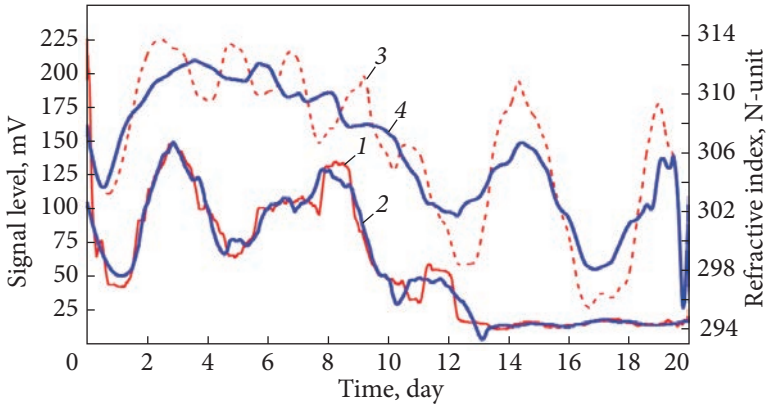

Fig. 4.8. Signal level data (*1*, *2*) and refractive indices (*3*, *4*), averaged over 1 day (*1*, *3*) and 3 days (*2*, *4*)

received by antennas spread over a distance can be used to estimate the effective value of the refractive index of the troposphere layer, which is essential for the propagation of radio waves [218].

4.3. Determination of the characteristics of inversion reflective layers in the troposphere based on changes in signal intensity on the over-the-horizon routes

For the mid-latitude zone, in which Ukraine is located, when receiving VHF radio waves in the zone of the near geometric shadow in conditions of a calm

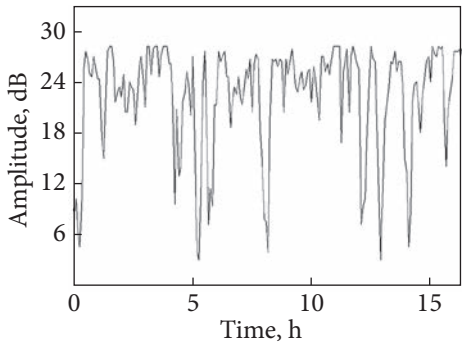

Fig. 4.9. Signal behavior in the presence of inversion reflective layers on the OTH path

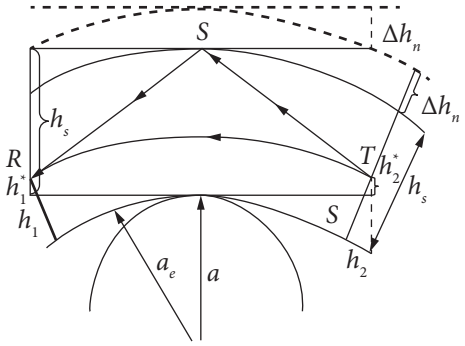

Fig. 4.10. Schematic presentation of the propagation channel

atmosphere, both seasonal [237] and diurnal changes in the signal level are observed, both after sunset and slightly later than sunrise, which is associated with a change in the refractive properties of the troposphere [71, 223, 231, 233—235]. However, in the spring-autumn period, in more than 30% of cases, along with a smooth increase in the signal (up to 10 dB) after sunset and the same decrease after sunrise, interference phenomena with deep fading were observed. Typical behavior of the signal on the OTH path in the presence of inversion layers is presented in Fig. 4.9. The presence of deep signal fades caused by multipath in the propagation channel is visible when not only the direct signal from the transmission point is present at the reception point but also the signal reflected from the inversion layer [238, 239].

$$\dot{S}_R = \dot{S}_{Tr}\dot{V} + \dot{S}_{Tr}\dot{\rho}, \tag{4.6}$$

where $\dot{S}_{Tr}$, $\dot{S}_R$ is the transmitted and received signal, $\dot{V}$ is the signal attenuation coefficient on the OTH path, and $\dot{\rho}$ is the reflection coefficient from the inversion layer.

In this case, the propagation channel, taking into account the presence of one raised inversion layer in the troposphere within the model of the equivalent radius of the Earth a_e [71], can be schematically presented as in Fig. 4.10.

This model takes into account the radius of curvature of both the Earth itself and the inversion layer and the height of the antennas. Fig. 4.10 shows the presence of one elevated inversion layer, although there may be many of them in the general case. Due to refraction in the troposphere within the model of the equivalent radius of the Earth a_e

$$a_e = \frac{a}{1+ga},$$

where a is the radius of the Earth; g is the gradient of the refractive index.

The change in the height of the inversion layer Δh_n can be determined by the interference pattern of the received signal

$$\Delta h_n = \frac{\left(h_1^* + h_2^*\right)}{2}\left[\sqrt{1+\frac{n\lambda R}{\left(h_1^* + h_2^*\right)}} - 1\right], \tag{4.7}$$

where n is the number of half-periods of fluctuations in the amplitude of the received signal because of the displacement of the raised inversion layer in the troposphere to a height of Δh_n, h_1^*, h_2^* are the given heights of the corresponding points relative to the inversion layer which are defined as:

$$h_1^* = h_s - h_1 - \Delta h_1, \quad h_2^* = h_s - h_2 - \Delta h_2,$$

where h_1, h_2, h_s, Δh_1, Δh_2 are the height of the corresponding points of the inversion layer, as well as their increase as a result of refraction.

The rate of change in the height of the inversion layer during the period of these fluctuations, Δt_n, can be estimated:

$$v = \frac{\Delta h_n}{\Delta t_n}. \tag{4.8}$$

The relative reflection coefficient from the inversion layer γ can be estimated by measuring the maximum and minimum levels of the received signal with a periodic change:

$$\gamma = \frac{1 - V_{\min}/V_{\max}}{1 + V_{\min}/V_{\max}}$$

and the reflection coefficient from the layer ρ is obtained using experimentally obtained data on the value of the attenuation coefficient [239].

The altitudinal profile of the gradient of the refractive index was estimated based on the information of the temperature, humidity and pressure indicators of the weather probes.

Fig. 4.11 shows the dependence of the displacement height of the layer Δh_n between adjacent maximum and minimum values in the received signal on the effective gradient of the refractive index, which was obtained using [223, 237, 240].

Theoretically expected estimates of the reflection coefficient from a layer with a gradual change in the refractive index by ΔN can be obtained using the relation [241]:

$$\rho \approx \frac{\Delta N}{2\theta_n^2},$$

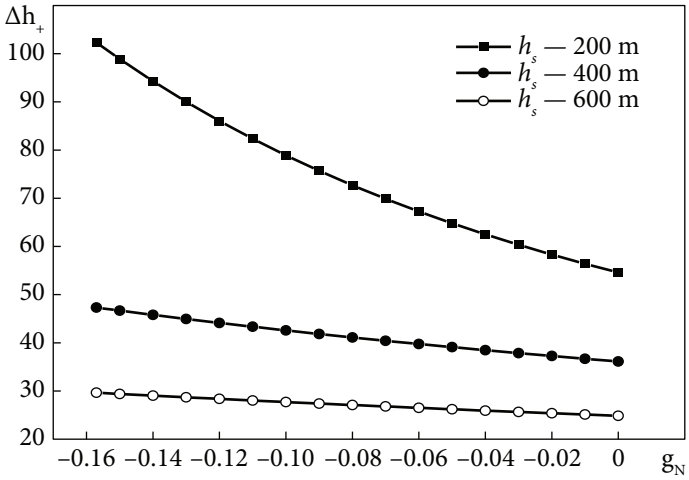

Fig. 4.11. Dependence of the change in the height of the layer between the adjacent max and min of the signal on the effective gradient of the refractive index

Table 4.5. **Characteristics of reflective inversion layers according to experimental data**

Parameter	The depth of fading, dB	Layer height, m	Average gradient of refractive index g_N, N-units per meter	Relative reflection coefficient	Reflection coefficient, dB	Height change, m	Signal fading period, hour	Rate of change in layer height, m/h
Average	10.35	369.64	−0.0529	0.5080	−24.08	67.32	2.03	38.41
Standard deviation	0.81	34.15	0.0031	0.0301	0.720	12.75	0.141	6.81
Median	10	450	−0.048	0.5195	−24.02	35.02	2	24.87
Mode	7	450	−0.049	0.3825	−16.67	34.84	1.5	
RMS	4.74	180.7	0.0164	0.1757	3.8824	67.45	0.813	36.05
Dispersion	22.43	32,655.4	0.00027	0.0309	15.07	4550	0.662	1,299.5
Kurtosis coefficient	0.471	−0.541	5.924	−0.515	−0.518	6.376	−0.85	1.921
Asymmetry	0.858	−0.389	−2.386	0.170	0.0487	2.592	0.374	1.684
Interval	19.5	600	0.072	0.669	14.474	258.6	3.25	131.95
Minimum	3.5	50	−0.105	0.1987	−31.14	23.77	0.5	9.27
Maximum	23	650	−0.033	0.8678	−16.67	282.4	3.75	141.22
Sum	352	1,0350	−1.532	17.273	−698.4	+1,885	67.15	1,075.5
Informant	34	28	29	34	29	28	33	28

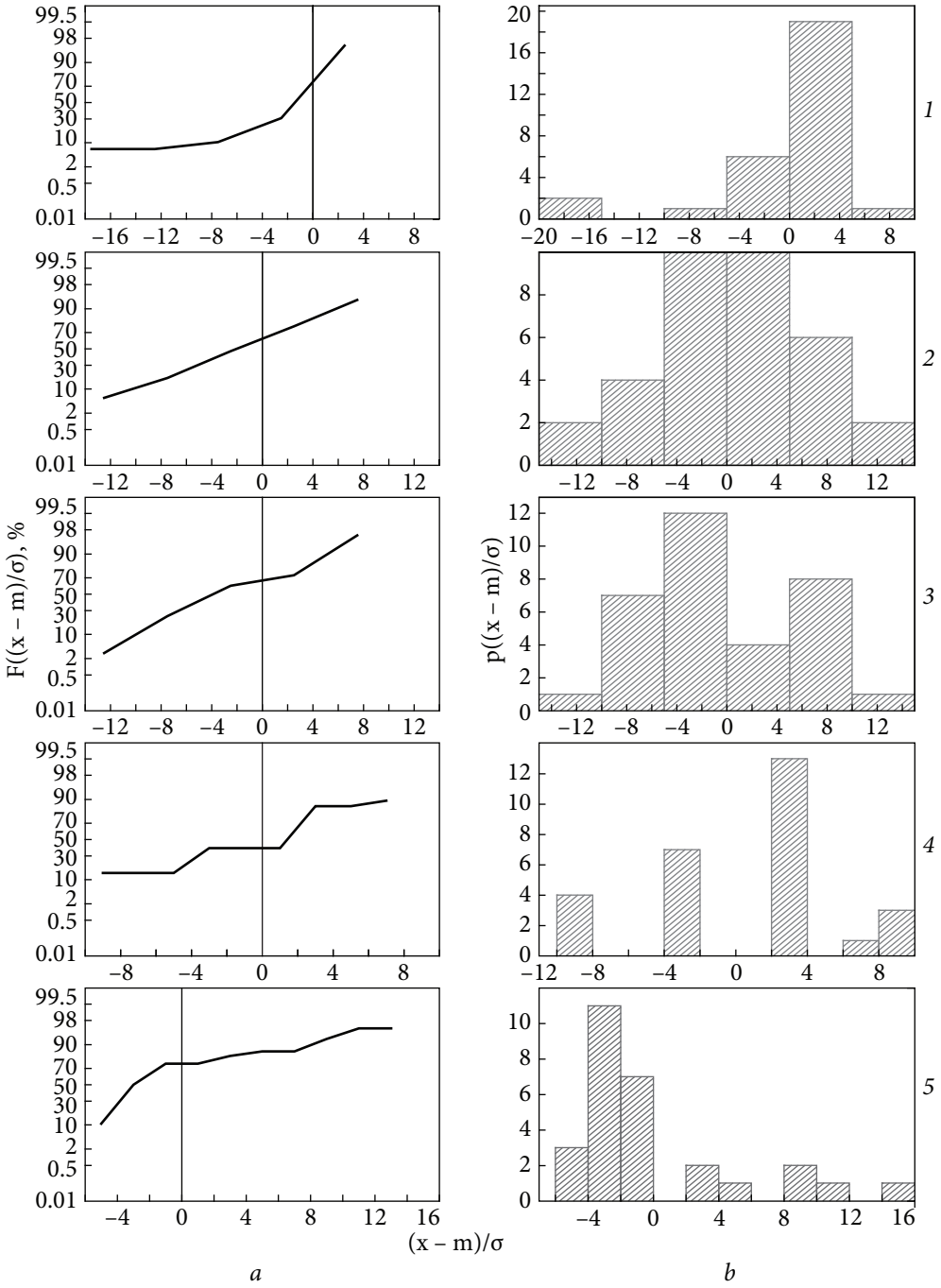

Fig. 4.12. Characteristics of inversion layers and signals reflected from them propagating on the OTH path: integral distribution functions (*a*) and histograms (*b*): effective gradient of the refractive index in the radio wave propagation layer (*1*), reflection coefficient from the layer (*2*), fading depth (*3*), the height of the reflecting inversion layer (*4*), the speed of its movement (*5*)

which is true for small but still greater than the angle of total internal reflection θ_n, for the signal hits the layer is determined by the relation:

$$\theta_n = \frac{h_2^* + h_1^*}{R}.$$

Viewing angles corresponding to the total internal reflection $\theta_n \le \sqrt{2\Delta N}$, where ΔN is expressed in N-units, and θ_n in mrad. The above-mentioned ratios make it possible to determine the reflection coefficients from the layer, the rate of change in its height, and the magnitude of the jump in the refractive index based on the interference structure of the signal on the external path.

Experimental data of signal levels obtained on the suburban path between the TV center located in the city of Bilhorod and the reception point in the city of Kharkiv in the spring-summer period (from May to August), when the presence of inversion layers is most likely, were analyzed.

Using methods for evaluating the characteristics of multipath channels [240, 242] for processing received signals, as well as data from aerological soundings, it was established that the number of inversion layers, as a rule, does not exceed 2, with a jump in the refractive index at the boundary of layers 6...14 N-units, the depth of the signal fading is from –3 to –23 dB, the height of the inversion reflecting layer is from 50 m to 650 m, the period of the signal fading is from 0.5 to 3.75 hours, the rate of change of the height of the layer is from 9.27 to 141.22 meters per hour, the reflection coefficient from –31.14 to –16.67 dB, the average gradient of the refractive index from –0.105 to –0.033 N-units per meter (Table 4.5).

In Fig. 4.12., distribution functions (*a*) and histograms (*b*) of the gradient of the refractive index in a layer along the path of radio wave propagation, characteristics of inversion layers, and signals reflected from them are presented.

In Fig. 4.12, integral distribution functions are given on a scale that linearizes the normal distribution law. In this case, the value of the process (abscissa) is centered and normalized to the root mean square value, the data of which are given in Table 4.5. Since the coefficients of asymmetry and kurtosis for the distribution of the difference in signal intensities, the height of the layer, the reflection coefficients from it, and the duration of fading are small — standard Gaussian models can be used to describe them.

At the same time, the distribution of the average gradient in the layer and the speed of its movement differ significantly from standard models, are more asymmetric and sharp than the Gaussian distribution.

4.4. Bistatic radars with illumination through the ionosphere

VHF signals have been used for environmental monitoring for quite some time. The first experiments on the use of changes in the level of signals on the OTH path to assess the refractive properties of the tropospheric propagation channel

were carried out in the 1950s. They received further development when using radiation from TV centers to illuminate the extraterrestrial tropospheric channel [243]. Signals from TV centers can be used not only to diagnose the propagation conditions and refractive properties of the troposphere but also to detect aerial objects [244]. However, the detection of objects using VHF signals is possible only within a direct line of sight. At the same time, the peculiarities of the propagation of HF signals in the Earth-ionosphere channel make it possible to use them not only to diagnose the state of the ionosphere [245] but also to detect OTH air objects [246]. For the HF band, the dimensions of aircraft are comparable to the wavelength, and their RCS can reach a significant value; therefore, the technologies for reducing radio visibility that are widely used at this time will be ineffective in reducing it. Recently, the so-called active-passive systems, which are used to illuminate the air condition of the radiation of existing radio broadcasting stations, are of particular interest. Such a detection system can be attributed to the class of bistatic radar stations, where detection is carried out using the radiation of broadcast stations scattered by air objects. For the selection of a useful signal reflected from an object against the background of passive interference created by reflections from the terrain, you can use coherent processing with the selection of a signal of the Doppler frequency, the appearance of which is due to a change in the distance traveled by an electromagnetic wave along the path: source of illumination — ionosphere — object — the receiver. The power of the signal P_T reflected from the target is determined by the ratio:

$$P_T = \frac{P_{Tr} G_{Tr} G_R F^2(\theta_T) \sigma_T(\theta_{Tr}, \theta_R) \lambda^2}{(4\pi)^3 R_{TrT}^2 R_{TR}^2 L_{TrT} L_{TR}}, \tag{4.9}$$

where P_{Tr}, P_T is power transmitted and received after reflection from the target; G_{Tr}, G_R are gain coefficients of transmitting and receiving antennas; R_{TrT}, R_{TR} is the range between the transmitter and the target and the target and the receiver, $\sigma_T(\theta_{Tr}, \theta_R)$ is bistatic RCS of targets, where θ_{Tr}, θ_R are directions to the transmitter and receiver, respectively; $F^2(\theta_T)$ is the value of the directional diagram of the transmitting antenna in terms of power in the direction of the transmitter, L_{TrT}, L_{TR} are losses during the propagation of radio waves from the transmitter to the target and from the target to the receiver, respectively; λ is operating wavelength of radiation.

The use of ratio (4.9) to estimate the received signal reflected from the target is difficult due to the a priori uncertainty of losses during signal propagation L_{TrT}, L_{TR} on the path, which leads to significant errors in estimating the range of such systems [61]. A technique that uses well-controlled values of the levels of the direct illumination signal at the reception point for evaluation was developed to reduce these errors.

The power of the received signal P_R from the transmitting station:

$$P_R = \frac{P_{Tr} G_{Tr} G_R F^2(\theta_{Tr}) \lambda^2}{(4\pi)^2 R_{TrR}^2 L_{TrR}}, \tag{4.10}$$

where R_{TrR} is the distance between the transmitter and receiver, $F^2(\theta_{Tr})$ is the value of the directional pattern of the receiving antenna in terms of power in the direction of the transmitter at an angle of θ_{Tr}, and L_{TrR} is propagation losses from the transmitter to the receiver.

Taking into account the fact that the distance from the illumination station to the target and the receiving system is significantly greater than the distance from the target to the receiver $R_{TrT}^2 \approx R_{TrR}^2 >> R_{TR}^2$ and the propagation losses to the target and the receiver are approximately the same $L_{TrT} \approx L_{TrR}$, and the target in this range can be considered such that it reflects isotropically $\sigma_T(\theta_{Tr}, \theta_R) \approx \approx \sigma_T = const$ and is within the direct line of sight of the receiving system $L_{TR} \approx 1$, the ratio of the power of the signals reflected from the target and direct from the transmitting broadcasting station μ_{TR} taking into account (4.9, 4.10), is determined by the ratio:

$$\mu_{TR} = \frac{P_T}{P_R} \approx \frac{F^2(\theta_T)}{F^2(\theta_{Tr})} \frac{\sigma_T}{(4\pi) R_{TR}^2}. \tag{4.11}$$

The obtained ratio (4.11) does not include parameters that are difficult to determine, such as losses on the propagation path. It follows from the expression (4.11) that it is necessary to form a minimum of the directional pattern of the receiving antenna in the direction of the illumination station and a maximum in the direction of the target to increase the detection range. The degree of suppression of the illumination signal by the pattern of the receiving station will limit the maximum detection range. It is necessary to pay attention to the fact that for aerial objects, the wavelength of the field of irradiating radio broadcasting stations can be comparable to their size, which can lead to an increase in RCS. In addition to choosing the resonant wavelength of the irradiating signal, forming the zero of the directional pattern in the direction of the illumination station, increasing the signal-interference ratio can be achieved by applying narrow-band Doppler filtering. The spectrum of backscattering from air objects above the surface of water and land, even in the microwave range, when the signal is reflected from the body of the object does not exceed 10 Hz [203, 247, 248]. Studies of backscattering from surface and air objects in the HF band [249, 250] allow us to conclude that the width of the reflected signal carrier is a hundredth of a Hz and is mainly determined by fluctuations of the projection of the object's velocity vector onto the direction of irradiation by the time of formation of a spectral estimate. When using Doppler selection, the signal-to-noise ratio (SNR) μ will

be determined by the ratio of the signal level from the target to the illumination signal μ_{TR} and the ratio of the carrier spectral line level to the noise spectral density in the range of Doppler frequencies μ_{SN}, where the target is detected:

$$\mu = \mu_{TR}\mu_{SN}. \tag{4.12}$$

The detection range for bistatic radars when using the signals of HF radio broadcasting stations for illumination, substituting (4.11) into (4.12), can be written as:

$$R_{TR} = \sqrt{\frac{\mu_{SN}}{\mu}\frac{\sigma_T}{(4\pi)}\frac{F^2(\theta_T)}{F^2(\theta_{Tr})}}. \tag{4.13}$$

For the first time, such an approach for estimating the detection range was proposed by us in [221]. It follows from (4.13) that for air objects with RCS in the resonant region $10^3...10^4$ m², SNR 10...15 dB necessary for detection with a probability of correct detection of 0.9...0.99 and false alarm $10^{-4}...10^{-5}$, the formation of the antenna's DP minimum in the direction of the illumination station is about 40 dB, the level of interference in relation to the spectral density of the carrier by 40...50 dB when adjusting for the Doppler frequency shift, the detection range can reach more than 100 km [40].

To estimate the RCS of air objects based on experimental data, you can also use the ratio (4.13). If the detection of the aircraft occurred at the maximum range $R_{TR\max}$ when used for illumination of a station in which the carrier level exceeds the noise level at Doppler frequencies by μ_{SN} times, then the RCS of the aircraft, as can be seen from (4.13), will be

$$\sigma_T = (4\pi)\frac{\mu}{\mu_{SN}}\frac{F^2(\theta_{Tr})}{F^2(\theta_T)}R^2_{TR\max}. \tag{4.14}$$

If non-directional antennas are used for detection, then $F^2(\theta_{Tr}) \approx F^2(\theta_T) \approx 1$ and relation (4.14) take the form

$$\sigma_T = (4\pi)\frac{\mu}{\mu_{SN}}R^2_{TR\max} \tag{4.15}$$

and can be used for experimental evaluation of RCS of objects.

4.5. RCS of aerial objects in the HF range

The currently available data on the RCS of aerial objects in the HF band were obtained using radar in monostatic mode; they are few and contradictory [102, 251].

Since the horizontal dimensions of aircraft in the HF band are comparable to the wavelength of the horizontal polarization of the field irradiating the object, scattering occurs in the resonant region, and the RCS of such objects can reach a

significant value. One of the main features of surface vertically polarized wave radar in the HF band is the fundamental possibility of detecting objects located in the zone of the near geometric shadow, which is due to the diffraction effect of radio waves on the surface of the sea, which has good conductivity. The practical implementation of this possibility when detecting low-flying objects is difficult, which is primarily due to their small RCS. Previously, it was believed that the RCS of aircraft near the distribution surface, in the zone where the vertical polarization of the probing radiation prevails, is small because the vertically oriented structural elements are small compared to the wavelength, and, at the same time, the Rayleigh scattering law occurs when $\sigma \approx \lambda^{-4}$, where σ is RCS of the object and λ is the wavelength of the irradiating field. According to various estimates [61, 251, 252], it was believed that the RCS of such objects lies within 0.1...20 m². At the same time, for high-flying aircraft, when they are in a field with a significant intensity of horizontally polarized radiation, which is characteristic of ionospheric wave radar, it was believed that the RCS of aircraft when choosing a radar wavelength commensurate with the wing span can reach values of $\sigma \sim \lambda^2$, which is 80...2,000 m² for the HF band. The purpose, overall dimensions of the main elements, and the obtained RCS estimates of some types of aircraft, including 5th generation aircraft, made according to the "stealth" technology on vertical and horizontal polarizations are given in Table 4.6. [40]. RCS and resonant frequency values are obtained using empirical ratios for complex structures, which are studied in papers [200, 252—253], where the results of model experiments in the resonant region with complex structures imitating aircraft elements are given.

For 5th generation aircraft manufactured using "stealth" technologies, the declared RCS values for the microwave range are 0.001...0.1 m² at the same time, they are given in Table 4.6. Estimates show that in the resonant region, their RCS can be 3...5 orders of magnitude more than in the microwave range. This means that with comparable radar potentials, the detection range in the HF band, as follows from (4.13), can be 30...300 times higher than their detection range in the microwave range. However, it should be noted that in the HF band, it is practically impossible to realize the same high potential in onboard aircraft radars as in the UHF band.

We conducted a series of experiments to assess the potential of detecting aerial objects using the illumination signal of radio broadcasting stations in the HF band [220—226].

The scheme of the experiment is determined by the physical location of the runway and the O.Ya. Usikov Institute for Radiophysics and Electronics of the National Academy of Sciences of Ukraine, where the receiving equipment is located, along the flight path of the planes. Several HF stations were used in the experiments. The stations were selected depending on the time of day, the number of reflections from the ionosphere, and the signal-interference ratio. The experiments included a series of consecutive measurements on horizontal and

Table 4.6. **Overall dimensions and RCS of the aircrafts**

Type of aircraft	Purpose	Length, m	Wing span, m	Height, m	Horizontal polarization		Vertical polarization	
					RCS/ 1,000 м²	Frequency, MHz	RCS/ 1,000 м²	Frequency, MHz
C-17A	T	53	51	16.79	9.7—9	2.8—2.9	1.25	4.5
EMB-145RS	T	30	20	6.75	3—1.4	5—7.5	0.2	11.1
"Mirage" F1	F	15.3	9.3	4.5	0.77—0.24	10—17.9	0.09	16.7
TA-7 "Corsair 2"	AA	14.1	11.8	4.9	0.67—0.56	10.7—17.9	0.1	15.3
Be-12	T	30.1	30.2	7.4	3.1	5	0.24	10.1
Be-200	T	32	32.7	8.9	3.7—3.5	4.6—4.7	0.35	8.4
An-24	P	23.5	29.2	8.3	1.9—2.9	6.4—5.1	0.31—0.33	9—8.7
An-26	T	23.8	29.2	8.6	1.9—2.9	6.4—5.1	0.31—0.33	9—8.7
An-22	T	57.3	64.4	13.5	12.5—13.5	2.6—2.3	0.81	5.6
An-72	T	28	31.9	8.7	2.7—3.5	5.4—4.7	0.34	8.6
An-74	T	28	31.9	8.7	2.7—3.5	5.4—4.7	0.34	8.6
Il-18	P	35.9	37.4	10.2	4.4—4.8	4.2—4	0.46	7.4
Il-62	P	53.1	42.5	12.3	9.7—6.2	2.8—4.5	0.67	6.1
Il-76	T	46.6	50.5	14.8	7.5—8.8	3.2—3	0.97	5.1
Il-114(T)	P(T)	26.9	30	9.3	2.5—3.1	5.6—5	0.38	8.1
Tu160	SB	54.1	35.6—55.7	13.1	4.4—10.7	4.2—2.7	0.76	5.7
Tu22M3	SB	41.46	23.3—34.28	11	1.9—5.9	6.4—3.6	0.54	6.8
B-52	SB	49.05	56.39	12.4	8.3—10.9	3.1—2.7	0.68	6
MiG-29	F	17.32	11.36	4.73	0.4—1	13.2—8.7	0.099	15.9
Su-57	F	19.7	14/10.8 HT	4.8	13.0	2.6—2.3	0.81	5.6
B2	SB	20.9	52.12	5.1	1.72—0.87	3.8—5.4	0.10	15.6
F-22	F	18.9	13.56	5.09	1.94—12.06	3.6—1.4	0.12	14.7
F-35	F	15.57	10.67	4.38	1.59—0.82	4.0—5.5	0.12	14.7
J-31	F	16.9	11.5	4.8	1.08—0.51	4.8—7.0	0.09	17.1
J-21	F	10.5	11.6	4.0	0.48—0.6	7.2—6.5	0.07	18.9

Notes: T — transport; SB — strategic bomber; B — bomber; P — passenger; AA — attack aircraft; F — fighter.

vertical polarizations. The objects of detection were airplanes of the AN-74 and AN-140 types.

In the telegraph reception mode, the carrier was shifted to a frequency of 1,700...1,850 Hz with the help of the 3rd local oscillator, which made it possible to study the reflected signals, both with positive and negative Doppler frequency shifts.

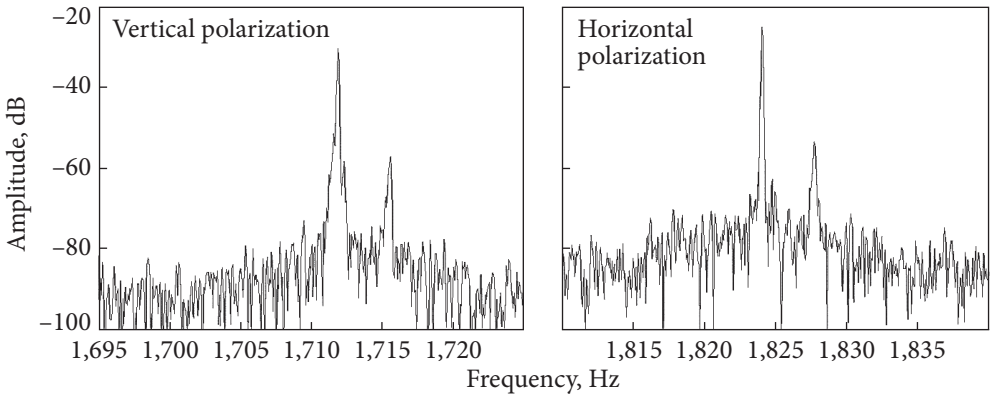

Fig. 4.13. Signal spectra after heterodyne conversion of the station's carrier frequency and Doppler-shifted reflections from aircraft

Table 4.7. **Characteristics of reflections from the lines of the aircraft body**

Frequency, MHz	Polarization	Body line		SNR, dB when rebuilding from the carrier on μ_{SN}		Signal-to-carrier ratio, dB μ_{TR}	RCS
		Frequency, Hz	Width, Hz	10 Hz	3 Hz		
15,130	VP	4.22	1.12	38.8	24.8	–27	4,010
15,130	HP	4.03	0.68	34.2	20.4	–26	5,047
15,130	VP	3.58	1.05	34.7	23.6	–28	3,185
15,130	HP	3.58	0.9	32.3	21.7	–29	2,529

Fig. 4.13 shows the spectra of signals of the carrier and Doppler-shifted lines of the AN-74 aircraft body for vertical and horizontal reception polarizations.

The radiation of a broadcasting station transmitting at a frequency of 15,130 kHz was used as the illumination signal for this experiment; the azimuthal angle θ_{TrT} is about 75° [40]. The plane's flight path — after taking off from the airfield, crossed the base of the measuring complex at an angle of about 40° and passed near the reception point. The distance between the runway and the baseline is about 1,500 m. The reception polarization was changed by turning the receiving antenna to an angle of 90°. A dipole with an effective length of about 0.4 m is used as a receiving antenna. During the experiment, a signal reflected from an aircraft approaching or moving away from the receiver was recorded.

The characteristics of the signal for several experiments, such as the ratio of the signal levels of the carrier frequency and the spectral line of the signal reflected from the aircraft [40], as well as its width at different polarizations of the received radiation, RCS values for the aircraft are given in Table 4.7.

Aircraft detection ranges in experiments are up to several kilometers.

Using the relation for the Doppler frequency shift,

$$\frac{V_D}{V_0} = \cos\left(\theta_{TrT} - \theta_T\right) + \cos\left(\theta_{TR} - \theta_T\right) \tag{4.16}$$

as well as the data of Table 4.7 by frequencies and azimuthal angles of the illumination station, it is possible to estimate the Doppler frequency shift of the signal reflected from the aircraft at the time of take-off (speed 230...240 km/h), which has a value of 4.06...4.23 Hz, which is in satisfactory agreement with the data obtained during the experiment. It should be noted that the signals of both horizontal and vertical polarization reflected from the aircraft have approximately the same magnitude and exceed the noise level. The experiments used a dipole that had a circular directional pattern in the azimuthal plane. The time to form a spectral estimate was about 15 seconds, the range of aircraft observation was a few kilometers. From Table 4.5, it can be seen that the SNR exceeds 30 dB when restoring from the carrier at 10 Hz and more than 20 dB when restoring at 3 Hz.

It can be seen that the obtained SNRs for the signal are sufficient for reliable detection. When forming a minimum in the directional pattern of the receiving antenna in the direction of the station, illumination with a depth of about 40 dB, with a slight weakening of the signal reflected from the target, will allow its detection at distances of more than 100 km. Measurements of the vertical and horizontal polarizations of reception when used to illuminate the ionospheric wave signal confirmed the absence of significant differences between the RCS and interference levels for the detected aircraft [40].

Using the relation (4.15), the experimentally obtained relation between the carrier level and interference in the Doppler frequency band, as well as the realized detection ranges, it is possible to estimate the value of the RCS of the aircraft observed in the experiments of approximately several thousand square meters (Table 4.7), which is consistent with the results of theoretical estimates. For the An-74 aircraft, which is found in the experiments, the calculated RCS values in the resonant region have values on the horizontal polarization of 2,700—3,500 m^2, on the vertical 340 m^2, although in the experiments, no significant difference was found when detecting the signal on the vertical and horizontal polarizations, which agrees with the results of model experiments on the study of scattering matrices of bodies of complex shape [200]. This can be crucially important for monitoring the HF band of inconspicuous objects using a surface wave on vertical polarization. [40, 220—226].

4.6. Monitoring of sea waves using GNSS signals

Environmental monitoring systems that use the radiation of TV centers and broadcasting stations make it possible to monitor atmospheric processes and detect anthropogenic objects on the path between the illumination station and the receiver, i.e., to perform local monitoring. The use of radiations that currently

exist GNSS, GPS — USA and GLONASS — Russia, and in the future Galileo — EU and BeyDou — China will be deployed, allow us to move to the construction of systems for global monitoring of the atmosphere and the study of processes in it. However, in addition to the analysis of a direct signal that is affected by the environment, an interesting issue is also related to the study of reflected signals from the earth and water surface, which carry information about their condition [240, 242, 254—257]. For testing GNSS receivers and improving the accuracy of measuring quantities, it is necessary to use special equipment, introduce corrections to the algorithms, and improve the algorithms for processing the received information [258].

A mobile measuring complex was created [219], consisting of a single-frequency domestic GNSS-receiver type CH-4706, a telescopic antenna, and a personal computer with software for collecting and processing navigational information to use GNSS signals for monitoring the sea surface.

The CH-4706 receiver is intended for use in integrated navigation systems as a coordinate sensor to determine the current values of the coordinates (latitude, longitude, altitude), the consumer's speed vector, as well as the current time according to the GLONASS, GPS, and SBAS SNS signals at any point on the globe, at any time and regardless of weather conditions. The main characteristics of the CH-4706 receiver are presented in Table 4.8.

Table 4.8. **Technical characteristics of the CH-4706 receiver**

Specifications	Value
Receiving signals	GPS/GALILEO/COMPASS/SBAS — L1 1,575.42 MHz GLONASS: L1 1,597.5…1,609.5 MHz
Number of tracking channels	32
Accuracy of obtaining navigation parameters (RMS)	In the plane: in offline mode — 2.5 m in differential mode — 1 m Height 3 m Speed of 0.05 mps Time (1PPS) ±25 ns
Time of receiving the first reliable navigation solution	Recapture <1 s "Hot start" <3 s "Cold" and "warm" start 30 s
Sensitivity	Accompaniment — 190 dBW "Cold" start — 173 dBW
Restrictions on use	Speed <500 m/s Acceleration <5 g Height <18 000 м
Coordinate systems	WGS-84, PZ-90 SK-42, SK-95
Antenna type	Active

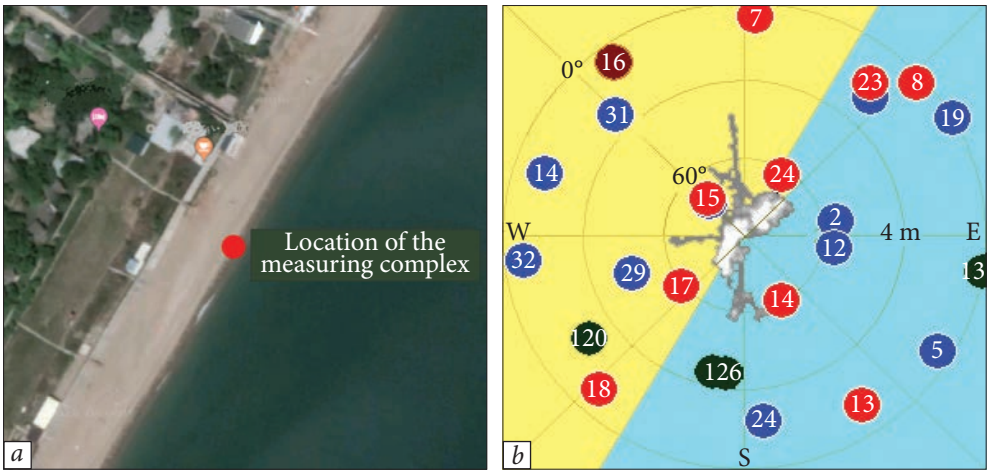

Fig. 4.14. Location of the measuring complex (*a*), target with measured coordinates and plotted positions and numbers of satellites (*b*) when the complex is located directly on the seashore

The location of the antenna on the terrain and the location of the satellites during the measurements are shown in Fig. 4.14.

The antenna was located at low altitudes (no more than 8 m) and at a distance from the coastline, where the radiation of incoming and outgoing satellites will be affected not only by the reflection from the sea surface but also by the characteristics of the near the sea surface layer of the atmosphere. Note that the pattern of the receiving antenna is formed in such a way as to minimize the influence of signals from the lower half-plane, therefore; at high viewing angles of the satellite, the contribution of reflected rays is significantly reduced.

In Fig. 4.15, the appearance and location of the measuring complex on the terrain (*a*, *b*, *c*), the antenna directional pattern (*d*), and the interface of the navigation data collection program (*e*) are shown.

The antenna was located on a telescopic mast, the height of which could vary from 1 m to 4 m (see Fig. 4.15, *a*, *b*). The measurements were carried out on the north-western coast of the Black Sea in the area of the city of Chornomorsk. The complex was located in the immediate vicinity of the sea (Fig. 4.15, *a*) or at the height of the shore, about 4 m high, and at a distance of approximately 50 m from the sea coastline (Fig. 4.15, *b*). The measuring complex received signals at different levels of sea surface disturbance and allowed us to register satellite signals even at negative viewing angles. The type of directional pattern of the antennas used in the measuring complex is shown in Fig. 4.15, *g*. Fig. 4.15, *d* shows the interface of the program for accumulating navigation data, on which the signal levels of the received GPS satellites and their numbers are shown in blue columns and in red — for GLONASS satellites. The target characterizing the spread of the measured coordinates is also shown there, as well as the results of the express statistical processing of coordinate estimation errors.

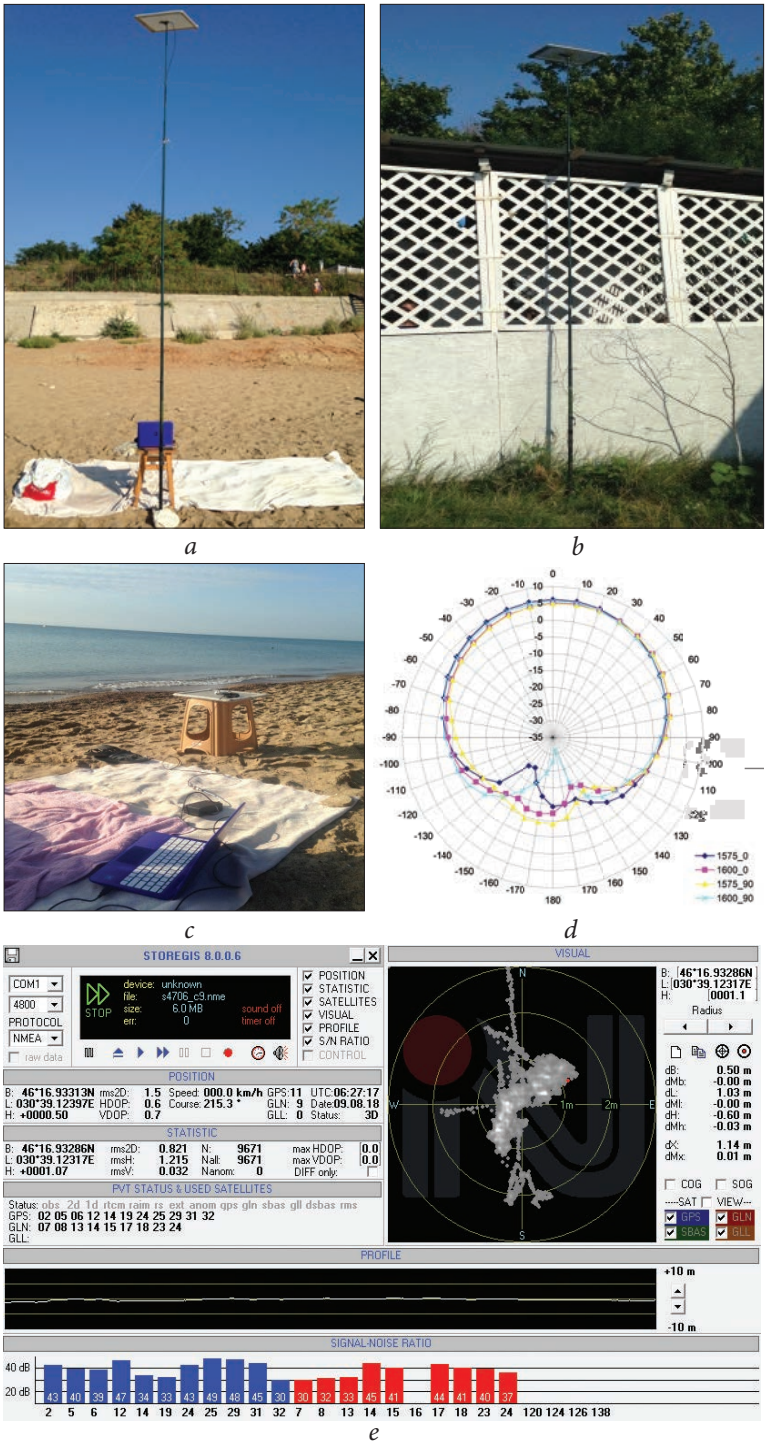

Fig. 4.15. The appearance and location of the measuring complex (*a*, *b*, *c*), antenna directional pattern (*d*), and the interface of the navigation data accumulation program (*e*)

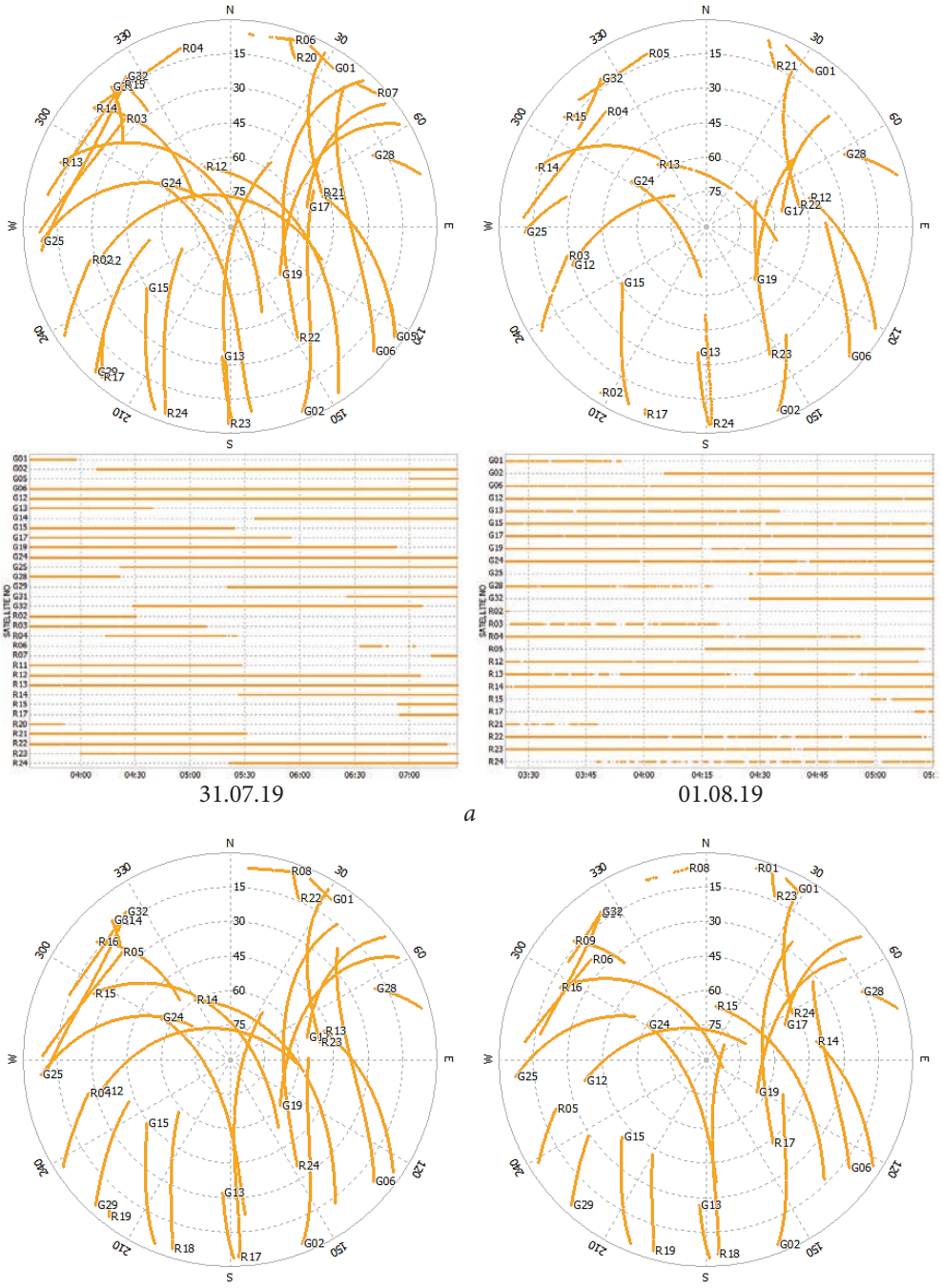

Fig. 4.16. Estimated positions of satellites (upper curves) and their observation time (lower) during navigation accumulations on all measurement days: G — GPS and R — GLONASS. See also p. 112

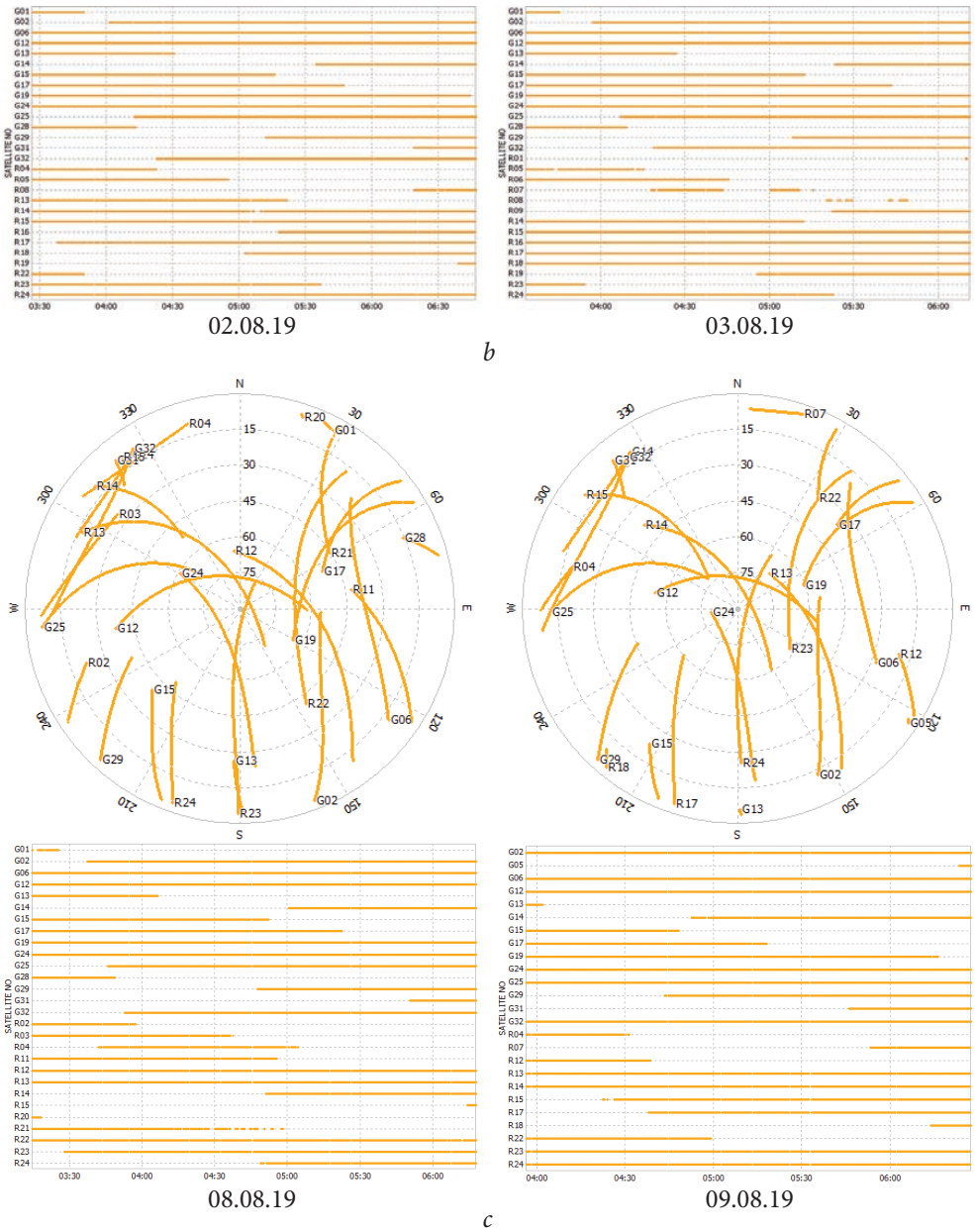

End of Fig. 4.16

The trajectories of the satellites and the time they were in the visibility zone of the measuring complex were estimated previously. They are shown in Fig. 4.16 for G — GPS satellites and R — GLONASS for all days.

The upper figures for each of the days show the trajectories of the satellites observed from the location of the complex, and the lower figures show the time of their visibility.

A similar approach allows you to select the satellites that will be of greatest interest based on the estimated time of the measurement sessions. Since the American GPS satellites are observed at the same angles after about 12 hours, it is advisable to use them to practice the method of monitoring the state of the sea surface. This allows, by comparing the fluctuation and trend characteristics of the observed GNSS GPS signals, obtained under different conditions of disturbance, to establish their relation necessary for solving the inverse problem — determining the state of the sea surface by GNSS signals.

When registering navigation signals as part of the conducted experiments, it was assumed that the resulting signals in the satellite-subsurface-receiving antenna model would present the sum of direct and reflected signals from the sea surface. In the presence of sea waves, fluctuating components will appear in the received signal, the frequency and intensity of which will depend on the roughness of the surface and the period of sea waves. Isolation of the fluctuation component was carried out in one of two ways. In the first case, high-frequency filtering of the signal received from the satellite and reflected from the sea surface was carried out. It was carried out with the help of a periodic compensation filter:

$$\hat{S}(\beta_i) = S(\beta_i) - S(\beta_{i-1}), \tag{4.17}$$

$S(\beta_i)$, $S(\beta_{i-1})$ are signals at elevation angles (satellite elevations β_i and β_{i-1}, respectively).

In another approach, the selection of the fluctuating component was carried out using the wavelet transformation, the selection of its high-frequency components, and the implementation of the inverse wavelet transformation.

Two approaches were also used to highlight the trend component. The first consisted of smoothing the output signal realization in a sliding window. The other also used a wavelet transform, filtering its low-frequency components, and then the inverse wavelet transform.

The depth of interference fading ($V_{\min}$, $V_{\max}$) makes it possible to estimate the value of the reflection coefficient from the sea surface R from the ratios:

$$V_{\min} = 1 - R, \quad V_{\max} = 1 + R, \quad \frac{V_{\max}}{V_{\min}} = \propto = \frac{1+R}{1-R}, \quad R = \frac{\propto +1}{\propto -1}. \tag{4.18}$$

Thus, evaluating the ratio of the maximum and minimum values of the signal $\frac{V_{\max}(\beta)}{V_{\min}(\beta)} = \propto(\beta)$, it is possible to determine the value of the reflection coefficient of the sea surface for these values of the viewing angle of the satellite:

$$R(\beta) = \frac{\propto(\beta)+1}{\propto(\beta)-1}; \ \propto(\beta) = \frac{V_{\max}(\beta)}{V_{\min}(\beta)}. \tag{4.19}$$

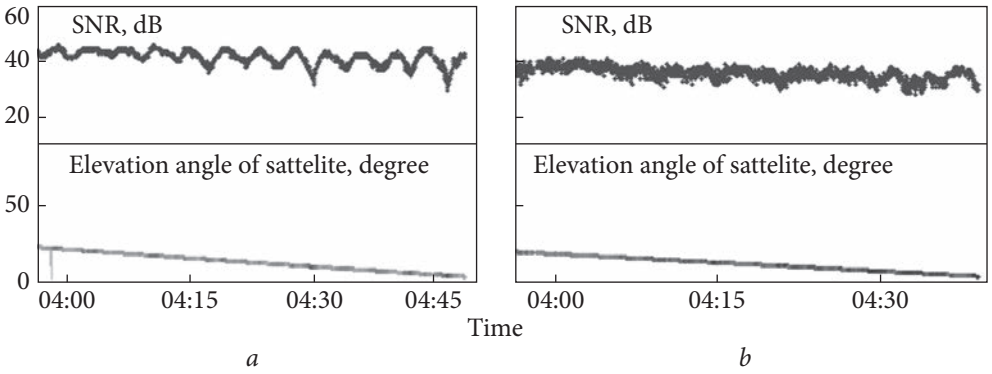

Fig. 4.17. Signals of navigation satellites depending on the type of substratum, *a* — GPS15 — reflection from land, *b* — GLN12 — reflection from the sea

The coefficient of specular reflection from the sea surface depends on the degree of its roughness [259] and is determined using the ratio:

$$R(\beta) = \exp - 2\left(\frac{2\pi\sigma_h \sin(\beta)}{\lambda}\right)^2, \tag{4.20}$$

proceeding from which, based on the known values of the reflection coefficient $R(\beta)$, the viewing angles of the GNSS β satellite, it is possible to determine the values of the rms values of the surface roughness:

$$\sigma_h = \frac{\lambda}{2\pi\sin(\beta)}\sqrt{-\frac{1}{2}\ln\left(R(\beta)\right)}. \tag{4.21}$$

Equation (4.21) can be used to estimate the RMS values of sea wave height using the method of least squares.

Navigational data received from satellites allow analysis of temporal and angular dependences of signal levels. Satellites can be observed at the same time, which are at approximately the same viewing angle but have different azimuthal directions. In this case, it is possible to simultaneously study the signals reflected from both the water and land surface, which allows comparing the behavior of the signals, the nature and intensity of which must differ for different states of the underlying surface and azimuths of its observation.

Fig. 4.17 shows signals from satellites when reflected from land and sea surface for the same viewing angles [219].

For satellites whose trajectory passes over the Earth's surface (Fig. 4.17, *a*), the receiving signal has a longer period of fluctuations, unlike a satellite whose trajectory passes over the surface of the sea, where the received signal has a high-frequency component in the presence of weak sea waves (Fig. 4.17, *b*).

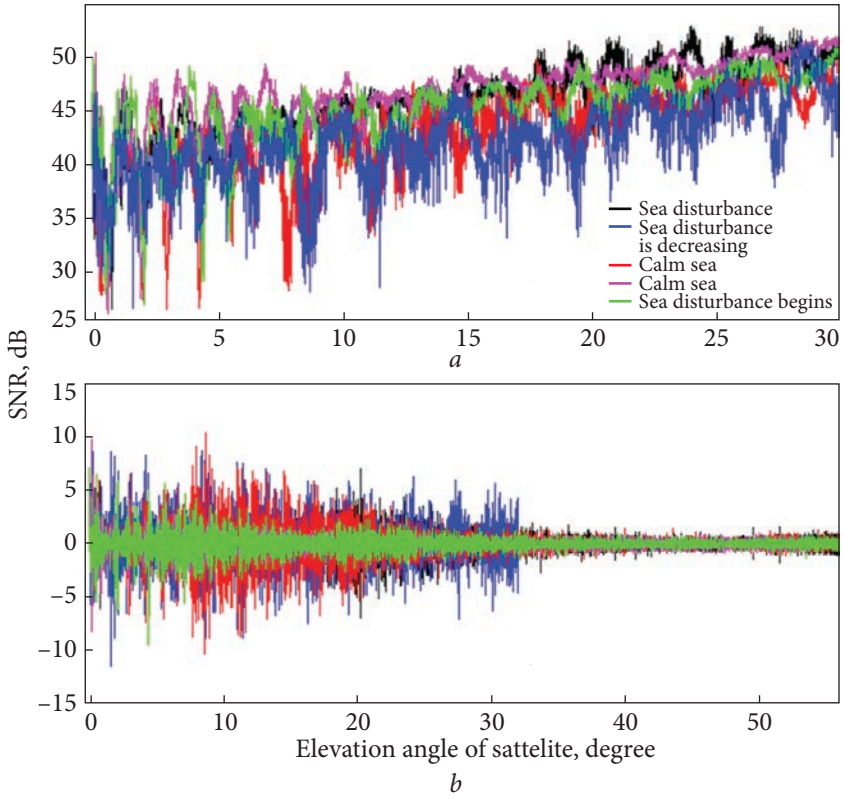

Fig. 4.18. Levels of signals from the satellite (*a*) and amplitudes of fluctuations of signals from the satellite (*b*) in the direction of the sea

It should be noted that both GPS and GLONASS satellites were used for comparison. Since the behavior of signals on similar trajectories of satellites has a similar nature, it makes it possible to compare data from different systems during simultaneous measurements. 5 days were chosen for the analysis, during which sea waves of varying intensity were observed from 3...4 points to near-calm sea conditions. It should be noted that with a calm state of the sea or a weak wave of the sea surface, the fluctuations observed in satellites flying in the direction perpendicular to the coastline have a stably regressive nature of the depth of fluctuations with an increase in the viewing angle, which is explained by the gradual increase in the effect of surface roughness and the decrease in the coefficient reflection.

The obtained results show that the presence of a reflecting sea leads to the mixing of high-frequency fluctuations (Fig. 4.18).

The level of the fluctuation component is simultaneously affected by several mechanisms, the degree of sea disturbance, and the size of the reflecting area. The maximum value that the diffuse scattering coefficient can take is 0.4. With a further increase in roughness, the coefficient of diffuse scattering remains constant.

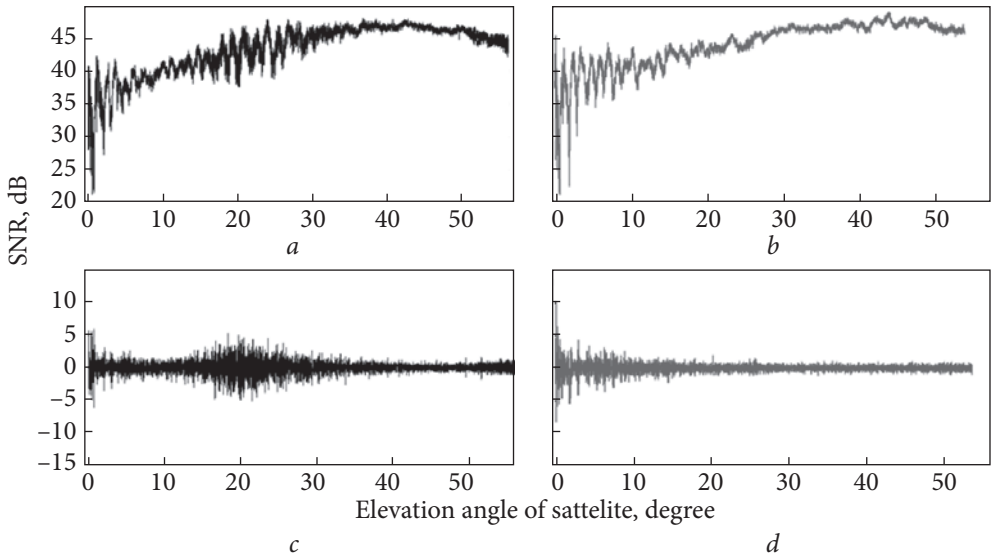

Fig. 4.19. GPS02 navigation satellite signals (*a*, *c*) in conditions of strong sea disturbance, *b*, *d* — calm sea, and *c*, *d* — fluctuation component of the signal

However, as the disturbance and degree of roughness change, this saturation may occur at smaller angles for large disturbances, and the angles and dimensions of the reflecting pad, defined by the dimensions of the Fresnel zone, may be smaller.

When analyzing a signal, it is necessary to divide observations into several sections:

• up to 3—4°, where the signal level increases significantly due to a significant increase in the thickness of the atmosphere and, accordingly, its influence [257];

• from 4 to 30°, where, depending on the state of the sea surface, interference effects caused by local changes in the intensity of reflections may be observed.

• angles higher than 30°, where the wave of the sea surface has a minimal effect because, on the one hand, the size of the reflecting area on the sea surface decreases, and on the other hand, the reflection coefficient decreases due to the increase in the roughness parameter.

Fig. 4.19 shows the signal levels for the GPS02 satellite and the amplitude of fluctuations obtained by subtracting the $(i-1)^{\text{th}}$ reading from the i^{th}.

Fig. 4.20, *a*, *c*, *e* shows the interference fading of the signal selected through averaging in a sliding window under different conditions of the sea surface and the values of the reflection coefficient of Fig. 4.20, *b*, *d*, *f*.

Fig. 4.21 shows the signal's interference fading at different states of the sea surface (*a*, *c*), determined using the wavelet transformation and estimated according to them using relation (4.18) and the reflection coefficient values (*b*, *d*).

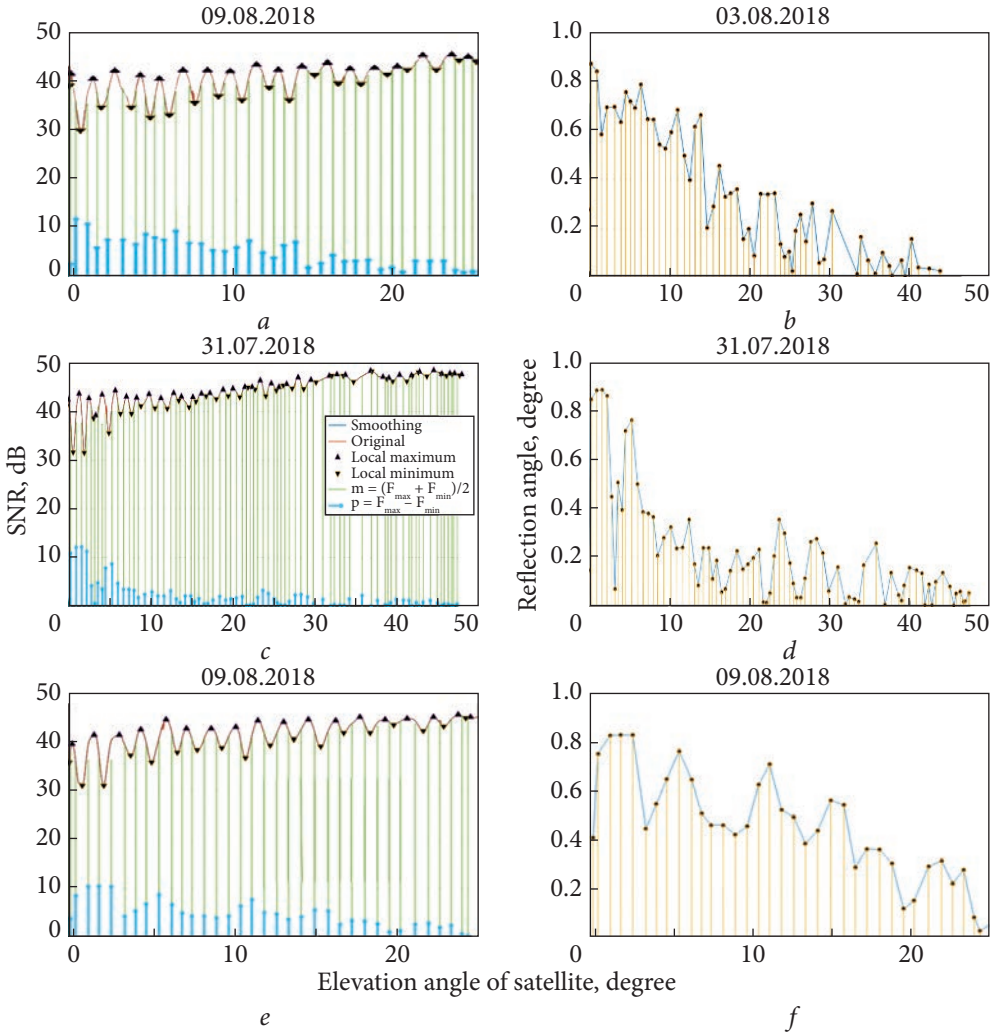

Fig. 4.20. The trend component of the signal radio rise of the GNSS satellite, selected using smoothing in the sliding window (*a*, *c*, *e*) and the values of the reflection coefficient from the sea (*b*, *d*, *f*) estimated from it for waves 0...1 point — (*a*, *b*), 1...2 points — (*c*, *d*), 3...4 points — (*e*, *f*)

In Fig. 4.21, *a*, *c*, it can be seen that with greater disturbance, when the viewing angle of the satellite is changed, the depth of dips in the interference structure of the signal field decreases faster, which means that the values of the observed reflection coefficient from the sea surface decrease faster.

When calculating the reflection coefficients of GNSS signals reflected from the sea surface, the influence of the directional pattern of the receiving antenna has not yet been taken into account, so the obtained estimates of the reflection coefficient are somewhat underestimated. In the future, it is planned to take into

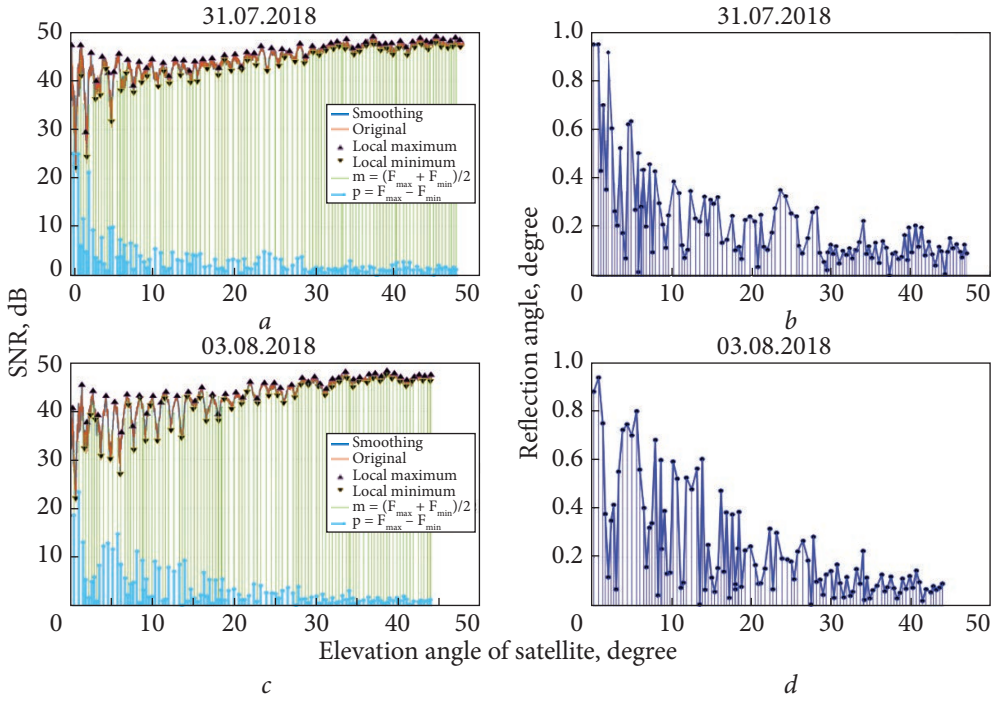

Fig. 4.21. The interference structure of the signal radio rise of the GNSS satellite, extracted using the wavelet transformation (*a*, *c*) and the values of the reflection coefficient from the sea (*b*, *d*) estimated from it for wave 3...4 points — (*a*, *b*) and 1...2 points — (*c*, *d*)

account the influence of antenna directional patterns by introducing diagrammatic corrections.

A comparison of the results obtained using a high-frequency filter and wavelet transformation shows their satisfactory correspondence [219]. Since both approaches give close results, they can be successfully used to estimate the reflection coefficient from the sea surface and, accordingly, its RMS irregularities (degree of disturbance).

Conclusions

1. A two-channel equipment complex has been created, which provides the possibility of measuring the level of signals on spatially distributed antennas in the frequency band of TV signals for monitoring tropospheric refraction by signal attenuation factors on the OTH path. We established a weak (less than 0.15) correlation of signals received on spatially spaced antennas (by 15...20 λ) for the same and different frequency channels.

2. Experimentally investigated interference phenomena in the propagation channel on OTH paths in the middle latitudes (Ukraine) based on changes in the

signal level from TV centers that occur in the presence of inversion layers. It is shown that the number of inversion layers, as a rule, does not exceed 2, with a jump in the refractive index at the boundary of the layers of 6...14 N units, the height of their placement does not exceed 650 m, the speed of movement is from units to several hundred meters per hour, the depth of signal fading is from –3 to –23 dB.

3. It was established that the standard Gaussian model can be used to describe the fading statistics, reflection coefficients, and heights of inversion layers, at the same time, the distributions of the effective gradient of the refractive index in the layer essential for the propagation of radio waves and the speed of inversion layers differ from Gaussian models.

4. The proposed technique for estimating the detection range and RCS of aerial objects for active-passive sounding systems. The spectral characteristics of the signals of radio broadcasting stations with different polarizations of the received radiation were experimentally investigated. Theoretical estimates of the RCS of airborne objects for different polarizations of the incident radiation are given.

5. It was experimentally established for the first time when the An-74 aircraft was detected using the ionospheric wave of HF radio broadcasting stations as an illumination signal that the RCS of aircraft in the resonant region on both horizontal and vertical polarizations reaches thousands of square meters. This makes it possible to use a surface wave of vertical polarization to illuminate the air condition in the HF band.

6. As a result of research conducted on signals from navigation satellites, the possibility of using them for remote monitoring and diagnostics of the state of the sea surface has been shown. The variability of the level of the fluctuation component and fading (related to the interference component) of the GNSS-satellite signals scattered by the sea surface, depending on the degree of sea disturbance, is experimentally determined. Experiments show that the levels of the fluctuation component and the depth of fading (trends) of signals of navigation satellites are sensitive to changes in the state of the underlying surface and the degree of sea disturbance. This can be used as a basis for monitoring sea waves based on GNSS signals.

CHAPTER 5

Interferences for active-passive monitoring systems

The range of active VHF and UHF radio systems is determined by the presence of interference created by reflections from terrain, "clear sky", hydrometeors, and rough seas. These disturbances, as a rule, are non-stationary and non-Gaussian. The spectral components of the transmitted information messages in the Doppler frequency band of signals reflected from objects act as obstacles to active-passive systems that are used to illuminate the radiation of broadcasting stations in the HF and VHF bands.

The range of acoustic reconnaissance systems, as was shown in Chapter 2, is limited by noise generated by wind, vegetation, rain, and moving foreign objects.

This chapter presents the results of an experimental study of the characteristics of non-stationary interference for active [193] and active-passive [260] radio systems, as well as acoustic reconnaissance systems [261]. Methods of their description based on the use of nested semi-Markov processes have been proposed [193], the main parameters included in the model have been determined, as well as the estimated detection losses arising due to non-Gaussian noise characteristics [194, 262, 263].

The main results of the section are published in papers [193, 194, 260—265].

5.1. Characteristics of radar scattering from land and its mathematical model

At a high resolution on distance and angular coordinates, significant deviations of the distribution laws of fluctuations of signals scattered from bounding surface (sea, land) from the standard ones are observed, which is due to the consistent observation of surface areas with statistical properties of unevenness, which differ, and that gives rise to non-stationarity and non-Gaussian character. For the first time, attention was drawn to this in the works of Trunk G.V., George S.F., and Michel H. [266—268].

An attempt to take into account the non-Gaussian character of the signal scattered by sea and land was the use of logarithmic normal for amplitudes and compound normal for quadrature distribution laws for scattering from the sea, as well as a model with a variable number of scatterers for land [267—269]. Non-Gaussian processes with spectral characteristics and distribution laws and characteristic of reflections from the sea and land were obtained using non-linear and non-inertial transformations of the Gaussian random process [262, 263, 269, 270, 271], followed by the spectral coloring of the obtained data. A significant advance in the creation of models of non-Gaussian processes was the use of nested Markov processes to describe the statistics of failures [272, 273]. One of the components of the process was used to select the phase state in which the process is located, and the other described the characteristics within it. This approach was used to evaluate the effectiveness of signal reception in conditions of non-Gaussian interference in communication systems [272, 273]. However, in the proposed model, it was assumed that the waiting time in each of the phase states before the transition to the next is subject to an exponential distribution, and the interference spectrum does not change when the phase states change. This is justified by the interference that exists in the communication channels. For disturbances created by scattering from underlying surfaces (land, sea), these conditions, as a rule, are not fulfilled. The density of the distribution of the times of existence of the disturbance in each of the phase states can have a distribution that is significantly different from the exponential one and a different spectral composition.

In papers [274, 275], a model of the scattered signal from the sea and "clear sky" in the class of two-component nested semi-Markov processes is proposed. A similar approach can be used to describe a wide class of nonstationary non-Gaussian processes [276—279]. This section considers the possibility of its use to describe disturbances created by scattering from land areas.

The proposed model of the signal scattered from land areas contains three levels of detail:

- a description of the statistical characteristics of the areas within the region based on the data of topographic surveys to determine the probability of existence of each type; characteristic sizes and distribution functions for specific areas (agricultural land, forest areas, built-up areas, etc.) within individual regions, as well as modeling of spatio-temporal characteristics of backscattering from the Earth's surface [270];
- description of the spatial distribution of zones with a high intensity of the reflected signal within fairly homogeneous areas [280—282], and sounding at several frequencies allows studying scattering from both vegetation and soil [282, 283];
- description of the spectra and statistics of certain types of plant covers, terrain areas, plant fragments, and their dependence on moisture. The model is a development of the model of radar reflections from the sea proposed in [274].

The statistical description of the model is based on the use of nested two-component random processes $\{\overrightarrow{S(t)},\theta(t)\}$ in which one component $\overrightarrow{S(t)}$ is continuous, and the other $\theta(t) = \nu_i$ is discrete, and t is a generalized time that can be represented by spatial coordinates. These components are dependent and, in general, non-Markovian. This means that no restrictions are imposed on the distribution of the process existence times in each of the phase states. At each moment of time, the process can be in one of K possible phase states $H_i \in \nu_i \ldots \nu_K$, and the initial state $\theta_0 = \nu_i$ at the moment of time $t = 0$ and one-step transition probabilities π_{ij}, where $\overrightarrow{i, j = 1...K}$ are assumed to be known. Let's assign to each non-zero element π_{ij} of the transition probability matrix a random variable T_{ij} with a distribution density $f_{ij}(t)$, which we will call the waiting time in state ν_i before transition to state ν_j. If the values of T_{ij} are distributed according to the exponential law, then such a process will be Markovian [284]. In practice, in many cases, this assumption is not fulfilled, and then the process in which the change of states is described by a Markov chain, and the density of the distribution of existence times in each of them differs from the exponential one, belongs to the class of semi-Markov [285].

Within each of the ν_i states, we will consider the process to be quasi-stationary, which is described by its statistical scattering matrix $\left[S_i(t)\right] = \left[\begin{pmatrix} s_{11i}(t) & s_{12i}(t) \\ s_{21i}(t) & s_{22i}(t) \end{pmatrix}\right]$, the density of the distribution of $\left[P_i(S)\right] = \left[\begin{pmatrix} P_{11i}(s); P_{12i}(s) \\ P_{21i}(s); P_{22i}(s) \end{pmatrix}\right]$ values, and the $\left[S_i(\omega)\right] = \left[\begin{pmatrix} s_{11i}(\omega) & s_{12i}(\omega) \\ s_{21i}(\omega) & s_{22i}(\omega) \end{pmatrix}\right]$ spectrum. This means that the statistical process scattering matrix $\left\|S(t)\right\|$, as well as the density matrix of the $\overrightarrow{\left\|P(S)\right\|}$ value distribution and the $\overrightarrow{\left\|S(\omega)\right\|}$ spectra, are block vectors — each element of the i vector is a 2×2 square matrix [193].

The mathematical model of the system is nested processes, one of which determines the change of phase states and is, in general, semi-Markovian, and the second determines the behavior of the system within the phase state and, in most practically interesting cases, can be described by an ergodic Gaussian process. At the same time, it becomes possible to cover a wider class of processes, the description of which is impossible with the help of Markov chains [274—279]. Thus, for a developed sea disturbance, the distribution of wave periods differs from the exponential model [286], which means that the distribution of emissions of reflections from the sea may also not obey the exponential distribution [274]. Reflections from the clear sky are created by structures, the distribution of sizes and distances between which also differ from the exponential [275].

For land, the size distribution of individual clusters, which are determined by terrain types, and the distances between them may also differ from the exponential ones. At the same time, inside the cluster, there is a possibility of describing the scattered signal as ergodic with Gaussian statistics for each of the orthogonally polarized components and its spectrum. Therefore, for the statistical description of all these types of scattered signals (from land, sea, and clear sky), a model of a vector Gaussian ergodic process embedded in a semi-Markov process with a given matrix of spectral densities is conveniently proposed [193].

The algorithm for modeling the signal scattered from the land surface has the following structure:

1. The initial state in which the process is at the moment $t = 0$ is given; let it be H_i for certainty.

2. The next phase state of the process is determined. For this, a random number (π_{ij}) is chosen with probability $j \in E \in (1 \ldots K)$.

3. The time of the process being in the i state before the transition to the j state is determined, for which a random number T_{ij} is generated, having a distribution density $f_{ij}(t)$. During this time, a vector random variable $\overrightarrow{S_{ij}(t)}$ is generated, which has a distribution density $P_i(\vec{S})$ and a spectrum $\vec{S}_i(\omega)$.

4. The state of $H_i \to H_j$ is changed and the calculation process is repeated.

To assess the performance characteristics of selection systems and identify targets, knowledge of the distribution functions and interference spectra described by the considered model at the observation interval $(t, t+T_0)$ is required, where T_0 is the time of accumulation of information from the resolution element. Determination of the spectrum $S(\omega, T_0)$ and density $P(S, T_0)$ for an arbitrary observation time T_0 presents significant difficulties. The general solution to this problem was obtained only for Markov processes [287]. However, in practice, two extreme cases are most interesting: small $T_0 \leq\leq \min_{i \in E}\left(\overline{T_{ij}}\right)$ and large observation times $T_0 \leq\leq \max_{i \in E}\left(\overline{T_{ij}}\right)$, for which the results become obvious. With short observation times, there is almost never a state change during the observation time, and the density of the distribution of process values, its spectrum, and all numerical characteristics correspond to its initial state. And if the choice of the starting point is unimportant, then these characteristics are realized with possibilities determined by the final probabilities of each of the states [276]. With long observation times, the density of the distribution of values, the spectrum, and all numerical characteristics, for example, moments of order, are determined as a weighted average of the characteristics in each of the states with weights determined by the final probabilities of their presence [193, 276, 277]:

$$\overrightarrow{P(S)} = \sum_{i=1}^{K} P_i \overrightarrow{P_i(S)}; \ \overrightarrow{S(\omega)} = \sum_{i=1}^{K} P_i \overrightarrow{S(\omega)}; \ \overrightarrow{M_m} = \sum_{i=1}^{K} P_i \overrightarrow{M_{im}}, \qquad (5.1)$$

where M_{im} is "m" being the moment for the i^{th} state and M_m as a whole, and P_i is the final probability of the existence of the process in the i^{th} state [193, 276, 277].

The average time of being in the i^{th} state before the transition to j:

$$\overline{T_{ij}} = \int_0^\infty t f_{ij}(t)dt \tag{5.2}$$

and the average time the process stays in the i^{th} state before transitioning to one of the following states:

$$\overline{T_i} = \sum_{j=1}^{K} \pi_{ij} \overline{T_{ij}} . \tag{5.3}$$

Since the second moment of the process characterizes the intensity of the scattered signal, which means the RCS, the scattering polarization matrix for the specific RCS of the $\overrightarrow{\sigma^0}$ surface can be written [193, 288]:

$$\left\|\sigma^0\right\| = \begin{pmatrix} \sigma_{11}^0 & \sigma_{12}^0 \\ \sigma_{21}^0 & \sigma_{22}^0 \end{pmatrix} = \sum_{i=1}^{K} P_i \begin{pmatrix} \sigma_{11i}^0 & \sigma_{12i}^0 \\ \sigma_{21i}^0 & \sigma_{22i}^0 \end{pmatrix}, \tag{5.4}$$

where σ_{lmi}^0 is the specific RCS of the i^{th} cluster of the land surface (phase state) with l irradiation polarization and m scattered signal reception.

Processes with a non-exponential distribution of existence times can be approximately described by introducing additional fictitious phase states [285, 287].

Let us consider the physical interpretation of the proposed model. For a signal scattered from the land surface, the discrete component $\theta(t)$ is determined by a set of typical surface sections, each of which is described by the specific RCS matrix $[\sigma_{lmi}^0]$, the distribution function of $[P_{lmi}(S)]$ values, and the spectrum $[S_{lmi}(\omega)]$ of the scattered signal.

Some remarks should be made about the parameters included in the proposed model:

1. The definition of $f_{ij}(t)$ and π_{ij} describing their spatial distribution for each specific type of terrain can be based on topographic survey data and additional results of radar mapping. The averaged statistical characteristics (5.1) are determined by taking into account the final probabilities P_i of each of the types of plots. To do this, it is necessary to determine the percentage of the area occupied by specific types of sites on the map of the area, which gives estimates of the final probabilities of a given phase state of the disturbance. These characteristics practically do not depend on the frequency of the irradiating field. For their determination, it is possible to use radar means of the microwave range, which have a good separation in terms of range and angular coordinates. The data obtained in this case on homogeneous areas of the terrain can be extended to other frequency ranges (up to the VHF and HF bands).

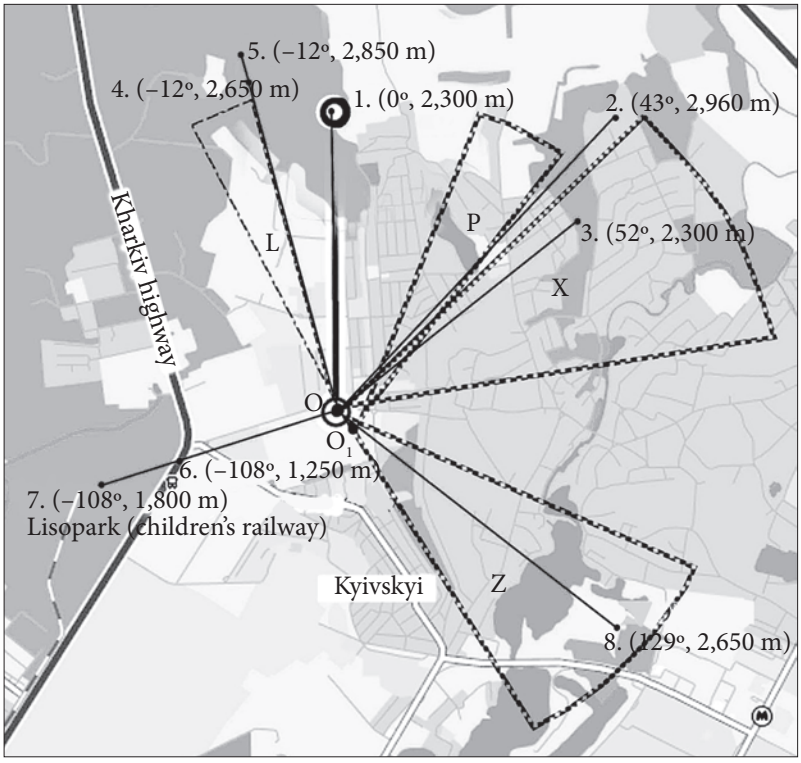

Fig. 5.1. Placement of measuring systems and studied terrain areas: 1, 4, 5 — deciduous forest; 2 — landing; 3 — a hill with a grass stand; 6, 7, 8 — deciduous forest; L — forest massif; Z — zone of construction of houses; X — a hill with a grass stand; P — agricultural land with plantings. Azimuth and range in meters are indicated next to the number of each measurement point. Range and azimuth resolution was 10 m, 10 mrad for $\lambda = 8$ mm and 60 m and 35 mrad for $\lambda = 2$ cm

2. The spectra $[S_{lmi}(\omega)]$ of the signal scattered by different types of terrain covered with vegetation with small changes in the wavelength F are proportional to it [193]:

$$\omega = 2\pi F = 2\pi \frac{2V}{\lambda}, \tag{5.5}$$

where V, F, ω are the speed of movement of the scatterer, Doppler frequency shift, and circular frequency shift, respectively.

This proportionality is preserved as long as the dimensions of the elementary scatterers d are significantly larger than the wavelength of the irradiating field λ. Proportionality is broken when $d \approx \lambda$ and the scattering occurs in the resonant region. When the dimensions of the scatterers become smaller than the wavelength of the irradiating field $d \leq \lambda$, scattering occurs in the Rayleigh region,

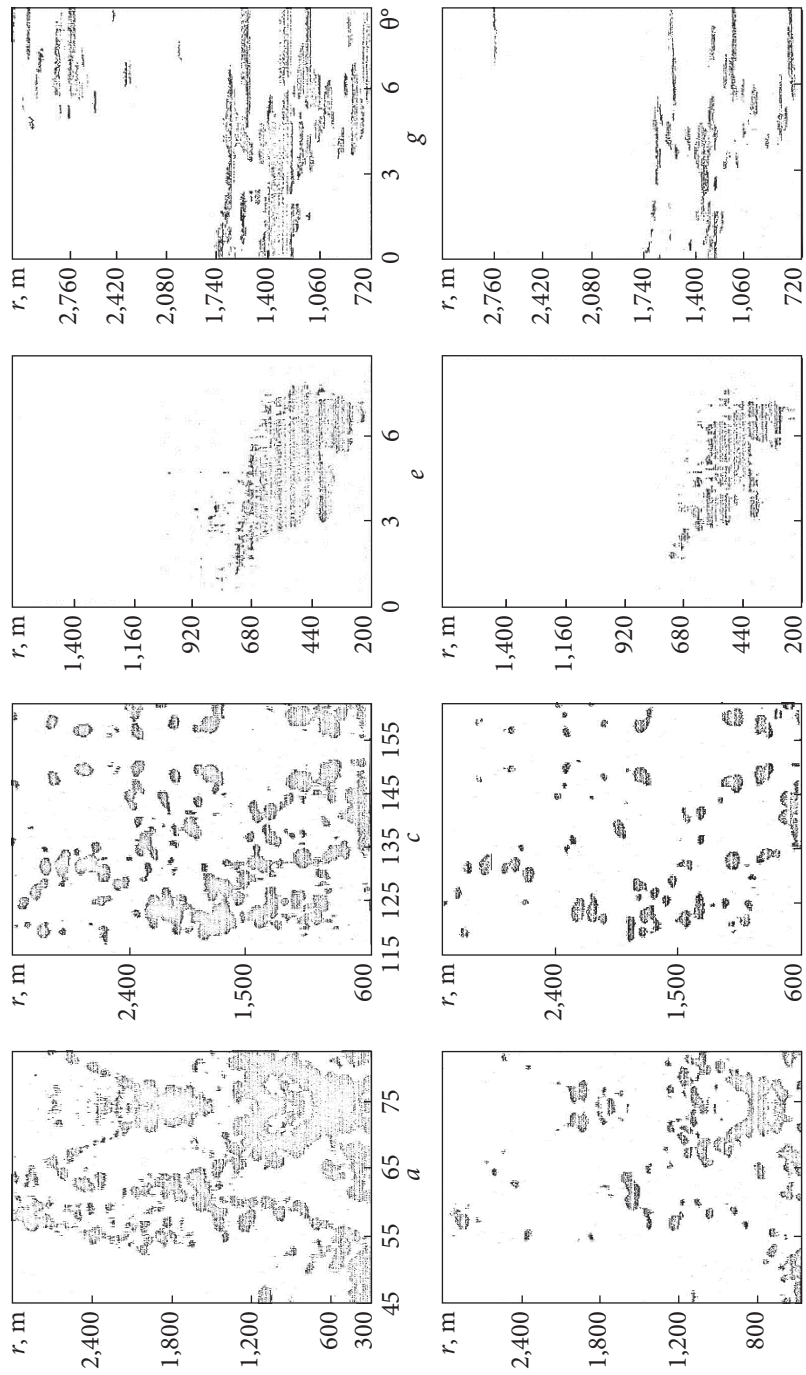

Fig. 5.2. Radar image of the area $\lambda = 2$ cm: *a*, *b* — a hill with grassy vegetation, sliding angle — $\psi = 3\ldots0.5°$; *c*, *d* — zone of construction with high-rise buildings, $\psi = 3\ldots0.5°$; *e*, *f* — forest massif, $\psi = 8\ldots1°$; *g*, *h* — agricultural land with plantings, $\psi = 2.4\ldots0.5°$; *a*, *c*, *e*, *g* — $\Pi = \overline{A}$; *b*, *d*, *f*, *h* — $\Pi = 4\overline{A}$; Π — display threshold; $\overline{A}$ is the average value for the frame — $\{\psi, \theta, r\}$ is the glide angle, azimuth and range to the surface area

and the intensity of scattering will be determined by the ratio d/λ, and the frequency of fluctuations will be determined not by the speed of movement of the scatterer, but by the frequency of its fluctuations.

Thus, in the short-wavelength region corresponding to $d \geq\geq \lambda$ the results of scattering spectra from vegetation obtained at one of the wavelengths can be successfully used to estimate similar characteristics for other wavelengths. In the long-wave and resonance regions, this proportionality is violated, and it is necessary to study these characteristics in these wave ranges. A model of two crossed half-wave vibrators can be used as a scatterer model in the resonance region — and two crossed Hertzian dipoles in the Rayleigh region [208, 210].

An experimental study of the spatial characteristics of homogeneous areas of the terrain was carried out based on the results of radar mapping of areas of the terrain using models of pulse measuring radars with wavelengths of 2 cm and 8 mm, the general appearance and technical characteristics of which are given in Appendix 2. Their location is shown in Fig. 5.1 by points O and O_1, respectively [193].

Mapping was performed in the summer-autumn period (from July to the beginning of September). Radar images of areas of the terrain are shown in Fig. 5.2 [193].

They are obtained after threshold processing and display of records of radar signals from the output of the radar amplitude detector, and the upper images in each of the figures refer to the case of the threshold Π equal to the average value of the signal $\bar{A}$ on the frame, and the lower ones — by 12 dB higher than its level. The recording of the radar image was performed at a discrete distance of about 11 m. The radar scattering from all areas of the terrain has a significantly heterogeneous structure on distance r and azimuth θ. The coefficient of variation (the ratio of the rms value of the amplitude fluctuation to the frame average) for the studied areas is 1.5...1.6 for a hill with a grass stand and agricultural land with plantings and 1.8...1.9 for a built-up area. For the forest massif, it was about 2. The given values indicate a significant excess of the random component of the stable signal scattered from the terrain. The analysis shows that the built-up zone — (Fig. 5.2, *c*, *d*) and the hill with grass — (Fig. 5.2, *a*, *b*) give approximately the same illumination density in the frame. At the same time, for the forest massif (Fig. 5.2, *d*, *e*), the leading edge and areas of the forest on the elevations provide the greatest illumination. The spatial distribution of the specific RCS can be determined using the same technique as when obtaining the temporal distribution. Fig. 5.3 shows the amplitude distribution functions of signals scattered by a hill with grass, a built-up area, agricultural land, and a forest massif [193].

They are built on a scale that linearizes the Rayleigh distribution law. Amplitudes of scattered signals were normalized to a value equal to the square root of the average intensity. Significant deviations of the experimental laws of distribution from Rayleigh's law are observed for all areas of the terrain. They have a higher probability of large values. To describe the distribution of amplitude A of interference from land within fairly homogeneous areas, you can use a

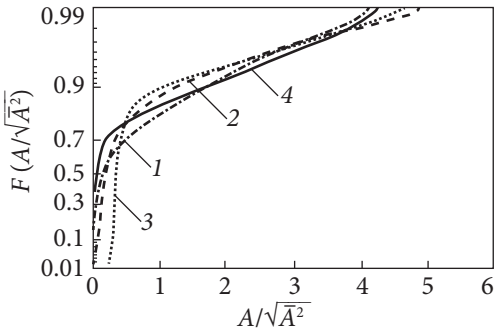

Fig. 5.3. Distribution functions of the amplitude of the signal reflected by parts of the Earth's surface: *1* — hill with a grass cover; *2* — building zone; *3* — agricultural land with plantings; *4* — forest massif

two-component model previously used to describe interference from the sea [274]. At the same time, bursts will be understood as reflections from those areas of the terrain, the RCS of which is significantly above the average, and pauses, respectively, where it is below the average level [193]. If we assume that in each of the phase states (burst, pause), the amplitude fluctuations of the scattered signals are described by Rayleigh's law, then the distribution function of the amplitude fluctuation of the signal scattered from the area of the terrain, as can be seen from relation (5.1), will be described by the composite Rayleigh distribution law:

$$p(A) = (1-P)\frac{A}{\sigma_0^2}\exp\left(-\frac{A^2}{2\sigma_0^2}\right) + P\frac{A}{\sigma_1^2}\exp\left(-\frac{A^2}{2\sigma_1^2}\right), \tag{5.6}$$

where P is the probability of a burst, σ_0^2, σ_1^2 is the intensity of pauses and bursts and their ratio $\gamma^2 = \sigma_1^2 / \sigma_0^2$, which characterizes the degree of non-Gaussianity of the process.

For this approximation, the probabilities of the presence of bursts in their radar image P and the ratio of signal intensities during bursts and pauses γ^2 are determined (Table 5.1)

Despite the heterogeneity of the studied areas, the values stability of the probability of the presence of zones with a high intensity of the reflected signal (interference emissions) and the ratio of high-intensity and low-intensity components in the scattered signal is observed. The largest difference in the intensity of the components is observed for areas built up by houses (up to 30 dB). For a forest massif with areas of meadows, a hill with grass, and agricultural land with planting zones, the intensity difference is 23...27 dB. The probability of having areas of intense signal reflection within the same type of area ranges from 0.15 to 0.3.

Table 5.1. **Radar characteristics of terrain areas**

Terrain type	Wave length, cm	P	γ^2, dB
Building zone with houses. Forest massif	2	0.17	30
A hill covered with grass	2	0.25	27
Agricultural land	2	0.3	2
Landing areas	0.8	0.17	5

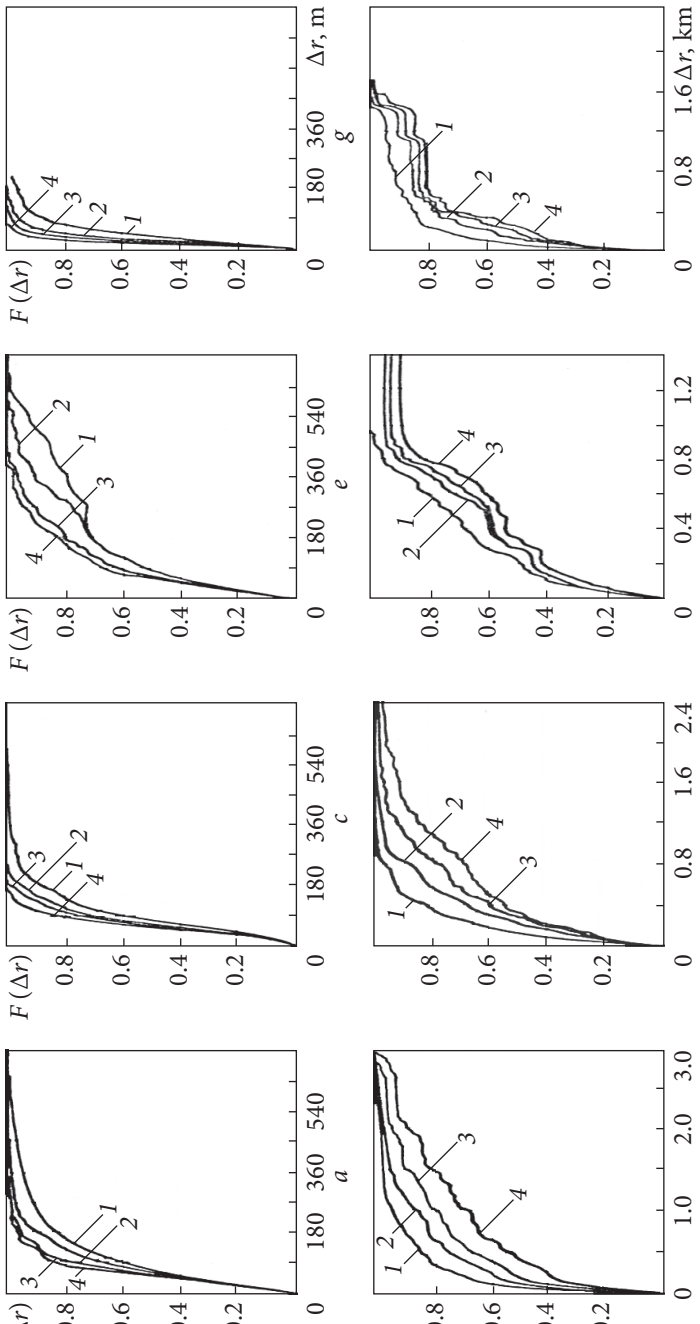

Fig. 5.4. Size distribution of reflective areas and distances between them: *a*, *c*, *e*, *g* — size distribution; *b*, *d*, *f*, *h* — distribution of distances; *a*, *b* — alkali; *c*, *d* — building zone; *e*, *f* — forest massif; *g*, *h* — field; *1* — $\Pi/(\overline{A^2})^{0.5} = 1$; *2* — $\Pi/(\overline{A^2})^{0.5} = 2$; *3* — $\Pi/(\overline{A^2})^{0.5} = 3$; *4* — $\Pi/(\overline{A^2})^{0.5} = 4$; Π — threshold

The description of the spatial heterogeneity of different types of the Earth's surface is based on the determination of the probabilities of the existence of areas with a given RCS, as well as the gaps between them. Integral distributions of the sizes of reflective areas by distance and the gaps between them for different types of terrain are shown in Fig. 5.4.

Values of the normalized value of the threshold Π obtained for a variable threshold from 0 dB to 12 dB ($\Pi/(\overline{A^2})^{0.5} = 1, 2, 3, 4$) relative to the average signal level. Their analysis shows that an increase in the threshold leads to a decrease in the size of the reflective areas and an increase in the distance between them.

According to the nature of the behavior, it can be noted that the distribution functions of reflective areas for meadows, built-up areas, and fields can be described by an exponential law. Two-dimensional distribution functions of the sizes $p(x_i, y_i)$ of reflective areas and the distances between them, assuming statistical independence of the characteristic sizes, can be described by exponential functions:

$$p(x_i, y_i) = p(x_i)p(y_i);$$

$$p(x) = \frac{1}{\overline{x}_1}\exp\left(-\frac{x_1}{\overline{x}_1}\right);\ p(y_1) = \frac{1}{\overline{y}_1}\exp\left(-\frac{y_1}{\overline{y}_1}\right), \tag{5.7}$$

where $\overline{x}_i, \overline{y}_i$ are the characteristic dimensions of the reflection areas $i = 1$ and the intervals between them $i = 0$ along the azimuth x_i and range y_i.

The dimensions of the reflective areas of different types of terrain for security levels of 0.5 and 0.9 are given in Table 5.2.

At an implementation level of 0.5 (median value), the dimensions of reflective zones are 50...80 m for a forest massif with a meadow, a built-up area, a hill with a grass standn and 20...40 m for agricultural land limited by plantings. The median values of the sizes between the reflective areas significantly exceed the characteristic sizes of the areas themselves and amount to hundreds of meters.

Table 5.2. **The sizes of the reflecting areas, the gaps between them at different levels of implementation, as well as the correlation interval Δ*r***

Area	Implementation						$R(\Delta r) =$ = 0.5/0.9
	0.5/0.9	0.5/0.9	0.5/0.9	0.5/0.9	0.5/0.9	0.5/0.9	
	Threshold, dB						
	0	6	12	0	6	12	
	The dimensions of the reflecting areas, m			Spaces between areas, m			Interval, Δ*r* m
Forest massif	80/489	67/236	58/204	204/720	276/800	336/1,066	93/307
Building zone	76/178	58/124	53/102	142/533	245/924	373/1,600	40/133
Meadow	71/231	56/138	53/124	71/675	124/1,066	391/1,991	47/207
Field	40/98	22/53	18/40	58/583	102/1,079	233/1,400	20/147

At the same time, with 90% implementation, they do not exceed 1...2 km. An increase in the classification threshold leads to a decrease in the characteristic sizes of reflective areas and an increase in the distance between them.

Using ratios (5.7) and the results given in Table 5.2, it is possible to estimate the characteristic dimensions $\overline{x}_i$ of reflective areas and the distances between them for different types of terrain when approximating the distribution of their sizes by an exponential function:

$$\overline{x}_i = \frac{x_i(P)}{\ln(1-P)}, \tag{5.8}$$

where $x_i(P)$ is the size of the reflective area $i = 1$ and the intervals between them $i = 0$ at the level of security P. The results of the obtained estimates are shown in Table 5.3.

It should be noted that for each of the types of terrain, there is an optimal classification threshold when solving the problem of recognizing a burst/pause, which depends on the ratio of the variances of the components in these phase states. The full probability of an error when describing the process in each of the phase states is determined by Rayleigh's law, taking into account expression (5.6):

$$\begin{aligned} P_{err} &= \text{Prob}(A \geq \Pi \,|\, H \in H_0) + \text{Prob}(A \leq \Pi \,|\, H \in H_1) = \\ &= (1-P)\exp\left(-\frac{\Pi^2}{2\sigma_0^2}\right) + P\left(1-\exp\left(-\frac{\Pi^2}{2\sigma_1^2}\right)\right). \end{aligned} \tag{5.9}$$

That is, an error will occur in situations where a pause is classified as a burst and a burst as a pause. Then, from the expression (5.9), we can obtain the condition for minimizing the total classification error:

$$\frac{\partial P_{err}}{\partial \Pi} = 0. \tag{5.10}$$

Table 5.3. **Characteristic sizes of the areas reflecting at different levels of security in the exponential approximation of the size distribution**

Area	Threshold, dB					
	0	6	12	0	6	12
	The dimensions of the scattering areas, m			Intervals between areas, m		
Implementation	0.5/0.9	0.5/0.9	0.5/0.9	0.5/0.9	0.5/0.9	0.5/0.9
Forest massif	115.4/212.4	96.7/102.5	83.7/88.6	294.3/312.7	398.1/347.4	484.7/463.0
Building zone	109.6/77.3	83.7/53.9	76.5/44.3	204.9/231.5	353.5/401.3	538.1/694.9
Meadow	102.4/100.3	80.8/59.9	76.5/53.9	102.4/293.1	178.9/463.0	564.1/864.7
Field	57.7/42.6	31.7/23.0	26.0/17.4	83.7/253.2	147.2/468.6	336.1/608.0

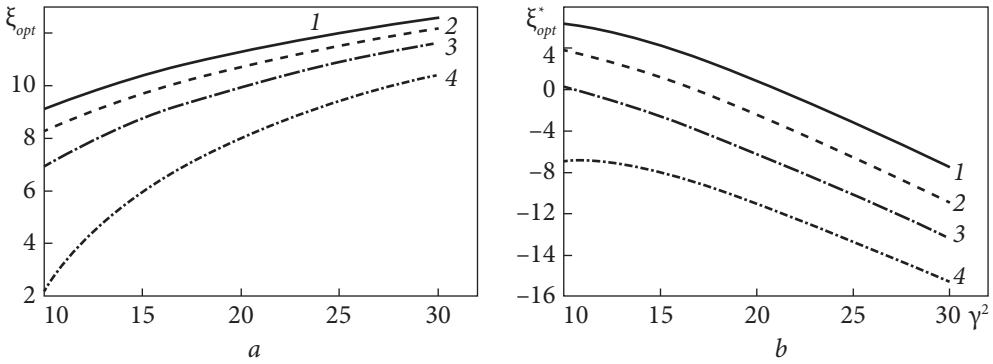

Fig. 5.5. Dependence of the optimal threshold on the ratio of component intensity and emission probabilities: *a* — normalization of the threshold by the dispersion of pauses ξ_{opt}; *b* — normalization of the threshold by the total variance ξ^*_{opt} (*1* — $P = 0.1$, *2* — $P = 0.2$, *3* — $P = 0.4$, *4* — $P = 0.8$)

Where we get:

$$\xi_{opt} = \sqrt{\frac{2\ln\left(\gamma^2 \frac{(1-P)}{P}\right)}{(\gamma^2+1)/\gamma^2}}, \qquad (5.11)$$

where $\xi_{opt} = \frac{\Pi}{\sigma_0}$ and $\gamma^2 = \frac{\sigma_1^2}{\sigma_0^2}$.

The threshold when normalized to the root mean square value of the process as a whole $\xi^*_{opt} = \frac{\Pi}{\sigma_\Sigma}$ will be determined taking into account the expression (5.11) as:

$$\xi^*_{opt} = \frac{\Pi}{\sigma_\Sigma} = \frac{\xi_{opt}}{\left(\sqrt{(1-P)+P\gamma^2}\right)} = \sqrt{\frac{2\ln\left(\gamma^2 \frac{(1-P)}{P}\right)}{(\gamma^2+1)/\gamma^2}} \frac{1}{\sqrt{(1-P)+P\gamma^2}}. \qquad (5.12)$$

In Fig. 5.5, the values of the optimal thresholds are given, which minimize the full probability of an error in the solution of the classification problem when normalizing for the dispersion of pauses in Fig. 5.5, *a* or the full dispersion of the process of Fig. 5.5, *b*. It can be seen (Fig. 5.5, *b*) that the selection of the threshold $\Pi / (\overline{A^2})^{0,5} = 1...2$ from the average intensity value is optimal for component intensity ratios from 10...30 dB and emission probabilities 0.1...0.4, which and took place during experiments.

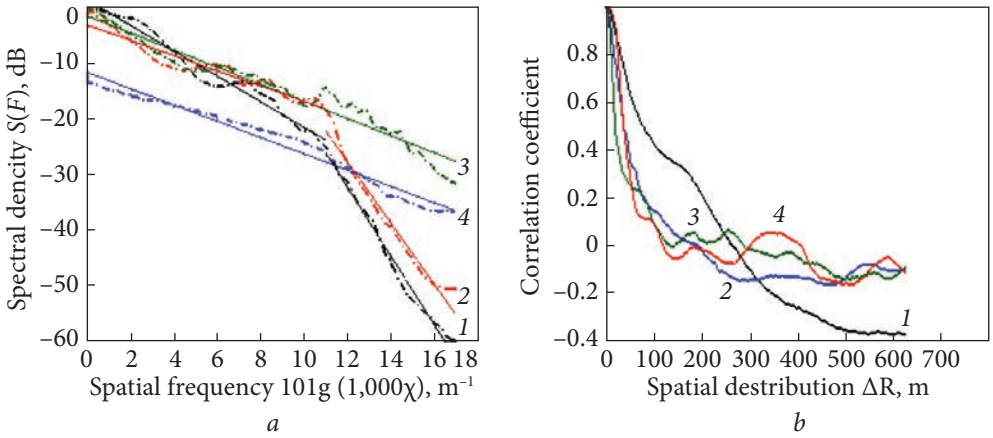

Fig. 5.6. Spectra and correlation functions of reflections from the forest and the built-up area: *a* — spectra; *b* — correlation functions; *1* — forest massif; *2* — building zone; *3* — field; *4* — meadow

Examples of spatial spectra, their approximations and correlation functions for different types of terrain are shown in Fig. 5.6.

The largest spatial radii of correlation are characteristic of the forest massif (Fig. 5.6, *b*). A significantly narrower spatial correlation is characteristic of the building zone, fields, and meadows (Fig. 5.6, *b*).

Correlation intervals for different types of terrain are shown in Table 5.2, and, at half level $R(\Delta r) = 0.5$, they do not exceed hundreds of meters. Spatial spectra of reflection from the terrain, as can be seen from Fig. 5.6, are satisfactorily described by static functions of the form

$$S(F) = S_0 \left(1 + \left(\frac{\chi}{\Delta\chi} \right)^n \right)^{-1}, \qquad (5.13)$$

where S_0 is the spectral density at zero frequencies, $\Delta\chi$ is the width of the spatial spectrum, and n characterizes the rate of decrease of the spectral density.

As can be seen from Fig. 5.6, the presence of regions of spatial frequencies with higher values of spectral density is characteristic for all spectra than according to (5.13). This means that spatial inhomogeneities with such dimensions occur for a given type of terrain more often than follows from the fractal spectrum model [280].

For construction zones with houses and forest massif, it is possible to distinguish sections of the spectrum with different slopes — Fig. 5.6. This means that within these zones, there may be areas with different characteristic scales of inhomogeneities. As can be seen from relation (5.1), the resulting spectrum is a superposition of the spatial spectra of areas having different spatial scales with

weights determined by the possibilities of observing these areas within the study area. The results of the approximation (5.13) of the spatial spectra for different types of localities are shown in Table 5.4. It should be noted that for almost all types of terrain in the low-frequency region of spatial numbers, the rate of decrease of the spectral density is approximately the same or slightly less than the spectrum of the exponential correlation function. In the high-frequency area for the forest massif and the building zone, it is approximately 3...3.5 times more.

Detection of signals against the background of non-stationary non-Gaussian disturbances from the underlying surface. Considering the task of detecting signals against the background of non-stationary disturbances described by nested semi-Markov processes, we have shown [194] that in non-Gaussian disturbances, larger signal/interference ratios are required than in Gaussian ones, i.e., additional losses in the signal/interference ratio appear due to non-Gaussianity. Their value, in the case of the description of the disturbance by a two-phase model (the signal consists only of bursts and pauses) with the given probabilities of correct detection D and false alarm F and ratios $F \leq\leq P_0$, $1 - D \leq\leq P_0$, that is, when the values of the given probability of false alarm and not detecting the signal are significantly less than the probability interference burst P_0 is determined [194]:

$$Z \approx \frac{\gamma}{\nu} \frac{\Phi^{-1}(1-F)}{\Phi^{-1}(1-F/P_0)} \approx A_q \ , \ F \leq\leq P_0 \, , \, 1-D \leq\leq P_0 \, , \tag{5.14a}$$

where $Z = z_{0NG}/z_{0G}$ and $Aq = q_{0NG}/q_G$ (ratio of thresholds and detection parameters for non-Gaussian and Gaussian interference statistics),

$$\begin{gathered} \sigma_\Sigma = \sigma_0 \nu, \quad \gamma = \sigma_1/\sigma_0, \\ \nu = \sqrt{1 + P_0\left(\gamma^2 - 1\right)}, \quad Z_0 = Z_0^* \nu, \quad q^* = q\nu; \end{gathered} \tag{5.14b}$$

and σ_Σ, σ_1, σ_0 — root mean square values of interference as a whole, as well as

Table 5.4. **Degree indicators in the approximation of spatial spectra of different areas of the terrain**

Terrain type	Curve No.	Frequency range, 10 lg(1,000χ) m^{-1}	Indicator degree, n	Correlation coefficient, R	Frequency range, 10lg(1,000χ), m^{-1}	Indicatordegree, n	Correlation coefficient, R
Forest massif	1	0…11	2.28	–0.98	11…17	6.14	–0.99
Building zone	2	0…11	1.36	–0.96	11…17	5.48	–0.98
Field	3	0…17	1.53	–0.97			
Meadow	4	0…17	1.46	–0.98			

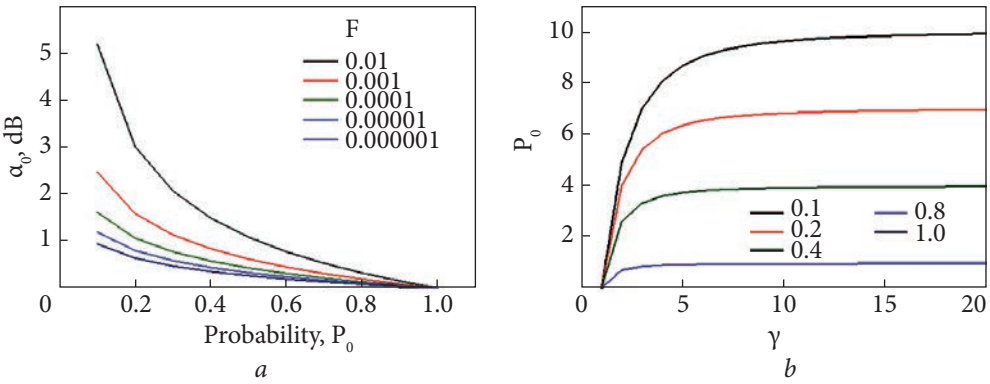

Fig. 5.7. Loss in the SNR arising due to non-Gaussianity: *a* — correction α_0, *b* — additional losses *L*

during bursts, pauses, and their ratio γ; Φ^{-1} is the inverse function of the integral of probabilities.

Since the loss in the signal/interference ratio Δμ [dB] during detection is proportional to the ratio of detection parameters and thresholds for interference with non-Gaussian and Gaussian statistics, then based on the ratios (5.14), we can write:

$$\Delta\mu[\text{dB}] \approx \alpha_0 + L, \tag{5.15a}$$

$$L = 20 \lg(\gamma/\nu), \tag{5.15b}$$

$$\alpha_0 = 20 \lg\left(\frac{\Phi^{-1}\left(1-\frac{F}{P_0}\right)}{\Phi^{-1}(1-F)}\right). \tag{5.15c}$$

Using ratios (5.15), estimated losses in the signal/interference ratio when detected in non-Gaussian noises are shown in Fig. 5.7.

Since the correction α_0 [dB] (Fig. 5.7, *a*) changes slightly (no more than 6 dB) in a wide range of changes in false alarm probabilities (from 10^{-2} to 10^{-6}) and final bursts probabilities (from 0.1 to 1), then the main contribution to the losses is made by the second term *L*, where the main influence is the parameter γ, which is determined by the ratio of the root mean square values of the interference components in each of the phase states (bursts and pauses) and characterizes the degree of non-Gaussianity of the process. In general, losses from non-Gaussianity for interference with rare intense emissions (5.15) can reach 20 dB.

For land, as can be seen from Table 5.1, the non-Gaussianity parameter reaches 30 dB, and the final emission probabilities are 0.15. At the same time, losses in the SNR ratio due to non-Gaussianity can be very significant (more than 10 dB).

To reduce them, as we have shown in [194], it is necessary to use adaptive detection with a controlled threshold for decision-making or apply automatic threshold adjustment (ATA) based on interference. In addition, it is possible to use blanking of interference when it is emitted. This will reduce the maximally achievable detection probabilities due to the passing of a useful signal during bursts of interference, at the same time significantly reducing the probability of a false alarm, preventing the passage of interference emissions to the output of the device. In addition, the use of non-parametric detection methods (sign and linear rank detectors) also allows you to significantly reduce losses in the SNR due to its non-Gaussianity.

Radar characteristics of areas with vegetation cover in the microwave range of radio waves. Studies [270, 280—283, 289, 290] are dedicated to the characteristics of the scattering of millimeter waves by separate areas of vegetation at angles typical for the placement of radio-technical facilities on aerospace carriers and consideration of models. A large amount of material on models of scattering by land covers is contained in the monograph [291]. In this section, the characteristics of scattering at sliding angles are considered. To study the characteristics of radar scatterings (RCS, spectra) of terrain areas, a coherent pulse radar with a radiation wavelength of 2 cm was used. The antenna was located on the roof of a building about 30 m high [193]. Reception of the signals reflected from the terrain was carried out both from the outputs of the amplitude and phase detectors of the radar. Measurements were carried out systematically, starting from early spring and ending in autumn, which made it possible to establish seasonal changes in the radar characteristics of the area covered with vegetation. The layout of the studied areas is shown in Fig. 5.1, and the appearance of the radar in Fig. 2.1 of Appendix 2. The sites differed in vegetation cover and relief, as well as in different angles of their irradiation.

In order to detect seasonal changes in the specific RCS of the vegetation cover and the influence of weather conditions (precipitation, wind speed) on it, it was averaged over all experiments. Fig. 5.8, *a* presents the average values of specific RCS for each day of observations. This figure shows three characteristic periods of vegetation and average values of σ^0 in these periods: *1* — the absence of leaves on trees and grass on the ground, *2* — intensive growth of leafy and grassy covers; *3* — the period of a stable state of fully developed leaf and grass cover. It can be noted that the appearance of leafy cover and the subsequent increase in biomass (May — early June) caused an increase in the specific RCS by approximately 5...7 dB, after which it practically did not change until deep autumn, when, due to the shedding of moisture by the leaves and the fall of the leafy cover, their RCS decreased again.

The change in leaf moisture in the spring-summer-autumn seasons was studied (Fig. 5.9 illustrates it). For spruce, the humidity is slightly lower than for deciduous tree species. This is consistent with the results of seasonal measurements of the content of free water in needles [292] — Fig. 5.10.

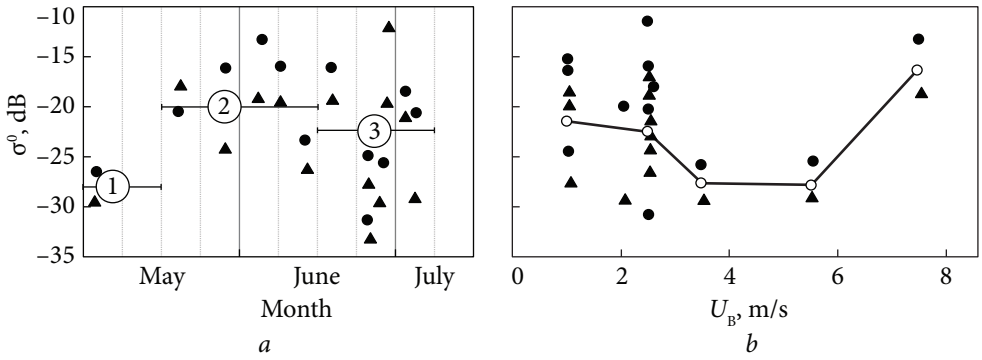

Fig. 5.8. Specific RCS of land areas covered with vegetation: *a* — seasonal change of specific RCS; 1 — the absence of leaves and grass, 2 — biomass growth, 3 — the period of stable state of biomass; radar operation mode: ▲ — coherent, ● — incoherent; *b* — specific RCS of land areas with vegetation at different wind speeds

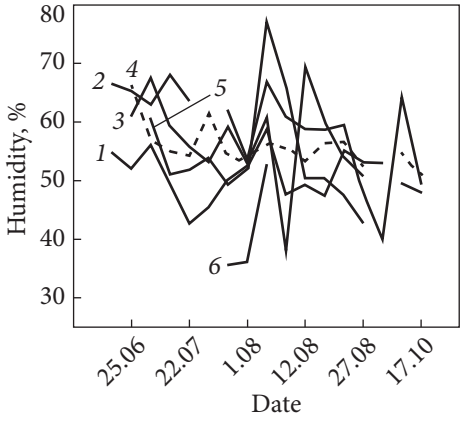

Fig. 5.9. Dependence of leaf humidity during the season: *1* — birch; *2* — linden; *3* — maple; *4* — oak; *5* — ash; *6* — spruce

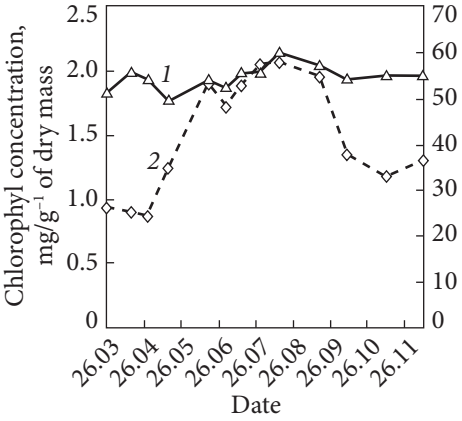

Fig. 5.10. Annual dynamics of the content of free water — *1* and chlorophyll — *2* in pine needles [292]

Study [293] of the dynamics of the chlorophyll index and the amount of biomass in herbaceous plants (Fig. 5.11) made it possible to establish that for herbaceous plants, the increase in the accumulation of chlorophyll in the leaf occurs in the transitional period to the reproductive phase, and its maximum content is in the flowering phase.

The chlorophyll index is related to the temperature in July and the complex moisture index by a regression equation [292, 293]. The total biomass content is maximal until the beginning of August. Kravchenko's finite atomic functions can be used to describe the process of biomass growth during the growing season [278, 294].

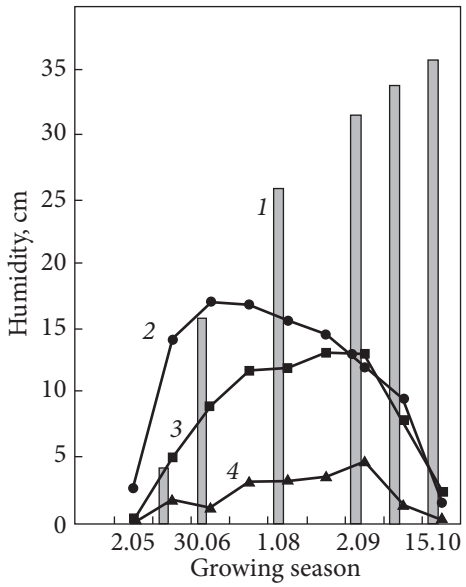

Fig. 5.11. Dynamics of green phytomass, chlorophyll index, and meteorological parameters (average air temperature and precipitation) during the growing season of 2003 [293]: *1* — precipitation; *2* — temperature; *3* — amount of biomass; *4* — chlorophyll index

Fig. 5.8, *b* shows the averaged RCS within each series of experiments obtained at different wind speeds. In the same place, circles show the average value of the specific RCS for a series of experiments with the same wind speeds; horizontal dashed lines show the limits of wind speed change during the experiment. It can be seen that the wind speed practically does not affect the RCS of vegetation. However, it significantly affects the spectrum width. Fig. 5.12, *a* shows the values of the average for each of the measurement days of the width of the spectrum of the signal reflected from the vegetation from the outputs of the amplitude and synchronous detectors. In the same figure, the expected width of the spectrum of the reflected signal according to the data of [295] is plotted as a dotted line. As can be seen, it satisfactorily describes the behavior of the spectrum width at wind speeds over 3 mps. For lower wind speeds, the experimentally observed values are much larger than predicted [295].

The width of the spectrum of the signal reflected from the vegetation from the output of the synchronous detector is smaller than that from the output of the

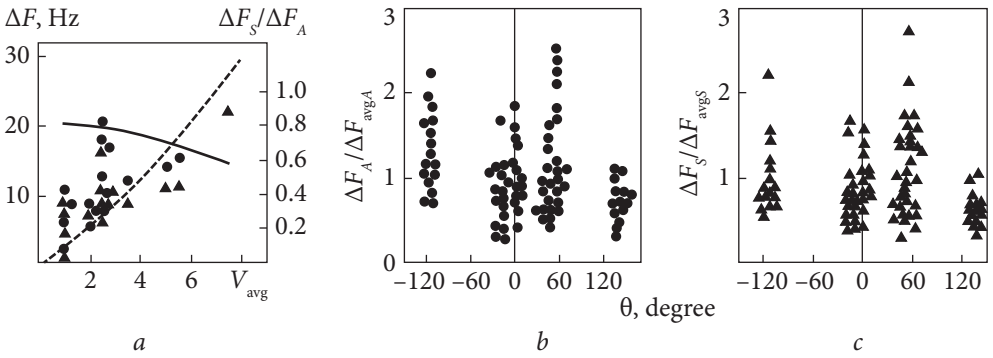

Fig. 5.12. Influence of wind speed and azimuth of surface irradiation on the spectrum width of the signal scattered by vegetation: *a* — spectrum width from wind speed: ▲ — Doppler spectrum; ● — amplitude spectrum; *b* — amplitude spectrum width from azimuth; *c* is the width of the Doppler spectrum from the azimuth

amplitude detector. The dependence of the ratio of the spectrum width at the input of the synchronous detector ΔF_S to the spectrum width at the output of the amplitude detector ΔF_A on the wind speed is shown in Fig. 5.12, *a* with a solid line. It can be seen that as the wind increases from 1 to 7 mps, this ratio decreases from 0.8 to 0.6.

Fig. 5.12, *b*, *c* illustrates the influence of the azimuthal angle of irradiation on the spectrum width of the scattered signal from the outputs of the amplitude and synchronous detectors, respectively. They are normalized to the average value of the spectrum width for experiments during the day. This made it possible to eliminate the influence on the value of the width of the wind speed. Since, at the same time, no distinction was made between the data obtained with different wind directions, the given dependences allow us to trace the influence of the topography surrounding the studied area on the spectrum width of the scattered signal. It can be seen, for example, that for a pine forest (point 8 azimuth about 124° — Fig. 5.1) located in a lowland, the width of the spectrum is always smaller and was approximately 60% of the average for the study.

The most broadband spectra of signals reflected from vegetation located on elevated terrain (points 2, 3, 7 — azimuthal angles 43, 52, –108° Fig. 5.1). At the same time, the differences in the width of the spectrum of the reflected signal, associated with the features of the surface relief, are approximately 2...2.5 times. In the same way, a change in the direction of the wind affects the width of the spectrum of the scattered signal. The width of the spectrum of scatterings from areas with vegetation located on the windward side is the largest. In the area on the leeward side is the smallest (Fig. 5.13, *a*).

The wind speed for the selected experiments is approximately the same and was 2...5 mps. In the same figure, arrows indicate the opposite direction of the wind for the area of the surface. It can be seen that the width of the reflection spectrum from the area covered with vegetation can change 2...3 times due to the change in the wind direction.

The shape of the spectrum of the signal scattered from vegetation depends on the wind speed and the type of terrain. As an example, Fig. 5.13, *b* shows the spectra of scattering from the terrain at the outputs of the synchronous and amplitude detectors. They were obtained for the vegetation located on the windward side (curves *1*, *2*) and for the case when the wind was directed perpendicular to this area of the terrain (curve *3*).

It can be seen that when the wind increases, the spectral density of high-frequency components increases. At low frequencies, in many spectra of the signal from the output of the synchronous detector, there is a spike of 2...10 dB of spectral density at low frequencies, which can be associated with reflection from stable scatterers (trunk, large branches). The shape of the spectra, in most cases, can be described by one of two approximation curves: exponential or power. Moreover, it should be noted that at low wind speeds (up to 3...4 mps), power approximation of the spectrum shape gives better results (curve *2*, Fig. 5.12, *b*),

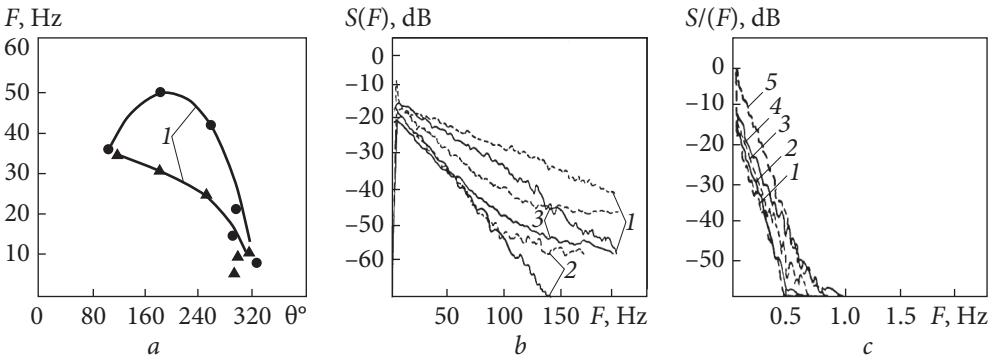

Fig. 5.13. The influence of wind speed and azimuth of radiation on the spectra of signals scattered from vegetation: *a* — spectrum width for a hill with grass; ▲ — Doppler spectrum; • — amplitude spectrum; *b* — spectra of reflection from vegetation: —— amplitude, – – – Doppler; $\Delta\theta = 0°$, *1* — $V_W = 7.5$ mps; *2* — $V_W = 2.5$ mps; $\Delta\theta = 45°$, *3* — $V_W = 7.5$ mps; *c* — spectrum of wind speeds: *1* — $V_W = 1.5$ mps; *2* — $V_W = 2$ mps; *3* — $V_W = 3.5$ mps; *4* — $V_W = 5$ mps; *5* — $V_W = 7$ mps

while at high wind speeds, exponential approximation gives better results. One of the reasons for the rise of the spectrum tails at low levels (–30...–40 dB relative to the maximum) may be the influence of equipment noise. This can explain the behavior of the spectrum at low wind speeds.

At the same time, if the surface section is irradiated at significant angles to the wind direction, that is, the projection of the velocity vector onto the direction of irradiation has small values, it is also advisable to use power functions — curve *3* in Fig. 5.13, *b* to describe the spectrum of the reflected signal. As a rule, the spectrum of the signal from the output of the amplitude detector has a larger width (Fig. 5.13, *a*) and the rate of decrease of spectral density with frequency (Fig. 5.13, *b*) than the spectrum from the output of the synchronous detector. Spectra of wind speed fluctuations, obtained when processing the results of wind speed registration by an inertial anemometer of a weather station, are close to exponential in shape (Fig. 5.13, *c*). This may be the reason for the observed exponential form of the spectrum of the signal scattered by the terrain, which is observed in many cases.

Characteristics of scattering of radio waves by plant parts. Laboratory experiments were conducted for determining the characteristics of radar scattering from plant fragments, and some electrodynamic parameters of individual plant elements (leaves, grass) were measured to study the scattering of centimeter and millimeter radio waves from vegetation objects. Experiments were carried out on wavelengths of 10 cm and 8 mm using models of measuring CW radars (Fig. 2.1 of Appendix 2) with technical characteristics listed in Table 2.1 of Appendix 2. Plant samples were blown by an air stream at a speed of 2 to 14 mps. The scattered signals on vertical and horizontal polarizations on a wavelength of 8 mm, as well as horizontal polarization on a wavelength of 10 cm in the band from 4 Hz to 2 kHz,

were registered. Samples were irradiated with a vertically polarized wave. A radio-absorbing material was placed behind the samples. Fig. 5.14 *a*, *b* shows the dependence of the width of the spectrum of the signal scattered on the horizontal polarization on the airflow speed at a wavelength of the irradiating field of 8 mm.

The width of the spectrum ΔF was calculated at the level of –3 dB (Fig. 5.1, *a*) and –10 dB (Fig. 5.14, *b*) from the maximum of the spectral density and was converted into the equivalent speed of movement of the scatterers according to the ratio:

$$\Delta V = \frac{\lambda \Delta F}{2}. \tag{5.16}$$

Analysis of the obtained data (Fig. 5.14, *a*, *b*) shows that the largest width of the *V* spectrum occurs when reflected from a pine tree (curve *1*). It is characterized by a sharper dependence on the airflow speed. Scattered signals from birch (curve *2*), aspen (curve *4*), and willow (curve *3*) have approximately the same spectrum width and a tendency to change with wind speed. The width of the scattering spectrum from the poplar (curve *5*) is characterized by a weaker dependence on the wind speed. This is because poplar leaves are, on average, larger in size

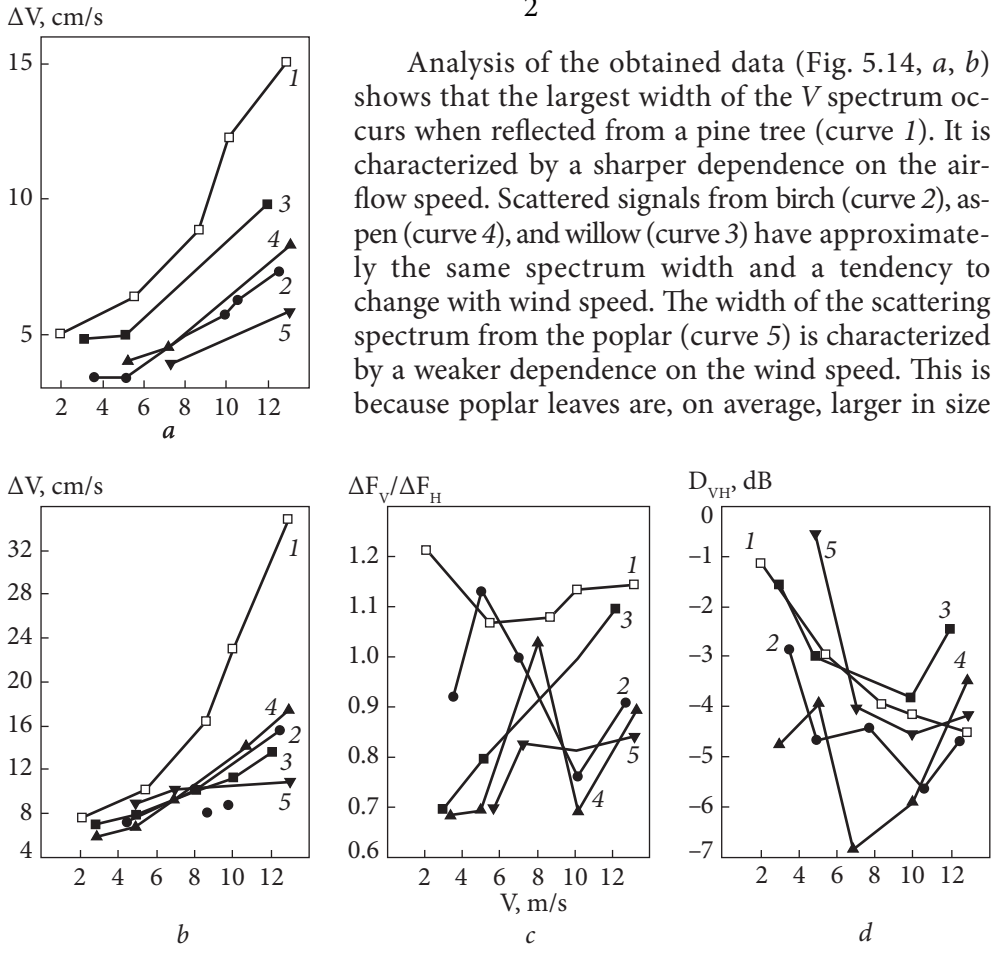

Fig. 5.14. The effect of wind speed on the spectrum width and depolarization coefficient of reflections from vegetation: *1* — pine; *2* — birch trees; *3* — willow, *4* — aspen; *5* — poplars; *a* — the width of the spectrum ΔV at the level of –3 dB, *b* — the width of the spectrum ΔV at the level of 10 dB; *c* — the ratio of the spectrum width at the –3dB level for vertical and horizontal polarizations ΔF

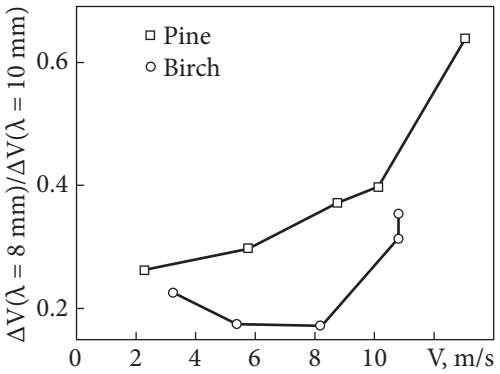

Fig. 5.15. Effect of wind speed on spectrum width

(mass), the stem of the leaf is stiffer, and to a lesser extent, they feel fluctuations under the influence of the wind. The most high-frequency oscillations of the needles of coniferous trees (which have the smallest mass) manifest in the expansion of the spectrum of the signal scattered from them. The analysis of the obtained data shows that for each type of vegetation, there is a certain wind speed, starting from which there is a sharp increase in the width of the spectrum of scattered signals. For coniferous trees, it is 6...8 mps, and 3...5 mps for deciduous trees. A comparison of the spectra of the scattered signals on the polarization of the aligned (vertical) and orthogonal (horizontal) radiation (Fig. 5.14, *c*) shows that for almost all tree species, their proportional expansion is observed when the wind speed increases.

However, if for deciduous species, the spectrum of the scattered signal on orthogonal polarization (horizontal) is somewhat wider than the main one (vertical) by approximately 10...30 %, then for coniferous species, it is narrower (by 10...20%).

The large width of the scattering spectrum on horizontal polarization for deciduous tree species and smaller for coniferous species is associated with the peculiarities of the orientation and fluctuations of the elements of deciduous and coniferous covers.

If we imagine the element of vegetation in the form of two crossed vibrators [208, 210] — horizontal and vertical, then the larger width of the spectrum on the horizontal polarization, compared to the vertical, can be explained by the larger amplitude of the movement of the horizontal vibrator compared to the vertical one and, because of it, the larger index of phase modulation of the scattered signal. This leads to a wider spectrum of the scattered signal. The leaves of trees make complex movements under the influence of the wind. In addition to oscillations, together with the branches of the tree, each leaf oscillates, both relative to the points of attachment to the branches, and performs a rotational movement relative to the stem of the leaf. In other words, each leaf is a complex vibrator that oscillates relative to the leaf stem and as part of the branch and the tree as a whole. At the same time, the phase modulation indices for each of the degrees of freedom can differ significantly. This will lead to a complex dependence of the spectrum parameters on the wavelength of the irradiating field.

The depolarization of signals scattered by vegetation also depends on the wind speed (Fig. 5.14, *d*), and the increase of the latter leads, as a rule, to a decrease in the depolarization coefficient. This is because that with a weak wind, the

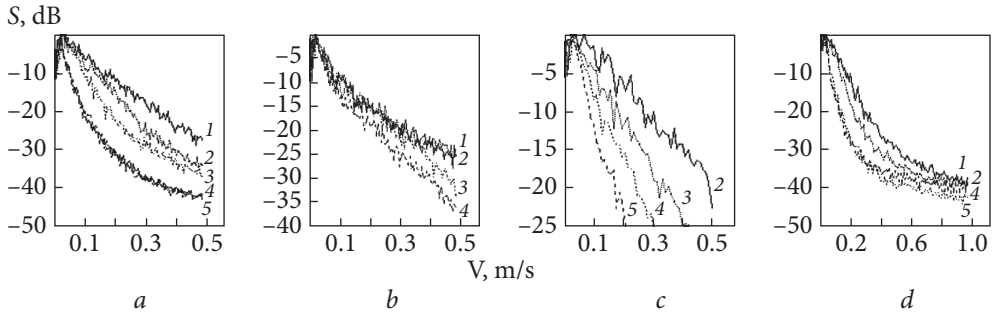

Fig. 5.16. The influence of wind speed on the signal spectrum from vegetation fragments: *1* — V_W = 13 mps, *2* — V_W = 10 mps, *3* — V_W = 7 mps, *4* — V_W = 5 mps, *5* — V_W = 3 mps ; *a* — aspen; *b* — poplar; *c* — pine; *d* — willow

leaves (needles of conifers) are most chaotically oriented in space, which leads to the strongest depolarization of the scattered signal. The depolarization coefficient reaches (–0.5...–2 dB). When the wind increases, starting with speeds of approximately 6...8 mps, the leaf sway occurs relative to the average position, in which the wind load on the leaf is minimal, and the depolarization coefficient drops to approximately (–3...–6 dB). In general, strong depolarization is characteristic of the signal scattered from foliage in the millimeter wave band. Data obtained at 10 cm and 8 mm wavelengths were used to assess the influence of the radiation wavelength on the spectrum width of the signal scattered from vegetation. The dependence of the ratio of the width of the spectrum of signals reflected from tree branches at 8 mm and 10 cm waves (calculated into the equivalent speed of the scatterers) on the wind speed at the reception polarization, orthogonal radiated (Fig. 5.15) was obtained.

The given data indicate the absence of proportionality of the spectrum width of the scattered signal to the operating frequency of radiation. This is because the Doppler spectrum of the signal reflected from vegetation is formed not only due to reciprocating but also due to the rotational movement of vegetation elements. At the same time, if the reciprocating movement of the leaves with a large amplitude leads to a change in the Doppler frequency shift (in the short-wave range) proportional to the operating frequency, then their oscillations and rotation relative to the points of attachment to the branches when the wavelength changes from comparable to significantly smaller leaf sizes such a change frequencies may not be given.

The energy spectra of signals scattered by different types of vegetation at a wavelength of 8 mm with a reception polarization consistent with the emitted one and different airflow speeds are shown in Fig. 5.16.

It was found that for all types of vegetation they can be approximated to the levels of spectral density (–30...–40) dB with respect to the maximum by a linear or logarithmic curve, which confirms the conclusions of works [295] that the scattering

spectra from vegetation are described by an exponential, or power dependencies:

$$S(F) = \begin{cases} \exp\left[-0.693(F/\Delta F)\right] \\ \left[1 + \left|F/\Delta F\right|^{n}\right]^{-1} \end{cases}, \qquad (5.17)$$

where ΔF is the width of the scattering spectrum at half power.

It should be noted that the spectra of signals scattered from aspen and birch up to wind speeds of 7 mps are better described by the power dependence with the exponent $n = 4$. At high speeds, the exponential description of the shape of the spectrum gives better results. For conifers, it is better to use the exponential function at all airflow speeds, while for poplar and willow, the best results are given by the static approximation with the exponent $n = 3\ldots4$. When the speed of the airflow increases, the level of spectral density in the high-frequency region of the spectrum increases by 5...15 dB. The change in the intensity of the signal scattered from vegetation in the band from 4 Hz to 2 kHz at 8 mm and 10 cm wavelengths on the wind speed is shown in Fig. 5.17.

For coniferous tree species, the intensity difference reaches 20 dB — for deciduous trees, it does not exceed 10 dB. Studying the depolarization of individual spectral components of signals scattered by tree branches, according to the method described in papers [270, 280—283], made it possible to establish that the depolarization coefficient has a value of (-6 ± 3) dB in the energy region of the interference spectrum and (-5 ± 4) dB on his wings. At the same time, the trends of its change depending on the wind speed are the same as those of the integral depolarization coefficient.

Grass and tree leaves make the main contribution to the signal scattered from plant objects, especially to its fluctuating component. The total scattered signal is the result of combining reflections from many elementary scatterers, and therefore, knowing the change in the properties of the latter depending on the season and meteorological conditions — it is possible to predict the relation with these factors of the specific RCS, fluctuation spectra and other characteristics. This approach to the study is all the more necessary because the data available in the literature mainly refer to large slip angles [270, 280—283, 289, 290], corresponding to the conditions of observation from aerospace carriers. Without knowledge of the electrodynamic properties of a separate vegetation element, it is dif-

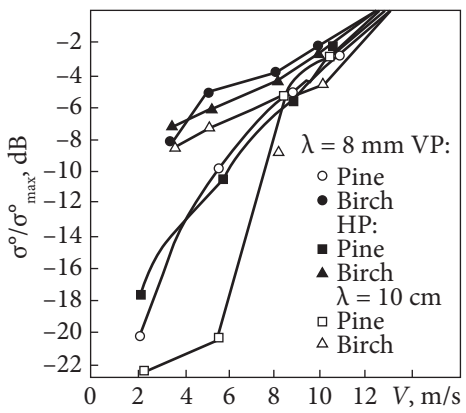

Fig. 5.17. The influence of wind speed on the RCS of vegetation at the output of the selection of moving targets (SMT) filter with a band of 4...2,000Hz

ficult to predict the weakening of radio waves when they pass through space with plants. To fill this gap, laboratory experiments were conducted to evaluate the scattering and attenuation of radio waves in the band from 27 GHz to 85 GHz by individual elements of plants at different conditions, primarily at different humidity levels. These measurements can serve as a complement to experiments in natural conditions [289, 290, 296, 297] and are necessary for creating a model of scattering from plant covers. Samples of leaves of various tree species were placed between mica spacers, and the reflection and absorption coefficients of millimeter waves were measured using SWR panoramic meters of the millimeter wave range P2-65 (27...37 GHz) and P2-69 (53...78 GHz) range of leaves. Dependencies of the signal absorption coefficient by various plant elements on the moisture content are presented in Fig. 5.18, *a*.

From Fig. 5.18, it can be seen that reed, willow, and poplar cause the greatest damping of millimeter waves and the least — sycamore maple. Since the amount of attenuation, even when passing through one leaf, is 6...10 dB, it allows us to conclude that scattering from targets located behind the vegetation zone will be significantly weakened. As the foliage dries in the fall, the attenuation when passing through a single leaf decreases to 0.5...1 dB. The dependence of the reflection coefficient on the humidity of the leaves is presented in Fig. 5.18, *b*. It should be noted that at an initial humidity of 50...70%, the highest reflection coefficients for reed, poplar, and willow leaves (approximately –3.5...–5 dB) and the lowest (approximately –6 dB) for poplar.

As the humidity of the leaves decreased, the value of the scattered signal also decreased, reaching –11...–13 dB for dry leaves.

For practical estimates of attenuation and scattering coefficients depending on humidity (H), you can use empirical relations you can use empirical:

$$\begin{aligned} \Gamma\left[\mathrm{dB}\right] &= -\Gamma_0\left[\mathrm{dB}\right] + \beta_{1\Gamma}H + \beta_{2\Gamma}H^2;\ \Gamma = \Gamma_0 \exp\left(\alpha_{1\Gamma}H + \alpha_{2\Gamma}H^2\right), \\ L\left[\mathrm{dB}\right] &= -L_0\left[\mathrm{dB}\right] + \beta_{1L}H + \beta_{2L}H^2;\ L = L_0 \exp\left(\alpha_{1L}H + \alpha_{2L}H^2\right), \end{aligned} \tag{5.18}$$

where $\alpha_{ij} = 0.1151 \times \beta_{ij}$; $i \in 0,1$; $j \in \Gamma, L$.

In Table 5.5, the results of the approximation of experimental data by empirical dependences (5.18), as well as the resulting root mean square errors $\sigma_{\beta 1}$, $\sigma_{\beta 2}$, are shown.

Let's consider the empirical models for describing the specific RCS of vegetation cover. The specific RCS of the plant cover will depend on several factors:

$$\sigma^0 = \alpha_0 \gamma_0 \Gamma_\Sigma L_\Sigma, \tag{5.19}$$

where Γ_Σ, L_Σ are the integral coefficients of scattering from leafy cover and attenuation when propagating through it, and coefficients α_0 and γ_0 take into account how much of the signal scattered from vegetation is reflected towards the radar, as well as the density of vegetation filling of the distinguishing element.

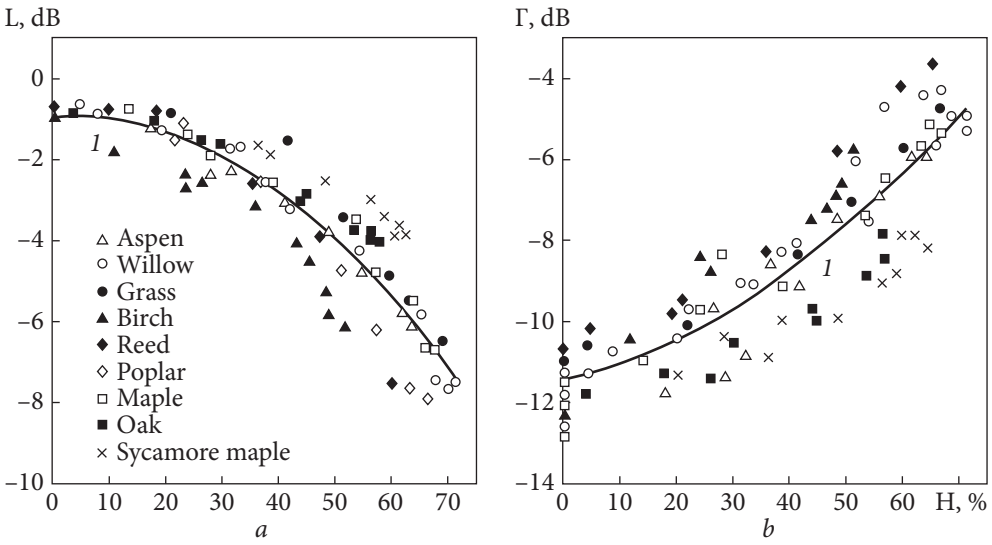

Fig. 5.18. Attenuation (*a*) and scattering coefficients (*b*) from leaves of trees and grass depending on humidity — 27 GHz...85 GHz

Table 5.5. **Values of approximation coefficients for absorption and scattering from leaves**

Parameter	β_1	$\sigma_{\beta 1}$	β_2	$\sigma_{\beta 2}$	Correlation coefficient, R	Number of points, N
Attenuation coefficient, L[dB]	$1.04 \cdot 10^{-2}$	$2.3 \cdot 10^{-2}$	$-1.4 \cdot 10^{-3}$	$3.0 \cdot 10^{-04}$	0.804	78
Scattering coefficient, Γ[dB]	$3.34 \cdot 10^{-2}$	$1.8 \cdot 10^{-2}$	$8.5 \cdot 10^{-04}$	$2.6 \cdot 10^{-04}$	0.788	90

The factor α_0 is about 1/6, and γ_0 can vary widely from about 5 to 100%. To estimate scattering and attenuation from a leafy cover, we will assume that it is equivalent to a multi-layered environment, each layer of which gives the same attenuation and reflection as a single leaf.

Then the integral reflection coefficient from the foliage, taking into account multiple scattering, will be determined as

$$\Gamma_\Sigma = \sum_{m=1}^{\infty} \Gamma^m \approx \frac{\Gamma}{1-\Gamma}, \tag{5.20a}$$

and the integral attenuation coefficient, when propagating through a leafy cover consisting of many layers,

$$L_\Sigma = \sum_{m=0}^{\infty} L^{2m} \approx \frac{1}{1-L^2}, \text{ while } L \le 1. \tag{5.20b}$$

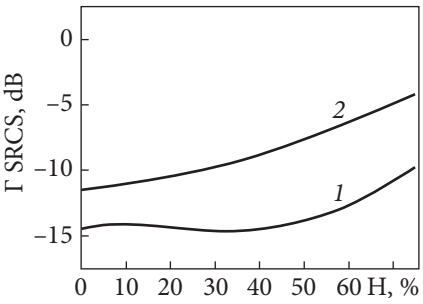

Fig. 5.19. Dependences of specific RCS — *1* and scattering coefficient — *2* of vegetation on humidity

It can be seen from relations (5.19, 5.20) that in the case of strong attenuation in the spring-summer period, that is, when the leaves are saturated with moisture, the specific RCS is determined by scattering from the surface layer of the leaves, while in autumn, with small attenuation, a contribution to the specific RCS can also be made by scattering from deeper layers of leaves. With the use of ratios (5.18—5.20), the specific RCS estimates of vegetation from humidity are obtained — Fig. 5.19. The fill factor γ_0 was assumed to be 100% during the calculation.

The same figure shows the values of the scattering coefficient. It can be seen that the presence of two competing mechanisms (decrease in attenuation and scattering coefficient when humidity decreases, in which not only the surface but also deeper layers of leaves are involved in the scattering process leads to a decrease in the range of changes in specific RCS. If for the reflection coefficient when humidity changes, the difference can be 8...9 dB, then for specific RCS, it is about 5...6 dB, which is consistent with experimental data.

5.2. Interferences of active-passive radar systems created by the radiation of broadcasting stations in the HF and VHF bands

Recently, active-passive systems that use the radiation of existing radio technical systems, both ground-based and space-based, are attracting increasing interest in solving radar tasks. So, in the works of Yu. M. Sedyshev and his students [38, 244], the possibilities of using the radiation of television centers for these purposes are considered. The possibilities of using VHF broadcasting stations were analyzed [251]. But the most interesting and promising, in our opinion, is the use of the radiations of broadcast stations in the HF band, which operate with an ionospheric wave, to illuminate the air environment. For the first time, this idea was experimentally confirmed in papers [220, 222, 224, 298, 299]. To develop algorithms for the selection of signals of broadcast stations scattered from objects, knowledge of the statistical characteristics of the illumination fields (spectral density, their distribution laws, diurnal and seasonal behavior), which act as an obstacle to useful signals of the secondary scattered field from objects, is necessary. This section is devoted to the presentation of some of these issues.

Equipment and methods of experiments. The spectral components of the transmitted information messages in the Doppler frequency bands of the signals

are scattered from the objects and act as obstacles to the active-passive systems that use the signals of broadcast stations in the HF and VHF bands to illuminate the environment. At object speeds of up to 2,500 kmph, as you can easily see, the Doppler frequency shifts for HF band of 10...30 m will be:

$$F_D = \frac{2V}{\lambda}, \tag{5.21}$$

about 140 Hz on a 10 m wavelehgth and less than 50 Hz on a 30 m wavelehgth.

Thus, in the HF band, the Doppler frequencies of scattering from aerial objects, even modern fighter jets, will lie in the range of frequencies up to the information signal of a broadcast station, which begins at approximately 100 Hz. At the same time, in the VHF broadcast band (wavelength of about 3...4 m), useful signals of high-speed objects can be in the broadcast frequency range, which will act as interference, preventing the detection of scattered secondary signals from objects. Therefore, it is extremely important to study statistics (spectra, distribution laws, numerical characteristics, and their behavior during the day) for illumination signals, which are the radiation of broadcasting stations in the ranges of detection of secondary scattering from objects.

For conducting experimental studies, improved professional HF receivers in the band 1...39 MHz were used: Kanal-R, Katran, a brief description and main technical characteristics of which are shown in Fig. 3.1, Fig. 3.2 and Table 3.1, Table 3.2 of Appendix 3, respectively, as well as the DEGEN DE-1127 all-wave radio receiver manufactured in the PRC — Fig. 3.4 of Appendix 3, its main technical characteristics are given in Table 3.3 of Appendix 3. The signals of the DEGEN DE-1127 radio receiver, from the output of the amplitude detector for the HF band and the frequency band for the VHF band, were recorded in mp3 and WAV formats and then used to estimate the spectra and power distributions of the signal emitted by the stations in the frequency range near the carrier. The sampling frequency is 8 kHz.

Experimental studies with Kanal-R receivers, Katran. Fig. 5.20 presents the signal spectra of the illumination stations, the characteristics of which are given in Table 3.4 of Appendix 3, which are received when receiving signals in telephone (Tlf) and telegraph (Tlg) operating modes of the receiver. In telephone mode, the carrier after detection lies in the region of zero frequencies — Fig. 5.20, *b*, while in the telegraph mode, it is shifted to the area of audio frequencies with the help of a local oscillator (for the examples shown in Fig. 5.20, *a*, about 50...100 Hz). It can be seen that, depending on the nature of the transmitted information, the frequency range in which the main signal energy is concentrated in the telephone mode is located from 100...200 Hz to 400...600 Hz. Higher frequency components have a level of about 10...15 dB lower and are located up to 1,500...1,600 Hz, after which their level gradually decreases by 30...35 dB at frequencies of about 2,000 Hz.

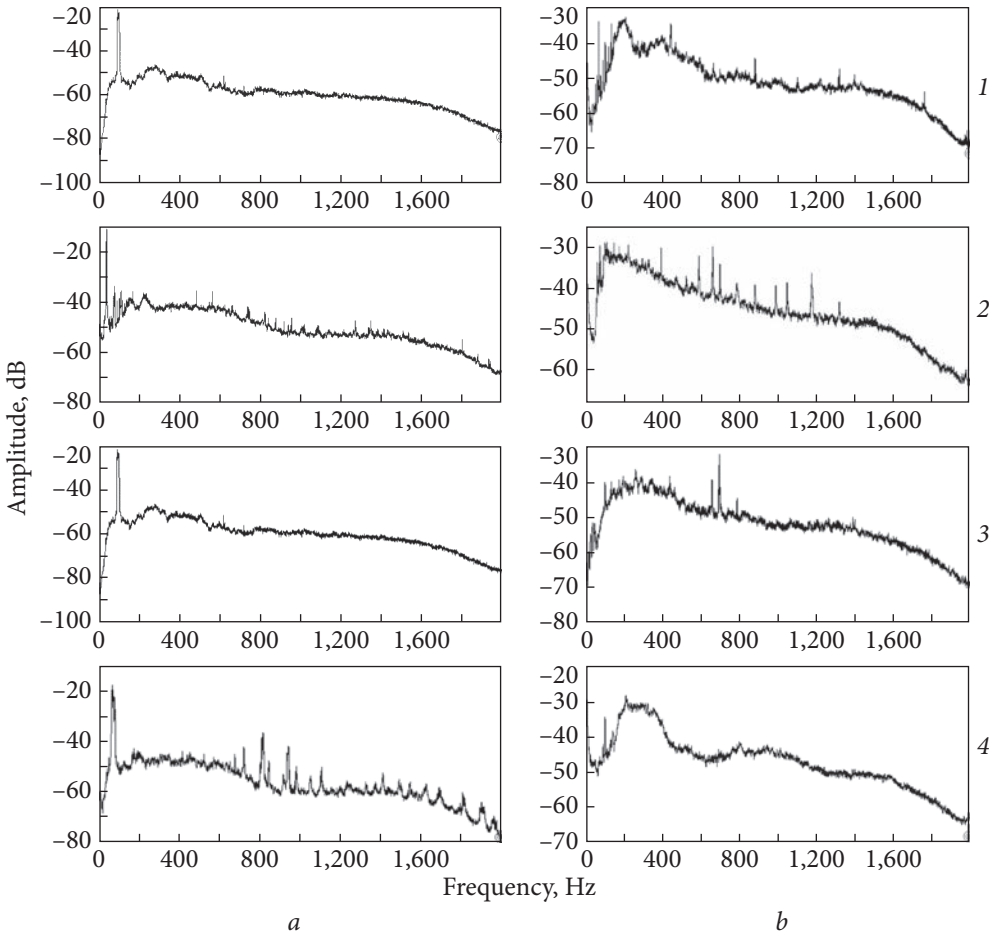

Fig. 5.20. Signal spectra at the output of the "Kanal-R" receiver in telegraph (*a*) and telephone (*b*) modes, *1* — Shijiazhuang, China 6,100 km, *2*— Kashi, China, 3,300 km, *3*— Issoudun, France, 2,500 km, *4*— Emirler, Turkey, 1,200 km

Numbers on the right in Fig. 5.20 correspond to illumination stations, the characteristics of which are given in Table 3.4. They were located at distances from the receiver from approximately 1,200 km to 6,100 km, at different azimuth angles. At frequencies up to approximately ±40...50 Hz relative to the carrier, the level of spectral density is significantly lower than that of the carrier and information signals, which are located in the frequency range of up to several kilohertz. The forms of the spectra are similar in both telegraph and telephone modes. Frequencies in the range, usually up to 600...800 Hz, have the highest spectral density, although in some cases, it can be up to 400 Hz — Fig. 5.20, *4*, *b*. At frequencies above 1,600 Hz, the spectral density gradually decreases. The level of

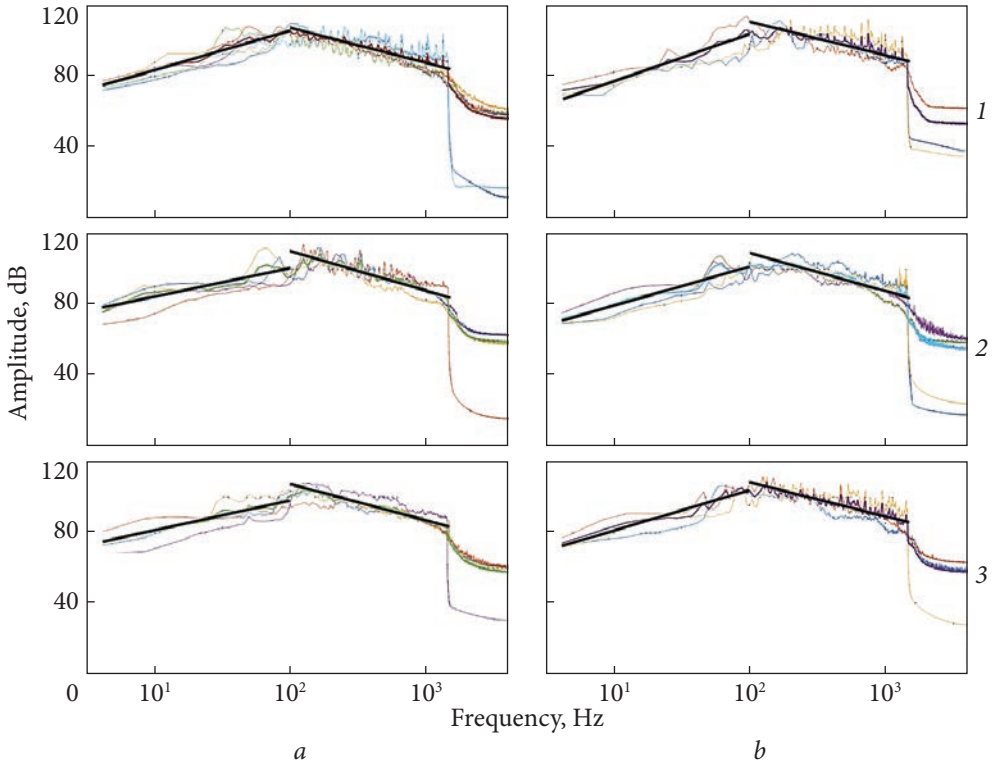

Fig. 5.21. Normalized spectrums of signals of broadcasting HF stations are given in Table 3.5 of Appendix 3. *1*, *a* — (1.1—1.6), *1*, *b* — (2.1—2.3), *2*, *a* — (3.1—3.4), *2*, *b* — (4.2—4.5), *3*, *a* — (5.1—5.4), *3*, *b* — (6.1—6.3), average spectra and their linear approximations

the spectral density of the carrier is approximately 35...50 dB higher than when it is adjusted to it by ±100 Hz.

The equations for describing the spectrum are as follows:

$$S(F)[\text{dB}] = \begin{cases} a_-[\text{dB}] + n_- \cdot 10\lg F[\text{Hz}], \ 2\text{Hz} < F[\text{Hz}] \le 100[\text{Hz}] \\ a_+[\text{dB}] - n_+ \cdot 10\lg F[\text{Hz}], \ 100\text{Hz} < F[\text{Hz}] \le 2000[\text{Hz}] \end{cases}.$$

The approximation of the low-frequency part of the spectrum was carried out from about 2 Hz to 100 Hz; and the high-frequency part from 100 Hz to about 2,000 Hz.

The results of the approximation of the spectra of radio broadcast HF stations of illumination by the method of least squares (LSM) and obtained estimates of the rate of decrease of the spectral density above and below the frequency of the maximum for each of the groups of spectra, the characteristics of which are given in Table 3.5 of Appendix 3, are shown in Fig. 5.21 by lines (for high and low frequencies separately).

The parameters of the approximation of the low-frequency (LF) and high-frequency (HF) parts of the spectrum of radio broadcasting stations are given in Table 5.6.

The values listed in Table 5.6 of the slopes of the spectra n_- and n_+ obtained as a result of the approximation of the low-frequency and high-frequency parts of the spectrum of radio broadcasting stations, regardless of the station's frequency and time of day, differ slightly and range from 1.6 to 2.3.

In the 8 Hz band, the power level at frequencies 8...50 Hz is approximately –40...–55 dB relative to the full power level of the information signal — at frequencies near 1 kHz it is about –30...–40 dB.

Experimental studies with the DEGEN receiver. Using the receiver, experimental studies of the signals of broadcast stations in the HF and VHF bands, which operate with ionospheric (over-the-horizon) and surface (within direct line of sight) waves at different frequencies and at different times of the day, were conducted. The list of stations and their technical characteristics are given in Table 3.5 of Appendix 3. Spectra of broadcasting stations in the HF band obtained with different recording formats are shown in Fig. 5.22, *a*, *b*, and spectra normalized to the full power of the information signal (5.22) at 8 Hz resolution (Fig. 5.22, *c*, *d*):

$$p\left(F, \Delta F = 8\,\text{Hz}\right) = \frac{\int_F^{F+\Delta F} S(F)\,dF}{\int_0^{F\max} S(F)\,dF}. \qquad (5.22)$$

It is worth noting that with the mp3 recording format, the spectrum is limited to frequencies up to approximately 1,500 Hz, because the frequency limitation of encoded spectral components. In the WAV format, the spectrum in the high-frequency region decays much more slowly.

Fig. 5.23 shows the spectra normalized to the full power of broadcast stations of different wavelength ranges at different times of the day.

Table 5.6. **Parameters of the approximation of radiation spectra of radio broadcasting stations**

No. of the spectrum in Fig. 5.21	LF part of the spectrum		HF part of the spectrum	
	a_- [dB]	n_-	a_+ [dB]	n_+
1, a	61.6	2.232	147.6	1.985
1, b	51.1	2.264	148.5	1.889
2, a	68.6	1.610	154.7	2.219
2, b	57.8	2.198	152.6	2.156
3, a	64.7	1.687	148.6	2.040
3, b	58.3	2.309	148.0	1.947

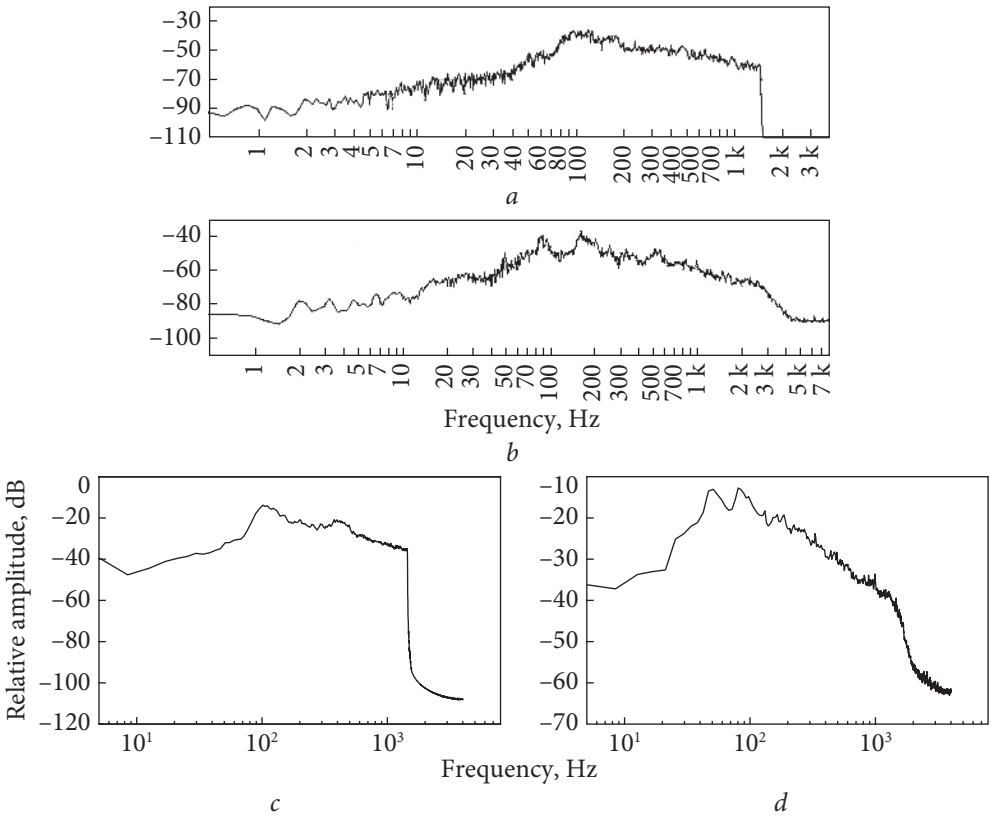

Fig. 5.22. Signal spectrum of Radio Taiwan International broadcasting station, frequency 7,385 kHz (*a*, *b*) and power distribution (*c*, *d*): *a* — mp3 recording format, *b* — WAV recording format

What they have in common is 20...30 dB lower values of spectral density at frequencies 6...60 Hz than at frequencies 100...200 Hz.

Relative to these frequencies, at frequencies of about 1,000 Hz, the level of spectral density decreases by approximately 15...20 dB.

The ratio can be used to approximate the spectrum:

$$S(F) = S_0 \left(\frac{1}{1 + \left(\left| F - F_0 \right| / \Delta F_{\pm} \right)^{n_{\pm}}} \right)^{-1}, \qquad \textbf{(5.23)}$$

where F_0, S_0 is the level and frequency of the maximum spectral density of the information signal, usually 80...160 Hz, $\Delta F_{\pm}$ is the half-width and the rate of decrease of $n_{\pm}$, the spectrum to the right of ΔF_+, n_+, and to the left of ΔF_-, n_- is the maximum frequency.

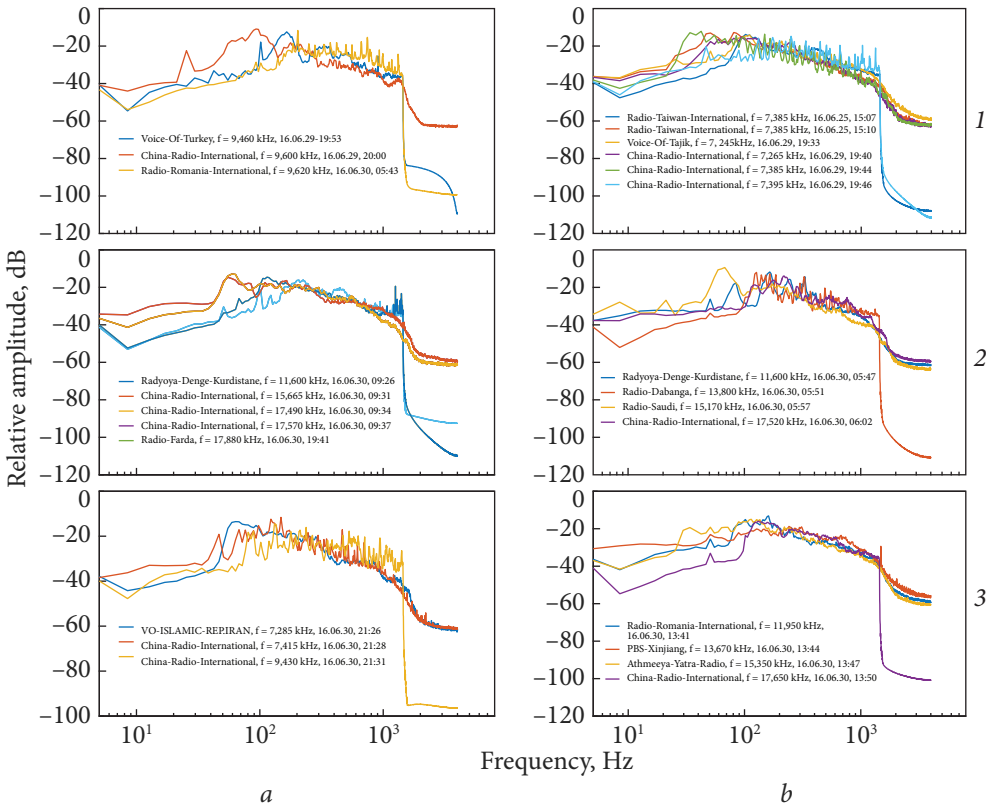

Fig. 5.23. Normalized spectrums of broadcast radio stations signals

Using relation (5.23) — it is possible to estimate the rate of decrease of the spectral density above and below the frequency of the maximum. As a rule, they have the value: $n_+ = 1.8...2.5$, and $n_- = 2.2...3$ so, in the first approximation, the same values can be used for approximation:

$$n \approx n_- \approx n_+ \approx 2. \tag{5.24}$$

The power level in the 8 Hz band at frequencies of 6...60 Hz is approximately 40...–55 dB relative to the full power level of the information signal. At frequencies of about 1,000 Hz, it is about –30...–40 dB. Changing the recording format affects not only the high-frequency but also the low-frequency components of the spectrum. Thus, with the mp3 recording format, the level of spectral density is approximately 10 dB lower than in the WAV format. With the mp3 recording format, the spectrum is limited at frequencies above 1.5 kHz, which leads to the fact that the level of spectral density at these frequencies is –90...–110 dB. While in the WAV format, it has a value of –55...–60 dB. For the given spectra, the frequency resolution was 8 Hz.

If the resolution differs from 8 Hz, then the obtained value of the spectral density must be recalculated using the ratio:

$$p\left(F, \Delta F = \delta F \,\text{Hz}\right) = p\left(F, \Delta F = 8\,\text{Hz}\right)\frac{\delta F\left[\text{Hz}\right]}{8}. \qquad (5.25)$$

Since with fairly narrow bands of Doppler filters, noise can be considered as white, narrowing the band from 8 to 1 Hz will lead to a decrease in the spectral density level by approximately 9...10 dB. It is advisable to use narrower bandwidths of Doppler filters to increase the potential of the detection and measurement system. This makes it possible to improve both speed resolution and reduce the level of interference in the useful signal detection band in proportion to the bandwidth.

The presence of a dip in the spectral density at frequencies of 6...60 Hz relative to the carrier radiation in the spectrum of broadcasting stations allows the detection of secondary fields created by the scattering of these signals from aerial objects.

5.3. Study of the density and distribution functions of amplitudes in different parts of the spectrum of radio broadcasting stations in the HF and VHF bands

The radiation of broadcast stations in the HF and VHF bands is used in active-passive radar systems to illuminate the environment [220—224]. When they are scattered from a moving object, they receive a Doppler shift, which makes it possible to select secondary signals scattered by objects against the background of interference created by the direct signal of a broadcasting station. The study of statistical characteristics of interference is necessary when evaluating the detection characteristics of active-passive radar and monitoring systems. Fig. 5.24 shows the implementation time of HF signals of broadcast stations from the amplitude output of the receiver with a duration of about 100 seconds for the modes of manual and automatic gain control (MGC, AGC).

It can be seen that in the absence of AGC (Fig. 5.24, *a*, *c*, *e*) at the output of the receiver, fading with a depth of 20...30 dB and a frequency of dozens of seconds is observed. The use of AGC (Fig. 5.24, *b*, *d*, *f*) significantly reduces the dynamic range of fluctuations, which has a positive effect on reception conditions but can lead to the appearance of negative effects associated with the limitation of large signals.

An increase in the signal level or the gain of the receiver leads to a decrease in the range of signal fluctuations and the appearance, even in the MGC mode, of effects characteristic of AGC — signal limitation — Fig. 5.24, *e*, *f*.

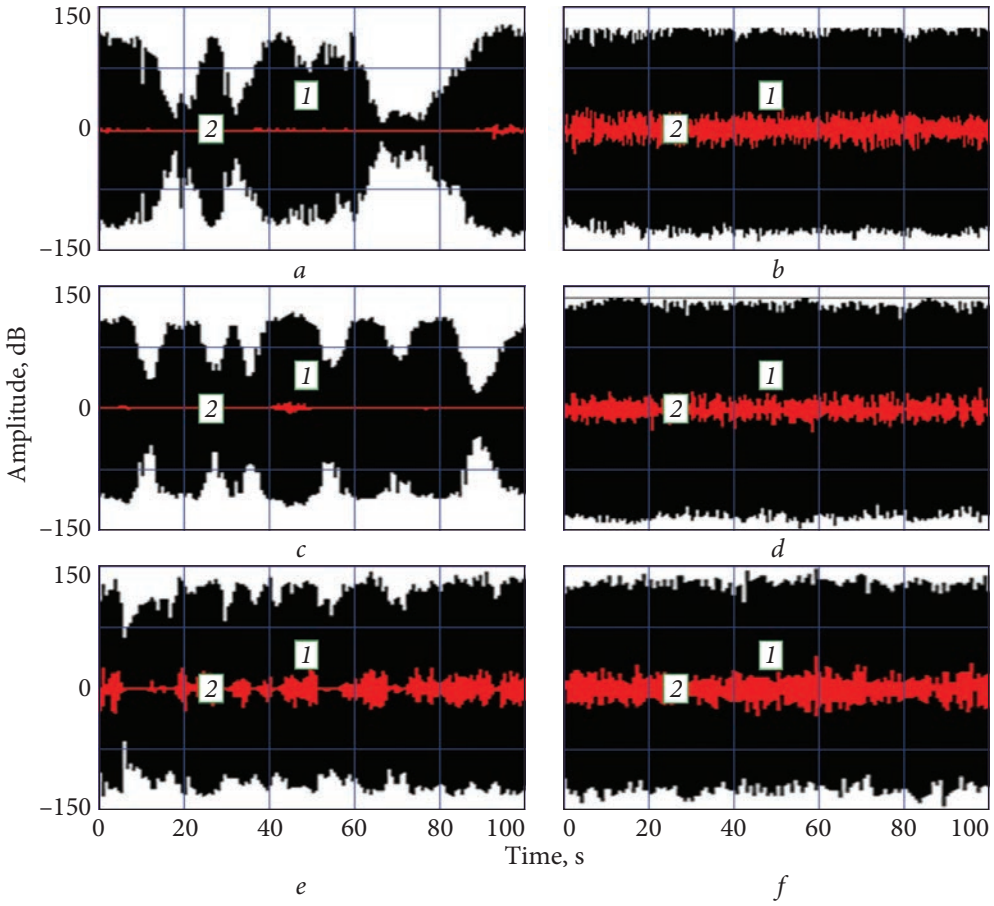

Fig. 5.24. Implementation time from the output of the amplitude detector of the signal of broadcasting stations of the illumination of the HF band: *1* — in the band 0...10 kHz, *2*— in the band 0...70 Hz; *a*, *b* — frequency 17,490 kHz, *c*, *d* — 12,160 kHz, *e*, *f* — 17,560 kHz; *a*, *c*, *e* — MGC mode, *b*, *d*, *f* — AGC mode

By filtering the useful signal in the Doppler frequency band, it is possible to significantly reduce the level of interference created by the broadcasting station's backlight signal. However, as can be seen from the comparison of Fig. 5.24 curves *1*, *2* filtering in the band 0...70 Hz leads to an increase in the range of signal fluctuations, which will lead to a change in its statistics.

In Fig. 5.25, on a scale that linearizes the normal distribution law, the distribution functions of the HF signals of the broadcast station range are presented, which act as interference for active-passive radar systems in the presence and absence of the receiver's AGC.

They are obtained at different frequencies for the low-frequency signal in the entire band from 0 to 10 kHz relative to the carrier and after filtering low-fre-

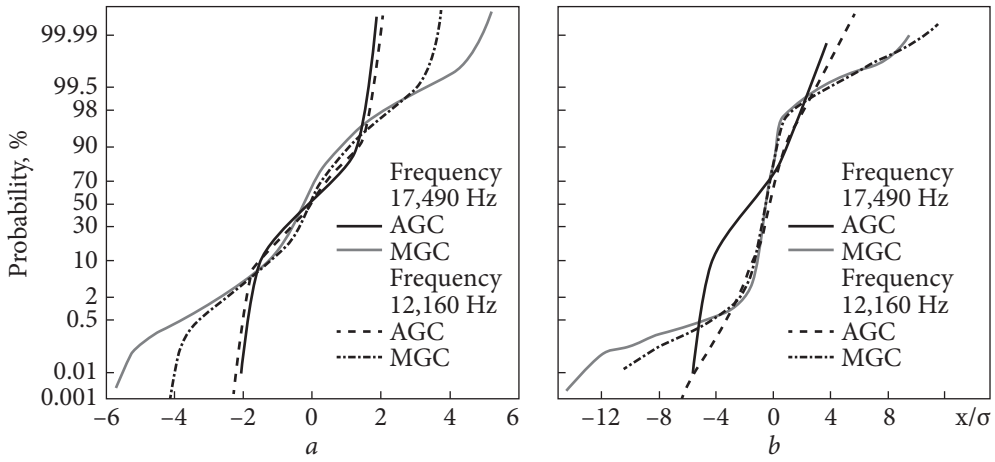

Fig. 5.25. Signal distribution functions at different frequencies in AGC and MGC modes in the entire band (*a*) and after filtering in the 0...70 Hz band (*b*)

quency components in the range of 0...70 Hz, which correspond to the Doppler frequencies of signals of aerial objects.

It can be seen that the distribution functions are characterized by non-Gaussianity, which is manifested in their deviation from linear dependence. The value normalized to the RMS value of the process is plotted along the abscissa axis. This makes it possible to eliminate both the daily variability of the power of the received signal and the influence of the reception frequency. The distribution functions at different frequencies (17,490 and 12,160 kHz), taken at different times of the day, are practically the same. The curves of the distribution functions at large values (modulo) are associated with the influence of the effect of limiting the signal by the receiver. This can also be seen on the histograms of the distribution — Fig. 5.26.

The limitation is manifested in the non-monotonic nature of the change in the distribution histogram. It should be noted that with AGC, in addition to reducing the dynamic range of signal fluctuations, there is a normalization of its statistics (Fig. 5.25, *a*). Filtering the signal in the LF region in the frequency band 0...70 Hz leads to an increase in the degree of non-Gaussianity of the signal received in the MGC mode. It manifests itself in a greater distortion of the distribution function constructed in the normalizing scale (Fig. 5.25, *b*). At the same time, the AGC mode leads to the receiver output signal normalization for the unfiltered signal (Fig. 5.25, *a*) and after filtering in the band 0...70 Hz (Fig. 5.25, *b*). In the first approximation, the signal received when using AGC can be considered as described by the normal distribution law. The results of the approximation of the distribution functions by the composite normal (poly-Gaussian) law (5.26) are shown in Table 5.7.

$$p(x) = \sum_{i=1}^{i=k} P_i p_i(x), \tag{5.26}$$

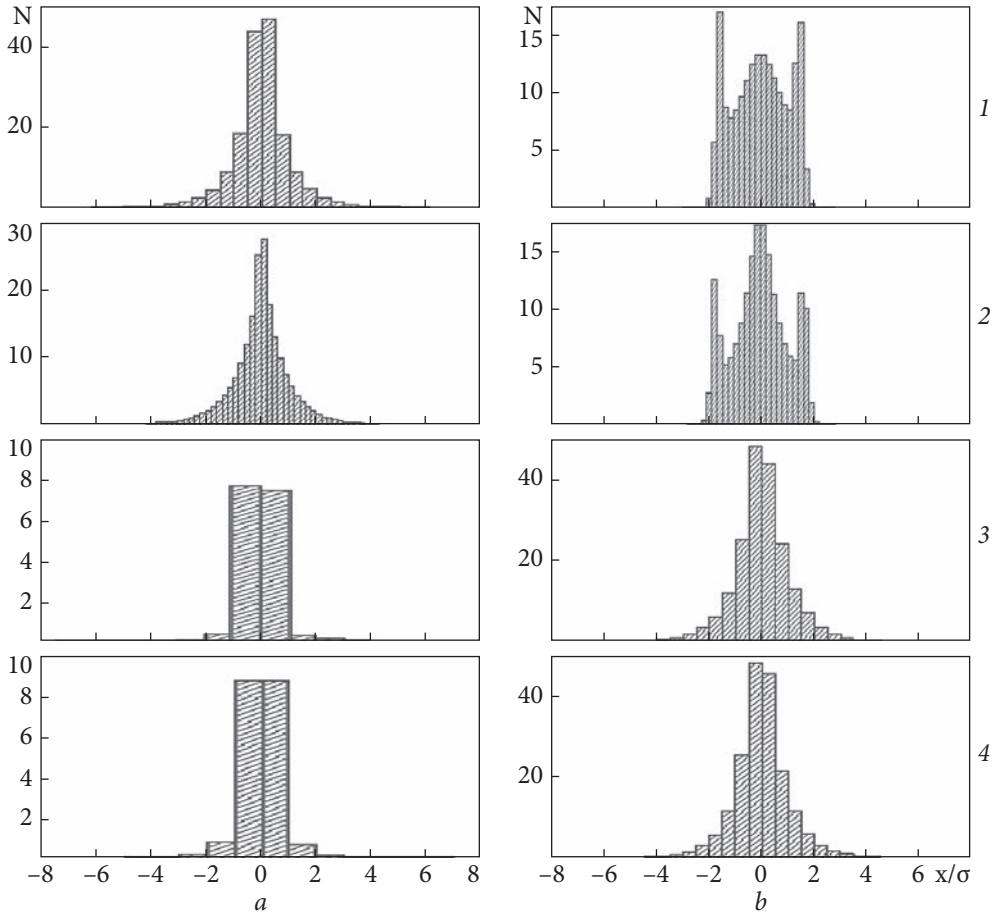

Fig. 5.26. Histograms of the distribution of values at the output of the receiver at different frequencies and at different times of the day: *a* — MGC; *b* — AGC; *1*, *2* — 10 kHz band; *3*, *4* — band 0...70 Hz; *1*, *3* — 17,490 kHz; *2*, *4* — 12,160 kHz

Table 5.7. **Approximation of backlight signal distribution functions by a complex normal distribution law**

Operating frequency, kHz	In the entire range of analysis				In the band 0...70 Hz			
	Non-Gaussianity parameter $\gamma = (\Sigma_2 / \sigma_1)$ 2, dB		Probability of spike, P %		Non-Gaussianity parameter $\gamma = (\Sigma 2 / \sigma_1)$ 2, dB		Probability of spike, P %	
	MGC	AGC	MGC	AGC	MGC	AGC	MGC	AGC
12,160	8.2	0	25	0	9.0	6.8	3.5	27
17,490	9.7	0	15	0	15.2	4.2	4	30
17,490	9.7	0	15	0	12.2	—	18.5	—
17,560	5.1	0	37	0	8.2	9.2	25	25

P_i, $p_i(x)$, $p(x)$ is the final probability and density of the distribution of the process in the i^{th} state, as well as the resulting density of its distribution.

At the same time, the distribution of the process in the phase state can be described as previously indicated by the normal distribution law:

$$p_i(x) = \frac{1}{\sqrt{2\pi}} \exp\left(-\frac{x^2}{2\sigma_i^2}\right). \quad (5.27)$$

σ_i^2 is the variance of the process in the i^{th} state, and the normalization condition applies to the final probabilities:

$$\sum_{i=1}^{k} P_i = 1, \quad (5.28)$$

where k is the total number of phase states of the process.

The parameters of the approximation of the distribution functions of the backlight signal of broadcasting stations in the AGC and MGC modes are given in Table 5.7, both in the entire frequency band and in the 0...70 Hz band, which corresponds to the Doppler shifts from the targets.

It can be seen that in the AGC mode, the interference of the illumination signal in the entire band at all frequencies of the decameter band, regardless of the time of day, is satisfactorily described by the Gaussian distribution function. At the same time, the non-Gaussianity of the distribution is characteristic of the MGC mode. The intensity ratio of the components (degree of non-Gaussianity) for the signal in the entire band has a value of 5...10 dB with a probability of the presence of the second component (spike) of 15...40%.

Filtering in the band of Doppler frequencies 0...70 Hz leads, as a rule, to the appearance of non-Gaussianity even in the AGC mode. The non-Gaussianity parameter has a value of 4...10 dB, increasing at MGC to 8...16 dB. At the same time, the emission probabilities, as a rule, decrease to 25...30% in the AGC mode and 3.5...25% in the MGC mode.

Since the description of the distribution function can be based on the Polygaussian distribution, the simulation model of the interference from the illumination signal can be built based on semi-Markov nested processes [288].

5.4. Non-stationary interferences for active-passive monitoring systems

In order to evaluate the performance characteristics of active-passive monitoring systems, it is necessary to develop models that allow simulation of real non-stationary interference-signal conditions. In papers [193, 274—277, 288], it is proposed to use nested semi-Markov processes for non-stationary non-Gaussian interferences created by scattering of radio waves from the surface of the sea [274, 288], land [193] and "clear sky" [275]. The proposed approach turned out to be

productive for the description of radar scattering from small above-the-water targets [288]. This section considers the possibility of using this approach to describe acoustic noises caused by wind, rain, tree leaves, footsteps of people and animals, gunshot sounds, and description of interference caused to active-passive systems by the radiation of broadcast stations in the HF band, both for the entire frequency band and in the Doppler frequency band.

Mathematical formulation of the model. The statistical description is similar to the model used to describe the scattering from land covered with vegetation and is based on the use of nested two-component random processes $\{\overrightarrow{S(t)}, \theta(t)\}$ in which one component $\overrightarrow{S(t)}$ is continuous, and the other $\theta(t) = \nu_i$ is discrete [193, 288, 300]. Here, t is a generalized coordinate, which is time. These components are dependent and, in the general case, are not Markovian [285]. This means that no restrictions are imposed on the distribution of the process existence times in each of the phase states. For each instant of time, in the general case, the process is in one of the K possible phase states $H_i \in \nu_1 \ldots \nu_K$. A special case is a system with two-phase states. Such a model can be used to describe the acoustic noise of wind, the noise of leaves under the influence of wind, as well as animal and human footsteps. It is assumed that the initial state $\theta_0 = \nu_i$ at the time $t = 0$ and the one-step transition probabilities π_{ij} are known, where $i, j = \overrightarrow{1...K}$. Let's assign to each non-zero element π_{ij} of the transition probability matrix a random variable T_{ij} with distribution density $f_{ij}(t)$, which we will call the waiting time in state ν_i before transition to state ν_j. If the values of T_{ij} are distributed according to the exponential law, then such a process will be Markovian. In practice, in many cases, this assumption is not fulfilled, in particular for scattering from the ground [193]. Then, the process in which the change of states is described by a Markov chain, and the density of the distribution of the existence times in each of them differs from the exponential one, belongs to the class of semi-Markov [285]. Within each of the ν_i states, we will consider the process to be quasi-stationary, which is described by its density distribution of $[P_i(S)]$ values and the spectrum $[S_i(\omega)]$. To describe the process inside the phase state, in some cases, standard models of Gaussian processes can be used. However, finite atomic functions can also be used [193, 278, 279].

For processes with a deterministic change in the phase states of the process, the one-step transition probabilities $(\pi) = ||\pi_{ij}||$, where $i, j = \overrightarrow{1...K}$ have the form: $\pi_{ij} = 1$ at $j = (i + 1)_{\text{mod } k}$ and $\pi_{ij} = 0$ in other cases. So, when the number of phase states is $k = 2$, then $(\pi) = ||\pi_{ij}|| = \begin{pmatrix} 0 & 1 \\ 1 & 0 \end{pmatrix}$.

This is typical for wind and related noises, as well as the sounds of human or animal footsteps, as well as interference created by the radiation of broadcast stations in the HF band, both for the entire frequency band and in the Doppler frequency band. In addition, a similar approach can be used to create simulation models of gunshot sounds.

5.4.1. Characteristics and model of non-stationary acoustic noises

Fig. 5.27 shows spectrograms of wind noise and sounds of human steps on snow. The noise of tree leaves in the wind and the sound of an automatic weapon shot have a similar appearance. It can be seen that these processes are characterized by the presence of two-phase states that differ significantly in their spectra and intensity. In one of them, the signal has a rather small value. It is characteristic, for example, of pauses in the interval between wind gusts — Fig. 5.27, *a*, *b*, curves *1*. Moreover, the strengthening of the wind leads to both an increase in noise intensity and the width of its spectrum (Fig. 5.27, *a*, *b*), and both during pauses (curves *1*) and during gusts (curves *2*). At the same time, in pauses, the spectrum of wind noise can, in the first approximation, be approximated by a uniform spectral density, so it can be considered "white noise".

Thus, with a weak wind of 3...5 mps, it can be assumed that during pauses, the spectrum width is approximately 1.5...2.5 kHz (Fig. 5.27, *a*), increasing to 5...7 kHz when the wind increases up to 5...8 mps (Fig. 5.27, *b*). During gusts, high wind speeds are characterized by a faster rate of decrease in spectral density with frequency. In Fig. 5.27 the spectra of each of the phase states of wind noise are shown in a double logarithmic scale.

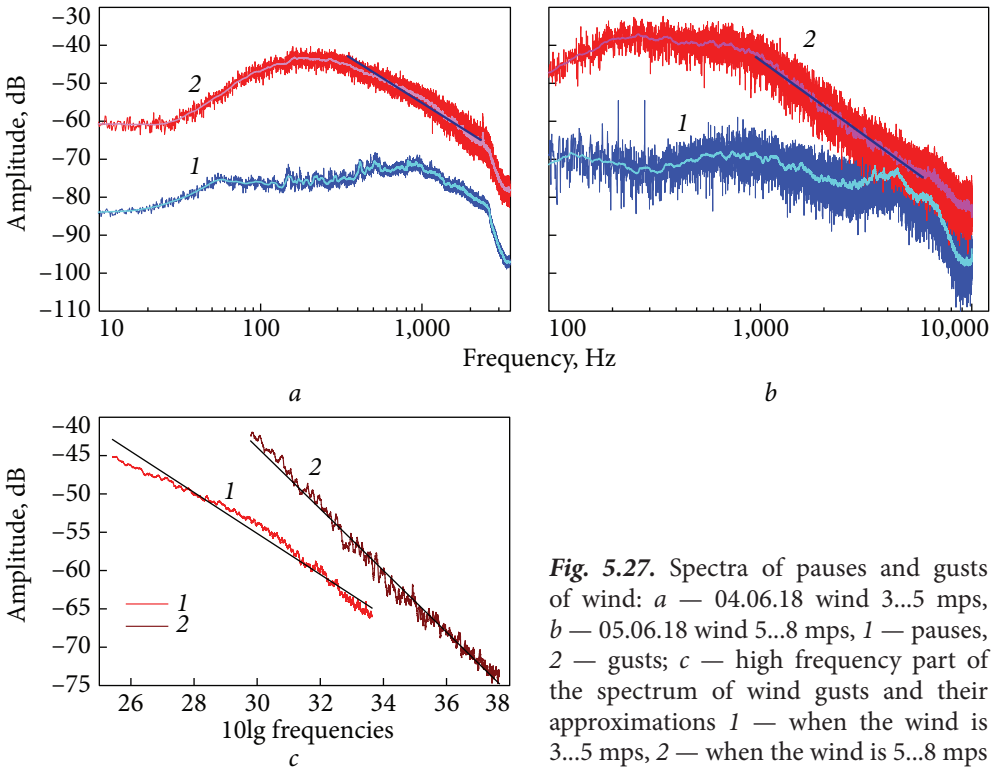

Fig. 5.27. Spectra of pauses and gusts of wind: *a* — 04.06.18 wind 3...5 mps, *b* — 05.06.18 wind 5...8 mps, *1* — pauses, *2* — gusts; *c* — high frequency part of the spectrum of wind gusts and their approximations *1* — when the wind is 3...5 mps, *2* — when the wind is 5...8 mps

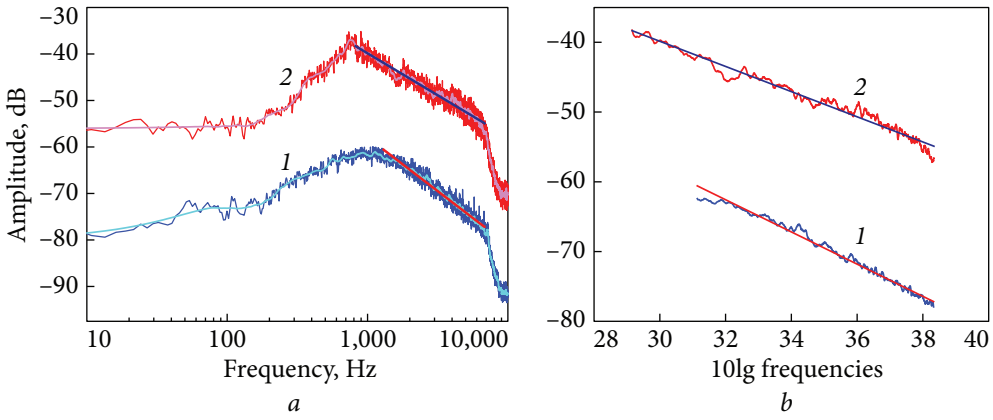

Fig. 5.28. Spectra of a person's steps on snow (*a*), their high-frequency section and approximations (*b*): *1* — pauses, *2* — bursts

It can be seen that with bursts, the spectra of the processes have a greater rate of decrease in spectral density with frequency. Since linear sections can be distinguished in the spectra, especially of wind gusts, the dependence can be used to describe their shape:

$$S_i(F) = S_0 \left(\frac{1}{\left(1 + \left(\frac{|F - F_{0i}|}{\Delta F_i} \right)^{n_i} \right)} \right)^{-1}, \qquad (5.29)$$

where F_0, ΔF_i, n_i are the central shift, half-width, and decay rate of the spectrum for i^{th} phase state, 1 — bursts, 0 — pauses.

Fig. 5.27 shows the high-frequency sections of wind gust spectra and their approximation (5.29). It should be noted that these parameters may differ for the high-frequency and low-frequency branches of the spectrum. The processes associated with it have the same features (noise of tree leaves, noise of rain). Analogous processes that occur during the movement of people and animals in the moments between placing the limbs on the ground. The other phase has a significantly greater intensity. The width of the spectrum and the speed of its reduction can be higher than during pauses.

Fig. 5.28 shows the spectra of different phase states of a person's steps on a snow bank, high-frequency areas — Fig. 5.28, *b* and their approximations by dependences (5.29). It can be seen that, in this case, the slope of the spectra during pauses and bursts is approximately the same.

The values of the exponent n obtained as a result of the approximation (5.29) of the high-frequency sections of the spectrum of different phase states for wind noise and human steps are listed in Table 5.8.

In contrast to wind noises, in which the pauses were characteristic, in the first approximation, the white noise model (i.e., $n_0 = 0$) for the steps on the crust, the burst spectra have a lower power index than the pauses. Equipment noise is added to the useful signal during the registration process, which can distort the appearance of their spectral density. The resulting spectrum, normalized to the spectral density of internal noise, will look like this:

$$s_i(F) = \mu^{-1} + \left(\frac{1}{\left(1 + \left(\frac{|F - F_0|}{\Delta F_i} \right)^{n_i} \right)} \right)^{-1}, \tag{5.30}$$

where μ is the signal (external noise)/noise (equipment) ratio during registration.

It can be seen that at large SNR, the ratio (5.30) gives results close to (5.29). At small SNR, it is necessary to consider the related spectrum description errors.

An example of how internal noise affects the spectra of recorded acoustic signals is shown in Fig. 5.29. Fig. 5.29, *a* shows the approximations of the spectra at the rate of decrease of the spectral density, which is determined by the exponent $n = 2$, and in Fig. 5.29, *b* by $n = 4$. It can be seen that a decrease in the SNR leads to a decrease in the rate of decrease of the spectral density on the wings of the spectrum and a limitation of the level of the minimum values of the spectral density.

For approximation by the piecewise-broken dependence of the spectra in a double logarithmic scale, the rate of decrease of the spectral density can be estimated using the relation directly derived from (5.29):

$$n = \frac{s(F_2)[\text{dB}] - s(F_1)[\text{dB}]}{10\left(\lg(F_2 - F_0) - \lg(F - F_{01})\right)}, \tag{5.31}$$

where F_2 and F_1 are the frequencies taken on the slope of the spectrum and $s(F_2)$ [dB] and $s(F_1)$ [dB] are the spectral density levels corresponding to them.

From Fig. 5.29 it can be seen that the exponent has a significant effect on the rate of decrease of the spectral density.

Table 5.8. **Characteristics of the spectra of bursts and pauses**

Process	Pauses				Bursts			
	F_{00}, Hz	S_0, dB	ΔF_0, Hz	n_0	F_{01}, Hz	S_0, dB	$2\Delta F_1$, Hz	n_1
Wind 3...5 mps	—	–72	—	0	200	–42	200	2.6
Wind 5...8 mps	—	–62	—	0	400	–27	800	4.0
Steps by crust				2.3				1.8

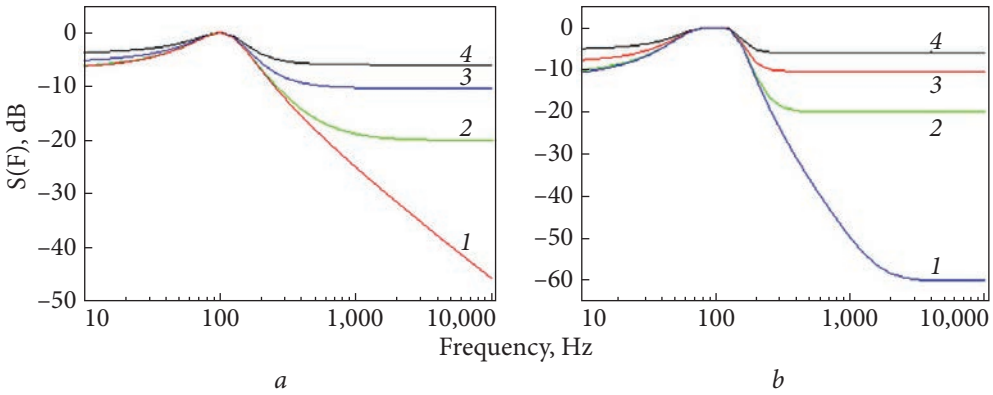

Fig. 5.29. Spectra of approximations at different SNR of acoustic noises: F_0 = 100 Hz, ΔF = = 50 Hz, *1* — μ = 60 dB, *2* — μ = 20 dB, *3* — μ = 10 dB, *4* — μ = 5 dB , *a* — *n* = 2, *b* — *n* = 4

The considered noise examples are characterized by the presence of several different spectral compositions and intensity of phase states. Thus, when describing wind noise and related processes, for example, the noise of tree leaves, it is enough to use two-phase states: bursts associated with wind gusts and pauses.

Since the sound level of the microphone is related to the acoustic pressure, which in turn is determined by the quadratic dependence on the wind speed, the acoustic signal will be characterized by the same regularities as the pulsations of the wind speed in the troposphere. Thus, the Kolmogorov-Obukhov model is the generally accepted model for describing the spectrum of atmospheric pulsations.

Consideration of wind speed pulsations in the part of mutual conditioning of inhomogeneities lying in the same spatial range with inhomogeneities of a larger and smaller spatial scale allows us to distinguish several main intervals [301] — Fig. 3.5 in Appendix 3.

In the surface layer of the atmosphere at a height of 8 m due to deformations of large-scale inhomogeneities, the frequency dependence of the spectral energy density $S(f) \sim f^{-3}$ is not manifested. In fact, the shape of this spectrum can be approximated by the dependence $S(f) \sim f^{-5/3}$ — in a wide range of scales: from $2.3 \cdot 10^{-6}$ Hz (120 hours) to $3.1 \cdot 10^{-5}$ Hz (9 hours). Using the hypothesis of "frozen" turbulence, with an average wind speed of V = 1.9 mps, the spatial scales of this range lie between 830 and 60 km, respectively. In the high-frequency part, the spectral density of the specific energy of speed pulsations decreases proportionally to the frequency in the degree of "–2/3". The increase in specific spectral energy in this range is associated with the processes of crushing large-scale inhomogeneities and convection processes. At heights of 121, 125 m, the dependence $S(f) \sim f^{-3}$ begins to manifest itself in the frequency range from $5.5 \cdot 10^{-6}$ Hz (50 hours) to $8.3 \cdot 10^{-6}$ Hz (33 hours), which corresponds to the spatial scales at the average wind speed V = 5.9 mps from 1,050 to 700 km. In the high-frequency range, the shape of the spectrum deviates from $-f^{-5/3}$, also in

the direction of increasing the energy of pulsations. This suggests that the convective component is weaker at this wind speed (V = 5.9 mps) compared to the level of 8 m, where V = 1.9 mps (Fig. 3.5 in Appendix 3). At an altitude of 301 m, the dependence $S(f) \sim f^{-3}$ covers the same frequency range (up to 1,500 km at V = 8.5 mps). In the high-frequency part, the spectrum in a wide range of scales is described by the dependence $S(f) \sim f^{-5/3}$. This suggests that the inflow of energy due to convection at these scales is significantly smaller than at lower levels. Thus, on the basis of studies of the shape of the spectrum in [301], the following conclusions were drawn: with an average flow velocity V > 8 mps, the shape of the spectrum in the range from 2 h to 7 days remains unchanged and can be approximated by a static dependence close to $S(f) \sim f^{-5/3}$; at an average wind speed of about 2 mps at heights above 8 m in the range from 9 h to 7 days, the shape of the spectrum can also be approximated by the static dependence $S(f) \sim f^{-5/3}$.

Comparing with the results obtained by us — Fig. 5.27 shows that the spectrum of acoustic wind noise during bursts has a slightly greater slope. This is probably due to the quadratic dependence of the noise level on the wind speed. At the same time, for steps along the snow cover during bursts, the rate of decrease of the spectral density during bursts is close to the 5/3 law. Spectrograms can provide additional information about wind noise and human and animal footsteps — Fig. 3.6 in Appendix 3, which allows us to estimate the dynamics of changes in the spectral composition of these non-stationary processes over time.

In the same figure, the spectrograms of the shots of the automatic cannon are given in Fig. 3.6 in Appendix 3 (3), and the machine gun in Fig. 3.6 in Appendix 3 (4). As with the sound of steps, shots from automatic weapons, in contrast to wind noise, are characterized by greater determinism in the change of phase states. In addition, it should be noted that in the case when there are no defects in the course of a person or in the weapon system when repeating individual cycles, their spectral characteristics and the times of existence of the process in these phase states are similar. The situation is significantly different when there are defects in a person's gait, for example, associated with lameness — Fig. 5.30. It can be seen that gait defects are revealed both in time realizations of the signal (*1*, *3*) by asymmetry of signals corresponding to different steps, manifested by differences in levels and duration, and are also indicated by asymmetry of spectrograms (*2*, *4*). This can be used to identify gait defects in humans or animals. Analysis of spectrograms in Fig. 5.30 (*2*, *4*) shows that they are a significantly non-stationary process, the spectral composition of which undergoes significant changes in time.

Spectrograms of the sound of shots from automatic weapons have a similar appearance in Fig. 3.6 of Appendix 3 — guns (*3*) and machine guns (*4*).

As an example, Fig. 5.31, *a* shows the time realization of the sound of a shot, and Fig. 5.31, *b* shows its spectrum in different time intervals. Several phases of the shot can be distinguished. Phase *1* is characterized by a sharp almost instantaneous, increase in sound power.

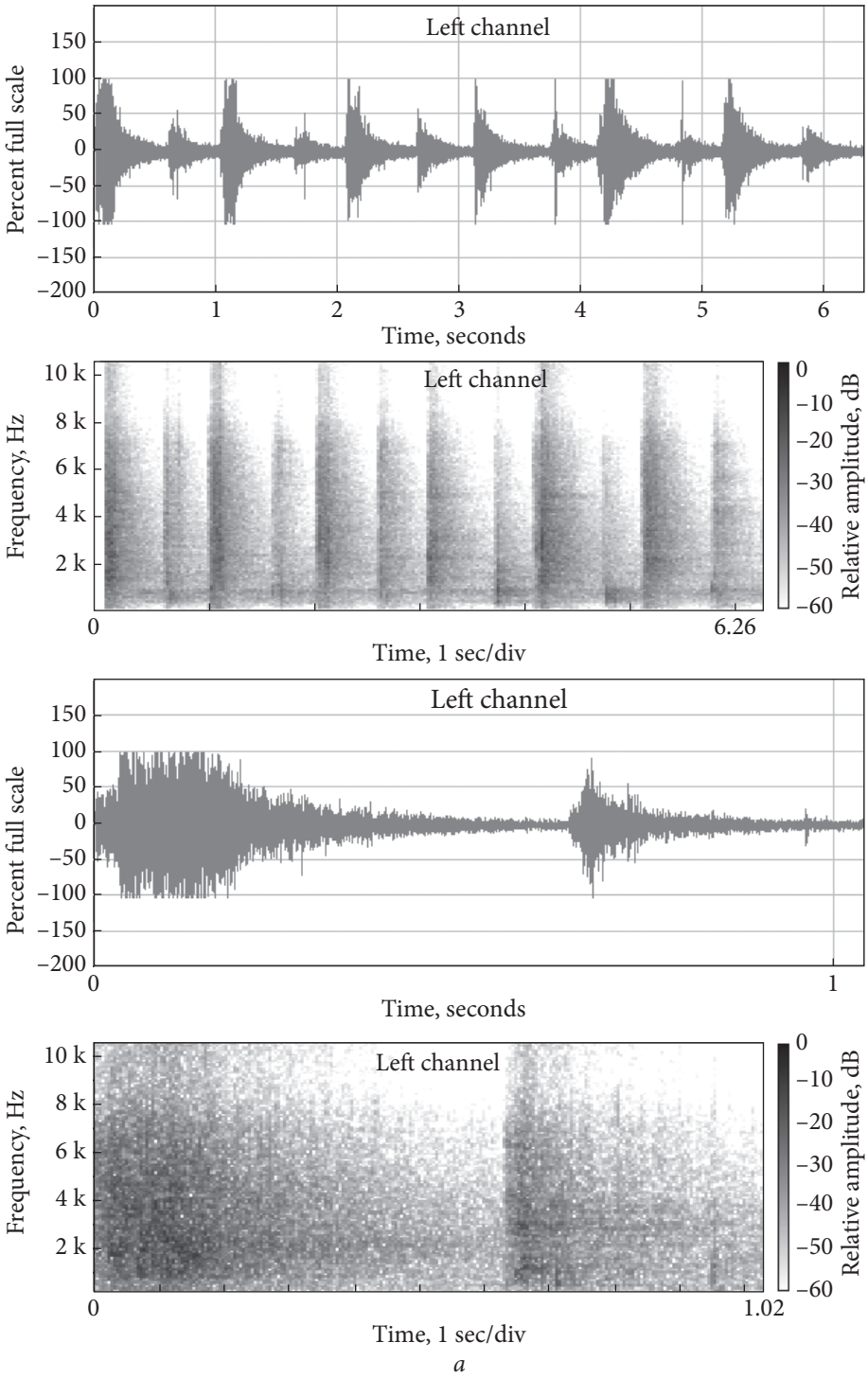

a

Fig. 5.30. Time realizations (*1*, *3*) and spectrograms (*2*, *4*) of steps: without gait defect (*b)*, with gait defects (limp) (*a).* See also p. 166

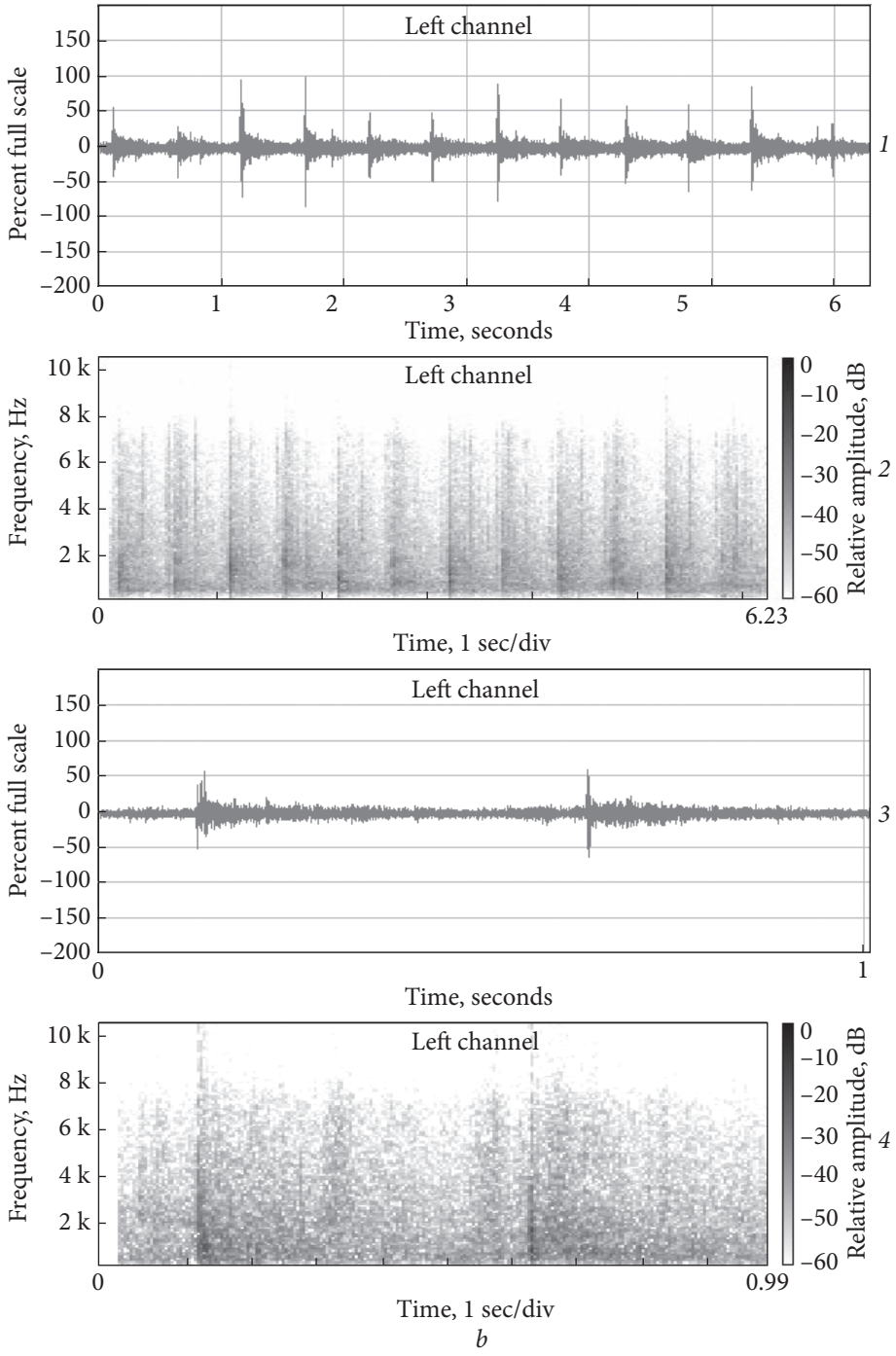

b

End of Fig. 5.30

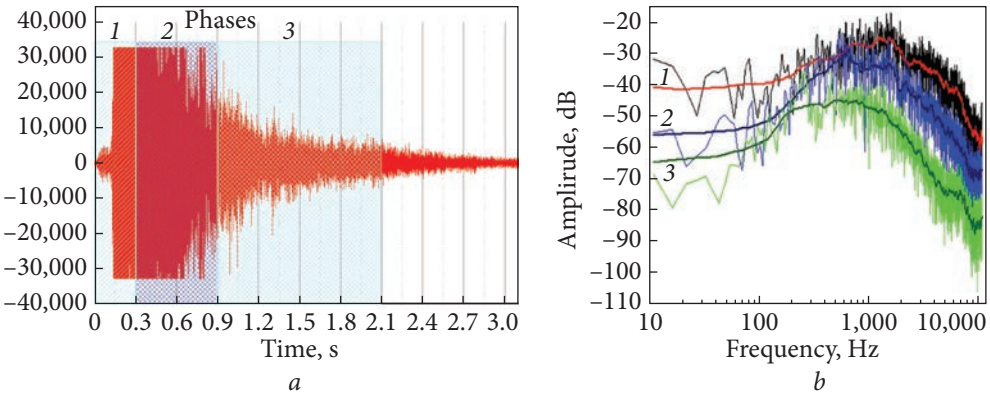

Fig. 5.31. Time realization of the sound of a gunshot (*a*) and its spectra (*b*) in different time sections: *1* phase — up to 0.3 s, *2* phase — up to 0.9 s, *3* phase — up to 2.1 s

In Fig. 5.31, it is observed in the time interval from 0.12 s up to 0.7 s, i.e. approximately 0.5 s. At this time, the recording equipment is overloaded. Then, during the second phase, at an interval of 0.7...3 s, there is an exponential decrease in sound power:

$$I(t) = I_0 \exp\left(-\frac{t}{T_0}\right), \tag{5.31a}$$

where $I(t)$, I_0 is the dependence of the average sound intensity on time and its value at the initial moment.

The intensity i of the sound will be described by time variables exponentially, the amplitude by the Rayleigh distribution density, and the instantaneous values by the normal distribution law:

$$p(i) = \frac{1}{I(t)} \exp -\frac{i}{I(t)}, \quad p(A) = \frac{A}{\sigma_A^2(t)} \exp -\frac{A^2}{2\sigma_A^2(t)},$$
$$p(S) = \frac{1}{\sqrt{2\pi}} \exp\left(\frac{S^2}{2\sigma^2(t)}\right). \tag{5.31b}$$

Moreover, the intensity $I(t)$ and dispersion $\sigma_A^2(t)$ of the process are related by known ratios:

$$I(t) = \sigma_A^2(t). \tag{5.32}$$

Fig. 5.32 shows the same spectra and approximations of their slopes by dependences (5.32). Their satisfactory correspondence can be seen. The numerical characteristics of the spectra in different time intervals are given in Table 5.9.

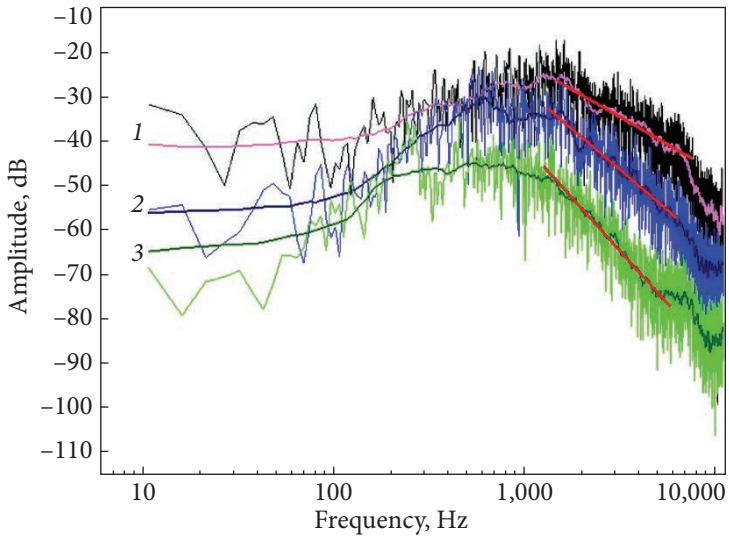

Fig. 5.32. Shot spectra at different phases and their approximation by dependencies (1): *1* — phase; *2* — phase; *3* phase

Table 5.9. **Numerical characteristics of shot spectra in different time intervals**

Phase No.	Central displacement, F_0, Hz	Half width of the spectrum ΔF, Hz	Exponent, n	Time since start, t C
1	1,286	584	–1.4	0.3
2	1,022	624.5	–2.4	0.9
3	586	457.5	–3.4	2.1

It can be seen that at the initial moment of the shot, the degree of the spectrum is close to that observed in the spectrum of a fully turbulent atmosphere $n \approx 5/3$.

As the sound power decreases, the central displacement of the spectrum decreases, its width increases and the exponent increases to approximately $n \approx 4$.

For the simulated wind model, it is enough to use two-phase states: burst (spike) and pause. The first for gusts of wind, the second for their absence. The same can be done when creating a leaf noise model under the influence of wind.

For disturbances created by the movement of people or animals, for example, on a snow surface or grass, it is also sufficient in many cases to use two-phase states.

At the same time, the density of the step duration distribution can be described, to a first approximation, by a Gaussian model

$$p(T) = \frac{1}{\sqrt{2\pi}\sigma_T} \exp\left(\frac{(T - T_1)^2}{\sigma_T^2} \right), \tag{5.33}$$

where T_1, σ_T are the average and root mean square values of the walking period.

However, if a person or animal has gait defects, they will be manifested in the divergence of distribution laws and spectra when walking with different limbs. At the same time, to describe these features, it is necessary to use a larger number of phase states. This means that for a person, having established the differences in the laws of the distribution of the duration of steps of the left and right limbs (the difference in the average duration of a step), it is possible to identify individual characteristics inherent to this person.

Similarly, for the shots of automatic weapons. In many cases, it is sufficient for modeling to use two-phase states — a shot and the interval between them. At the same time, the coefficient of variation

$$K_{\text{var}} = \frac{\sigma_T}{T}, \tag{5.34}$$

which is determined by the ratio of the RMS to the average period, will characterize the wear of the weapon and can serve as an informative feature for diagnosing its condition. If the cyclogram of the automatic system contains more than two phase states, for example, automatic six-barreled guns will have 12 phase states during the period of the cyclogram, then the same number of phase states must be used in the simulation model of this process. At the same time, it is necessary to study the characteristics of each of them (phase states), and the spread of their duration will indicate the degree of wear of weapons and design defects. The distribution of the shot duration and its spectrum is also an informative characteristic of the system. This phase also should not have large values of the coefficient of variation. Spectral characteristics of shots and weapon systems during normal operation should not differ much.

The proposed approaches can be used to create acoustic systems for diagnosing the technical condition of various systems, as well as to assess the degree of perfection of its design.

The laws of distribution of instantaneous values of acoustic noise in each of the phase states can, in the first approximation, be described by the normal law of distribution.

5.4.2. Characteristics and model of non-stationary interference of broadcasting stations in the HF and VHF bands

The presence of two phases of different intensities, which are physically determined by the discrete character of the modulating signals: speech sounds and music. The distribution functions were built after normalizing the values by the mean square value to obtain an opportunity to compare the behavior of the signal at different frequencies and at different times of the day. It can be seen that the distribution functions taken at different times and at different frequencies after

normalization have approximately the same behavior (Fig. 5.25, *a*). Differences appear on the "tails" of the distribution functions, at values of $\left|\frac{X}{\sigma}\right| \geq 3.5$, when the effects of signal limitation by the receiving device begin to show. The use of AGC leads to a decrease in the dynamic range of fluctuations of the illumination signal, which can be seen in the histograms — Fig. 5.33 and Fig. 5.34, and integral distribution functions (Fig. 5.35). It can be seen that with AGC, the limitations begin to appear already at $\left|\frac{X}{\sigma}\right| \geq 1.5$. The use of AGC allows you to normalize the statistics of a signal that acts as an interference. It can be seen that after filtering in the Doppler frequency band, the non-Gaussianity of the illumination signal statistics increases significantly when the overall interference level in the analysis band decreases. The interference suppression coefficients K_p during filtering in this band are given in Table 5.10.

$$K_p = \frac{P_0}{P_1},$$

where P_0, P_1 is the power of the interference signal (illumination) at the input and output of the suppression device. Measurements were oerformed in two modes: telephone and telegraphic. In the telephone mode, a standard reception was performed using the amplitude detection mode. At the same time, the power of the information signal in the entire band 0...6,000 Hz acted as a full signal. The power of the carrier, which was in the region of zero frequencies, was not taken into account, which gives underestimated values of the suppression coefficient. In the telegraph mode, the carrier was shifted by 70...100 Hz with the help of a local oscillator. This made it possible to estimate the full power of the output signal, taking into account the carrier and, accordingly, to eliminate errors in the obtained suppression coefficients of the backlight signal when filtering in the Doppler frequency band 0...70 Hz.

Table 5.10. **Coefficients of interference suppression from the backlight signal when filtering in the Doppler frequency band — 0...70 Hz**

Frequency, kHz	Regime	Suppression coefficient, dB	
		MGC	AGC
17,490	Phone	29.8	20.2
12,160	Phone	34.8	24.8
17,560	Phone	30.2	20.6
17,560	Telegraph	29.8	20.2

It can be seen that in the receiver with AGC, the interference suppression factor of the illumination signal in telephone mode in the Doppler frequency band is 20...25 dB, while without AGC — approximately 30...35 dB. The addition of gain in MGC leads to the appearance of a limiting effect, as in AGC, and reduces the suppression factor to about 20 dB. This means that the interference level in the Doppler frequency band is 20...35 dB lower than the interference in the entire analysis band. The dispersion

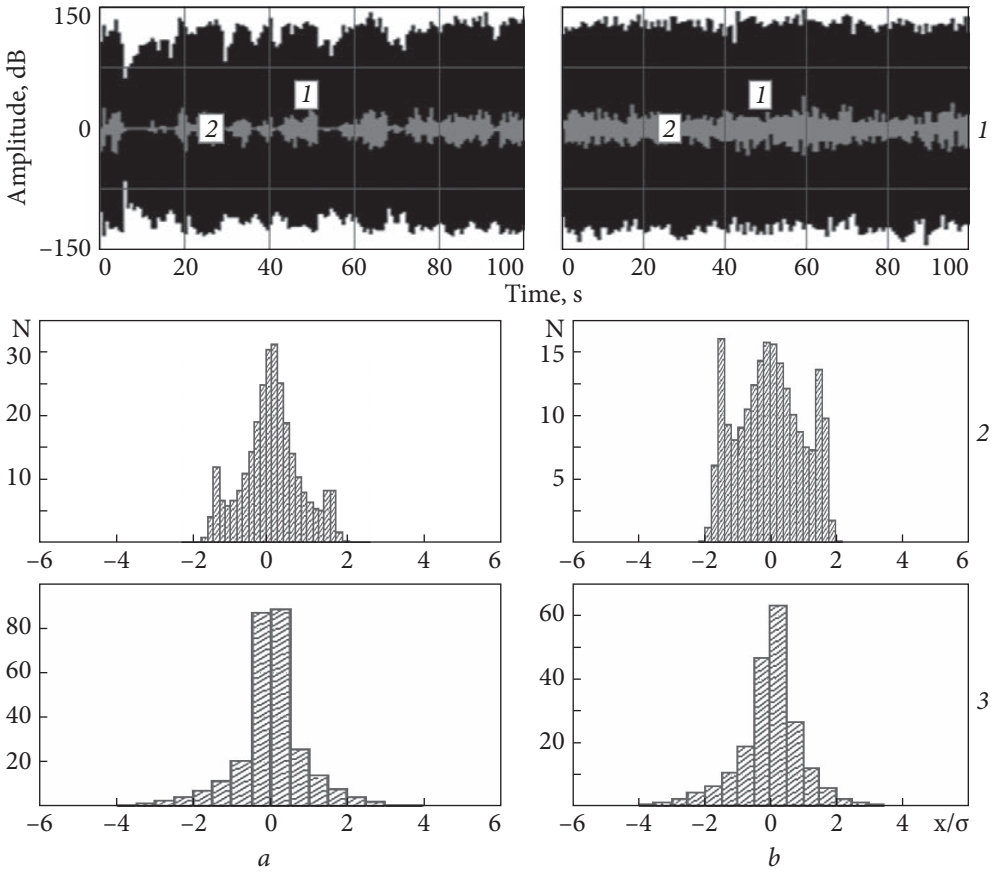

Fig. 5.33. Illumination signal (*1*) of a broadcasting HF station with a frequency of 17560 kHz in telephone mode and the density of its distribution (*2*, *3*) with manual MGC (*a*) and automatic AGC (*b*) gain adjustment in the entire frequency band (*2*) and after filtering in band 0...70 Hz (*3*)

ratio of the components, which characterizes the degree of non-Gaussianity of the output illumination signal in the MGC mode, is about 4...10 dB, increasing to 8...16 dB after filtering in the Doppler frequency band. When non-Gaussianity is detected, it causes the appearance of additional losses in the SNR, which for the given values of the non-Gaussianity parameter can be up to 10 dB [265]. When the signal level increases, the effects of the restriction, as already indicated, begin to manifest themselves earlier. Fig. 5.33 and Fig. 5.34 show the output records and signal distribution densities of the 17,560 kHz illumination station.

Signals were recorded in the MGC and AGC modes, in the entire frequency band, and after filtering in the 70 Hz band.

In the telephone mode, only the fluctuation (informational component) Fig. 5.33, while when the receiver is operating in telegraph mode, and the

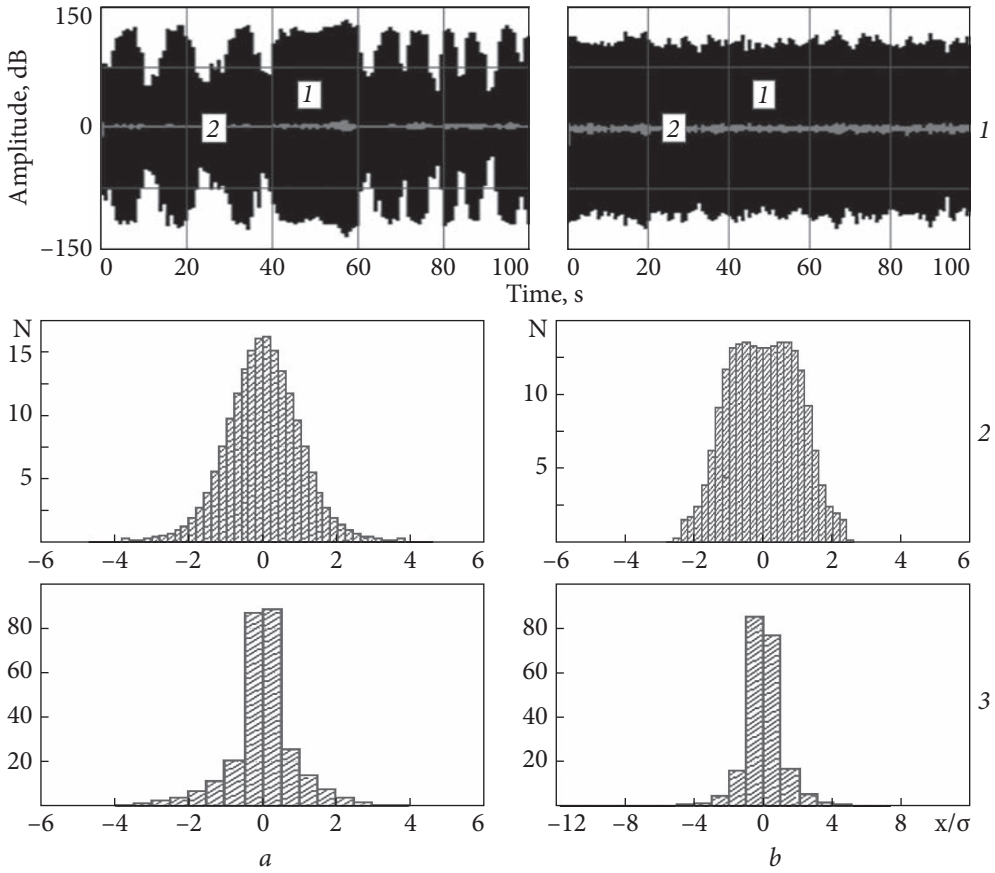

Fig. 5.34. Illumination signal (*1*) of a broadcast HF station with a frequency of 17,560 kHz in the telegraph mode and the density of its distribution (*2, 3*) with manual MGC (*a*) and automatic AGC (*b*) gain adjustment in the entire frequency band (*2*) and after filtering in band 0...70 Hz (*3*)

frequency of the third local oscillator is shifted by 100 Hz relative to the carrier, the carrier of Fig. 5.34.

Fig. 5.35 and Fig. 5.36 show the integral distribution functions and spectra of the HF signals of the broadcasting station for telephone and telegraph modes of operation on a scale that linearizes the normal distribution law, which acts as interference for active-passive radar systems in the presence and absence of an AGC mode in the receiver.

The distribution functions are obtained for the low-frequency signal in the entire band from 0 to 10 kHz relative to the carrier and after filtering low-frequency components in the range of 0...70 Hz, which correspond to the Doppler frequencies of signals of aerial objects.

It can be seen that the distribution functions in this case are also characterized by non-Gaussianity, which is manifested in their deviation from linear

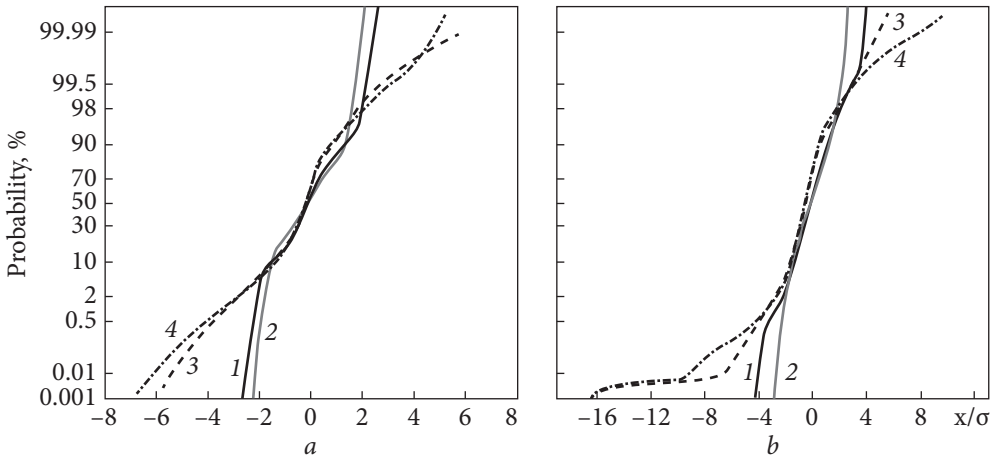

Fig. 5.35. Distribution functions of the HF station illumination signal (17,650 KHz) in the telephone (*a*) and telegraph (*b*) modes, the ARP time constant is 0.05 sec: *1* — PRP AD, *2* — ARP 0,05 s AD after filtering in the 0—70 Hz band, *3* — ARP 0,05 s AD, *4* — PRP AD

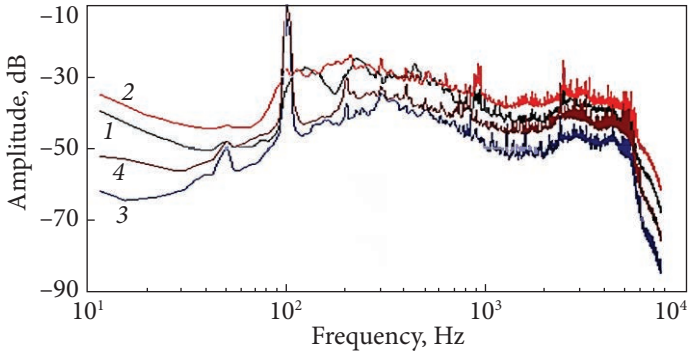

Fig. 5.36. Signal spectra in telephone (*1*, *2*) and telegraph (*3*, *4*) modes when using manual (*1*, *3*) and automatic (*2*, *4*) gain control, where *1* — PRP AD, *2* — ARP AD, *3* — PRP FD, *4* — ARP FD

dependence when plotted on normal paper. The value normalized to the root mean square value of the process is plotted along the abscissa axis. This allows you to eliminate the daily variability of the signal distribution. Distribution functions, taken at different times of the day, practically do not differ. Decays of the distribution functions at values that are large in modulus are associated with the influence of the signal limitation effect by the receiver. It should be noted that with AGC, in addition to reducing the dynamic range of signal fluctuations, there is a normalization of its statistics (Fig. 5.35 — curves *1*, *2*). Filtering of the signal in the LF region in the frequency band 0...70 Hz leads to an increase in the degree of non-Gaussianity adopted in the MGC mode of the signal in Fig. 5.35 (curves *3*, *4*), which is manifested in a greater distortion of the distribution function constructed in the normalizing scale (Fig. 5.35, *b*). At the same time, in the

AGC mode, both for the initial signal (Fig. 5.35, *a*) and after filtering in the 0...70 Hz band (Fig. 5.35, *b*), its normalization occurs. In the first approximation, the received signal, when using AGC, can be considered as described by the normal distribution law. Fig. 5.36 shows interference spectra in different modes of operation of the receiver.

The appearance of the carrier when using the telegraph mode is visible when the carrier signal was shifted to a frequency of 100 Hz using a local oscillator, and the signal spectra were analyzed in the telephone and telegraph modes for the illumination station with a frequency of 17,560 kHz. When using manual and automatic gain control, the spectra have a similar character. The level of the carrier, as can be seen, exceeds the spectral density of information frequencies by approximately 20...30 dB. At the same time, frequencies shifted relative to the carrier by approximately 40 Hz, that is, lying in the Doppler frequency band, have a level 35...45 dB lower.

5.4.3. Experimental study of interference levels for bistatic radars

When used as an illuminating signal of broadcasting stations in the HF wavelength band, the signal $\dot{S}_T(t)$ scattered by the object has a structure similar to the structure of the illuminating signal $\dot{S}_{Tr}(t)$. The Doppler shift of the frequency ω_D of the signal scattered from the object is determined by the rate of change of the sum of the distances from the transmitter to the target and from the target to the receiver:

$$\omega_D = \frac{2\pi}{\lambda_0}\frac{\partial\left(R_{TrT} + R_{TR}\right)}{\partial t} \le \frac{2\pi}{\lambda_0} 2V_0, \tag{5.35}$$

where $\vec{R}_{TrT}(\theta_{TrT})$ is the distance between the transmitter of the illumination station and the object; $\vec{R}_{TR}(\theta_{TR})$ is the distance between the object and the receiving antenna; $\lambda_0 = \frac{2\pi c}{\omega_0}$ is the length of the carrier; V_0 — flight speed.

The speed of distance change is determined by the projection of the velocity vector onto the direction of propagation of the electromagnetic wave (the direction between the transmitter of the illumination station and the object — $\vec{R}_{TrT}(\theta_{TrT})$, as well as the direction between the object and the receiving system — $\vec{R}_{TR}(\theta_{TR})$). At the same time, θ_{TrT}, θ_{TR} are the angles characterizing the direction of the object from the illumination station and from the object to the receiver, and θ_T is the heading angle of the object.

Taking into account that:

$$\frac{\partial R_{TrT}}{\partial t} = \frac{\left(\vec{V}(\theta_T)\vec{R}_{TrT}\right)}{\left|\vec{R}_{TrT}\right|} = V_0 \cos\left(\theta_{TrT} - \theta_T\right),$$

$$\frac{\partial R_{TR}}{\partial t} = \frac{\left(\vec{V}(\theta_T)\vec{R}_{TR}\right)}{\left|\vec{R}_{TR}\right|} = V_0 \cos\left(\theta_{TR} - \theta_T\right)\cdot \tag{5.36}$$

Relations (5.35, 5.36) allow us to write the equation that describes the behavior of the Doppler velocity $V_D = \lambda_0 \omega_D / 2\pi$ and therefore, the Doppler frequency shift:

$$\frac{V_D}{V_0} = \cos\left(\theta_{TrT} - \theta_T\right) + \cos\left(\theta_{TR} - \theta_T\right). \tag{5.37}$$

If the range to the illumination station R_0 significantly exceeds the range to the target: $R_0 \approx R_{TrT} >> R_{TR}$, then $\theta_{TrT} \to 0$ from relation (5.37) can be written:

$$v_D = \frac{V_D}{V_0} = \cos\left(\theta_T\right) + \cos\left(\theta_{TR} - \theta_T\right). \tag{5.38}$$

The dependence of the normalized Doppler speed on the heading angle, calculated using the relation (5.38), is presented in Fig. 5.37.

It can be seen that in a fairly wide range of course angles, the Doppler frequency shifts have values sufficient for the selection of the object signal against the background of the scatterings from the terrain. And only in the sector of angles $150° \le \theta_{TR} \le 210°$ there are certain problems associated with the impact of the Doppler frequency shift in the region of the carrier frequency of the illuminating signal. Estimates using the ratio (5.35) show that for air objects with cruising speeds of 600...2,000 kmph, the range of Doppler frequency shifts in the decameter band of wavelengths is 60...20 m within 3...30 Hz. At the same time, the spectrum of the information signal of broadcasting stations is concentrated on frequencies above 50 Hz. This means that in the frequency interval between the carrier and information message frequencies, it is possible to detect signals reflected from aerial objects. For the experimental study of interference levels in the frequency range between the carrier line and the information signal, a dipole with an effective height of about 0.4 m was used as an antenna. It was placed on a support-rotating device that provides a change in the reception polarization by turning the dipole by 90°. Through the balancing device, the antenna was connected to the superheterodyne receiver P-399A ("Katran"), which the output of the phase detector was connected to the computer through

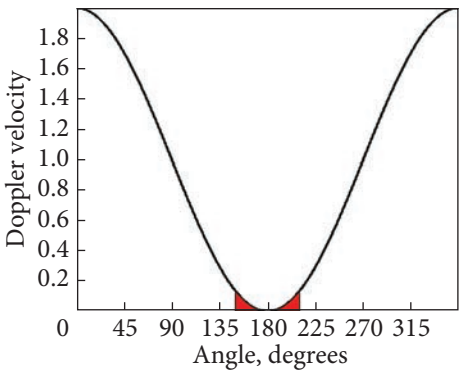

Fig. 5.37. Dependence of the normalized Doppler velocity on the heading angle

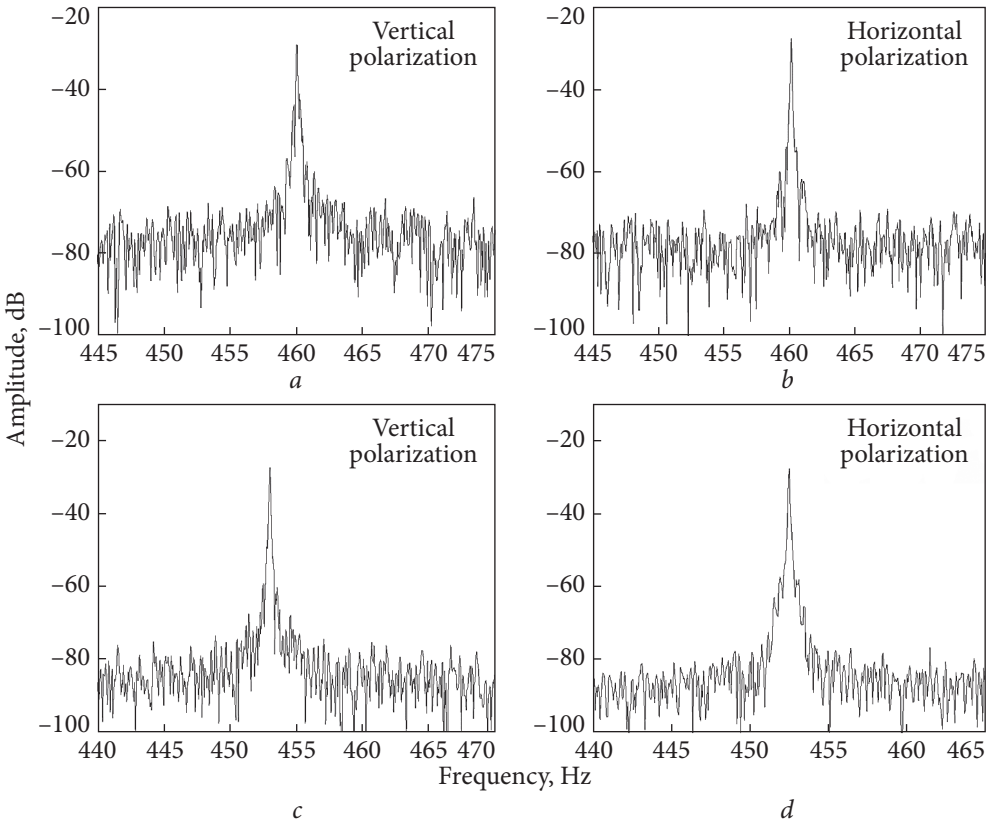

Fig. 5.38. Signal spectra of broadcasting stations in the vicinity of the carrier at frequencies of 5,909 kHz (*a*, *b*) and 9,490 kHz (*c*, *d*), when receiving horizontal (*b*, *d*) and vertical (*a*, *c*) polarizations

Table 5.11. **The main technical characteristics of the measuring complex**

Technical characteristics	Marking	Unit measurement	Dimension
The effective height of the antenna	h_e	m	0.4
Operating frequency range	f	MHz	1.0—31.999
Sensitivity	$U_{\min}$	μV	≤0.6
Receiver bandwidth	Δf	kHz	0.3; 1.0; 3.0; 6.0
Dynamic range of the receiver	A	dB	≥70
Conversion bit rate		bit	16
Accuracy of setting the frequency of the local oscillator	Δ	Hz	1
Frequency stability of heterodynes	$\Delta f / f$		$2.5 \cdot 10^{-8}$
Frequency resolution	ΔF	Hz	0.06

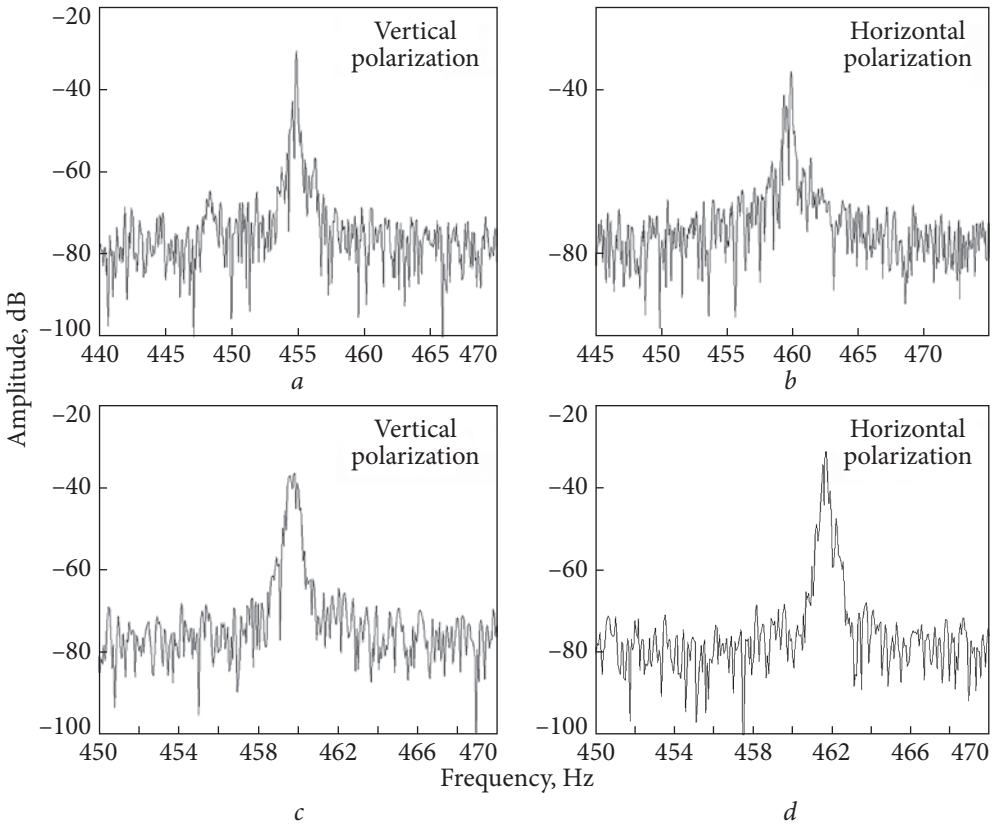

Fig. 5.39. Signal spectra of broadcasting stations in the vicinity of the carrier at frequencies of 13,904 kHz (*a*, *b*) and 15,130 kHz (*c*, *d*), when receiving horizontal (*b*, *d*) and vertical (*a*, *c*) polarizations

Table 5.12. **Signal-interference ratio at different reception frequencies and polarizations**

Frequency, MHz	Polarization	Width of carrier lines, Hz	Signal-interference, dB when detuning from the carrier	
			–10 Hz	+10 Hz
15,130	VP	0.56	61.1	57.8
15,130	HP	0.5	54.2	52.9
9,590	HP	0.34	60.4	60.4
9,590	VP	0.28	57.9	58.2
13,840	VP	0.77	50.1	48.2
13,840	HP	1.17	44.3	44.3
5,990	VP	0.34	52.0	52.9
5,990	HP	0.42	47.9	49.5

a sound card. The main technical characteristics of the measuring complex are given in Table 5.11.

Since the computer's sound card has limitations on the lower limit frequency of the input signal, the local oscillator signal was detuned from the carrier frequency during reception.

It should be noted that this shift was different in different experiments and for different reception polarizations. Signal spectra of broadcast stations operating at frequencies 5,909, 9,490 kHz and 13,904, 15,130 kHz in the vicinity of the carrier with vertical and horizontal polarizations of reception are shown in Fig. 5.38 and Fig. 5.39.

In Fig. 5.38, one-hop propagation of radio waves takes place, while in Fig. 5.39, double jump. It can be seen that for radio stations that broadcast on frequencies of 5,909 and 9,490 kHz, the carrier level exceeds the interference level by more than 40 dB. The conducted experimental study of interference levels in the frequency range between the carrier line and the information signal showed that both carrier frequency levels and interference change slightly when the reception polarization changes.

The ratios of the carrier to the interference level obtained during the experiments at different frequencies and the reception polarization are given in Table 5.12.

The analysis of the data obtained during the experiments shows that the interference level is practically the same when shifted both to the left and to the right of the carrier frequency. The difference, as a rule, does not exceed 3 dB. It was not possible to draw an unequivocal conclusion about the influence of the change in polarization on the ratio between the carrier and the level of interference; however, in some cases, larger signal-to-interference ratios were observed with vertical polarization of reception.

At the same time, it can be noted that the width of the carrier line, as a rule, is smaller in cases where there are large signal-to-interference ratios. This is probably due to the effect on the direct signal of the range between the transmitter and the receiver. In cases of single-hop propagation, a narrower width of the carrier band and a greater signal-to-interference ratio are observed than in cases of multi-hop propagation.

5.5. Optimum reception of signals propagating in media with absorption and dispersion

Correlation processing occupies a special place in the analysis of the process of propagation of radio waves in the atmosphere and outer space, solving the problems of detection, measuring the coordinates of objects, as well as recognizing their types [302-305]. The correlation integral is a sufficient statistic used in the detection of signals against the background of Gaussian noise [302, 303]. The theory of discrimination is based on the use of a two-dimensional correla-

tion function — the function of uncertainty in time and frequency [302, 303]. Recognition of signal types, optimal filtering, and correlational guidance methods are based on the use of correlation processing. Recently, new methods of description and analysis of ultrabroad-band processes and fields have been widely used [306—312]. This subsection discusses the peculiarities of signal reception during their propagation in media with dispersion and absorption. The concept of a modified correlation integral and its Fourier image in the form of a matched filter are introduced, which can be useful in solving the problems of detection, measurement, and recognition of objects in dispersed media with losses.

Propagation of a wave packet in the environment. When a wave packet propagates in a medium with a complex propagation constant , each of its spectral components $S(\omega)$ can be written in the form:

$$\dot{\hat{S}}(\omega) = \dot{S}(\omega)\exp(i(\omega t - \dot{k}z)), \tag{5.39}$$

where

$$\dot{k} = k' - ik'' = k_0(n' - in'') \tag{5.40}$$

and n', n'' is the real and imaginary part of the refractive index of the medium, $k_0 = \omega/c$ is the wave number, c is the speed of light.

Then from relations (5.38, 5.39) we can write:

$$\dot{\hat{S}}(\omega) = \dot{S}(\omega)\exp\left(i\omega\left(t - \frac{z}{\tilde{n}}n'\right) - \omega\frac{z}{\tilde{n}}n''\right). \tag{5.41}$$

At the same time, the real part of the refractive index of the medium, which is included in the first coefficient, affects the phase delay of the spectral component by $\phi(\omega, z) = \omega(z/c \cdot n') = \omega\tau_0 n'$, where τ_0 is the time delay in a vacuum when the wave propagates over a distance z and n' takes into account its increase in the medium with the refractive index n'.

The imaginary part of the refractive index of the medium, which is included in the second coefficient, affects the attenuation $L(\omega, z) = \exp(-\omega \cdot z/c \cdot n'')$ of the spectral components of the signal during its propagation in the medium over a distance z. If the medium is not dispersive and has small values of the imaginary part of the refractive index, i.e., $n' \approx const$, $n'' \approx 0$, then the signal in such a medium propagates with small losses, and all its spectral components receive a constant time delay. In the case of a dispersed medium, i.e., when the refractive index $n' = n'(\omega)$ depends on the frequency (wavelength), as can be seen from (5.41), different frequency components receive different time delays and, in addition, are attenuated differently in the medium. This circumstance must be taken into account when implementing optimal and quasi-optimal

reception. Correlation integral:

$$Z(\tau) = \int_0^{\infty} X(t)Y(t-\tau)dt \tag{5.42}$$

characterizes the degree of "similarity" of the tested $X(t)$ and reference functions $Y(t)$ at the mutual delay τ. It also determines the type of frequency response of the optimal filter.

When a signal is detected against a background of Gaussian noise, it acts as a sufficient statistic, which is compared with the decision threshold. When detecting a signal with a random initial phase, the module of the correlation integral is used as a sufficient statistic. At the same time, the reference function is understood as the radiated (probing) signal, which is compared with the tested one — received (reflected) from the object. If the reference function $Y(t)$ is understood as the impulse transient characteristic $Y(t) = h(t)$, then the expression (5.42) is the integral of the convolution (Duhamel's) and will describe the signal at the output of the linear system. In the theory of optimal reception, the reference functions are recognized signals. Considering analytical signals, the concept of a two-dimensional correlation function was introduced [302, 303]:

$$\psi(\tau, F) = \frac{1}{2}\left|\int_{-\infty}^{\infty} X(t)X^*(t-\tau)\exp(-i2\pi Ft)dt\right|, \tag{5.43}$$

which characterizes the result of correlation-filter processing when the delay time τ and the frequency F differ from the expected ones. This approach allows analyzing the discrete properties of signals by time and frequency, the accuracy of measuring these parameters. The Fourier transform is used to describe processes in the frequency domain:

$$Z(i\omega) = \int_{-\infty}^{\infty} Z(t)\exp(-i\omega t)dt. \tag{5.44}$$

In terms of frequency spectra, the optimal reception of signals during their propagation in a medium without absorption and dispersion consists in the formation of the frequency characteristic of the matched filter as frequency-coupled with the frequency characteristic of the signal [302, 303]. It is obvious that for environments with low losses and the absence of dispersion, regardless of the range at which optimal reception is carried out, the type of frequency characteristic of the optimal filter does not change. The delay time is the same for all spectral components of the signal.

The correlation integral and its Fourier spectra make it possible to analyze the propagation and scattering processes of radio waves in media whose dielectric and magnetic properties are spatially homogeneous and have a small dispersion, i.e., $\sigma_\varepsilon / \varepsilon \leq\leq 1$, $\sigma_\mu / \mu \leq\leq 1$. At the same time, the spectral components of the radiated wave packet propagate in space at the same speed and with approximately the same attenuation. This leads to the fact that the signal scattered by objects located at different points in space differs only in the delay time and the scale multiplier of the amplitude, which allows it to be used for its selection and comparison with the radiated signal by mutual correlation processing. However, in many cases, during the propagation of a wave packet, both its time scale and its individual spectral components are deformed, which leads to a change in its shape. It is clear that the use of the original process as a reference function in this case turns out to be ineffective. It is necessary to take into account changes in the type of support function in the process of propagation in such an environment. Such a situation is characteristic, for example, of subsurface sounding systems that use ultra-wideband (UWB) signals.

Electrophysical characteristics of the soil. Wet soil is a dispersed environment consisting of many components. Its complex dielectric permeability is determined by volume fractions and dielectric properties of components, the main of which are solid soil particles, air, bound, and free water. Until now, there is no physically determined model of the dielectric constant of dispersed media, which would allow determining the dielectric constant of a mixture through the dielectric constants and volume fractions of individual components, although interest in this problem arose a long time ago. Ideas on determining the dielectric constant of layered dielectrics were expressed by Maxwell and Rayleigh.

Electromagnetic radiation from lightning discharges is an example of UWB signal in the atmosphere of natural origin. The spectrum of a lightning discharge lies in the range of 1...106 Hz; the main part of the energy is concentrated in the range of 102...105 Hz [314]. The bandwidth coefficient of these processes is [313]: $\mu = \Delta f / f_0 = (f_{max} - f_{min}) / (f_{max} + f_{min}) \approx 0.9\ldots1.1$.

In such a wide frequency range of radiation, the propagation medium (waveguide Earth-ionosphere) has dispersive properties and different linear attenuation for different parts of the radiation spectrum. This leads to the fact that the spectrum of the signal changes at different distances from the lightning discharge source, and this circumstance must be taken into account when implementing the optimal receiver of such signals.

Acoustic noises of technical objects (cars, airplanes, etc.) are also UWB processes that lie in the frequency range from dozens of Hz to units of kHz.

The width of the spectrum of acoustic signals when propagating in the atmosphere due to the uneven attenuation of various spectral components varies greatly depending on the reception range (see Chapter 2). The narrowing of the effective spectrum width of the source with the range will lead to a deterioration of the resolution and, as a consequence, a deterioration of the accuracy of the acoustic systems.

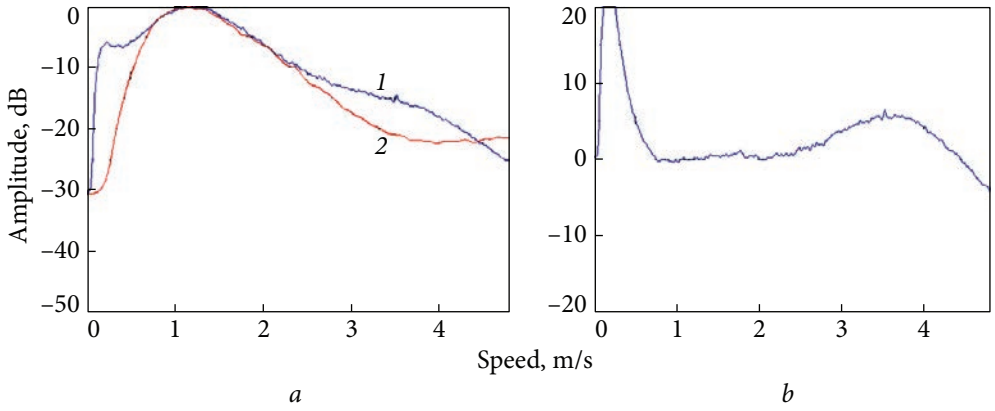

Fig. 5.40. Spectra of reflections from the sea on waves in the centimeter and millimeter bands with horizontal polarization of radiation and reception: wind speed 11...12 mps, slip angle 0.25°, radiation towards the wave; *a* — reflection spectra; *1* — λ = 3cm, *2* — λ = 8 mm; *b* — difference spectrum

A modified correlation function was proposed by us to account for the possible deformation of the time scale [183]:

$$Z(\tau) = \int_0^\infty X(t) Y\left(\frac{t-\tau}{b}\right) dt \,. \tag{5.45}$$

Fourier images of signals

$$\begin{gathered} X(t) \Rightarrow X(i\omega) = \int_0^\infty X(t) \exp(-i\omega t) dt, \\ Y\left(\frac{t}{b}\right) \Rightarrow Y(bi\omega) = \int_0^\infty Y\left(\frac{t}{b}\right) \exp(-i\omega t) dt \end{gathered} \tag{5.46}$$

also have a deformed frequency scale. Such a transformation is useful for describing processes, for example, at different wavelengths of the radar signal. Thus, the Doppler shift of the frequency F_i of a signal scattered by an object moving at a speed V:

$$F_i = \frac{2V}{\lambda_i} = 2V \frac{f_i}{c}, \tag{5.47}$$

where λ_i — wavelength and f_i frequency of the irradiating signal. It is clear that the Doppler shift of the frequency of signals scattered at different frequencies will be significantly different, which prevents their joint processing and analysis. Moreover, this difference is determined by the proportionality factor $\lambda_i/2$. If the

Doppler frequencies are recalculated through this coefficient, i.e., the frequencies are scaled (5.46), then the obtained spectra in terms of the scatterer movement speeds can be compared and jointly processed. As an example, Fig. 5.40 shows scaled Doppler spectra of reflection from the sea surface, obtained at 8 mm and 3 cm waves using pulse radars.

The frequencies are listed in the speed of movement of the scatterers using the well-known Doppler ratio. Despite the significant difference in radar frequencies (approximately four times), after bringing them to the same scale, using the proposed approach, their analysis and joint processing are possible. The same can be done using modified correlation functions (5.45) with changed time scales introduced for analysis in such cases. Analysis of Fig. 5.40 shows that in the millimeter range when scattering from the sea, a more significant contribution is made by the high-frequency components of the spectrum (scatterers with high movement speeds) associated with destructive waves and splashes. The same can be done when constructing a two-dimensional distance-speed correlation function. The proposed approach is similar to the use of scaling in wavelet analysis.

Optimal filtering of signals in environments with losses and dispersion. If the signal is at the input of the communication channel $\dot{S}(\omega)$ and a distance from the source, it can be written, taking into account (5.41), in the form:

$$\dot{\hat{S}}(\omega, z) = L(\omega, z)\exp\big(\varphi(\omega, z)\big)\dot{S}(\omega)\,, \tag{5.48}$$

where the first coefficient, which depends on the imaginary part of the refractive index, will determine the attenuation of the spectral components of the signal during their propagation in the medium, and the second, which depends on the real part of the refractive index — the phase distortion obtained during propagation. The optimal filter for a signal received at a distance z from the source should have a frequency characteristic complexly combined with its spectrum:

$$\dot{\hat{S}}_{opt}(\omega, z) = \dot{\hat{S}}^{*}(\omega, z)\,, \tag{5.49}$$

so, it is obliged to take into account the amplitude distortions of the signal in medium $L(\omega, z)$ and introduce phase predistortions $\exp{-\varphi(\omega, z)}$, which compensate for the influence of the propagation medium and also ensure the coherent addition of all its spectral components $\dot{S}^{*}(\omega, z)$. Unlike non-dispersive media without losses, in this case, depending on the distance to the source, the phase-frequency composition of the signal will change, which means that the type of frequency response of the matched filter should also change.

The ratio (5.49) for the case of UWB signals allows us to estimate the bandwidth of the communication channel and, therefore, the bandwidth of the optimal filter:

$$L(\Delta\omega, z) \approx \frac{1}{2}\,. \tag{5.50}$$

Estimates using data [29, 315] and ratio (5.50) show that if it is necessary to detect sources of acoustic noise at distances of 1...10 km, the bandwidth of the optimal receiving device does not exceed 1 kHz.

Conclusions

1. The description of space-time non-stationarity of the signal scattered from areas of land covered with vegetation can be based on the use of nested semi-Markov processes.

Within each of the phase states, the process can be considered as locally Gaussian. Comparable Rayleigh or Gaussian distribution laws can be used to describe amplitude fluctuations or instantaneous values at the output of a phase detector. Spatial spectra of signals scattered from the terrain are satisfactorily described by static functions with an exponent of degree 2...4.

2. Specific RCS of scattering from areas with vegetation cover in the VHF and UHF bands changes during the growing season, reaching a maximum before its end. The difference is up to 6...7 dB. The increase in specific RCS is associated with the increase in biomass. Kravchenko's finite atomic functions can be used to describe the process of biomass growth and changes in the specific RCS of vegetation. Humidity during the growing season changes slightly, decreasing significantly before dropping the leaves.

3. The spectra of signals scattered from individual fragments of plants are satisfactorily described by exponential functions in the dynamic range up to 30 dB.

4. The experimentally obtained data on the distribution of the sizes of reflective areas covered by different types of vegetation, their spatial spectra, as well as scattering characteristics (specific RCS, frequency spectra) and their dependence on the season, wind speed, and direction make it possible to create a simulation model of the signal scattered by vegetation covers, which takes into account the spatio-temporal non-stationarity of scatterings.

5. In the spectrum of signals of broadcast stations of HF and VHF bands, which can act as illumination signals for active-passive radar systems at frequencies from 6 to 60 Hz, corresponding to the Doppler shift of the frequency of reflections from aerial objects, the spectral density is significantly lower — by 20...30 dB than in the field of information frequencies, which will ensure the possibility of their application to solve the problems of radar and remote sensing. This ratio depends slightly on the operating frequency and time of day.

6. A simulation model of non-stationary acoustic noises of natural (wind, leaves) and anthropogenic (human steps, automatic weapon shots) using semi-Markov nested processes with two-phase states is proposed. Spectral characteristics (width, spectral density, decay rate) and times of existence of these processes in each of the states (burst/pause) were determined. It is shown that during bursts, the expansion of the noise spectrum for some of the processes exceeds by an order of magnitude the width of the spectrum during pauses, for

example, during the sound of a gunshot. The shape of the spectrum in each of the phase states is satisfactorily described by fractal dependences, and the densities of the distribution of the existence times in each of the phase states differ significantly from the exponential ones. The distribution laws of instantaneous noise values differ from the Gaussian model, but in each of the phase states, they can be approximated by a normal distribution law. Therefore, the distribution density of the process as a whole can be approximated by the relative normal distribution for instantaneous values and the Rayleigh distribution for amplitudes. This means that in each of the phase states, the process can be described locally by a Gaussian model. The proposed simulation model of acoustic noises of terrain and objects allows evaluation of the operating characteristics of acoustic reconnaissance systems (range) and can be used in the development of algorithms for estimating coordinates and recognizing the type of objects.

7. Characteristics of the sound of a shot is a non-stationary process. Its statistics can be described by a time-varying normal noise model and the spectra by fractal dependencies, with the rate of decrease of the spectral density varying with time.

8. Defects in the human gait are manifested in differences in the existence times of the process in different phase states, their intensity, and spectra. The difference in these characteristics for different phase states can serve as an informative criterion for detecting gait defects. A similar approach can be used to detect weapon defects by the sound of a shot. Differences in spectra and firing rate (changes in the firing period) can be informative signs for detecting defective samples.

9. A modified correlation function is proposed, which allows taking into account the deformation of the spectra (time scales). The influence of the propagation medium on the characteristic of the matched filter is considered. The use of the proposed approaches is promising for describing the processes of propagation, detection, measurement, and recognition of signals in environments with dispersion and loss. The use of such an approach can be useful in analyzing the results of multi-wavelength remote sensing of the environment.

10. As a result of the approximation of the spectrum of broadcasting stations, estimates of the rate of decrease of the spectral density above and below the frequency of the maximum spectral density of the information signal were obtained. The approximation of the low-frequency part of the spectrum was performed from 2 to 100 Hz and the high-frequency part from 100 to 2,000 Hz. It should be noted that for all frequencies of the HF band, regardless of the time of day, the slope of the spectrum, as a rule, has a value of $n \approx 1.6...2.3$.

11. As a result of experimental studies of interference levels in the frequency range between the carrier line and the information signal, it was established that the level of the carrier frequency and the level of interference change slightly — when the reception polarization changes, the difference in the interference

levels when shifting both to the left and to the right of the carrier frequency, as a rule, does not exceed 3 dB. It is established that the width of the carrier line, as a rule, is smaller in those cases where there are large signal-to-interference ratios.

12. Experimental studies of the signals of HF stations showed that in the absence of AGC, at the output of the receiver, there are fadings with a depth of 20...30 dB with a frequency of dozens of seconds. An increase in the distance between the transmitter and the receiver leads to a decrease in the fading period, i.e., multi-hop paths will have a shorter fading period than single-hop paths. The use of AGC significantly reduces the dynamic range of fluctuations, which has a positive effect on reception conditions but can lead to the appearance of negative effects associated with the limitation of large signals.

13. It has been established that an increase in the signal level or the gain of the receiver leads to a decrease in the range of signal fluctuations and the appearance in the MGC mode of the effects of signal limitation, characteristic of AGC.

14. It was established that the filtering of the useful signal in the Doppler frequency band 0...70 Hz, which is necessary to reduce the level of interference created by the information signal of the illumination station, leads to an increase in the range of signal fluctuations, which will lead to a change in its statistics.

15. In view of the presence of two phases of different intensity, which are physically determined by the discrete nature of the modulating signals of radio broadcast stations, a simulation model is proposed that describes the disturbances created by the radiation of broadcast stations to active-passive systems based on nested two-component random processes.

16. As a result of the approximation of the illuminating signal distribution functions by the component normal distribution law, it was established that in the AGC mode, the backlight signal interference in the entire band at all frequencies of the decameter range, regardless of the time of day, is satisfactorily described by the Gaussian distribution function. At the same time, non-Gaussianity is characteristic of the MGC regime for the signal statistics. The ratio of component intensities (degree of non-Gaussianity) for the signal in the entire band has a value of 5...10 dB with a probability of the presence of the second component (bursts) of 15...40 %. Filtering in the band of Doppler frequencies 0...70 Hz leads, as a rule, to the appearance of non-Gaussianity even in the AGC mode. The non-Gaussianity parameter has a value of 4...10 dB, increasing at MGC to 8...16 dB. At the same time, the emission probabilities, as a rule, decrease to 25...30 % in the AGC mode and 3.5...25% in the MGC mode.

CHAPTER 6

Kravchenko-Rvachev distribution functions describing some non-stationary non-Gaussian processes

In this section, the possibility of using Kravchenko-Rvachev atomic functions to describe the laws of distribution of various non-stationary processes, the apparatus of correlation matrices of spectral component (CMSC) for describing the statistical relations of various spectral components of a signal scattered by objects, substratum surfaces, and hydrometeors is considered. The internal spectral correlation of interference of active-passive systems of the decameter band from the radiation of broadcasting stations in the HF band was experimentally studied. The main results of the section are published in papers [120, 248, 263, 316, 317, 318, 319, 320].

6.1. Descriptions of the statistics of the signal scattered by the sea

At high resolution on the range and angular coordinates, significant deviations of the laws of distribution of fluctuations from standard signals scattered from underlying surfaces and the "clear sky" are observed [288]. This is due to the consistent and separate observation of surface areas with distinct statistical properties of irregularities, which generate non-stationarity and non-Gaussianity of the scattered signal. For the sea surface, these are areas in which the crests of sea waves are located, which are characterized by increased reflectivity. Gaussian distributions were used to describe the statistics of the signal scattered from the sea in burst-pause phase states. Consider the possibility of using atomic Kravchenko-Rvachev functions.

Photographic images of radar scatterings from the sea surface obtained from the screen of a pulse-coherent radar with a wavelength of 2 cm and a duration of the emitted pulse of 0.4 μs

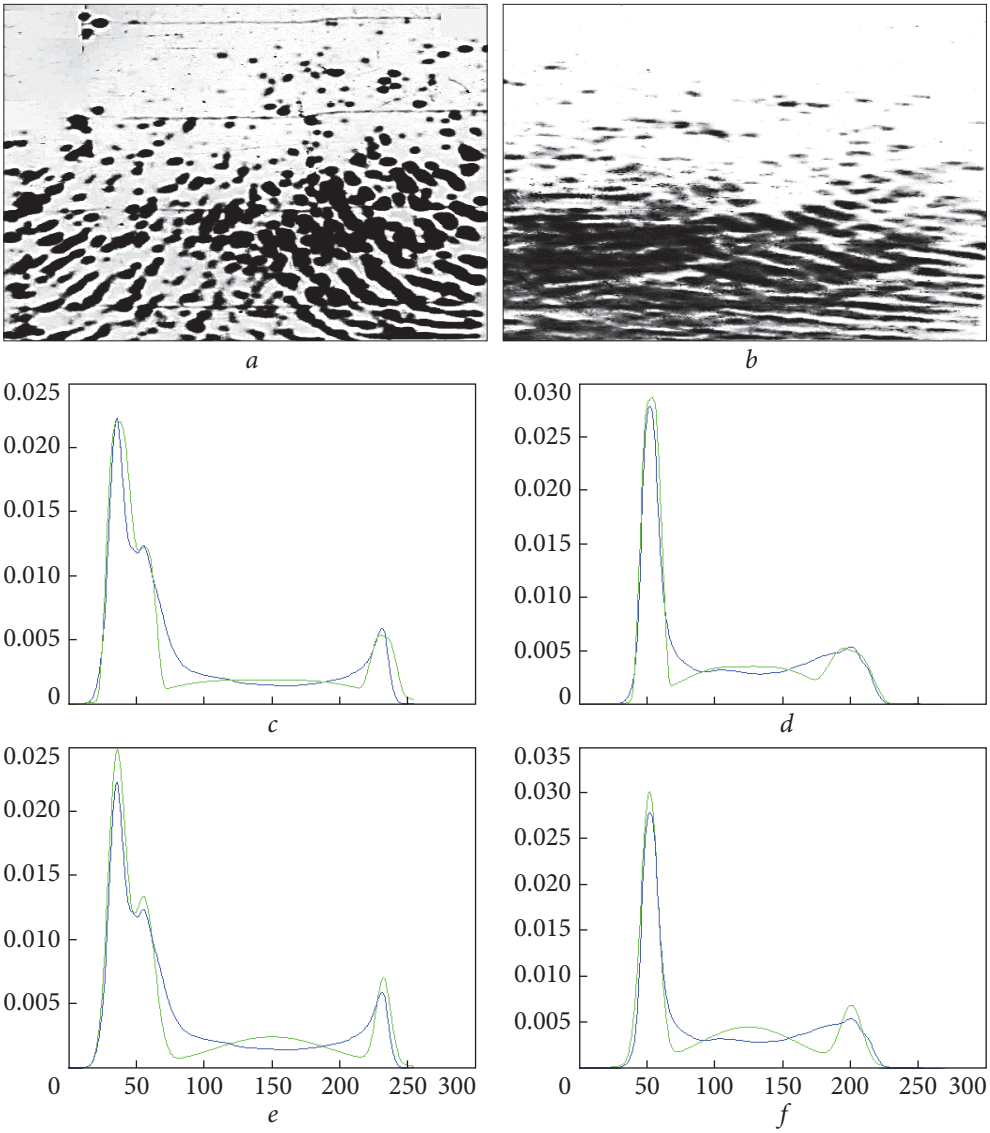

Fig. 6.1. Radar images (*a*, *b*) of the sea surface at distances of 0.5...5 km, in the scanning sector 120 degrees, radar wavelength 2 cm, sea waves 6 points; density distribution of values and their approximation by Kravchenko-Rvachev (*c*, *d*) and Gauss (*e*, *f*) functions: *a*, *c*, *e* — 1 scan; *b*, *d*, *f* — 4 scans

(resolution at a distance of 60 m) were used for processing, which works in the mode of sectoral survey of space — Fig. 6.1, *a*, *b* and Fig. 6.2, *a*, *b* [319]. Periodicity associated with the period of sea waves and the direction of radiation can be traced on the radar images. The behavior of the density distribution of the radar image of the sea surface for the zone of intense reflection is bimodal. The first

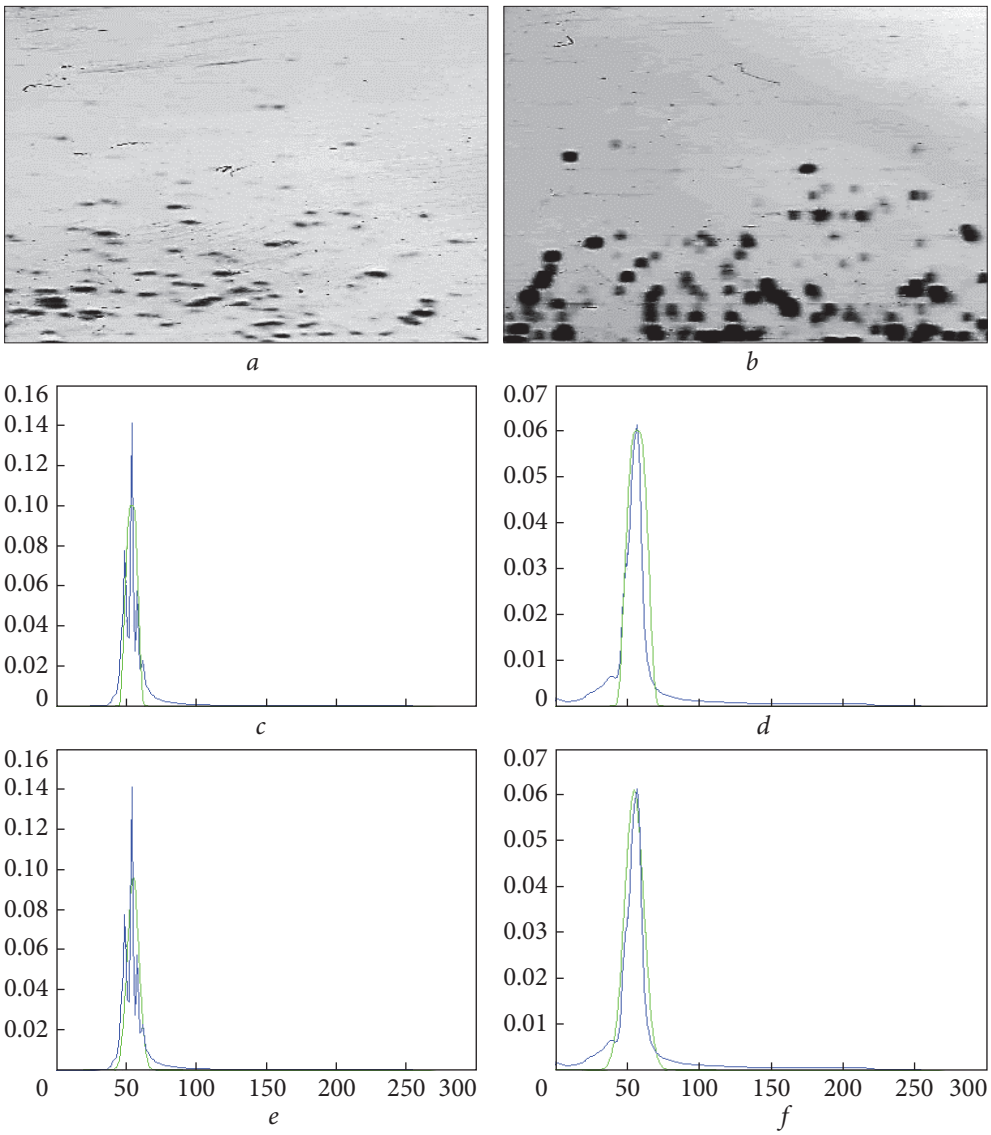

Fig. 6.2. Radar images (*a*, *b*) of the sea surface at distances of 5.5...10 km, in a sector of 60 degrees, radar wavelength 2 cm, sea turbulence 6 points, density distribution of values and their approximation by Kravchenko-Rvachev functions (*c*, *d*) and Gaussian (*e*, *f*): *a*, *c*, *e* — 2 scans, *b*, *d*, *f* — 4 scans

maximum corresponds to zones of weak reflection, and the second to strong (crests of sea waves).

At long distances Fig. 6.2, the difference in the maximum values of the distribution density for the "black" and "white" levels becomes so great that only one maximum is actually visible — the black level.

Approximation of experimentally obtained distribution densities was performed by functionals:

$$p(I) = \sum_{k=1}^{k_0} p_k \phi_k(I), \tag{6.1}$$

where p_k are the final probabilities of each of the k phase states, and, in general, $k \in (1, 2, 3)$, where $k = 1$ is the black level, $k = 2$ is the gray level, and $k = 3$ is the white level. Gaussian distribution densities were used as approximating functionals:

$$\phi_k(I) = \frac{1}{\sqrt{2\pi}\sigma_k} \exp\left(\frac{(I - I_k)^2}{\sigma_k^2} \right), \tag{6.2}$$

as well as finite Kravchenko-Rvachev functions:

$$\phi_k(I) = \frac{1}{b_k} \mathrm{up}\left(\frac{I - I_k}{b_k} \right). \tag{6.3}$$

The calculation of the density of the distribution of the Kravchenko-Rvachev function up(x) can be carried out by inverse Fourier transformation of the characteristic function obtained as a product of the characteristic functions of rectangular pulses or by calculating the density of the distribution of a series

Table 6.1. **Dispersions of the approximation error of experimental densities and distribution functionsby Gaussian and Kravchenko-Rvachev functions [319]**

Density distribution		Distribution function	
Functions of Kravchenko-Rvachev	Gaussian functions	Functions of Kravchenko-Rvachev	Gaussian functions
2,30e-06	2,14e-06	6,36e-04	7,04e-04
1,46e-06	1,86e-06	8,07e-04	1,10e-03
1,34e-04	9,96e-05	1,35e-02	1,16e-02
1,05e-05	8,03e-06	2,00e-03	1,60e-03
1,61e-06	2,06e-06	2,50e-04	7,42e-04
8,63e-05	6,36e-05	1,20e-03	9,07e-04
2,32e-05	2,32e-05	4,59e-04	5,60e-04
3,98e-05	2,60e-05	1,70e-03	8,73e-04
8,91e-06	1,47e-05	5,50e-04	5,49e-04
4,97e-06	3,69e-06	3,60e-04	7,34e-04
2,04e-06	2,003e-06	4,68e-04	8,31e-04
1,86e-05	1,16e-05	3,10e-03	2,60e-03

formed as the sum of a series of random numbers with uniform distribution laws [321]. The latter approach was used to obtain the basic parent function up(x).

The resulting random variable was scaled by coefficients b_k and shifted by I_k. Thus, the quantity I with the distribution density $\phi_k(I)$ was formed, which was used to approximate the experimental data. The approximation was performed of both the experimentally obtained distribution densities and the integral distribution functions according to the criterion of minimizing the error variance. The resulting approximation errors for various fragments of radar images of the sea are shown in Table 6.1.

It can be seen that both approximations give approximately the same results. However, in about one-third of the cases for the distribution density and half of the cases for the integral distribution function of radar images of the sea surface, the Kravchenko-Rvachev functions give better results than the standard Gaussian functions.

6.2. Seasonal variation of the specific RCS of the signal scattered by vegetation covers

Processes of biomass growth of plant covers are seasonal in their nature and are caused by many processes, for example, changes in humidity and heat flow. The change in the amount of biomass is associated with a change in the reflective properties of plant covers. So, if the specific RCS (SRCS) of deciduous forests and areas covered with grass are presented in the form of two components: one of which gives the value of SRCS in the winter period σ_0, and the other in the growing season during the growth of biomass is the addition of SRCS, which is obtained at the expense of this can be written:

$$\Delta\sigma(t) = \Delta\sigma \frac{m(t)}{\max m(t)} = \Delta\sigma \,\mathrm{up}\left(\frac{t - t_0}{\alpha \Delta t_0} - 1\right), \tag{6.4}$$

where $m(t)$ is the biomass of vegetation, t_0 and $\alpha\Delta t_0$ are the start time and duration of its vegetation cycle, α is the empirical coefficient, $\Delta\sigma$ is the increase in SRCS due to the growth of biomass, usually 5...7 dB [274]. Fig. 6.3, as an example, shows the behavior of biomass during the season [293] and its approximation by various functions. Table. 6.2 shows resulting approximation errors.

Since the beginning of the growing season is associated with average temperatures, this allows us to link the seasonal

Table 6.2. **Approximation errors of biomass growth by different functions**

	Kravchenko	Gauss	Lorenz
$D_{min} \cdot 1{,}000$	0.0052	0.0051	0.0169
$D_o \cdot 1{,}000$	0.0092	0.0118	0.0215
$D_{min} \cdot 1{,}000$	0.0236	0.0246	0.0499
$D_o \cdot 1{,}000$	0.0354	0.0458	0.0538

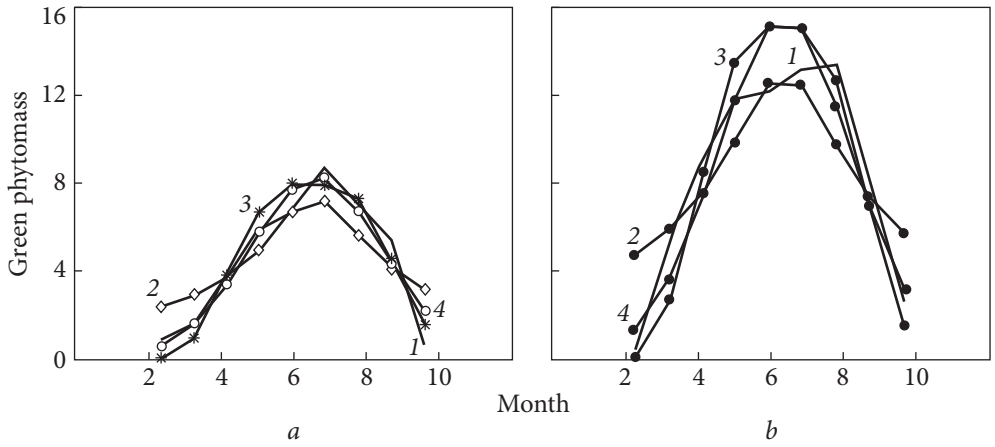

Fig. 6.3. Dynamics of the monthly growth of green phytomass during the growing season of 2002 (*a*) and 2003 (*b*) [293]. Experiment *1* — biomass; approximation by functions: *2* — Lorentz, *3* — Kravchenko, *4* — Gaussian

change in the SRCS of vegetation covers with the seasonal change in temperatures and, ultimately, with the cycles of solar activity.

Table 6.2 shows the approximation results of biomass growth by various functions: Gauss, Kravchenko-Rvacheva, Lorentz [319].

At the same time, D_0 is the variance of the approximation error when the mean and variance were taken from experimental data, and $D_{\min}$ is the mean value and variance that minimize the variance of the approximation.

It can be seen that, in some cases, the use of finite functions of Kravchenko-Rvachev gives better results than the use of Gaussian and even more than Lorentz functions.

6.3. Application of correlation matrices of spectral components for visualization of statistical relations of spectral components during detection and recognition

When synthesizing multi-channel detection systems, it is necessary to study statistical relations between signals of different channels. Knowledge of statistical relations between different spectral components of a signal is important for target-type recognition systems [120, 248, 317].

Since the signals of radio broadcast stations in active-passive systems are used to illuminate the environment and are an obstacle to secondary fields scattered by the target, it is necessary to study intraspectral correlations in illumination signals. The study of statistical interrelations of signal components scattered from objects and the noise opens up opportunities for creating multi-channel detection and recognition systems.

Correlation matrices of spectral components (CMSC). Let there be a signal $S(t)$. The module of its window Fourier transform on a time segment of duration T: $S(F_i, t)$.

$$S(F,t) = \left|\dot{S}(F,t)\right| = \left|\int_{t-T/2}^{t+T/2} S(t)\exp -i2\pi Ft\,dt\right|. \quad (6.5)$$

It is possible to use the CMSC proposed in papers [288, 317] to study interspectral correlations for non-stationary signals S_1 and S_2:

$$\rho(F_i,F_j) = \frac{\left\langle S_1(F_i,t)S_2(F_j,t)\right\rangle - \left\langle S_1(F_i,t)\right\rangle\left\langle S_2(F_j,t)\right\rangle}{\sqrt{\left(\left\langle S_1{}^2(F_i,t\right\rangle - \left\langle S_2(F_i,t)^2\right\rangle\right)\left(\left\langle S_2{}^2(F_j,t)\right\rangle - \left\langle S_2(F_j,t)\right\rangle^2\right)}}, \quad (6.6)$$

where $S(F_i, t)$, $S(F_j, t)$, $\rho(F_i, F_j)$ is the modulus of the spectral density at F_i and F_j frequencies at time t and their mutual correlation coefficient, respectively.

At the same time, the S_1 and S_2 signals can be reflections from underlying surfaces, hydrometeors, and objects with different polarizations. Then $S_1 = S_H$, $S_2 = S_V$ where H and V refer to horizontal and vertical polarization, respectively. This makes it possible to investigate statistical relations between different spectral components of reflections at different polarizations. Sometimes, it is important to study the statistical interrelations of spectral density fluctuations at different frequencies for one non-stationary signal. Then $S_1 = S_2 = S$. Recordings of the backscatter signal from the sea and objects previously obtained experimentally, using coherent radars with pulsed and continuous radiation, were used to study the CMSC.

Scatterings from the sea and rain are the noise to radar systems. The study of intraspectral correlations on orthogonal polarizations is necessary for the synthesis of detection and recognition systems.

The polarization-spectral structure of radar reflections from the sea can be studied using matrices of mutual correlation coefficients of spectral components (6.6).

The calculated matrix of correlation coefficients $\rho(F_i, F_j)$ is presented graphically. Matrix elements are depicted as a circle, the diameter of which is proportional to the correlation coefficient. Fig. 6.4 shows the following matrices for reflections from the sea obtained using radar with a wavelength of 8 mm when emitting pulses of 0.2 μs at an inclined 45° polarization for sea waves of 5...6 points (Fig. 6.4, *a*), as well as weak (about two points) excitement (Fig. 6.4, *b*).

They are calculated based on previously obtained experimental data of reflections from the sea.

The frequency analysis range was 500 Hz with a resolution of 32 Hz. It should be noted that with strong sea waves, correlation coefficient matrices have approximately the same form when the surface is irradiated with signals, both with oblique and vertical polarization.

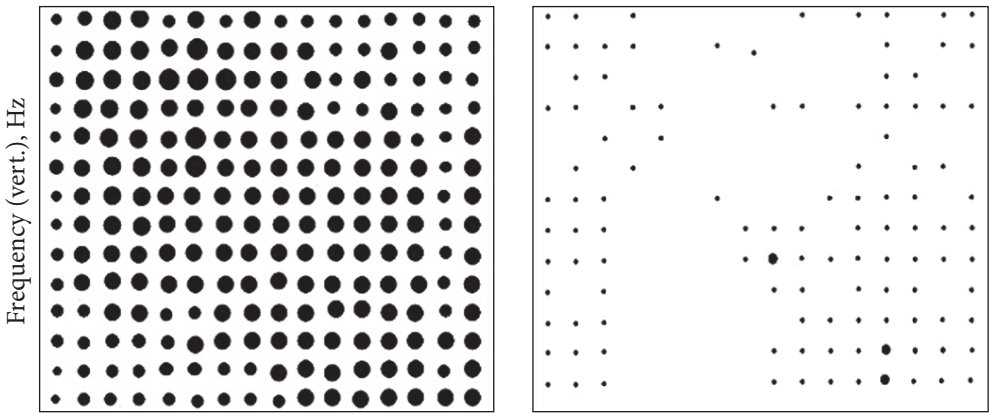

Fig. 6.4. CMSC of reflection on orthogonal polarizations from the sea surface at waves of 4...5 points (*a*) and 1...2 points (*b*); ● — 0.8; • — 0.4

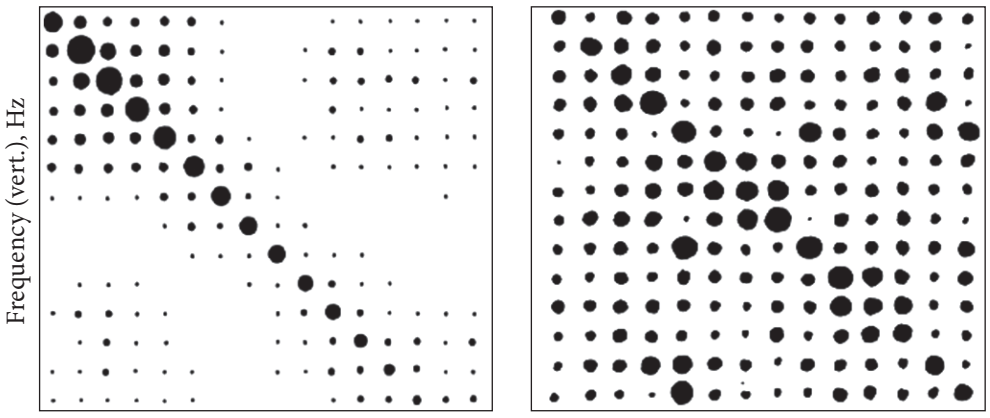

Fig. 6.5. CMSC of scatterings on orthogonal polarizations from from rain (*a*), ship (*b*); ● — 0.8; • — 0.4

Diagonal elements have the largest value, that is, spectral components that are more strongly correlated on orthogonal polarizations and coincide in frequency. With weak excitation, the correlation of spectral components on orthogonal polarizations is practically absent (Fig. 6.4, *b*). For scatterings from rain and objects, the correlation of only coincident spectral components (diagonal elements) is characteristic (Fig. 6.5, *a*, *b*). The correlation coefficient for rain can reach 0.95, and for targets (vehicles, ships), the values are slightly lower ≈ (0.5÷0.85). The characteristic appearance of the CMSC for objects, rain, and the sea surface can be used to solve problems of detection and recognition.

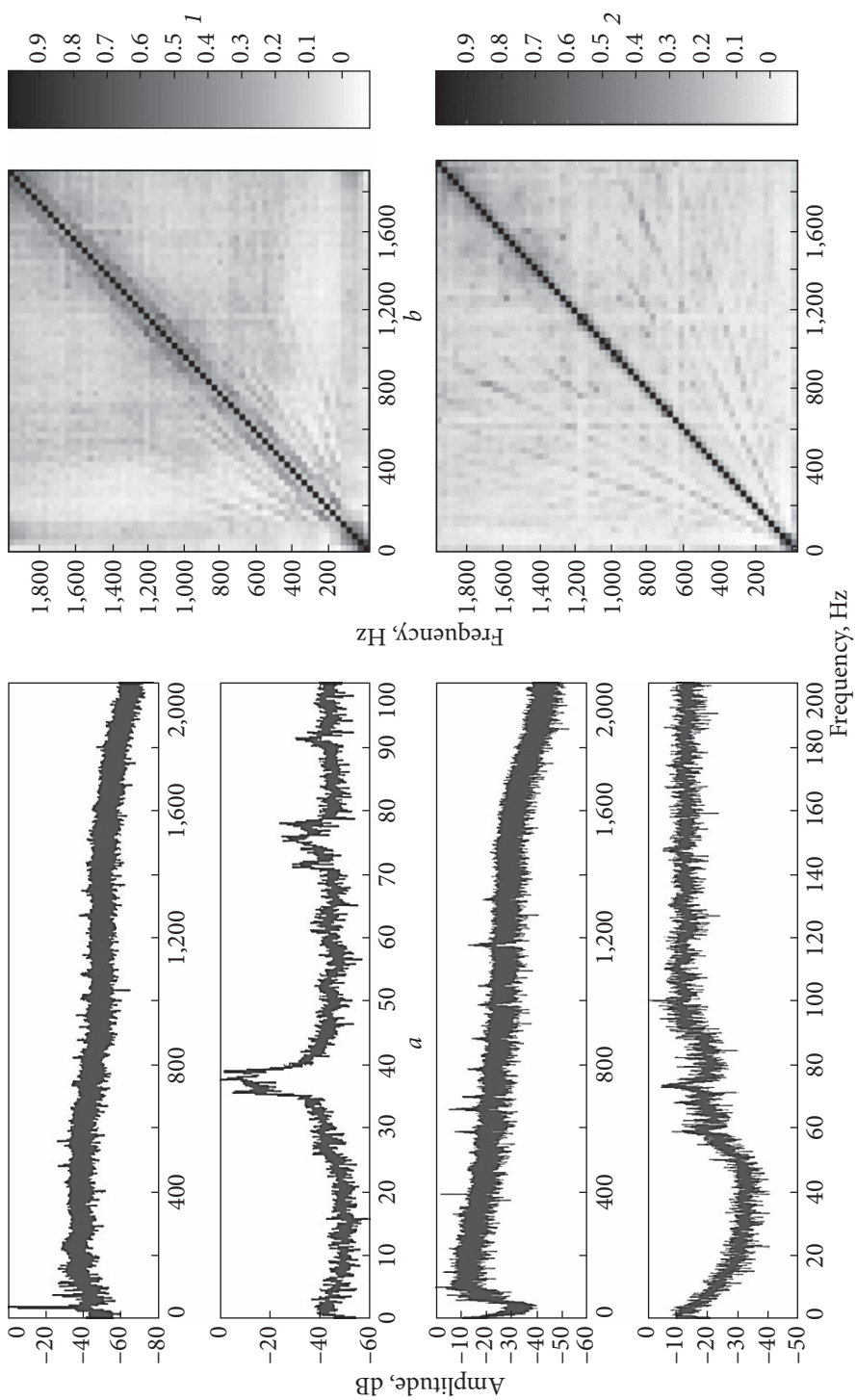

Fig. 6.6. Spectra (*a*, *c*) and correlation matrices of spectral components (*b*, *d*) of the broadcast station Kashi, China. Frequency 17,490 kHz, power 500 kW, distance 5,350 km, illumination azimuth 950, *1* — telegraph and *2* — telephone mode

Study of intra-spectral correlations of noise from radio broadcasting stations. The study of the mutual correlation coefficients of various spectral components made it possible to reveal the presence of a correlated region in the spectrum of signals of radio broadcasting stations.

Fig. 6.6 shows the spectra (*a*, *c*) and matrices of correlation coefficients (*b*, *d*) of the spectral components $\rho(F_i, F_j)$ at the frequencies F_i, F_j for the illumination station with a frequency of 17,490 kHz, located on the territory of China at a distance of 5,350 km.

Spectra (Fig. 6.6) and the upper spectrograms in the wide band and the lower spectrograms in the narrow initial section are shown. The value of the cross-correlation coefficient is determined by the brightness. The brightness scale is given next to the figure. In the telegraph mode, the carrier was shifted by the local oscillator by approximately 40Hz.

From the appearance of the correlation matrices of the spectral components (Fig. 6.6, *b*, *d*), it can be seen that the highest correlation is observed in the diagonal elements. When moving away from the diagonal, the correlation coefficient drops sharply. In addition, the increase in the gain of the receiver and the appearance of non-linear distortions in the path leads to the appearance of correlation zones on the harmonics of the spectral components of the information message. They look the same as the main correlation zone but at angles depending on the harmonic number (Fig. 6.6, *d*). This can be used to diagnose the presence of non-linear distortions in the signal transmission path.

Conclusions

1. It is shown that the finiteness of the Kravchenko-Rvachev functions is the physical reason for their use to describe the statistics of many types of non-stationary processes.

2. It was established that the errors that arise when using atomic functions for approximation (radar scatterings from the sea, seasonal growth of biomass) in most cases are approximately the same as when using standard models (Gaussian or Lorentzian).

3. It has been established that the use of the apparatus of correlation matrices of spectral components allows the establishment of the synchronicity of the appearance of individual spectral components in signal spectra and can be used to create spectral-polarization portraits of scattered signals, which can be used in solving recognition problems and synthesizing multi-channel detection systems.

4. The study of the mutual correlation coefficients of various spectral components of the signals of radio broadcasting stations made it possible to reveal the presence of a correlated region in the spectra. It was established that the appearance of additional elements with a high correlation at harmonic frequencies indicates the presence of nonlinear distortions in the receiving path and can be used for their monitoring.

CHAPTER 7

Non-equidistant two-dimensional antenna arrays based on magic squares

In this chapter, the possibility of synthesis of two-dimensional non-equidistant antenna arrays for environmental monitoring systems, active-passive radar, and radio astronomy based on magic squares is considered, and their properties are investigated.

The influence of the introduction of additional elements, turns, and shifts on the directional pattern (DP) of a sparse antenna array formed by the elements of a magic square was studied.

Algorithms for obtaining the maximum coverage of spatial frequencies of a sparse antenna array by supplementing the elements of the array formed by the elements of the magic square with additional elements are proposed [322—325].

The deceleration of the electromagnetic wave, the distribution of the surface current, and the input impedance of a symmetrical vibrator whose arms consist of cylindrical spirals with a diameter and a pitch small compared to the length of the vibrator were experimentally investigated [326, 327]. Also, a reflector calibrator was proposed on the database of structures for external calibration of the radar and simulation of the RCS of a moving radar target [328].

The main results are published in works [322—328].

7.1. Synthesis of a non-equidistant antenna array using magic squares

Non-equidistant linear antenna arrays (AA) have attracted attention for a long time [329—341]. Their main advantage is reducing the number of elements in the antenna without a noticeable loss of resolution while maintaining a fairly low level of side lobes. The need to obtain high spatial resolution, which requires large apertures, the complexity, and time-consuming implementation of individual antenna elements lead to the need to use unfilled apertures. A large number of attempts to find a simple

way to construct a non-equidistant array with small side lobes were unsuccessful at most. The search for the global minimum of lateral radiation at fixed array dimensions, in particular elements and resolution, led to the fact that the task turned out to be so difficult that it required huge computational costs. Previously used simplifications led to a noticeable loss of quality. Therefore, when creating non-equidistant arrays, in most cases, statistical methods were used [330].

A significant shift was achieved in 1978 by Leeper [333], who proposed placing elements of a linear antenna in some nodes of a uniform grid, and the nodes were chosen in such a way that the sequence of their numbers formed a cyclic difference set (CDS). This approach was further developed in the works of L. E. Kopylovych [334—339]. This approach was generalized to the case of designing two-dimensional antenna arrays. However, the generalization was made based on the use of the product of one-dimensional bases of its sides, which was made somewhat artificial.

It is interesting to study the possibility of using various mathematical constructions, for example, such as magic squares, for the construction of two-dimensional non-equidistant antenna arrays.

A magic square is a square Table (matrix) filled with numbers in such a way that the sum of numbers in each row, each column, and on both diagonals is the same. The sum of the numbers in each row, column, and diagonal is called the magic constant, *M*.

The idea of using magic squares from a series of natural numbers is that in the square, each number is repeated only once, which means that if you consider its element as the distance between two elements of the interferometer, then when using a natural series of numbers as the elements of the square will be guaranteed spatial frequencies from 1 to n are covered. At the same time, the frequencies on the entire aperture 1...M will be partially covered. When using magic squares of prime numbers, the possibility of reducing the redundancy factor and the aperture filling factor is of interest.

When considering the elements of the magic square as the distance between adjacent elements of the interferometer S_{lj}, the element of the square is at S_{lj} distances along the abscissa and ordinate axes from the adjacent elements of the antenna array. Then the coordinates x_{lj}, y_{lj} of the components of the antenna array can be written through the value S_{lj} of the elements of the square in row l and column j.

The number of elements is determined by the order of the square of n

$$y_{lj} = \sum_{l=1}^{l} S_{lj} = y_{l-1\,j} + S_{lj}\,;\; x_{lj} = \sum_{j=1}^{j} S_{lj} = x_{l-1\,j} + S_{lj}\,, \tag{7.1}$$

where x_{lj} is the abscissa, y_{lj} is the ordinate.

The resulting complex integers $Z_{lj} = x_{lj} + iy_{lj}$ are Gaussian numbers that determine the coordinates of the antenna array elements. The number of array elements is determined by the order of its generating square and is equal to n^2.

At the same time, the matrix $\|Z\|$ determines the coordinates of the elements of the two-dimensional non-equidistant antenna array. The Z_{lj} coordinates of the element are shifted from the previous elements along the abscissa and ordinate axes by the S_{lj} value. The frequencies y_q and x_g, which are covered along the y and x axes, are determined by the difference in the coordinates of the array elements:

$$y_q = y_{lj} - y_{km} \text{ and } x_g = x_{lj} - x_{km}. \tag{7.2}$$

Since in normal magic squares $S_{lj} \in (1, n^2)$, it means that the two-dimensional antenna array synthesized based on the square of the n-th order will completely cover, at least, the spatial frequencies corresponding to the numbers from 1 to n^2.

When creating antenna arrays, it is tempting to create such an array that, with full coverage of the required frequency range, has a minimum number of elements and acceptable sidelobe-level values. One of the important tasks is to find a non-redundant configuration (NRC) with a given number of elements that provides complete coverage of the central region of maximum size in the plane of spatial frequencies (u, v-plane) [335]. Full coverage of the entire frequency grid in the area of the antenna location is characteristic of non-redundant arrays.

It is obvious that a magic square built from a sequence of natural numbers $(1, n^2)$ — a normal square, by definition, covers the frequencies $(1, n^2)$ in the u and v-planes. The coordinates of the lattice elements are the elements of the complex matrix $\|Z\|$ obtained using (7.1) and the generating matrix $||S||$, the elements of which are the elements of the magic square.

We can define the matrix $\|\hat{Z}\|$, which will be called the inverse of the matrix $\|Z\|$ modulo M:

$$\|\hat{Z}\| + \|Z\| = \|M\|, \tag{7.3}$$

where $\|\dot{M}\| = M\|i\|$, and

$$\|i\| = \begin{pmatrix} 1+i\ 1+i...1+i \\ 1+i\ 1+i...1+i \\ ..... \\ 1+i\ 1+i...1+i \end{pmatrix}. \tag{7.4}$$

Despite the appearance of the arrangement of elements, which is significantly different from $\|Z\|$, the inverse matrix $\|\hat{Z}\|$ is equivalent to it since the grid, the coordinates of the elements, which it defines, covers the same range of spatial frequencies as the $\|Z\|$ grid.

Indeed, the frequencies that are covered are determined by the difference in the coordinates of the elements, and for an inverse array, they can be written as:

$$\hat{y}_l = \hat{y}_{ij} - \hat{y}_{km} = M - y_{ij} - \left(M - y_{km}\right) = y_{km} - y_{ij} \tag{7.5}$$

$$\hat{x}_m = \hat{x}_{lj} - \hat{x}_{kl} = M - x_{lj} - \left(M - x_{kl}\right) = x_{kl} - x_{lj}, \tag{7.6}$$

that is, the frequencies of the lattice for the matrix $\|\hat{Z}\|$ coincide in magnitude with the frequencies covered by the elements of the array, which is determined by the original matrix $\|Z\|$.

Using the matrices $\|Z\|$ and $\|\hat{Z}\|$, which describe the coordinates of the antenna arrays, you can form a matrix:

$$\|Z^*\| = \|Z\| \cup \|\hat{Z}\|, \tag{7.7}$$

which contains elements both of the matrix $\|Z\|$ and $\|\hat{Z}\|$. In the future, we will call it the matrix connected with $\|Z\|$. While the elements of these matrices cover the areas of frequencies that coincide when one of them is supplemented with the elements of the other, the area of coverage can be expanded since additional frequencies of coverage between the elements of these two matrices can appear.

7.2. Properties of antenna arrays based on magic squares

It is obvious that the elements in the last column x_{ij}, i.e., at $j = n$, and the last row y_{ij}, i.e., at $i = n$, have a value equal to the constant of the magic square, i.e., $x_{in} = M$, and $i \in (1, n)$ and $y_{nj} = M$, $j \in (1, n)$.

The DP of the antenna array is determined by the relations [329]:

$$G\left(\cos\alpha_x, \cos\alpha_y\right) = \sum_{\substack{m=1 \\ n=1}}^{\substack{m=m-1 \\ n=n-1}} \left|A_{mn}\right| \exp it\left(x_{mn}\cos\phi + y_{mn}\sin\phi\right), \tag{7.8}$$

where $\cos\alpha_x = \sin\theta\cos\phi$ and $\cos\alpha_y = \sin\theta\sin\phi$ are direction cosines, $t = \frac{2\pi}{\lambda} d_0$, λ is the wavelength, d_0 is the grating pitch, $|A_{mn}|$ is the amplitude of the supply mn of the lattice element. In our case, $|A_{mn}| = 1$.

The average level of radiation on the side lobes can be estimated using the ratio:

$$\delta = \sqrt{\sum_{l=l_0}^{N} \left|\dot{G}\left(\Delta\phi l\right)\right|^2 \Big/ \left(N - l_0\right)}, \tag{7.9}$$

where the summation is carried out $l \in (l_0, N)$ outside the main petal of the DP.

If the elements of a magic square are elements of an arithmetic progression, in a separate case, a series of natural numbers $i, j \in (1, n^2)$ (so-called normal squares), then n, n^2 determine the order of the square and the number of its elements. It is clear that if we add a constant number a to each element of the square S_{lj}, i.e., $\hat{S}_{lj} = S_{lj} + a$, or multiply it by a constant b, i.e., $\hat{\hat{S}}_{lj} = bS_{lj}$, then the generating matrices $\|\hat{S}\|$ and $\|\hat{\hat{S}}\|$ are obtained, which also will be magic squares. Non-equidistant arrays obtained on their basis will be equivalent since adding a constant leads to displacement of all elements of the lattice in space, and multiplication by a constant leads to compression or stretching of the regions of spatial frequencies.

When changing the direction of columns or rows in a magic square, the sum of the rows or columns does not change; that is, the square obtained in this way will be at least semi-magical.

7.3. Research of antenna arrays based on magic squares

The results of studies of several antenna arrays obtained using (7.1) for well-known magic squares are shown in Fig. 7.1 and Fig. 7.2: the devil's square of Khajuraho, the squares of Dürer and Dudenay, the square Johnson, as well as the pan-diagonal square [322—325].

The first three are squares of the fourth order, and if the first two are normal (consisting of numbers from 1 to 16), then the squares of Dudena and Johnson are composed of prime numbers. They are unconventional. The last square is a square of the fifth order. All squares, except for Dudenay`s and Johnson`s, are pandiogonal, the so-called devil's squares. For Dürer's square, in addition to the fact that the sum of the numbers on any horizontal, vertical, and diagonal is 34, this sum is also found in all 2 × 2 corner squares, in the central square (10 + 11 + + 6 + 7), in the corner square cells (16 + 13 + 4 + 1), in squares built by the "knight's move" (2 + 8 + 9 + 15 and 3 + 5 + 12 + 14), and in rectangles formed by pairs of middle cells on opposite sides (3 + 2 + 15 + 14 and 5 + 8 + 9 + 12).

Important characteristics of antenna arrays are the filling factor — α:

$$\alpha = \frac{m}{v} \tag{7.10}$$

and the redundancy factor — β:

$$\beta = \frac{m}{\sqrt{S}}, \tag{7.11}$$

where m is the number of array elements and v is the number of numbered nodes of the array in the area where it is located, S is the area occupied by the array.

7	12	1	14
2	13	8	11
16	3	10	5
9	6	15	4

1

7.7	19.12	20.1	34.14
2.9	15.25	23.9	34.25
16.25	19.28	29.19	34.30
7.7	15.34	30.34	34.34

2

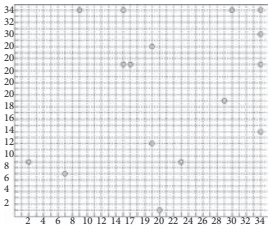

3

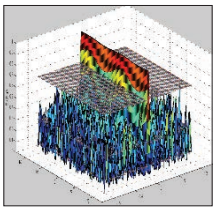

4

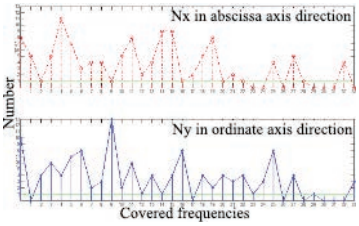

5

16	3	2	13
5	10	11	8
9	6	7	12
4	15	14	1

6

16.16	19.3	21.2	34.13
5.21	15.13	26.13	34.21
9.30	15.19	22.20	34.33
4.34	19.34	34.34	34.34

7

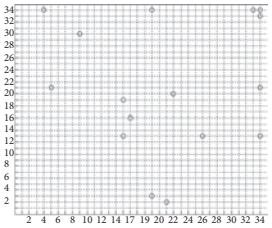

8

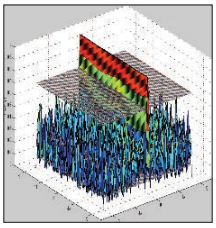

9

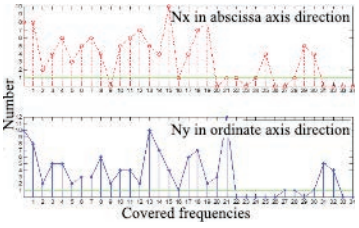

10

Fig. 7.1. Magic squares and characteristics of the antenna arrays obtained from them: Khajuraho devil's square (*1—5*); Dürer's square (*6—10*); *1*, *6* — magic squares; *2*, *7* — coordinates of array elements obtained based on squares; *3*, *8* — arrays based on squares; *4*, *9* — DP of antenna arrays in Cartesian coordinates; *5*, *10* — frequencies that are covered, the upper curve along the abscissa axis, the lower one along the ordinate axis

For rectangular completely filled equidistant array, $S = v = n^2$ and $m = n^2$.

Then the filling factor for them is $\alpha = 1$, and the redundancy factor $\beta = n$ is significant.

For antenna arrays in the form of a Mills cross, $S = v = n^2$, and $m = 3n$. The filling factor $\alpha = \frac{3}{n}$ and the redundancy $\beta = 3$.

3	64	19	37
243	31	5	41
7	11	73	29
67	17	23	13

1

3.3	64.61	83.19	120.37
43.46	74.92	79.24	120.78
7.53	18.10	91.97	120.11
67.12	84.12	107.12	120.12

2

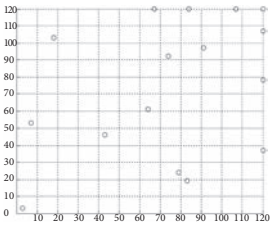

3

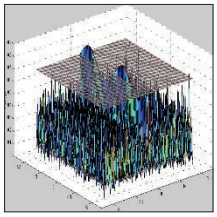

4

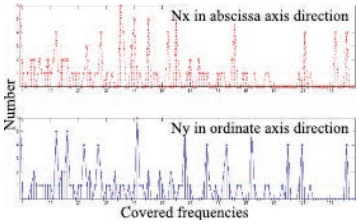

5

1	15	24	8	17
9	18	2	11	25
12	21	10	19	3
20	4	13	22	6
23	7	16	5	14

6

1.1	16.15	40.24	48.8	65.17
9.10	27.33	29.26	40.19	65.42
12.22	33.54	43.36	63.38	65.45
20.42	24.58	37.49	59.60	65.61
23.65	30.65	46.65	51.65	65.65

7

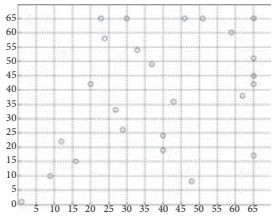

8

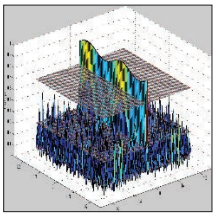

9

Fig. 7.2. Magic squares and characteristics of antenna arrays obtained from them: Johnson square (*1*—*5*); pan-diagonal (5 × 5) square (*6*—*9*); *1*, *6* — magic squares; *2*, *7* — coordinates of array elements obtained based on squares; *3*, *8*, — arrays based on squares; *4*, *9* — DP of antenna arrays in Cartesian coordinates; *5* — the frequencies that are covered, the upper curve along the abscissa axis, the lower one along the ordinate axis

For the antenna array obtained on the basis of the magic square

$$S = v = M^2 = \left(n(n^2+1)/2\right)^2, \text{ and } m = n^2.$$

Fill factor

$$\alpha = 4/\left(n^2+1\right)^2 \qquad (7.12)$$

and excesses:

$$\beta = 2n^2 / n\left(n^2+1\right) = 2n/\left(n^2+1\right). \quad (7.13)$$

Thus, an increase in the order of the magic square used to construct the AA leads to a significant decrease, proportionally $\alpha \approx 4/n^4$ — the filling factor and proportionally $\beta \approx 2/n$ — the redundancy factor.

The basis of the array D is a set of elements, the intervals between which cover the given area D_f.

The optimal basis for the array D is characterized by the minimum values of the redundancy factor.

Since the first lattice element is not located at the origin of the coordinate system, the effect of shifting the origin of the coordinates was investigated so that the nearest of the sources is located on one of the axes. In addition, the option of introducing an additional source at the beginning of the coordinate system was considered. The obtained results are shown in Table 7.1.

It can be seen that in the absence of a source at the origin of the coordinates, when the origin of the coordinates is shifted so that the nearest of the sources falls on one of the axes, the parameters of the main lobe do not change. Adding a source to the origin of the coordinate system, both the initial one and the one obtained by shifting the AA, leads to both a narrowing of the main petal and a decrease in the level of the side lobes. By definition, the element of the magic square is the distance between the elements of the interferometer. Therefore, the first elements of MS are the distance between the AA element placed at the origin of the coordinates and the next AA element, the distance to

Table 7.1. **The influence of the coordinate shift and the introduction of an additional source at the origin of the coordinates on the array DP**

Characteristics of antenna array	Array Start (0.0) No source (0.0)	Array Start (0.0) With a source (0.0)	Array Start (2.1) No source (0.0)	Array Start (2.1) With a source (0.0)
w	0.1572	0.1485	0.1572	0.1499
m	0.2452	0.2447	0.2525	0.2446

Table 7.2. **Characteristics of AA obtained by turning magic squares**

Characteristics of antenna array	S	S*	S′	S′*	S″	S″*	S‴	S‴*
w	0.1485	0.1572	0.1483	0.1585	0.1443	0.1561	0.1441	0.1578
n	0.2447	0.2452	0.2456	0.2536	0.2403	0.2476	0.2459	0.2533

* The element at the origin of the coordinates (0,0) of the array is missing and S′, S″, S‴ denote the rotation of the magic square matrix by 90, 180, 270°, respectively.

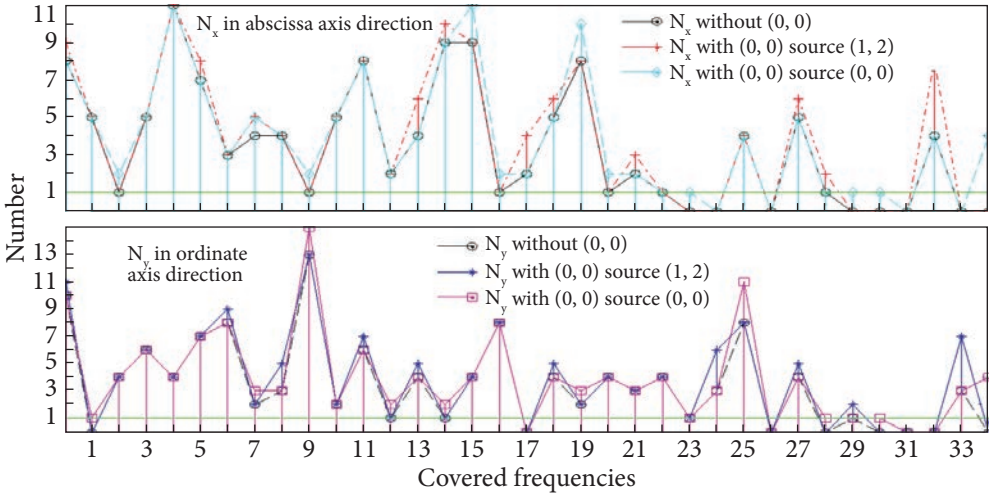

Fig. 7.3. Changing the range of frequencies covered when adding source coordinates to the origin

which determines this element of the square. Initially, this fact was not taken into account; therefore, lattices without a zero element and with it were studied separately. Transferring the coordinate system in the presence of a source to its origin reduces the size of the lattice and expands the level of the main lobe [322—325].

Table 7.2 gives the numerical characteristics of the arrays obtained by rotating the original matrices.

Analysis of the given results allows us to draw the following conclusions:

1. The width of the DP without an element at the beginning of the array is greater than the width in the AA with it, i.e., W (Without (0,0)) > W.

2. The level of side petals without an element at the beginning of the array is greater than with it, i.e., n (Without (0,0)) > n.

3. The width of the DP when turning the AA can decrease in some cases. That is, wS > wS′ > wS′′ > wS′′′.

The change in the frequencies covered when adding the source coordinates to the origin is illustrated in Fig. 7.3.

Additional elements of the array formed by the elements of the magic square were added to ensure full coverage of frequencies. The addition algorithm was as follows. The maximum uncovered frequency was selected, and the coordinates of the element that allowed it to be covered were calculated. After that, frequency coverage was checked, taking into account the new element. If there were still uncovered frequencies, the process was repeated. Again, the maximum uncovered frequency was taken, and the coordinates of the element covering it were determined, and so on, until full frequency coverage was realized. In the second version, a special "Greedy" algorithm was used for full coverage of frequencies due to the introduction of additional elements.

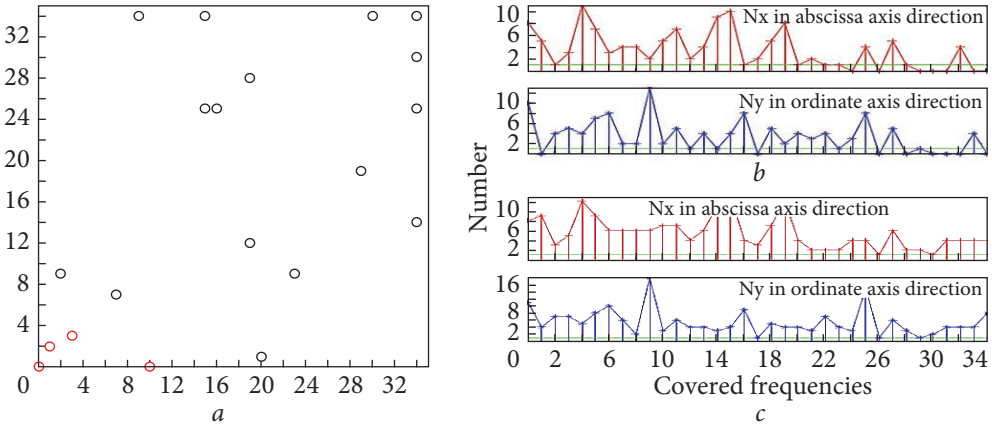

Fig. 7.4. Khajuraho antenna arrays with additional elements (marked in red) provide full coverage (*a*), initial coverage of frequencies (*b*), after the addition of elements (*c*)

Table 7.3. **Comparison of array parameters based on the Khajuraho square with additional elements**

Characteristics of antenna array	Option No.						
	1	2	3	4	5	6	S
Coordinates of additional elements	(1,2) (25,2) (32,32)	(1,32) (25,2) (32,2)	(1,2) (25,32) (32,2)	(1,2) (25,32) (32,32)	(1,32) (25,2) (32,32)	(1,32) (25,32) (32,2)	
Antenna array parameters							
w	0.1476	0.1436	0.1463	0.1532	0.1473	0.1472	0.1572
m	0.2340	0.2305	0.2303	0.2333	0.2337	0.2300	0.2525

The Greedy algorithm is an algorithm that consists of making locally optimal decisions at each stage, assuming that the final solution will also be optimal.

6 options were considered, in each of which the addition was made by 3 elements. The coordinates of the additional elements obtained at the same time, the values of the width of the main lobe, and the average level of the side lobes of the arrays, obtained based on the Khajuraho square, are given in Table. 7.3. The following designations are used in the table: w — the width of the main lobe at the 3dB level, m — the average level of the side lobes.

As an example, Fig. 7.4 shows AA with additional elements, built on the basis of the square of order 4, the frequency range covered, as well as the DP obtained in this case [322—325]. The introduction of additional elements into a rarefied antenna array, as expected, leads to a decrease in the level of side lobes. When comparing the characteristics of the grids given in Table 7.3 for different options for completing the square with elements, it can be seen that option 6 (1,32) (25,32)

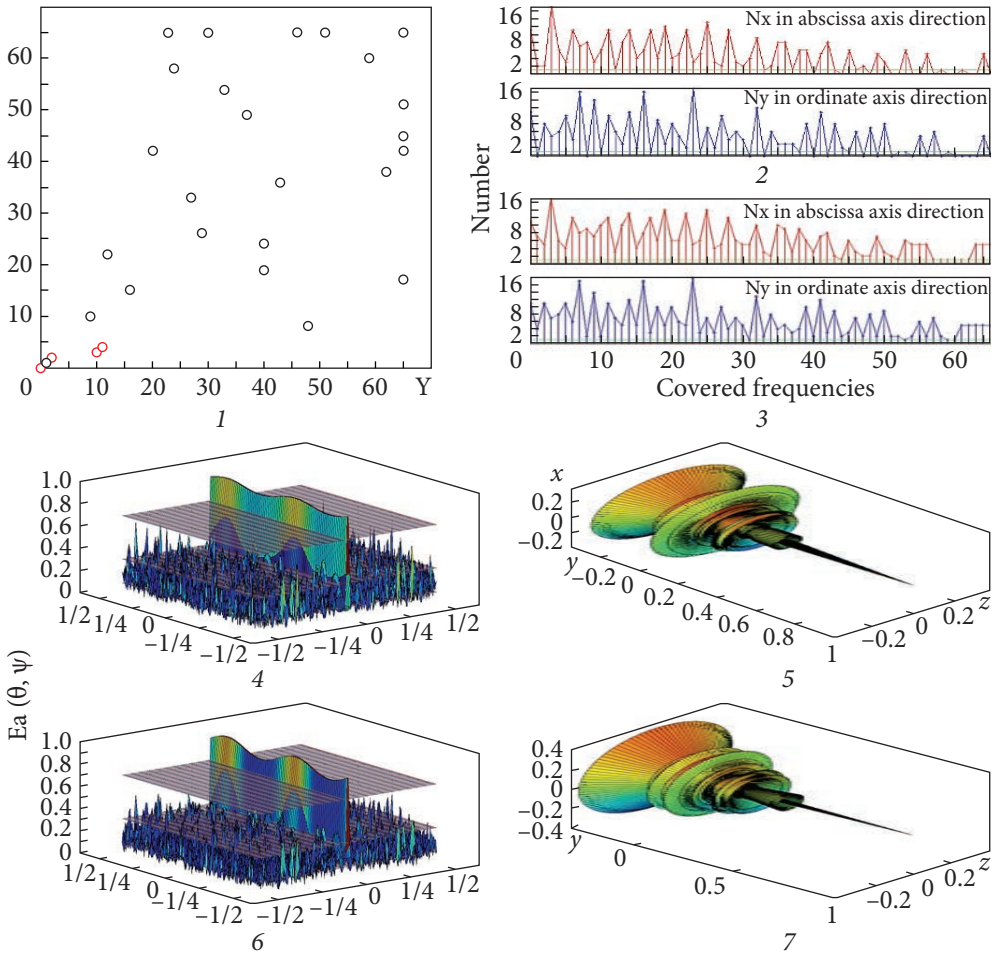

Fig. 7.5. AA based on the pan-diagonal square of the 5th order (*1*), frequencies covered (*2*) (original AA), (AA with additional elements) (*3*), DP of the original AA (*4*, *5*), and with additional elements (*6*, *7*). Cartesian (*4*, *6*) and polar (*5*, *7*) coordinates

(32,2) is the best because it has the lowest average level of side lobes m and the smallest width of the main lobe.

Options 2 (1, 32) (25, 2) (32, 2) and 3 (1, 2) (25, 32) (32, 2) also give good results. Comparison of options 2, 3, and 6 shows that they have one point in common (32, 2). When comparing options 2, 5, and 6, it can be noted that these three options also have one point in common (1, 32).

Fig. 7.5 presents the AA of the pan-diagonal "magic" square and the frequency ranges covered, as well as the obtained DP.

The characteristics of the pan-diagonal "magic" square shown in Fig. 7.5 are presented in Table 7.4.

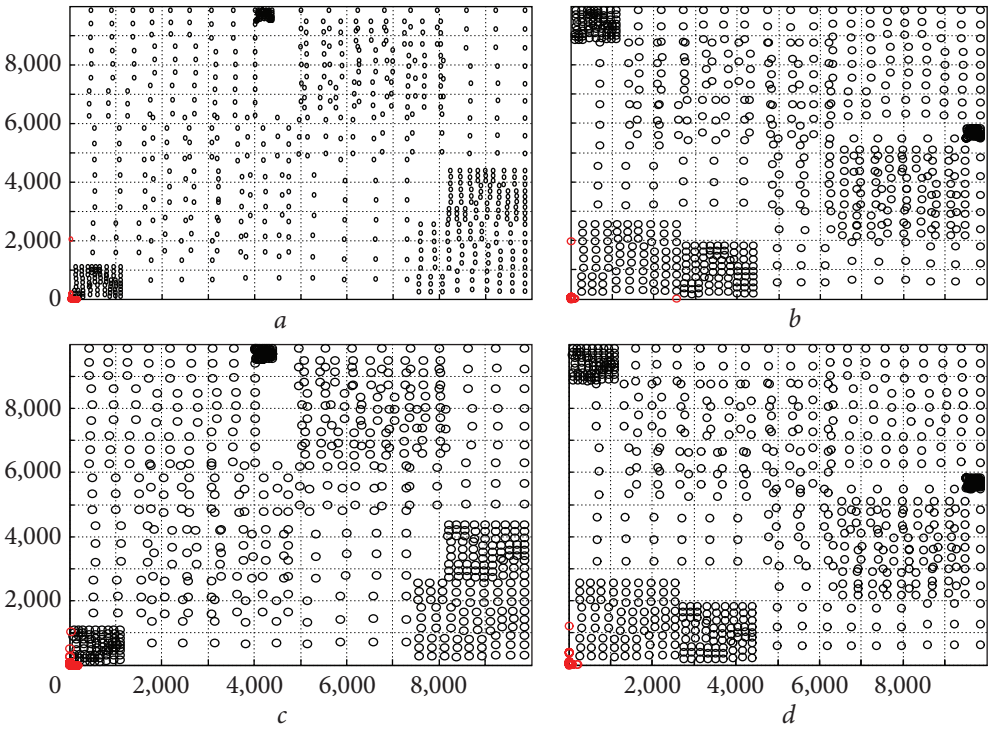

Fig. 7.6. AA of the third level of nesting based on the "magic" square of Khajuraho: *a* — initial AA based on the "magic" square; *b* — AA with the second layer rotated by 90° and with the third layer rotated by 180°; *c* — AA with the first layer rotated by 90°; *d* — AA with the first and second layers rotated by 90°

Table 7.4. **AA parameters for various coordinate matrices based on the "magic" pan-diagonal square**

AA parameters	$\|\|Z_0\|\|$	$\|\|Z_0^*\|\|$	$\|\|Z_{0+}\|\|$	$\|\|Z_+^*\|\|$
$\Delta w_{0.707}$ (Rad)	0.1723	0.0936	0.1345	0.0905
m	0.2032	0.1546	0.2023	0.1506
α	0.0059	0.0118	0.0069	0.0123
β	0.3846	0.7692	0.4462	0.800

$||Z_0||$ original matrix, $||Z_0^*||$ — conjugated matrix, $||Z_{0+}||$ — original matrix supplemented with elements up to full coverage, $||Z_+^*||$ — conjugated matrix supplemented with elements providing full coverage.

For most of the existing methods of synthesis of sparse antenna arrays, serious difficulties arise with large aperture sizes and many elements. Currently, there are no problems with creating magic squares up to order 35. At the same time, the creation of larger arrays is of interest. For this purpose, nested magic

(0.1)	(0.12)	(1.2)	(1.11)
(2.0)	(3.4)	(3.9)	(5.0)
(6.0)	(7.5)	(7.8)	(10.6)
(10.7)	(11.0)	(15.3)	(15.10)

a

(0.0)	(0.3)	(0.4)	(0.7)
(4.0)	(4.3)	(4.4)	(4.9)
(5.0)	(5.3)	(5.4)	(5.9)
(6.0)	(6.3)	(6.4)	(6.9)
(13.0)	(13.3)	(13.4)	(13.9)

b

(67.67)	(68.1)	(111.43)
(13.80)	(50.38)	(111.104)
(31.111)	(104.111)	(111.111)

c

(7.7)	(19.12)	(20.1)	(34.14)
(2.9)	(15.25)	(23.9)	(34.25)
(16.25)	(19.28)	(29.19)	(34.30)
(9.34)	(15.34)	(30.34)	(34.34)

d

(3.3)	(64.61)	(83.19)	(120.37)
(43.46)	(74.92)	(79.24)	(120.78)
(7.53)	(18.103)	(91.97)	(120.107)
(67.120)	(84.120)	(107.120)	(120.120)

e

(16.16)	(19.3)	(21.2)	(34.13)
(5.21)	(15.13)	(26.13)	(34.21)
(9.30)	(15.19)	(22.20)	(34.33)
(4.34)	(19.34)	(33.34)	(34.34)

f

(1.1)	(16.15)	(40.24)	(48.8)	(65.17)
(9.10)	(27.33)	(29.26)	(40.19)	(65.42)
(12.22)	(33.54)	(43.36)	(62.38)	(65.45)
(20.42)	(24.58)	(37.49)	(59.60)	(65.51)
(23.65)	(30.65)	(46.65)	(51.65)	(65.65)

g

Fig. 7.7. Coordinate matrices of AA elements: $Z_{\text{CDS }16}$ — based on the CDS with the number of elements 16 [197] ($\nu = 15 \times 12$) (*a*), $Z_{\text{CDS }20}$ — based on the CDS with the number of elements 20 [197] ($\nu = 13 \times 9$) (*b*), $Z_{\text{Deu }3}$ — based on "magic" square of Deudena of the 3rd order (*c*), $Z_{\text{Kh }4}$ — based on the "magic" square of Khajuraho of the 4th order (*d*), $Z_{\text{J }4}$ — based on the "magic" square of Johnson of the 4th order (*e*), $Z_{\text{Dür }4}$ — based on the Dürer's "magic" square of the 4th order — *f*, $Z_{\text{pan }5}$ — based on the pan-diagonal "magic" square of the 5th order (*g*)

squares [241] can be used, making it possible to synthesize antenna arrays of large sizes using the proposed approach.

As an example, Fig. 7.6 presents antenna arrays of the third nesting level, built based on a "magic" square of the fourth order with different rotation parameters of the first, second, and third layers of nested matrices. There, additional elements shown in red make it possible to achieve full frequency coverage. It should be noted that the density of the placement of elements along the antenna array is significantly uneven.

The algorithm for supplementing the elements of the array formed by the elements of the magic square with additional elements to ensure full coverage of

the AA frequencies can be used just as effectively to build an AA based on the nested square [322—325].

We compare the parameters of antenna arrays built based on some well-known "magic" squares of the 3rd, 4th, and 5th orders with antenna arrays based on cyclic difference sets (CDS). Fig. 7.7 shows the parameters of the coordinate matrices of the compared AA.

Table 7.5 presents the characteristics of antenna arrays built based on the specified coordinate matrices.

The "$_+$" index indicates the AA parameters based on the original coordinate matrices with the addition of elements for full spatial frequency coverage, and the "*" indicates the combined matrices.

Table 7.5. **Comparative analysis of parameters of different AA**

Parameters	$\Delta w_{0.707}$(Rad)	m	α	β
$Z_{\text{CDS 16}}$	0.3739	0.2396	0.0889	1.1926
$Z_{\text{CDS 20}}$	0.4225	0.2029	0.1709	1.8490
$Z_{\text{CDS 20+}}$	0.3726	0.1926	0.1966	2.1264
$Z^*_{\text{CDS 20}}$	0.2444	0.1423	0.3419	3.6980
$Z^*_{\text{CDS 20+}}$	0.2297	0.1360	0.3761	4.0678
$Z_{\text{Deu 3}}$	0.2235	0.3601	0.00073	0.0811
$Z_{\text{Deu 3+}}$	0.1002	0.1942	0.0028	0.3153
$Z^*_{\text{Deu 3}}$	0.1025	0.2577	0.0015	0.1622
$Z^*_{\text{Deu 3+}}$	0.0638	0.1510	0.0044	0.4865
$Z_{\text{Kh 4}}$	0.1572	0.2525	0.0138	0.4706
$Z_{\text{Kh 4+}}$	0.1958	0.2465	0.0173	0.5882
$Z^*_{\text{Kh 4}}$	0.1473	0.1792	0.0277	0.9412
$Z^*_{\text{Kh 4+}}$	0.1524	0.1870	0.0294	1.0000
$Z_{\text{J 4}}$	0.1109	0.2643	0.0011	0.1333
$Z_{\text{J 4+}}$	0.0731	0.2022	0.0023	0.2750
$Z^*_{\text{J 4}}$	0.0728	0.1905	0.0022	0.2667
$Z^*_{\text{J 4+}}$	0.0602	0.1552	0.0033	0.4000
$Z_{\text{Dür 4}}$	0.1563	0.2617	0.0138	0.4706
$Z_{\text{Dür 4+}}$	0.1467	0.2300	0.0173	0.5882
$Z^*_{\text{Dür 4}}$	0.1464	0.1847	0.0277	0.9412
$Z^*_{\text{Dür 4+}}$	0.1465	0.1778	0.0294	1
$Z_{\text{pan 5}}$	0.1723	0.2032	0.0059	0.3846
$Z_{\text{pan 5+}}$	0.1345	0.2023	0.0069	0.4462
$Z^*_{\text{pan 5}}$	0.0936	0.1546	0.0118	0.7692
$Z^*_{\text{pan 5+}}$	0.0905	0.1506	0.0123	0.800

Table 7.5 shows that:

• AA based on the CDS with a matrix of coordinates connected to the original $Z^{*}_{\text{CDS }20}$ has a much smaller width of the main one and a lower level of side lobes of the DP, although, at the same time, the redundancy of AA is much higher. Adding additional elements ($Z_{\text{CDS }20+}$ and $Z^{*}_{\text{CDS }20+}$) allows you to achieve full coverage of spatial frequencies and also reduces the width of the main lobe and the level of the side ones;

• the use of "magic" squares for AA synthesis generally provides better characteristics than the use of CDS. Moreover, the use of related coordinate matrices allows the narrowing of the width of the main petal and reducing the level of the side lobes in comparison with the original matrices, although at the same time the redundancy of AA increases (compare, for example, with $Z_{\text{Deu }3}$ and $Z^{*}_{\text{Deu }3}$);

• the application of the algorithm proposed above to ensure full coverage of spatial frequencies leads to a slight narrowing of the main and side lobes of the DP and also increases the redundancy of the AA;

• among the presented AA based on "magic" squares, the AA based on the Khajuraho square of the 4$^{\text{th}}$ order had the worst characteristics (see $Z_{\text{Kh }4}$, $Z^{*}_{\text{Kh }4}$, $Z^{*}_{\text{Kh }4+}$). At the same time, the smallest width of the main lobe and the level of the lateral ones among AA based on "magic" squares of the 4-th order are ensured in AA based on the Johnson square ($Z^{*}_{\text{J }4+}$). This is obviously due to the fact that the squares of Johnson and Dudeney are not normal but are composed of simple numbers. Because of this, they allow covering rather large areas of spatial frequencies with a low density of elements.

7.4. Elements of measuring complexes of active-passive remote sensing of the environment in the HF band

When solving the problem of optimizing antenna systems of the decameter band along with minimizing the total number of antenna array elements, it is necessary to create small-sized antenna devices with satisfactory electrical parameters. To solve this problem, both experimental and theoretical research on the electrical characteristics of small-sized antennas, as well as research into qualitatively new methods of developing small-sized antennas, are necessary.

A promising direction for improving existing and creating new non-traditional antennas is the use of delayed electromagnetic waves [342]. The slowing down of electromagnetic waves is accompanied by an increase in the efficiency of the wave's interaction with the environment, proportional to the amount of the slowing down. Slow electromagnetic waves are often called surface waves, referring to the surface nature of their distribution. Specific systems that slow down require the use of appropriate models. As a retarding structure that reduces the phase speed of the wave excited in the antenna structure, consider a spiral

vibrator, which can be represented by a set of frames and rectilinear segments through which current flows [343], Fig. 7.8.

Each of the turns of the spiral, due to its small size, can be represented as the sum of a flat turn, where D is its diameter and an axial linear segment of length S equaled the distance between the turns, as shown in Fig. 7.8.

The radiation field of such a conductor in directions normal to the axis, that is, at $\theta = 90°$, has only one component of the electric vector E_θ, equal to

$$E_\theta = -j\frac{30kI_0S}{r}e^{-jkr}. \tag{7.14}$$

A flat turn creates a field having one component E_φ, which is equal

$$E_\varphi = \frac{60I_0}{r}\frac{\pi}{2}(ka)^2 e^{-jkr}, \tag{7.15}$$

where I_0 is the current amplitude, k is the wave factor and $a = D/2$ is the spiral radius.

$$\left|\frac{E_\varphi}{E_\theta}\right| = \frac{\left(\frac{\pi D}{\lambda}\right)^2}{\left(\frac{2S}{\lambda}\right)}. \tag{7.16}$$

The ratio (7.16) is determined by the electrical dimensions S/λ and D/λ of the spiral and characterizes the ellipticity of the radiated field in the far zone.

When $L << \lambda$, where L and λ are the length of the spiral turn and the wavelength, the antenna works in the transverse radiation mode. In this mode, the currents in diametrically opposite points of the coil have the opposite direction in space, and the radiation resistance of the coil will be very small (frame effect). For a multi-turn spiral at $\frac{nL}{\lambda} < 1$, where n is the number of turns, the radiation along the axis of the spiral is zero, the maximum radiation of each turn and the entire antenna is in the transverse plane of the spiral, and the standing wave mode is established in the antenna. From the analysis of dependencies (7.14) — (7.16), it follows that along the spiral structure of the antenna operating in the mode of transverse radiation, there is a slowing down of the electromagnetic wave on the surface of the vibrator, which depends on the diameter and pitch of the spiral, as

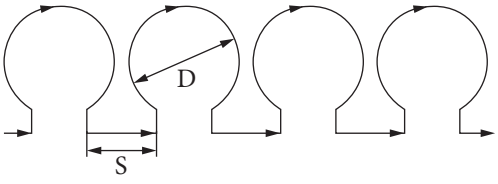

Fig. 7.8. Equivalent circuit of a spiral vibrator in the form of round flat frames and electric dipoles

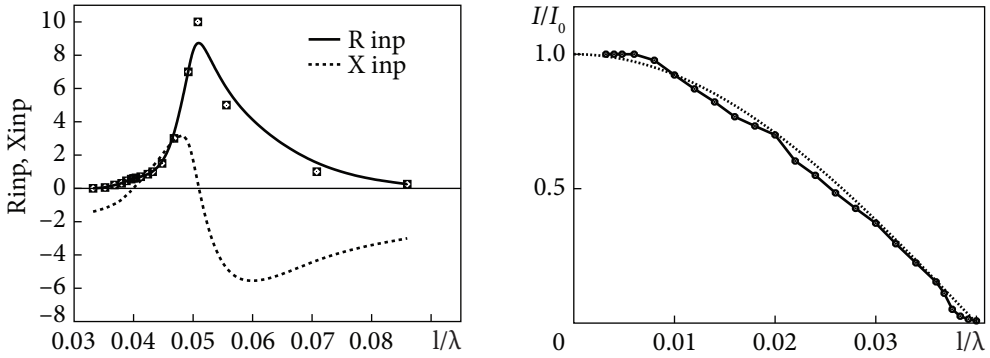

Fig. 7.9. Active and reactive components of the input impedance of the vibrator

Fig. 7.10. Current distribution along the shoulder of a spiral vibrator at the first resonance

well as on the working wavelength, which indicates the presence of dispersion in the spiral structure of the antenna. Fig. 7.9 and Fig. 7.10 present the results of experimental studies of the input impedance and surface current distribution of a symmetrical vibrator, the arms of which consist of cylindrical spirals with a diameter and pitch small compared to the length of the vibrator.

In Fig. 7.9, it can be seen that the first resonance (sequential) occurs at 0.04 l/λ; at 0.051 l/λ, a second resonance (parallel) is observed with a significant increase in active resistance. Fig. 7.10 shows the surface current distribution along the arm of the spiral vibrator at the first series resonance, which is close to sinusoidal in shape and corresponds to the current distribution of a half-wave symmetrical vibrator. At the same time, the measured wave retardation factor was 6.25. From the expression for the amount of deceleration given in [344],

$$\frac{c}{v} = \sqrt{1 + 20(ND)^{2.5}\left(\frac{D}{\lambda}\right)^{0.5}}, \qquad (7.17),$$

where c is the speed of light, v is the phase speed of the wave along the vibrator, N is the number of turns per unit length, D is the diameter of the turn, λ is the wavelength at resonance, we get the value of the retardation coefficient $c / v = 5{,}3$.

Fig. 7.11 shows the dependence of the deceleration of the electromagnetic wave on the surface of the vibrator on the ratio of the diameter D of the spiral and the length l of the vibrator arm; an increase in the D/l ratio from 0.01 to 0.3 leads to an increase in the deceleration coefficient from 3.7 to 8.2.

Fig. 7.12 presents the measured dependence of the Q-factor of a spiral vibrator on its electrical length (curve *2*) and the Q-factor of a rectilinear vibrator with a shoulder length of 1 m (curve *1*). Because the ohmic losses of the spiral vibrator are relatively small (0.1 Ohm), the spiral vibrator is more broadband and convenient for matching with the load.

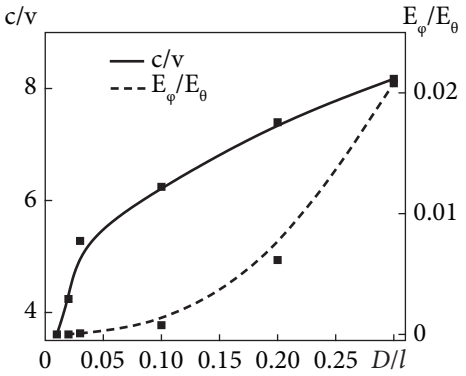

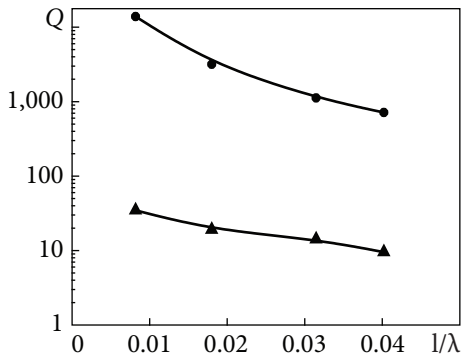

Fig. 7.11. Dependence of the wave deceleration on the surface of the spiral vibrator and the relative intensity of the electric field of the orthogonal component on the ratio D/*l*

Fig. 7.12. Dependence of the Q factor of a linear thin (curve-1) and a spiral symmetric vibrator (curve-2) on the ratio *l*/λ

In view of the small dimensions of this vibrator and the lack of disadvantages of asymmetrical antennas, which require good grounding, which is practically impossible when using them in mobile radio complexes based on a retarding radiating structure in the form of a spiral half-wave symmetrical vibrator operating in the mode of transverse radiation, a reflector-calibrator for external calibration is proposed Radar and RCS simulations of moving radar targets [328].

By its structure, the reflector-calibrator is an ordinary wire antenna operating in the mode of reflecting signals. The specified mode is achieved by short-circuiting the antenna at the feeder connection point. When a wave falls on such a reflector, an electromotive force is induced in it, under its influence flows a current, which creates a secondary, scattered field. In the general case, the RCS of an object scattering an EM wave field is described by formula (7.18) [345]

$$\sigma = 4\pi R^2 \left(\frac{E_s}{E_i} \right), \tag{7.18}$$

where R is the distance from the scattering object to the observation point; E_s is the amplitude of the scattered field at the point of observation; E_i is the field amplitude of the irradiating wave at the location point of the scattering antenna.

In an antenna made of a perfect conductor, all the received energy is reflected, creating a scattered field.

If the wave falls on the dipole at an angle θ, the polarization of the incident wave and the vibrator coincide, the electrical length of the vibrator l is equal to λ/2, then the value of its RCS is determined by formula (7.19).

$$\sigma = 0.86\lambda^2 \cos^4 \theta \,. \tag{7.19}$$

If the angle θ = 0, then the RCS will be maximum and will be from 86 to 8,600 m^2 for the decameter range (λ = 10…100 m). For an antenna with impedance Z_a, loaded with a load with impedance Z_l, the RCS can be estimated using formula (7.20) [346].

$$\sigma \approx \frac{4AGR_a^2}{\left|Z_a + Z_l\right|}, \qquad (7.20)$$

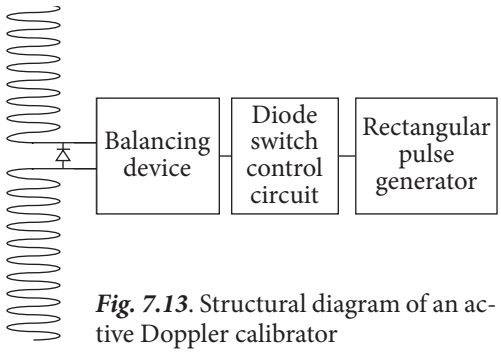

Fig. 7.13. Structural diagram of an active Doppler calibrator

where the aperture value $A = \frac{\lambda^2}{4\pi}G$, G is the gain of the antenna, $R_a = Re(Z_a)$. Based on the formula (7.20), if the antenna is not loaded at all (mode OC), then the RCS will be equal to 0, and there will be no scattering. For a half-wave resonant vibrator, if its shoulders are opened, 2 quarter-wave vibrators will reflect, and their RCS is 22...25 dB lower than a half-wave one, and given the fact that there are two of them and they are in-phase, the level will be approximately 16 dB lower than that of a short-circuited one [200, 347].

The dependence of the RCS antenna on the load can be used to modulate the scattered signal by amplitude [346, 348]. Switching the input of the reflector leads to the appearance of deterministic components in the signal spectrum, which allows the simulation of the RCS of a moving radar target.

Structurally, the vibrator consists of a dielectric cylinder with a diameter of 5 cm, on which two arms of the vibrator are placed in the form of spirals with a step of 1 cm. A switching unit is installed in the center of the vibrator [328].

The simplest modulator circuit is a diode key circuit with the inclusion of a diode at the antenna input. The key circuit is controlled by a modulating pulse signal with a repetition rate corresponding to the Doppler frequency of the moving target.

Fig. 7.13 shows the structural diagram of the Doppler reflector. It consists of a rectangular pulse generator that can be rebuilt, a diode switch control circuit, and a balancing device connected to the input of a spiral half-wave symmetrical vibrator operating in the mode of transverse radiation.

Periodic opening and closing of the diode at the antenna input lead to amplitude modulation of the scattered signal with two sidelines in the spectrum corresponding to the spectrum of the modulating signal. When the scattered signal is modulated by the responder with a pulse sequence of the "meander" type, the spectrum of the reflected signal contains odd multiples of the frequency of repetition of the modulating signal, shifted relative to the carrier in both directions, spectral lines that imitate targets approaching and receding at different speeds and RCS.

The large deceleration factor of the surface wave of the spiral vibrator creates the first resonance at a frequency of ~10 MHz with the full geometric length of the vibrator ~1.8 m, which corresponds to the electrical length of the vibrator at this frequency ~15 m.

Conclusions

1. Solving the problem of optimizing antenna systems, which is especially relevant when creating antenna systems of the decameter range, a technique for the synthesis of non-equidistant antenna arrays was developed based on the use of the properties of magic squares. The properties of the obtained antenna arrays were studied. It is shown that when placing array sources, using the values of elements of "magic" squares, it is possible to obtain almost complete coverage of spatial frequencies in the area of placement of elements with small filling factors of up to 0.01 and redundancy of less than 0.5.

2. It was established that supplementing the aperture of the antenna synthesized based on the "magic" square with elements obtained by inversion modulo the "magic" constant allows to reduce the level of side lobes significantly and improve the coverage of spatial frequencies.

3. It is shown that the synthesis of large AA is possible using the nesting of several magic squares. The algorithm for supplementing the elements of the grid formed by the elements of the magic square with additional elements to ensure full coverage of the AA frequencies can be used just as effectively to build an AA based on a folded square. By using the mutual rotations of individual layers included in the grid being synthesized, it is possible to improve its characteristics significantly.

4. It is shown experimentally that a symmetrical spiral vibrator with a small diameter and pitch of the spiral compared to the wavelength is a retarding structure in which resonances take place when an integer number of half-waves is stacked along the vibrator. The geometrical dimensions of such a vibrator can be up to 10 times smaller than those of a traditional linear symmetrical vibrator, while differing in a wider band of operating frequencies.

5. A reflector-calibrator created based on a decelerating structure in the form of a spiral half-wave symmetric vibrator operating in the mode of transverse radiation is proposed for the external calibration of the radar and simulation of the RCS of a moving radar target.

CHAPTER 8

Smart Grid technology for increasing the efficiency of ground equipment facilities

The development of robotic sensors, communication channels, and means of information storing and processing leads to the fact that control systems become fully intelligent systems with distributed intelligence (Smart Grid). Until now, Smart Grid technologies have not found a worthy application for increasing the efficiency of using ground facilities. The scientific foundations of building cloud-based intelligent networks from ground technology objects, integration of sensors of various types and wavelength ranges, and methods of evaluating the effectiveness of the proposed approaches are considered in this section. The main results of the section are published in papers [322, 349, 350—352, 353].

8.1. Introduction of the concept of Smart Grid

Initially, the Smart Grid was considered a promising concept for future energy [174, 175]. Then, these approaches were used in many areas, including in the development of the "smart house" concept [354—357].

Recently, Smart Grid systems have been understood as systems with separate intelligence, so-called cloud systems, in which each link solves tasks within the scope of its competence, exchanging the obtained results with links of both higher and lower levels and using the capabilities of subsystems of a higher level of the hierarchy to solve its problems.

Smart Grid can be described by the following aspects of functioning [174, 175, 354—357]: flexibility, availability, reliability, and economy.

Similar principles can be used in the construction of intelligent distributed networks for the management of objects of military equipment.

For the first time, the principles of Smart Grid technologies were implemented in the Granit missile complex with the P-700 anti-ship cruise missile of long-range underwater-surface launch,

developed in 1970, 20th century [176]. It is designed to defeat aircraft carrier groups. The complex provides volley fire with all ammunition with a rational spatial arrangement of missiles and allows it to act against a single ship according to the principle of "one missile-one ship" or "swarm" against an order of ships. In flight, missiles exchange information about targets. If the "gunner" missile is intercepted, then one of the other missiles automatically takes over its functions [176]. The computer contains data on countermeasures against the enemy's radio-electronic warfare, capable of deflecting missiles away from the target by creating obstacles and tactical techniques for evading the fire of anti-aircraft defense [176].

These ideas were further developed in the following anti-aircraft missile complexes — "Yakhont", "Onyx", and "BraMos" [177, 358, 359]. In order to avoid mistakes when choosing a maneuver and hitting a specific target, the on-board computer contains "portraits" of all modern classes of ships in the form of information about electromagnetic and other force fields, peculiar only to this type of ship, as well as information about the type of orders of ships, which allows the missile to attack the main targets in the group.

And if the principles of building intelligent distributed networks are already used in air defense and anti-missile defense systems, their implementation is now an urgent task for ground equipment objects.

The first steps in this direction were taken with the creation of the Russian platform "Armata" (T-14) [178].

Unlike traditional tanks, the T-14 is a "network-centric tank", i.e., it is not intended for single combat but for working with a group of different combat vehicles in one tactical link, performing the functions of reconnaissance, targeting, and remote control through a unified tactical link control system from the "Suzirya" concern [178]. This allows all the machines of the Armata platform to receive the operational situation in real-time and automatically calculate ballistic data for fire control systems in the scenario of hitting targets not by one Armata but by the entire group at once, which includes, in addition to the T-14, several T-15 heavy infantry fighting vehicles, 2C35 "Koalitsiya-SV" self-propelled guns and an attack helicopter [178].

The given examples show that in the implementation of Smart Grid technologies for the management of objects of military equipment, the key issues are the creation of multi-channel sensors for displaying information scenes that use different physical fields, as well as the automation of information exchange processes between different participants of scenes and control points.

8.2. Sensors and channels for obtaining information about the surrounding environment of ground equipment objects

Sensors that use electromagnetic fields. The main channels for obtaining information in ground equipment facilities, in particular armored vehicles (AV), are

optical and infrared devices with a range of up to 5 km during the day and up to 3 km at night.

The main technical characteristics of the optical and IR sensors used in domestic and foreign AV, borrowed from the work [179], are given in Table 4.1 of Appendix 4.

In addition to electromagnetic waves of the optical and IR ranges, existing radiations of ground and space-based systems of other wavelength ranges [38, 244, 251], TV centers [38], HF broadcasting stations [39, 40, 41, 61, 222, 224, 298, 299, 360], geostationary TV and navigation satellites [128, 148, 149] as well. For reconnaissance tasks, the acoustic noises of technical objects can be used [1, 12, 13, 30, 67, 68, 180]. Below, we will briefly consider the possibilities of using each of these additional information channels, as well as the resulting effect.

RCS of technical objects in the HF and VHF bands. In order to calculate the range of active-passive systems, which are used for illumination of the signals of HF and VHF broadcasting stations, the own radio stations of ground equipment objects, the signals of navigation and geostationary TV satellites, knowledge of the RCS of detected ground and air objects is necessary.

Using the results of experimental studies on models [167, 201, 253], in papers [40, 198] a method was proposed and the RCS of air objects was calculated. The RCS values of aerial objects (planes, helicopters, UAVs), both in the resonant and short-wave bands, obtained using these techniques are given in Chapter 3. The RCS values of ground objects were evaluated in a similar way. General RCS data of various types of equipment are given in Table 4.2 of Appendix 4.

In the resonant region of scattering, RCS for both air and ground objects can have a significant value, reaching hundreds of square meters. At the same time, in the short-wave band, their RCS is significantly lower. The obtained results show the expediency of using HF and VHF systems to solve the tasks of reconnaissance of ground and air objects of equipment.

Illumination with the use of radiation from broadcast radio stations. The peculiarity of this type of radar is the use of an ionospheric wave of a broadcasting station to illuminate the place. The power of the signal scattered from the target is determined by the ratio:

$$P_T = \frac{P_{Tr} G_{Tr} G_R F^2(\theta_T) \sigma_T(\theta_{Tr}, \theta_R) \lambda^2}{(4\pi)^3 R_{TrT}^2 R_{TR}^2 L_{TrT} L_{TR}}, \tag{8.1}$$

where P_{Tr}, P_T is the power of the received signal transmitted and scattered from the target; G_{Tr}, G_R is the gain coefficients of transmitting and receiving antennas; R_{TrT}, R_{TR} are the range between the transmitter and the target, the target and the receiver, respectively; $\sigma(\theta_{Tr}, \theta_R)$ is bistatic RCS of the target with directions to the transmitter and receiver θ_{Tr}, θ_R, respectively; L_{TrT}, L_{TR} are losses during the propagation of radio waves from the transmitter to the target and from the target to the receiver, respectively; λ is the wavelength of the signal at the carrier.

Power P_R of the signal received from the transmitting station:

$$P_R = \frac{P_{Tr} G_{Tr} G_R F^2(\theta_{Tr}) \lambda^2}{(4\pi)^2 R_{TrR}^2 L_{TrR}}, \tag{8.2}$$

where $F^2(\theta_{Tr})$ is the value of the power directional pattern of the receiving antenna in the direction of the transmitter — θ_{Tr}.

When the distance from the illuminating station to the target and the receiving system is significantly greater than the distance from the target to the receiver $R_{TrT}^2 \approx R_{TrR}^2 >> R_{TR}^2$, taking into account that the losses during propagation to the target and the receiver are approximately the same $L_{TrT} \approx L_{TrR}$ (the target in the first approximation can be considered isotropically reflective $\sigma_T(\theta_{Tr}, \theta_R) \approx \approx \sigma_T = const$ and that which is within the direct line of sight of the receiving system $L_{TR} \approx 1$), the ratio of the power of the signals received from the target and the transmitter of the broadcasting station μ_{TR} is determined by the ratio:

$$\mu_{TR} = \frac{P_T}{P_R} \approx \frac{F^2(\theta_T)}{F^2(\theta_{Tr})} \frac{\sigma_T}{(4\pi)\ R_{TR}^2}. \tag{8.3}$$

It can be seen from (8.3) that in order to increase the ratio of the signal from the target to the direct signal of the transmitter of the illumination station, it is necessary to increase the ratio of the values of the diagram multiplier in the directions to the target and to the illumination station. At the same time, it is advisable to orient the maximum of the directional pattern in the direction of the target and form the "zero" of the directional pattern of the illumination station. The depth of the "zero" in the pattern will limit the maximum detection range. Also, increasing of the SNR can be achieved through the use of narrow-band Doppler filtering. It is known that the spectrum of backscattering from air, surface, and ground objects is quite narrow, even in the microwave range. The spectrum width of the body line does not exceed 10 Hz [40, 288]. In the HF and VHF wavebands, it is even narrower — less than 1 Hz. The value of the Doppler frequency shift (from several Hz to tens of Hz) has approximately the same order of values [40]. With Doppler selection, it is possible to distinguish the spectral line of the signal scattered by the object at the Doppler frequency. The SNR μ will be determined by the ratio of the signal of the target μ_{TR} to the illumination signal, as well as the ratio of the carrier spectral line level to the spectral noise density in the range of Doppler frequencies (velocities) where the target μ_{SN} is detected:

$$\mu = \mu_{TR} \mu_{SN} \tag{8.4}$$

Using relation (8.3), you can write down the expression for estimating the detection range in bistatic radars:

$$R_{TR} = \sqrt{\frac{\mu_{SN}}{\mu} \frac{\sigma_T}{(4\pi)} \frac{F^2(\theta_T)}{F^2(\theta_{Tr})}}. \tag{8.5}$$

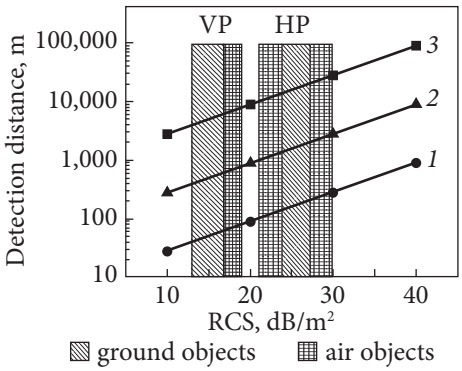

Fig. 8.1. Distances of object detection when using backlighting by broadcasting stations of the HF band (the depth of the "zero" of the antenna directional pattern in the direction of illumination: *1* — 0 dB, *2* — 20 dB, *3* — 40 dB); HP, VP — horizontal and vertical polarization

For detection probabilities of 0.9, false alarms of m^{-2} (the required SNR is about μ = 10 dB), noise levels in relation to the carrier μ_{SN} = 40...50 dB when tuned to Doppler frequency shifts, the expected detection ranges of objects with different RCS at different depths of "zero" of the receiving antenna directional pattern in the direction of the transmitter, obtained using ratio (8.5), are shown in Fig. 8. 1. In the same figure, shaded areas show RCS values of ground and air objects of equipment, taken from Table 4.2 of Appendix 4. To obtain RCS estimates of various types of objects in the decameter wavelength range, the results shown in Fig. 8.1, 8.2 were used.

The analysis shows that by ensuring the suppression of the direct illumination signal by at least 30...40 dB, it is possible to ensure detection distances in several kilometers for targets with an RCS of more than 10 m^2.

Such or larger RCS in the decameter band have objects of both ground and air equipment. Detection distances are slightly longer when using horizontal polarization of radiation and reception than vertical polarization, which is explained by larger values of their RCS in this polarization. To implement a deep suppression of the direct signal of illumination, it is necessary either to form the "zero" of the directional pattern in the direction of the transmitter, for example, by the interferometric method using two antennas or to use polarization methods of suppression of the direct signal.

Illumination of the environment using the radiation of our own radio stations of the HF and VHF bands installed on the equipment. In addition to external sources of illumination by objects of ground equipment, own means of communication in the form of HF and VHF radio stations can be used for these purposes. For a group of technical objects, the following algorithm can be proposed for the use of its own means of radio communication to illuminate the situation. Each of the objects in the group continuously emits a monochromatic or amplitude- or frequency-modulated signal during a certain time Δt, which is determined by the required Doppler frequency difference Δf:

$$\Delta t = 1/\Delta f. \tag{8.6}$$

Since the width of the Doppler line of scattering from the body of aerial objects is less than 1 Hz, the duration of the illumination signal should be several seconds so that it does not expand due to the limited exposure time. Each of the objects can illuminate the environment at its own frequency. At the same time, the frequency can be used to determine the number of the object and its coordinates. At the same time, it is possible to combine the walkie-talkie mode with the emission of a chirp signal. Therefore, the mode proposed by us can be called chirp-walky-talkies. A feature of this mode of active-passive radar, in comparison with the previously considered case, is the illumination of the situation by a surface wave, which is prone to significant interference fading due to the influence of the boundary surface.

The power of the direct signal and the illumination signal reflected by the target can be determined by taking into account the ratios (8.1, 8.2):

$$P_R = \frac{P_{Tr} G_{Tr} G_R \lambda^2}{(4\pi)^2 R_R^2} V_R^2, \tag{8.7a}$$

$$P_T = \frac{P_{Tr} G_{Tr} G_R \sigma_T(\theta_{Tr}, \theta_R) \lambda^2}{(4\pi)^3 R_T^4} V_T^4, \tag{8.7б}$$

where $V_R = \frac{h_{Tr} h_R}{\lambda R_R}$, $V_T = \frac{h_{Tr} h_T}{\lambda R_T}$ is the surface attenuation coefficient at the communication range R_R and the radar range R_T, and h_{Tr}, h_R, h_T are the heights of the antennas of the transmitter, receiver, and target, respectively, and $h_{Tr} = h_R$. Let N and ΔF be the noise ratio and bandwidth of the receiver.

Then, taking into account that these powers must exceed the noise level μ_T times when detecting a target and μ_R times when transmitting a broadcast signal:

$$P_R = \mu_T k t \Delta F_R N \tag{8.8a}$$

$$P_T = \mu_R k t \Delta F_T N, \tag{8.8b}$$

as well as the fact that the required SNR in these cases are approximately the same $\mu_T \approx \mu_R$, using ratios (8.7, 8.8) it is possible to write:

$$\frac{\Delta F_T}{\Delta F_R} = \frac{\sigma_T(\theta_{Tr}, \theta_R)}{(4\pi) R_T^4 R_R^{-2}} \left(\frac{h_{Tr} h_T}{\lambda R_T} \right)^4 \left(\frac{h_{Tr} h_R}{\lambda R_R} \right)^{-2} = \frac{\sigma_T}{(4\pi)} \frac{R_R^4}{R_T^8} \left(h_T\right)^4 \left(\lambda\right)^{-2}. \tag{8.9}$$

Then the distance with this version of active-passive radar will be determined from the ratio (8.9):

$$R_T = \left(\frac{\Delta F_T}{\Delta F_R} \right)^{-1/8} \left(R_R^4\right)^{1/2} \left(\frac{\sigma_T}{(4\pi)} \right)^{1/8} \left(h_T\right)^{1/2} \left(\lambda\right)^{-1/4}. \tag{8.10}$$

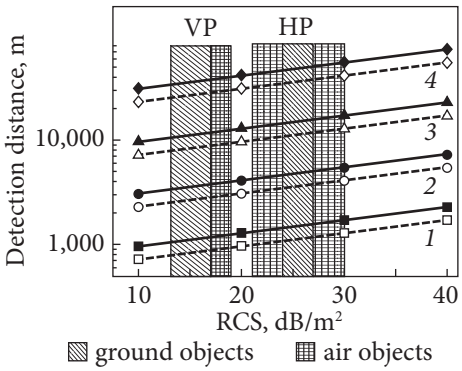

Fig. 8.2. Object detection distance when the situation is illuminated by our own radio stations of the HF band (λ = 20 m; frequency bands: —— — 0.1 Hz, – – – – — 1 Hz; object heights: *1* — 10 m, *2* — 100 m, *3* — 1 km, *4* — 10 km; HP, VP — horizontal and vertical polarization

The results of the estimation of detection distances from RCS of the target are shown in Fig. 8.2. When tanks are operating in a group, the ideology of using their own means of radio communication consists in the sequential illumination of the situation by each of the tanks of the group with its own radio station, by emitting a monochromatic or modulated signal of a certain frequency for some time, which can be associated with the number of this object in the group, as well as its place in the group. The rest of the radio stations of the group work at the same time.

Then, the illuminating of the environment is carried out by the next car, and the rest work for the reception. The modulation frequency can be used to estimate the difference in times (distances) between the signal that passed from the source of illumination to the receiver and the total distance between the source of illumination, the target, and the receiver. When evaluating the range of communication and radar systems (8.7, 8.10), the values of radiation power, receiver sensitivity, and realized signal/interference ratio at a given communication range are taken from Table 4.3 of Appendix 4.

Use for illumination of GNSS signals (GLONASS, GPS, Galileo, Compass). The radiation of global navigation satellite systems (GNSS), both existing Russian and American ones (GLONASS, GPS) and those created by European and Chinese ones (Galileo, Compass), can be used to illuminate the air situation. This subsection presents the results of estimates of the detection range of ground and air objects based on the methodology developed in works [128, 148, 149].

To estimate the level of the GNSS signal P_{R0} at the output of a standard antenna of a consumer receiver with a wide directional pattern with gain G_{R0}, one can use relation (8.2). It should be at least P_{R0} [dB]~ –61 dB/W. This value is regulated in the interface control documents of the owners of the GLONASS and GPS navigation systems.

This means that at the point of reflection from the object, GNSS signals at frequencies L1 and L2 have a power of at least –161 dB/W at the output of a linearly polarized antenna with a gain of 3 dB at elevation angles greater than 5 degrees. In terms of power flux density, this is $1{,}38 \cdot 10^{-14}$ W/m². The signal search

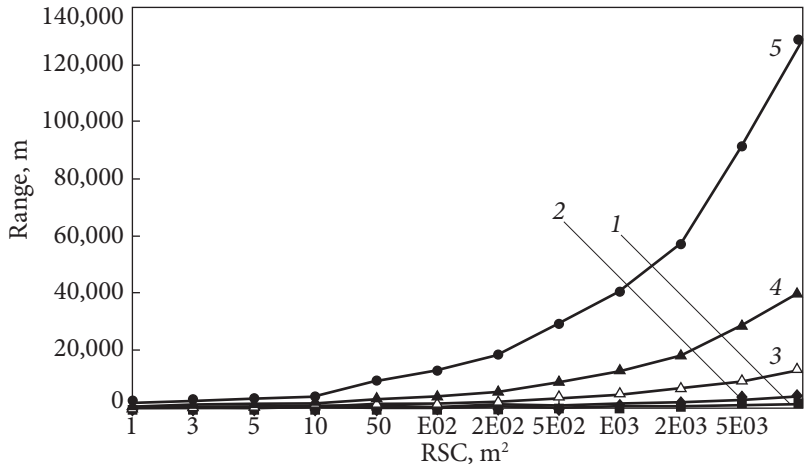

Fig. 8.3. Radar range for different accumulation times [139]: *1* — accumulation time 1 ms; *2* — 10 ms; *3* — 100 ms; *4* — 1 s; *5* — 10 s. The gain of the receiving antenna array is 20 dB

sensitivity of GNSS receivers (S_r) at the moment is –175 dB/W when accumulating signal measurements at a code epoch of 1 ms and with a typical antenna gain of + B (at the zenith) to –2 dB at angles less than 15 degrees [128]. Using the ratio (8.1), it is possible to write down the detection range for systems that use the GNSS signal to illuminate the situation:

$$R_r^2 < 4 \cdot 10^{-17} \cdot \frac{\sigma}{S_r} \cdot G_r \,. \tag{8.11}$$

The results of estimations of detection range [128], using relation (8.11) for receiver sensitivity: S_r = –171 dB/W — accumulation of measurements at an interval of 1 ms, S_r = –181 dB/W for 10 ms, S_r = –191 dB/W for 100 ms, S_r = = –201 dB/W for 1 s and S_r = –211 dB/W for 10 s and the use of PAR with G = = 1,000 (30 dB) are shown in Fig. 8.3.

The analysis shows:

a) the use of GNSS as "illumination" is unacceptable for the location of dynamic objects with a small RCS;

b) starting with an accumulation time of more than 1 s, location is possible for objects with a large RCS;

c) this type of illumination is unpromising for use on armored vehicles to illuminate air and ground conditions.

Using those data given in Table 4.2 of Appendix 4 and results of calculations in Fig. 8.1 and Fig 8.2, it is possible to estimate the detection ranges of various objects of equipment when they are illuminated, both by broadcasting stations of the HF band and by our own radio stations installed on armored vehicles. They are shown in Fig. 8.1 and Fig. 8.2 with shaded areas.

The analysis shows that for high-altitude aerial objects, the detection range can be dozens of kilometers. At the same time, ground and low-flying objects can be detected only at small distances of one kilometer.

Use of acoustic reconnaissance systems to detect ground and air objects. The possibility of using the objects own acoustic noises for their detection is discussed in detail in papers [67, 68, 180], analyzed in Chapter 2, and it is shown (Table 2.6) that the use of this channel allows detecting objects (planes, tanks, gunshots) in the absence of interference from rain and wind noise at distances of more than 8 km. At the same time, under unfavorable climatic conditions, the detection range is significantly reduced and, in some cases, does not exceed 1 km.

8.3. Information exchange channels and their integrated use

Currently, HF and UHF radio stations are used to exchange information between the objects of the group. They provide communication support at distances of several dozens of kilometers. However, the speed of information exchange in this mode is very limited. The next stage is the automation of the process of transferring data about the situation between individual participants of the scene, the creation of automated systems for displaying the situation, taking into account the risks for each participant of the scene. Regular radio stations operating in the mode of automatic transmission of telemetry data can also be used for this purpose. In addition, it is necessary to display both the tasks performed by the neighbors and the technical readiness of each of the participants to perform them. Integration into the unified management system (UMS) of the group also dramatically reduces the problem of "friendly fire". Accurate determination of the coordinates of a group of own equipment (using GNSS receivers) by UMS guarantees that the objects of the group will not accidentally destroy their own colleagues. The exchange of information between the objects of the group with their coordinates and the data of the enemy's coordinates allows for an increase in the efficiency of their use.

GNSS receivers — positioning together with an automated system of information exchange with the command post and group members allows to defeat the enemy based on the calculated coordinates of his location. Each member of the group, having detected the enemy, after determining his coordinates towards their own, using a laser rangefinder and angle-measuring optical systems, can transmit them to the UMS, which distributes this data to the rest of the group members.

An example of such information exchange is modern anti-ship missile complexes [176, 177].

Obviously, if the adversaries have the same type of information systems with the same technical capabilities, then they will have the same probability of survival. If one of the adversaries has better technical capabilities of reconnaissance

systems, weapons management, and the weapon itself, then the probability of its survival in the conflict increases. The appearance of additional information channels that use other physical fields, for example, electromagnetic fields of the radio range or acoustic radiation of objects, leads to a similar result.

Let the dependence of the probability of detection of enemy objects on the distance by different systems (optical, infrared, radio systems) be approximately the same. Then, their joint use allows you to significantly expand the zone of confident detection of the enemy, which means the probability of survival. The use of additional information received from other participants in the scene can lead to the same result (expansion of the enemy's detection zone).

Effectiveness of the integration of systems that use different physical fields. When detecting a signal with a random initial phase and amplitude, the detection probability D and false alarm F are related by the ratio [361]:

$$D = F^{\frac{1}{1+\mu}}, \tag{8.12}$$

where μ is SNR.

When a signal is detected against the background of internal noise of the receiving equipment, it is possible to record:

$$P_r = \frac{P_{Tr} G_{Tr} G_R \lambda^2 \sigma_T}{4\pi^3 R^4} V^4. \tag{8.13}$$

Given that the potential of the system:

$$\Pi = \frac{P_{Tr} G_{Tr} G_R \lambda^2}{4\pi^3 P_N}, \tag{8.14}$$

where P_{Tr}, P_r is radiated and received power, RCS and range to the target, G_{Tr}, G_R is gain coefficients of transmitting and receiving antennas, Π, P_N is radar potential and noise power at the receiver input, and V is interference coefficient of surface attenuation. Given that $P_r = \mu P_N$ the SNR can be written as:

$$\mu = \Pi \frac{\sigma_T}{R^4} V^4. \tag{8.15}$$

For high-altitude purposes $V^4 \approx 1$ and for targets located on the bounding surface (ground or surface) and also near it (low-altitude aerial):

$$V^4 \approx \frac{1}{R^4} \text{ for heights } h_T < \frac{\lambda R}{4h_R},$$

where h_T, h_R is the height of the target and the radar antenna.

To approximate the attenuation factor, the relation [288] can be used:

$$V^4 \approx \frac{1}{1+\left(\frac{R}{R_1}\right)^4} = \frac{\left(R_1\right)^4}{\left(R_1\right)^4+\left(R\right)^4}, \tag{8.15a}$$

where

$$R_1 = \frac{4h_R h_T}{\lambda} \tag{8.15b}$$

is the range of the first interference lobe of the field at the heights of the location of the target h_T and the radar h_R and the wavelength of radiation λ.

Thus, the SNR is directly proportional to the potential of the system and RCS of the target and inversely proportional to the fourth degree of range for high-altitude objects and to the eighth degree for low-altitude or surface-located ones.

In the case of low-altitude or surface-located targets, the factor limiting their detection range is not the internal noise of the equipment, but interference from local objects — reflections from areas of land, sea, or clear sky. Then, taking into account the expressions (8.12—8.15), we can write:

$$D \approx F^{\frac{1}{1+\Pi\frac{\sigma_T}{R^4}V^4}}, \tag{8.16}$$

which means that for high-altitude objects it looks like

$$D = F^{\frac{1}{1+\Pi\frac{\sigma_T}{R^4}V^4}} \approx F^{\frac{R^4}{\Pi\sigma_T V^4}} \approx F^{\frac{R^4}{\Pi\sigma_T}} \tag{8.17a}$$

and for low-altitude

$$D \approx F^{\frac{R^8}{\Pi\sigma_T\left(R_1\right)^4}}. \tag{8.17b}$$

From the relations (8.17), it is possible to determine the ranges R_0, at which the given probabilities of correct detection D_0 and false alarm F_0 are ensured for high-altitude

$$R_0 = \left(\Pi\sigma_T \frac{\ln\left(D_0\right)}{\ln\left(F_0\right)}\right)^{1/4} \tag{8.18a}$$

and

$$R_0 = R_1^{1/2}\left(\Pi\sigma_T \frac{\ln\left(D_0\right)}{\ln\left(F_0\right)}\right)^{1/8} \tag{8.18b}$$

for low-altitude targets, respectively.

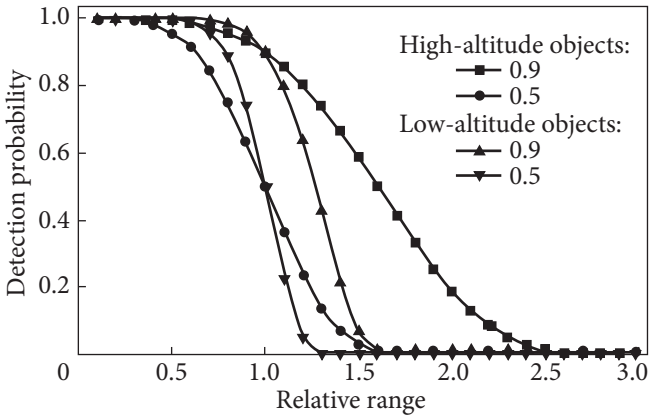

Fig. 8.4. Dependencies of the probability of detecting a fluctuating signal on the range

Then the relations (8.16—8.18) can be written in the form

$$D = D_0^{x^{4m}}, \tag{8.19}$$

where $m = 1$ for altitude targets, $m = 2$, and $x = \frac{R}{R_0}$ is the relative range. Fig. 8.4 shows the nature of the dependence of detection probabilities on distance for two fixed detection probabilities ($D = 0.5$ and 0.9).

Fig. 8.4 shows that the dependence of the probability of detection is a monotonically decreasing function of the distance and, in most cases, its approximation can be used in practical calculations in the form of a step function with a constant value from zero distances to distances when the probability of detection is equal to 0.9 and considering it equal to zero at greater distances. This will give slightly underestimated data during calculations.

For real intelligence systems, as well as weapons, as a rule, the dependence of detection and damage probabilities on the distance to the target is unknown. In the best case, during the tests, ranges can be determined at which the given detection probabilities (usually 0.9 or 0.99) and the given probabilities of hitting objects by weapons systems are realized.

The relation (8.19) can be rewritten in the form

$$D = D_0^{\left(\frac{R}{R_0}\right)^{4m}} \tag{8.19a}$$

convenient for further calculations. It includes the given detection probabilities D_0 at the range R_0 for high-altitude $m = 1$ and low-altitude $m = 2$ objects. We will assume that a similar ratio (5.19*a*) describes the probability of hitting an object with a weapon system at $m = 1$. At the same time, R_0 is the enemy's hit range with probability D_0.

If several situation control sensors (optical, radio wave, acoustic) and several weapon systems (artillery, missile) are used, then with statistical independence of the results obtained by them, the probabilities of eliminating P_e^k and not eliminating $\overline{P}_e^k$ of the k^{th} enemy are determined

$$P_e^k = P_{det}^k P_{el}^k, \tag{8.20a}$$

$$\overline{P}_e^k = 1 - P_{det}^k P_{el}^k \tag{8.20b}$$

due to the probability of detection of the k^{th} enemy object by the situation lighting sensors P_{det}^k and the probability of the elimination of the k^{th} enemy by the weapons systems P_{el}^k. The latter are determined

$$P_{det}^k = 1 - \Pi_{i=1}^{i=i_0}\left(1 - P_{det}^{k_i}\right), \tag{8.21a}$$

$$P_{el}^k = 1 - \Pi_{j=1}^{j=j_0}\left(1 - P_{el}^{k_j}\right) \tag{8.21b}$$

due to the probability of detection of the k^{th} enemy object i_0 by the situation lighting sensors $P_{det}^{k_i}$ and the probability of the elimination of the k^{th} enemy j_0 by the weapons systems $P_{el}^{k_j}$. Ratios (8.19—8.21) make it possible to evaluate the effectiveness of the integrated use of situational lighting sensors of various types and weapons systems. The probability of successful completion of the task P_{01} by its object, in the case of the presence of one enemy object $k = 1$, will be determined by creating probabilities of hitting P_d^1 of the enemy object and not hitting $\overline{P}_d^0$ with it (8.20):

$$P_{01} = P_d^1 \overline{P}_d^0 = P_d^1\left(1 - P_d^0\right), \tag{8.22a}$$

where the indices 0 and 1 refer to your object and the object of the enemy.

Similarly, the successful completion of the task by the enemy object is determined:

$$P_{10} = P_d^0 \overline{P}_d^1 = P_d^0\left(1 - P_d^1\right). \tag{8.22b}$$

It is possible to introduce the concept of the efficiency functional, which characterizes the degree to which the probability of the enemy's elimination in a duel between two objects, provided that one's object remains survivable, is greater than the probability of the enemy's elimination of own object, provided that the enemy's object remains survivable, determined from relations (8.22) as

$$\Delta = P_{01} - P_{10} = P_d^1\left(1 - P_d^0\right) - P_d^0\left(1 - P_d^1\right) = P_d^1 - P_d^0. \tag{8.23a}$$

and will be equal to the difference between the probability of elimination of the enemy's object by its object and the probability of elimination of its own object by

the enemy. Using (8.20a), we can write

$$\Delta = P_{det}^1 P_{el}^1 - P_{det}^0 P_{el}^0 = \left(\Delta_{det} + P_{det}^0\right)\left(\Delta_{el} + P_{el}^0\right) - P_{det}^0 P_{el}^0 = \\ = \Delta_{det} P_{el}^0 + \Delta_{el} P_{det}^0 + \Delta_{det}\Delta_{el}, \qquad (8.23b)$$

where $\Delta_{det} = P_{det}^1 - P_{det}^0$ and $\Delta_{el} = P_{el}^1 - P_{el}^0$ is the difference in the detection probabilities of the sensors of one's object and the enemy's, as well as the difference in the probability of being hit by the weapons systems of one's object and the enemy's.

It follows from the relation (8.23b) that the provision of higher probabilities of detection $\Delta_{det} > 0$ by situational sensors, which is achieved by the enemy and greater probabilities of elimination $\Delta_{el} > 0$ of it, leads to an increase in the values of the function of the quality of performance of the task $\Delta > 0$. It follows from relations (8.21) that supplementing the detection system with an additional situation sensor or the weapon system with an extra weapon system leads to an increase in the probability of detecting the enemy and the probability of its elimination:

$$P_{det}^{k,i_0+1} - P_{det}^{k,i_0} = \Pi_{i=1}^{i=i_0}\left(1 - P_{det}^{k_i}\right) - \Pi_{i=1}^{i=i_0+1}\left(1 - P_{det}^{k_i}\right) = P_{det}^{k,i_0+1}\Pi_{i=1}^{i=i_0}\left(1 - P_{det}^{k_i}\right), \quad (8.24a)$$

$$P_{el}^{k,j_0+1} - P_{el}^{k,j_0} = \Pi_{j=1}^{j=j_0}\left(1 - P_{el}^{k_j}\right) - \Pi_{j=1}^{j=j_0+1}\left(1 - P_{el}^{k_j}\right) = P_{dest}^{k,j_0+1}\Pi_{j=1}^{j=j_0}\left(1 - P_{el}^{k_j}\right) \quad (8.24b)$$

by values proportional to the detection capabilities of the implemented added situation sensor and the capabilities of defeating the enemy implemented by the added weapons system.

Thus, the appearance of additional situational control sensors and new weapons systems at the adversary allows it to solve the assigned tasks more successfully. Therefore, in order to increase the survivability of one's own objects, it is necessary to use a greater number of channels for receiving information about the external environment, with improved characteristics, as well as the use of additional weapons systems and increasing the range of the old systems.

Using the approach developed in the paper [349], an assessment of the effectiveness of the use of technical objects in the integration of sensors of various types and systems was carried out. It is shown that the use of an additional active-passive system for monitoring the HF band and passive acoustic reconnaissance systems has a significant impact on the effectiveness of the application.

Conclusions

1. To transform modern platforms and their management system into a modern spatially distributed intelligent smart-grid network, it is necessary to combine them with automated information exchange systems, indicating the priority

and degree of danger of individual elements of the environment for each of the platforms. The system of transmission of telemetric information about the situation can be built based on the HF and VHF radio stations available at the facilities.

2. To increase the reliability and survivability of a distributed intelligent network, information sensors of individual platforms must be built using fields of different physical nature (electromagnetic and acoustic) of different wavelength ranges (from hundreds of nanometers for the optical range to dozens of meters for the radio range). In addition, it is necessary to apply various environmental sensing methods, both active with the emission of special signals and active-passive — based on the reception of secondary fields created by reflections from equipment objects of existing ground and space-based radiation sources, as well as passive — based on the use of own optical, thermal and acoustic radiation of equipment objects. This will make it possible to increase the informativeness of the channels of receiving information about the situation and the survivability of the technical objects themselves in the conditions of the influence of the opposing party on them.

3. Besides the existing and widely used optical and infrared systems on equipment objects, it is necessary to use acoustic means of reconnaissance and targeting, which can ensure the detection of equipment objects (land and air) and enemy weapons at distances of up to 10 km.

4. To obtain information about the surrounding state, secondary fields created by the objects of the enemy's equipment when reflecting the illumination signals of broadcast stations of the HF band, satellite and terrestrial TV and broadcasting systems can be used. Their use can make it possible to detect moving objects of land and air equipment at distances of several kilometers.

5. It is necessary to create automated channels of information exchange between individual participants of the scene and information display systems, both from own sensors and received from other participants of the scene with an indication of the potential degree of danger, as well as passive — based on the reception of the objects own radiation in the optical and infrared ranges of electromagnetic waves, as well as the own acoustic noises of technical objects.

6. The use of technical objects for illumination of the situation of the radiations of broadcasting HF stations and their own radio stations can allow the detection of high-altitude air targets at distances of more than 10 km.

7. The integration of detection systems that use physical fields of different ranges and nature allows for an increase in the probability of detecting the enemy's means and, therefore, the effectiveness of combating them.

8. The creation of robotic complexes built into the Smart Grid system of distributed intelligence will allow for an increase in their survivability and efficiency of use in the conditions of enemy countermeasures.

General conclusions

The monograph provides a solution to an actual scientific and practical task — the use of HF broadcasting, VHF television stations, and global navigation satellite systems GPS and GLONASS, as well as the acoustic emissions of objects of anthropogenic and natural origin for monitoring the environment. During many years of research, the characteristics of VHF and HF station signals have been experimentally studied. The interference created by the radiation of VHF and HF broadcasting stations for active-passive radar systems has been studied. Methods of optimization of antenna systems of the HF band have been developed. The possibility of using new approaches to describe the laws of distribution of various non-stationary processes, including interference to active-passive systems of the decameter range from HF broadcasting stations, is considered. The method of monitoring tropospheric refraction by signal attenuation coefficients on the OTH path on spatially spaced antennas in the VHF frequency range and experimental studies of interference phenomena in the propagation channel on the OTH paths in the mid-latitudes (Ukraine) that occur in the presence of inversion layers are presented, it is shown that the number of inversion layers, as a rule, does not exceed 2, with a jump in the refractive index at the boundary of the layers 6...14 N units, the height of their placement does not exceed 650 m, the speed of movement is from several meters to several hundred meters per hour, the depth of signal fading is from –3 dB to –23 dB. When the An-74 aircraft was detected, using the ionospheric wave of HF broadcasting stations, it was established that the RCS of the aircraft in the resonant region on both the horizontal and vertical polarizations reached thousands of m^2. This means that with comparable radar potentials, the detection range in the HF band can be 30...300 times higher than their detection range in the microwave range, and also makes it possible to use a surface wave of vertical polarization to illuminate the air condition in the HF band. The technique of using GNSS signals for remote monitoring and diagnosis of the state of the sea surface is given. It is shown that the levels of the fluctuation component and the

depth of fading (trends) of signals of navigation satellites are sensitive to changes in the state of the underlying surface and the degree of disturbance. A simulation model of the disturbances created for active-passive systems by the radiation of radio broadcasting stations based on nested semi-Markov processes, taking into account the presence of two phases of different intensities in the signal, which are physically determined by the discrete nature of the modulating signals, is given. An analysis of the ratios of the carrier level to the interference level obtained during the experiments at different frequencies for different reception polarizations and signal frequencies was carried out. It is shown that their ratio reaches 40 dB. A technique for the synthesis of non-equidistant antenna arrays has been developed, which is based on the use of the properties of "magic" squares. It is shown that when placing grid elements, using the numbers from which the "magic" square is composed, it is possible to obtain almost complete coverage of spatial frequencies in the area of placement of elements with small filling factors of up to 0.01 and redundancy less than 0.5. It is shown that the synthesis of large antenna arrays (AA) is possible using the nesting of several "magic" squares. The algorithm for supplementing the elements of the grid formed by the elements of the "magic" square with additional elements to ensure full coverage of the AA frequencies can be used just as effectively to build an AA based on the nested square. Its characteristics can be significantly improved using mutual rotations of individual layers included in the synthesized lattice. A symmetric spiral vibrator with a small diameter and pitch of the spiral compared to the wavelength was experimentally investigated, and it was shown that it is a retarding structure in which resonances occur when a whole number of half-waves are arranged along the vibrator — and a reflector-calibrator for external calibration of the radar was proposed on its basis.

The possibility of using Kravchenko-Rvachev atomic functions to describe the distribution laws of non-stationary non-Gaussian processes is considered. It is shown that the finiteness of atomic Kravchenko-Rvachev functions has physical prerequisites for their use for processes with several phase states, where Gaussian distribution densities are used as approximating functionals in the middle of each phase state. The analysis of approximation errors of experimental densities showed that the use of finite Kravchenko-Rvachev functions in most cases gives better results than the use of Gaussian functions and, even more so, Lorentzian functions.

A description of the statistical interrelationships of various spectral components of the signal of HF and VHF radio broadcasting stations using the CMSC apparatus is proposed. The study of the mutual correlation coefficients of various spectral components of the signals of radio broadcasting stations made it possible to reveal the presence of a correlated region in the spectra. It was established that the appearance of additional elements with a high correlation at harmonic frequencies indicates the presence of nonlinear distortions in the receiving path and can be used for their monitoring.

Data on the acoustic noise levels of ground equipment and small-sized aerial objects (such as UAVs) are presented for different observation ranges. The connection between the dimensions of the helicopter blades and their rotation frequency, which is a signature for recognizing the type of helicopter and can be estimated from optical portraits and acoustic noises, has been established theoretically and confirmed experimentally. Bursts with a variable width of the spectrum of the high-frequency components of reflections caused by the frequency modulation of the scattered signal by the rotating blades of the helicopter propellers were detected. The presence of a broadband burst in the high-frequency region, which appears with the frequency of rotation of the propeller, which is caused by a change in the angle between the blade and the front of the electromagnetic wave, can be used as an informative feature when detecting a stationary helicopter against the background of the terrain and its recognition. It is possible to extract information about the frequency of rotation of helicopter propellers or the frequency of rotation of the crankshaft of internal combustion engines using cepstral processing of their acoustic noises or radar reflections. The possibility of using correlated spectral components obtained at different reception polarizations and wavelengths of the irradiating field, associated with the vibration of the skin under the influence of the propulsion system, is shown to increase the contrast of the signal selection of the object with a working engine against the background of interference from the terrain. Quality functionals are proposed, which allow us to conduct a comparative analysis of the effectiveness of the use of ground equipment objects when using different combinations of sensors. The integration of detection systems that use physical fields of different ranges and nature and the construction of robotic complexes built into the Smart Grid system of distributed intelligence will allow for an increase in their survivability and the efficiency of the use of technical objects. The use of broadcast radio stations and own radio stations installed on the objects to illuminate the environment can allow the detection of high-altitude air targets at distances of more than 10 km. The inherent acoustic noises of equipment objects allow their detection in the absence of external obstacles at distances of up to 8 km and are significantly reduced due to wind and rain noise.

Appendix

APPENDIX 1

Apparatus and methodology of researching acoustic radiations of ground equipment objects and small UAVs

The noise level was measured using a standard JTS-1357 noise meter, the appearance of which is shown in Fig. 1.1, *a*, and the technical characteristics are given in Table 1.1. To study the spectral characteristics of the emitted signals, they were recorded with the "Olympus VN-480 PC" digital recorder, the appearance of which is shown in Fig. 1.1, *b*, and the characteristics are given in Table 1.2.

Noise measurements were carried out for both stationary ground objects and moving objects at different angles of location of the receiving equipment relative to the noise source. The height of the location of the microphone was 1...1,7 m from the ground. The fixed parameters were the distance to the noise source and the weather conditions during the experiment (temperature, air humidity, wind speed, and type of substrate).

a *b*

Fig. 1.1. Appearance of noise level meter (*a*) and recorder (*b*)

Table 1.1. **Technical characteristics of noise meter JTS-1357**

Variable parameter	Value
Resolution	0.1 dB
Precision	±1.5 dB
Frequency range	31.5…8.5 kHz
Measurement range	30…130 dB
Linear range	50 dB

Table 1.2. **The main technical characteristics of the digital recorder "Olympus VN 480 PC"**

Measured parameter	Value
Recording duration	
HQ (high quality)	About 177 minutes
SP (normal quality)	About 267 minutes
LP (lasting quality)	About 493 minutes
Sampling frequency:	
Regime HQ	16.0 kHz
Regime SP	10.6 kHz
Regime LP	5.75 kHz
General frequency characteristics:	
Regime HQ	300…7,200 Hz
Regime SP	300…4,700 Hz
Regime LP	300…2,600 Hz
Connecting to a computer	USB port
Memory capacity	64 MB
Headphone jack	Resistance — 8 Ohms
Microphone jack	Resistance — 2 kOhm

Appendix 2

Characteristics and general view of radio location measurement systems

a *b*

Fig. 2.1. General view of measuring complexes *a* — multi-frequency polarimeter; *b* — radar with FM radiation

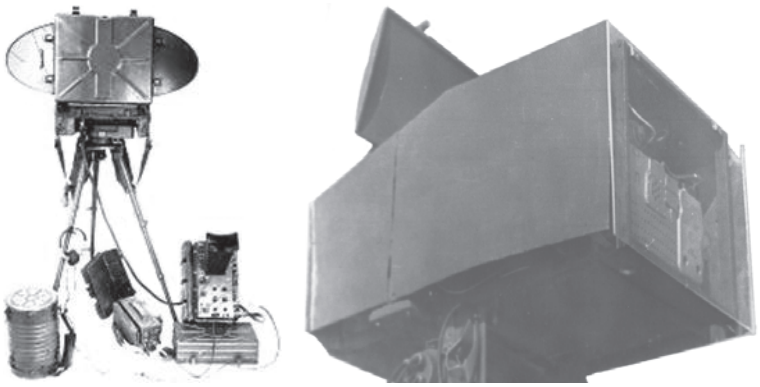

a *b*

Fig. 2.2. Pulsed radars with a cyclic survey of space: radar antennas with wavelengths of 2 cm (*a*) and 8 mm (*b*)

Table 2.1. **The main parameters of CW measuring radar**

Characteristic	Multi-frequency polarimeter			FM Radar
Wave length, cm	10	0.8	0.4	0.8
Power, mW	150	100	50	100
Chart width, degrees	20	6	6	3
Sensitivity, dB/W	–120	–120	–115	–160
Analysis band, Hz	4—500	4—5,000	4—5,000	50—2,000
Resolution by polarization, dB	25	30	25	25

Table 2.2. **Technical characteristics of pulse radars with scanning**

Specifications	Parameters	
Wave length, cm	0.8	2
Impulse power, kW	10	1
Pulse duration, ns	66	400
DN width: in azimuth, mrad	10	30
by the corner of the place, mrad	34	55
Threshold sensitivity, Vt	$3 \cdot 10^{-12}$	10^{-12}
Dimensions of the antenna in azimuth, cm	80	60
Space survey speed, degree/s	360	4.8
Scanning sector, degree	36	240
Repetition frequency, kHz	7.5	4
Polarization	VP	VP

Appendix 3

Equipment and characteristics of illumination stations for measuring interference caused by radiation of broadcasting stations in VHF and HF bands

a *b*

Fig. 3.1. Appearance of the "Kanal-R" radio receiver: *a* — unit of a two-channel receiver; *b* — receiver power supply unit

Table 3.1. **Technical characteristics of the professional receiver "Kanal-R"**

Characteristic	Value
Frequency range	2—32 MHz
Scale	Digital
Discretion of adjustment	No more than 5 Hz
The speed of automatic rebuilding	0.3—20 kHz/sec (the reverse direction of the reconstruction is provided)
Limits of automatic adjustment	
in the range of 2—4 MHz	Not less than 160 kHz
in the range of 4—12 MHz	Not less than 300 kHz
in the range of more than 12 MHz	Not less than 540 kHz
Types of signals	CW, AM
The scheme of the radio receiver	Double-conversion superheterodyne
Dynamic range	At least 60 dB (for two powerful signals that differ from the main one by 5—10 kHz)
IF frequencies	1) 1.73 MHz 2) 215 kHz
Selectivity (by mirror channel)	
in the range up to 20 MHz	Not less than 80 dB
in the range of 20-28 MHz	Not less than 70 dB
in the range of more than 28 MHz	Not less than 60 dB
Selectivity (two-signal)	
with a frequency difference = IF or the 1st IF	Not less than 70 dB
with a frequency difference = 2nd IF	Not less than 80 dB
Selectivity (for the 1st and 2nd IF)	Not less than 80 dB

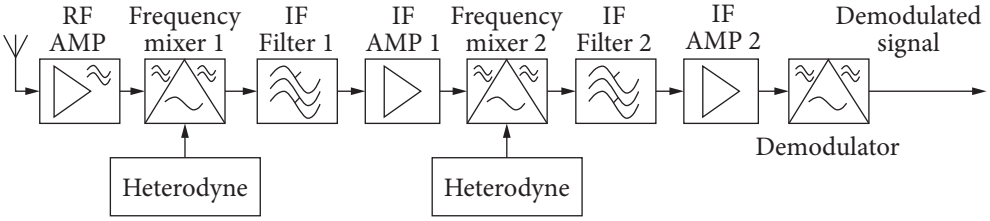

Fig. 3.2. Structural diagram of one channel of a superheterodyne radio receiver Kanal-R with double frequency conversion

Fig. 3.3. Stationary superheterodyne short-wave radio receiver "Katran R-399A"

Fig. 3.4. Multimedia, all-wave digital radio receiver DEGEN DE-1127 with MP3 player and voice recorder

Table 3.2. **Main technical characteristics of the receiver "Katran R-399A"**

Frequencies range	1—31.999999 MHz
Setup step	
manually	1/10 Hz
automatically	From 2 ± 1 to 60 ± 20 kHz/s
Number of memory channels	60
Tuning time to any frequency by external code	No more than 50 ms
Daily volatility (relative) of the tuning frequency	No more than $2.5 \cdot 10^{-8}$ (after a four-hour warm-up with RG "Hyacinth-M")
Intermediate frequencies	1. IF = 34.785 MHz; 2. IF = 215 kHz
Sensitivity	2.0 mkV (AM); 0.6 mkV (CW/SSB)
Dynamic range	Not less than 70 dB
Levels of attenuation of the signal at the input by the attenuator	0; 10 ± 3; 20 ± 3; 30 ± 3; 40 ± 3 dB
Efficiency of the manual amplification control (MGC) on the IF	Not less than 80 dB (relative to the initial level at the input of the RPU 1 mkV)
The effectiveness of the MGC on LF	Not less than 34 dB
Desensitization	Not less than 80 dB (on mirror, half-mirror, and side reception channels) Not less than 82 dB (on reception channels at frequencies equal to intermediate ones)

Table 3.3. **Technical characteristics of the DEGEN receiver, model: DE-1127**

No.	Characteristic	Value	Notes
1	FM, MHz or	64.0…108.0 87.0…108.0	Set in the menu
2	AM, for Europe and Asia kHz or for North America	522…1,710 520…1,710	9 kHz tuning step 10 kHz tuning step
3	SW, MHz	2.30…23.00	
4	Noise-limited sensitivity: FM, mkV, MW, mV/m SW, mkV	< 5 < 2.5 < 50 > 40	
5	Selectivity, dB	> 40	
6	Digital volume control	31 levels	

Table 3.4. **Characteristics of illuminating stations**

No. Fig.	Illumination station	Distance to Kharkiv, km	Azimuth, degree	Type	Broadcast frequency, kHz	Transmitter power, kW
1	Shijiazhuang, China	6,098	70.4	Many-jumping	17,735	500
2	Kashi, China	3,302.6	95.2	Single-jump	17,490	500
3	Issoudun, France	2,524	275.6	Single-jump	17,735	500
4	Emirler, Turkey	1,196	194	Single-jump	13,635	500
5	Sirjan, Iran	2,805	137.1	Single-jump	15,150	500
6	Islamabad, Pakistan	3,523	107.3	Single-jump	11,645	100
7	Issoudun, France	2,524.2	275.6	Single-jump	17,735	500
8	Issoudun, France	2,524.2	275.6	Single-jump	17,735	500
9	Emirler, Turkey	1,196.0	194.1	Single-jump	13,635	500

Table 3.5. **Characteristics of illuminating HF broadcast stations of ionospheric wave**

No.	Name of the station	Record Time, (UTC)/Date	Frequency, kHz	Power, kW	Field of work, degree	Coordinates	Angle to Kharkiv, degree
1.1	Radio Taiwan Int.	15:07 25.06.2016	7,385	100	352	25°4'N 121°31'E	
1.2	Radio Taiwan Int.	15:10 25.06.2016	7,385	100	352	25°4'N 121°31'E	124.8769
1.3	Voice Of Tajik	19:33 29.06.2016	7,245	100	ND	37°32'N 68°42'E	93.5524

The End of the Table

No.	Name of the station	Record Time, (UTC)/Date	Frequency, kHz	Power, kW	Field of work, degree	Coordinates	Angle to Kharkiv, degree
1.4	China Radio Int.	19:40 29.06.2016	7,265	500	308	39°21'N 75°45'E	97.2126
1.5	China Radio Int.	19:44 29.06.2016	7,385	500	294	39°21'N 75°45'E	97.2126
1.6	China Radio Int.	19:46 29.06.2016	7,395	500	308	39°21'N 75°45'E	97.2126
2.1	Voice Of Turkey	19:53 29.06.2016	9,460	500	310	39°29'N 32°51'E	199.7819
2.2	China Radio Int.	20:00 29.06.2016	9,600	500	308	39°21'N 75°45'E	97.2126
2.3	Radio Romania Int.	05:43 30.06.2016	9,620	300	285	47°15'N 27°26'E	257.6368
3.1	Radyoya Denge Kurdistane	05:47 30.06.2016	11,600	300	116	47°17'N 29°24'E	252.1593
3.2	Radio Dabanga	05:51 30.06.2016	13,800	250	335	18°43'N 47°37'E	156.2493
3.3	Radio Saudi	05:57 30.06.2016	15,170	500	335	24°30'N 46°23'E	154.4945
3.4	China Radio Int.	06:02 30.06.2016	17,520	500	294	39°21'N 75°45'E	97.2126
4.1	Radyoya Denge Kurdistane	09:26 30.06.2016	11,600	300	116	47°17'N 29°24'E	252.1593
4.2	China Radio Int.	09:31 30.06.2016	15,665	500	308	43°35'N 87°30'E	114.9813
4.3	China Radio Int.	09:34 30.06.2016	17,490	500	308	39°21'N 75°45'E	97.2126
4.4	ChinaRadio Int.	09:37 30.06.2016	17,570	500	308	43°35'N 87°30'E	114.9813
4.5	Radio Farda	09:39 30.06.2016	17,880	100	85	49°41'N 8°30'E	266.3638
5.1	Radio Romania Int.	13:41 30.06.2016	11,950	300	285	47°15'N 27°26'E	257.6368
5.2	PBS Xinjiang	13:44 30.06.16	13,670	100	230	44°08'N 86°53'E	115.2369
5.3	Athmeeya Yatra Radio	13:47 30.06.2016	15,350	250	89	52°38'N 12°54'E	291.0183
5.4	China Radio Int.	13:50 30.06.2016	17,650	500	308	39°21'N 75°45'E	97.2126
6.1	VO ISLAMIC REP. IRAN°	21:26 30.06.2016	7,285	500	289	29°28'N 60°53'E	118.4624
6.2	China Radio Int.	21:28 30.06.2016	7,415	500	308	39°21'N 75°45'E	97.2126
6.3	China Radio Int.	21:31 30.06.2016	9,430	500	308	43°35'N 87°30'E	114.9813

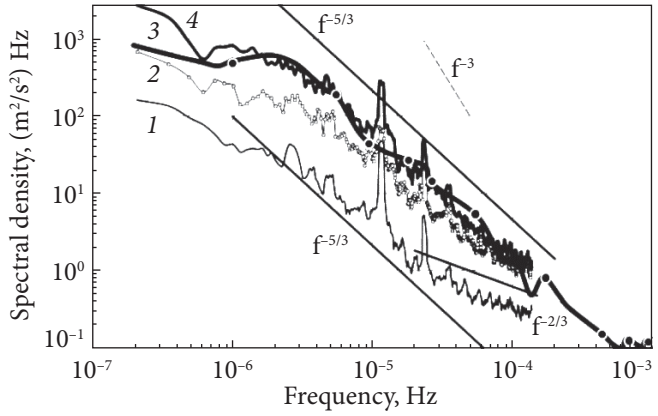

Fig. 3.5. [301] Energy spectra of wind speed pulsations at different altitudes *1* — height 8 m, *2* — 121 m, *3* — 125 m, *4* — 301 m

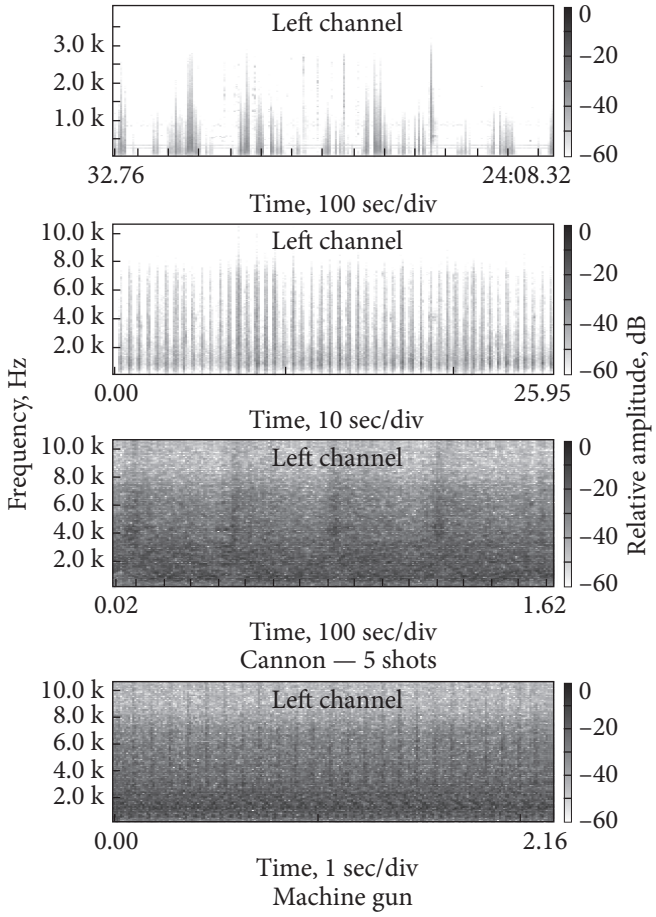

Fig. 3.6. Spectrograms of acoustic noises: *1* — wind, *2* — human steps on the snow, *3, 4* — sounds of shots: *3* — cannons, *4* — machine guns

Appendix 4

Main technical characteristics of research objects and detection systems

Table 4.1. **The main characteristics of surveillance and aiming devices [179]**

Optical and technical characteristics	Sights		Surveillance devices					
			daytime		nighttime			
	PP-61 AM	1PZ-2	TPKU-2B	TNP-B; TNPO-115; TNP-165; TNP-205	TKN-1S	TKN-3	TVNO-2B	TVNE-4B
Increase, times. post./pancrat.	2.6	1.2/3.0	5	—	2.75	3.0/2.2	1.0	1.0
Periscopicity, mm	285	285	200	200	200	200	200	200
Aiming range, vision, m (day/night)	2,000	2,000	3,000	vision	—/300	4,000/400	—/100	—/120

Table 4.2. **The average RCS value of objects in the resonant region**

Object	Purpose	Horizontal polarization		Vertical polarization
		RCS in the resonant region		
		Fuselage, dB/m^2	Rotor, dB/m^2	Fuselage, dB/m^2
Helicopter	MP	27.3	26.3	18.3
	S	28.6	27.5	17.4
	T	31.5	30.3	21.4
		Fuselage, dB /m^2	Wing, dB /m^2	Fuselage, dB /m^2
Plane	AA	26.7	25.4	17.2
	B	35.6	36.6	23.6
	F	30.5	26.7	19.8
	P	37.6	36.9	26.6
		Fuselage with cannon, dB/m^2	Fuselage, dB/m^2	Fuselage, dB/m^2
Tank		25.3	16.0	13.4

The following designations are used in the table: S — strike, T — transport, MP — multi-purpose, AA — attack aircraft, F — fighter, B — bomber. P — passenger.

Table 4.3. **Technical characteristics of radio stations**

Radio station R-030U VHF band [363]	
Frequency range	30—110, MHz
Power	30 ± 5, W (for a load of 50 Ohms)
Frequency instability	No more than 1×10^{-6}
Frequency deviation	5.6 ± 1.2, kHz
The level of own noises	130, dB
Receiver sensitivity	0.5, mkV
Signal-to-noise ratio	12, dB
Communication range	20—30, km
Radio station R-163-50K HF band [150]	
Frequency range	2—30, MHz
Power	50, W
Frequency instability	4.5×10^{-7}
Receiver sensitivity	3, mkV
Signal-to-noise ratio	12, dB
Communication range	50—300, km

Table 4.4. **Detection sensor ranges, km**

Objects	Sensors					
	Optical TPKU-2B, TKN-3 [1]	IR TKN-3 [1]	RTS HF and VHF bands [41]		Passive acoustic RTS [67, 68]	
	Day	Night	Active	Active-passive	Quietly	Wind, rain
On the ground	3.0 km; 4.0	0.4	0.4...1.0	0.3...0.7	6.0	0.5
Air (planes, helicopters)	—	—	...20	1...	7.3	0.7
Shot	—	—	—	—	8	3.4
UAV	—	—	1...8	0.5...1.5	6.0	—

References

1. Anipko O.B., Biryukov I.Yu., Busyak Yu.M. The complex problem of searching and detecting ground targets for their destruction by weapons installed on armored vehicles. *Academy of Internal Troops of the Ministry of Internal Affairs of Ukraine: Collection of Scientific Papers*. 2011. Iss. 2 (18). P. 43—47.
2. Anipko O.B., Biryukov I.Yu. Physical principles of the creation of a complex optzical-acoustic subsystem for the detection of ground targets by armored vehicles. *Integrated Technologies and Energy Saving*. 2012. No. 3. P. 48—53.
3. Anipko O.B., Biryukov I.Yu. The complex method of detection and recognition of ground targets based on the analysis of digital images and registration of acoustic disturbances. *Integrated Technologies and Energy Saving*. 2014. No. 4. P. 51—55.
4. Biryukov I.Yu. Acoustic component of reconnaissance of ground targets. *Problems and solutions. SNUNE&I: Collection of Scientific Papers*. 2013. P. 98—104.
5. Biryukov I.Yu. Acoustic component of reconnaissance of ground targets. *Problems and solutions. SNUNE&I: Collection of Scientific Papers*. 2013. P. 98—104.
6. Karlov V.D., Ulyanov Y.N., Mysailov V.L., Maksimova N.G. Application of powerful ultrawideband acoustic pulses in radioacoustic sounding systems. *Information Processing Systems*. Kharkiv. 2010. Vol. 6 (87). P. 95—99.
7. Characteristics and Classifications Noise and Vibration. URL: https://issuu.com/judu3/docs/dstu_gost_31295_2_2007__shum__zatuh
8. Divyzynyuk M., Goncharenko Yu., Goncharenko D. On the problem of calculating the range of reception of acoustic information from open platforms. *Legal, Regulatory and Metrological Support of the Information Protection System in Ukraine*. 2012. Iss. 1 (23). P. 29—35.
9. DSTU 31295.2-2005 (ISO 9613 - 2:1996) Noise. Attenuation of noise when spread over the area. Part 2. General calculation method [Valid from 2007-10-17]. Kyiv, 2007. 25 p.
10. Samokhin V.F. Noise of aviation gas turbine engines (introduction to aviation acoustics): Lecture Notes. Moscow: MAI. 2007. 156 p.
11. *Komkin A.I. GOST 31295.2-2005 As a guide for acoustic calculations.* Bauman MSTU. URL: https://studylib.ru/doc/981408/gost-31295.2-2005-kak-rukovodstvo-dlya-akusticheskih-raschetov

12. Korshikova Zh.S. Algorithms of direction finding and recognition of localized sources of broadband radiation against the background of space-distributed interference: Candidate of technical sciences thesis. Moscow, 2010. 16 p.
13. Krasko A.S. Supporting the adoption of a decision to ensure public security at urban territorial facilities based on the operational analysis of audio information: author's review: Candidate of technical sciences thesis. Ufa, 2011. 16 p.
14. Klyukin I.I. The amazing world of sound. Leningrad: Shipbuilding, 1978. 168 p.
15. Sopin A. A. Radio diagnostics of ionospheric disturbances stimulated by powerful tropospheric processes. Candidate of technical sciences thesis. Kharkiv, 2013. 171 p.
16. Forbes J. M., Palo S. E., Zhang X. Variability of the ionosphere. *J. Atm. Solar-Terr. Phys.* 2000.Vol. 62. P. 685—693.
17. Lastovicka J. Forcing of the ionosphere by waves from below. *J. Atmos. Solar-Terr. Phys.* 2006. Vol. 68. P. 479—497.
18. Gershman B. N., Grigor'ev G. I. Traveling ionospheric disturbances. *Radiophysics and Quantum Electronics. A Review*. 1968. Vol. 11. No. 1. P. 5—27.
19. Kazimirovsky E. S. Coupling from below as a source of ionospheric variability: a review. *Ann. of Geophys*. 2002. Vol. 45. No. 1. P. 1—29.
20. Lazorenko O.V., Chernogor L.F. Ultrawideband signals and processes. Kharkiv: V.N. Karazin Kharkiv National University, 2009. 576 p.
21. Rizos C. Principles and Practice of GPS Surveying. Sydney: SNAP, School of Geomatic Engineering, UNSW, 1999. URL: http://www.gmat.unsw.edu.au/snap
22. Nasylov D.N. Radiometeorology. Moscow: Science, 1966, 336 p.
23. Bean B. R., Dutton E. J. Radio meteorology. Transl. from engl. T. I. Arsenyan. Ed. A.A. Semenov. Leningrad: Hydrometeoizdat, 1971. 362 p.
24. Smirnov V. Masking of mobile ground objects in modern conditions. URL: http://samlib.ru/s/ smirnow_wasilij/masikirovka.shtml
25. Zvereva S. V. In the world of solar light. Leningrad: Hydrometeoizdat, 1988. 160 p.
26. Travnikova N. P. Effectiveness of visual search. Moscow: Mash., 1985. 128 p.
27. Krylov I.S. Study of radiation characteristics of tanks and natural formations, assessment of the range of action of optical-electronic direction finding and homing systems. *Questions of Defense Technology, Series XX*. Iss. 26—27. Moscow: Ministry of Defense Industry of the USSR, 1972. 202 p.
28. Reshchikov I.F. [and others]. Reduction of the effective scattering area of objects of armored vehicles due to low-reflective external forms and the use of radio-absorbing coatings. *Questions of Defense Technology, Series XX*. Iss. 26—27. Moscow: Ministry of Defense Industry of the USSR, 1972. 202 p.
29. Lutsenko V.I., Lutsenko I.V., Sobolyak A.V. Range of action of acoustic reconnaissance systems. *Applied radio electronics*. 2015. Vol. 14. No. 2. P. 125—136.
30. Drozdenko O.I., Drozdenko K.S., Kozeruk S.O. Acoustic devices and systems-1: Educational Vis. Stud. Guide. Kyiv: National Technical University of Ukraine "Igor Sikorsky Kyiv Polytechnic Institute", 2019. 154 p. URL: https://ela.kpi.ua/bitstream/ 123456789/ 52346/1/Akustychni.pdf
31. Tansyura O.B., Kozhushko Y.M., Radetskyi, V.V., Shevchuk O. Analysis and prospects for the development of technical means of counter-sniper combat. *Kharkiv National University of the Air Force: Collection of Scientific Papers*. 2019. Vol. 4(62). P. 79—84. DOI: 10.30748/zhups.2019.62.11

32. Chan Liu, Ibraimov I.K., Panchenko A.Yu. Acoustic method of sounding the boundary layer of the atmosphere. Current state and perspectives of development. *Visnyk NTUU KPI Seriia — Radiotekhnika Radioaparatobuduvannia*. 2018. Iss. 73. P. 17—27.
33. Dzhereleiko R. Fire Detection System "SOVA". *Military equipment*. 2011.
34. Barkhatov A.V., Veremyev V.I., Kovalev D.A., Konovalov A.A., Mikhailov V.N. Radar based on signals from third-party sources. Part 1: Illumination of the air situation and environmental monitoring. *Innovations*. 2013. No. 9 (179). P. 114—119.
35. Barkhatov A.V., Veremyev V.I., Kovalev D.A., Konovalov A.A., Mikhailov V.N. Radar based on signals from third-party sources. Part 2: Clarification of the air situation and environmental monitoring. *Innovations*. 2013. No. 10 (180). P. 7—11.
36. Tkachev G.N., Gotochyts I.V., Krylov B.N. Results of research on the problem of semi-active radar in the short wave range. *Radiolocation and Radiocommunication: Conf. Proc*. Moscow: IRE RAS, 2010. P. 264—267.
37. Suharevsky O.I., Vasylets V.A., Kukobko S.V. et al. Scattering of electromagnetic waves by air and ground objects. Ed. O.I. Sukharevsky. Kharkiv: Kharkiv National University of the Air Force, 2009. P. 90—191.
38. Sedyshev Yu.N., Tyutyunnik V.A. Information technologies for the creation of spatial-temporal modems of multi-position active-passive radar systems. *Applied Radioelectronics*. 2015. Vol. 14. No. 1. P. 105—110.
39. Lutsenko I.V., Popov I.V., Lutsenko V.I. Bistatic radar with illumination of ionospheric signals of communication stations of the short-wave range. *Radiophysics and electronics*. Kharkiv. 2007. Vol. 12. No. 1. P. 193—204.
40. Lutsenko V.I., Lutsenko I.V., Popov I.V. Monitoring of air conditions with the use of radiation from short-wave broadcasting stations. *Radiophysics and Quantum Electronics*. 2015. Vol. 58. No. 1. P. 10—20.
41. Vylenchyk L.S., Melyanovsky P.A., Minaev V.N. Fundamentals of passive short-wave radar. *Radiotechnique*. 2009. P. 61—66.
42. Beketov A.A., Belokon A.P., Chermashentsev S.Ch. Masking of the actions of units of the ground forces. Moscow: Voenizdat, 1976. P. 19—27.
43. Griffiths H.D., C. Eng., Long N.R.W. Television based bistatic radar. *Communications, Radar and Signal Processing. IEE Proceedings F*. 1986. Vol. 133. (7). P. 649—657. DOI: 10.1049/ip-f-1.1986.0104
44. Howland P.F Target tracking using television-based bistatic radar. *Radar, Sonar and Navigation. IEE Proceedings*. 1999. Vol. 146 (3). P. 166—174.
45. Lanterman A.D. Tracking and Recognition of Airborne Targets via Commercial *Television and FM Radio Signals. Proc. SPIE 3692, Acquisition, Tracking, and Pointing XIII, (15 July 1999)*. P. 189—198. DOI: 10.1117/12.352861
46. Baniak J., Baker G, Cunningham A. M. & Martin L. Silent Sentry™ Passive Surveillance. Lockheed Martin Mission Systems. 1999. 12 p.
47. Tan D. K. P., Sun H., Lu Y., Lesturgie M., Chan H. L. Passive radar using global system for mobile communication signal: *Theory, implementation and measurements. Radar, Sonar and Navigation. IEE Proceedings*. 2005. Vol. 152. Iss. 3. P. 116—123. DOI: 10.1049/ip-rsn: 20055038
48. Sun H., Tan D.K. P., Lu Y. Aircraft target measurements using A GSM-based passive radar. *2008 IEEE Radar Conference*. Rome. 2008. P. 1—6. DOI: 10.1109/RADAR.2008. 4721053

49. Guo H., Woodbridge K. and Baker C. J. Evaluation of WiFi beacon transmissions for wireless based passive radar. *2008 IEEE Radar Conference*. Rome. 2008. P. 1—6. DOI: 10.1109/RADAR.2008.4720810
50. Falcone P., Colone F., Macera A., Lombardo P. Localization and tracking of moving targets with WiFi-based passive radar. *2012 IEEE Radar Conference*. Atlanta, GA, USA. 2012. P. 0705—0709. DOI: 10.1109/RADAR.2012.6212229
51. Sinha N. B. et al. Target localization accuracy using WiMAX radar networks. *Journal of Theoretical & Applied Information Technology*. 2011.Vol. 27. No. 2. P. 99—104.
52. Wang Q., Hou C., Lu Y. An experimental study of WiMAX-based passive radar. *IEEE Transactions on Microwave Theory and Techniques*. 2010. Vol. 58. No. 12. P. 3502—3510.
53. Salah A. A., Raja Abdullah R. S. A., Ismail A., Hashim F., Leow C. Y. et al. Feasibility study of LTE signal as a new illuminators of opportunity for passive radar applications. *2013 IEEE International RF and Microwave Conference (RFM)*. Penang. 2013. P. 258—262. DOI: 10.1109/RFM.2013.6757261
54. Salah A.A., Raja Abdullah R.S.A., Ismail A., Hashim F., Abdul Aziz N.H. Experimental study of LTE signals as illuminators of opportunity for passive bistatic radar applications. *Electronics Letters*. 2014. Vol. 50. No. 7. P. 545—547. DOI: 10.1049/el.2014.0237
55. Poullin D. Passive detection using digital broadcasters (DAB, DVB) with COFDM modulation. *Radar, Sonar and Navigation. IEE Proceedings*. 2005. Vol. 152. Iss. 3. P. 143—152. DOI: 10.1049/ip-rsn:20045017
56. Kutuza, B.G., Kravchenko, V.F., Lutsenko, V.I. et. al. Use of emission of GNSS (GPS, GLONASS) for remote sensing of the environment. *Contemporary Problems of Remote Sensing of the Earth from Space: Conf. Proc*. Moskow: SRI RAS. 2014. P. 123.
57. Dzvonkovskaya A., Helzel T., Petersen L., Merz C. R., Liu Y., Weisberg R. H. Initial results of ship detection and tracking using WERA HF ocean radar with MIMO configuration. *2014 15th International Radar Symposium (IRS)*. Gdansk. Poland. 2014. P. 1—3. DOI: 10.1109/IRS.2014.6869265
58. Melyanovsky P.A., Turgenev I.S. Bistatic HF radar for oceanography applications with the use of both ground and space waves. *Telecom. and Radio Eng*. 1997. 51. No. 2. P. 30—41.
59. Thomas J. M., Griffiths H. D., Baker C. J. Ambiguity function analysis of Digital Radio Mondiale signals for HF passive bistatic radar. *Electronics Letters. Stevenage*. 2006. Vol. 42. Iss. 25. P. 1—2.
60. Thomas J. M., Baker C. J. and Griffiths H. D. DRM signals for HF passive bistatic radar. *2007 IET International Conference on Radar Systems*. Edinburgh. UK. 2007. P. 1—5. DOI: 10.1049/cp:20070642
61. Vychkan A.V., Melyanovsky P.A., Shut A.I. Passive coherent radar in the short-wave range. Part 1. Detection of aerial targets. *Radiophysics and electronics*. 2010. Vol. 15. No. 1. P. 72—77.
62. TROPHY® Active Protection System for AFVs. The Only Fully Operational APS That Has Saved Lives. RAFAEL Advanced Defense Systems LTD. URL: https://www.rafael.co.il/worlds/land/trophy-aps/
63. Korniichuk S.P., Turinskyi O.V., Pievtsov H.V. Modern weapons and military equipment of the Armed Forces of the Russian Federation. Handbook of the OCF participant; ed. S.P. Korniichuk. Kharkiv: DISA, 2020. 1220 p. URL: https://nvkarta.com/project/library/uploads/military/tactics/[tactics]_suchasne_ozbroyennya_i_vijskova_texnika_rosijskoyi_federacziyi.pdf

64. Zubov V.N., Lugin D.V. High-precision weapon systems: textbook. Moscow: Bauman MSTU, 2007. 56 p.
65. "Kolchuga" mobile long-range radio-technical reconnaissance station. State Enterprise "Ukroboronservis". URL: https://ru.uos.ua/produktsiya/tehnika-pvo/rls/111
66. Ukrainian "Kolchuga" (radio-technical intelligence station). *Military review*. URL: https://topwar.ru/13650-azerbaydzhan-prodolzhaet-vooruzhatsya-na-ocheredi-ukrainskaya-kolchuga-m.html
67. Lutsenko V.I., Lutsenko I.V., Sobolyak A.V. Action range and resolution ability of passive acoustic reconnaissance systems. *5th Int. Radio Electronic Forum. Applied radioelectronics (IREF-2014)*. Integrated Information Radioelectronic Systems and Technologies, Oct. 14—17: Conf. Proc. Kharkiv, 2014. Vol. 1. P. 41—44.
68. Lutsenko V.I., Lutsenko I.V., Sobolyak A.V. Passive acoustic reconnaissance systems, the range of their actions and resolution. *Integrated technologies and energy saving, quarterly scientific and technical journal*. Kharkiv: NTU "KhPI". 2014. No. 3. P. 60—64.
69. Liu Ch., Panchenko A.Yu., Slipchenko M.I. Atmospheric radio acoustic sounding systems with controlled array antennas. Part 2: Diffraction problem. *Telecommunication and Radio Engineering*. 2015. Vol. 74(19) P. 1745—1753. DOI: 10.1615/TelecomRadEng.v74.i19.70
70. Liu Ch., Panchenko A.Yu., Slipchenko M.I., Ulyanov Y.N. Atmospheric radio acoustic sounding systems with controlled array antennas. Part 1. Performance evaluation of controlled AA. *Telecommunication and Radio Engineering*. 2015. Vol. 74(17) P. 1545—1552. DOI: 10.1615/TelecomRadEng.v74.i17.50
71. Propagation of ultrashort waves; Transl from English. Ed. B. A. Schillerova. Moscow: Sov. Radio, 1954. 710 p.
72. Stepanenko V.G., Halperin S.M. Radio engineering methods for studying thunderstorms. Leningrad: Gidrometeoizdat, 1983. 204 p.
73. Sukhonin E. V. Attenuation of millimeter and submillimeter waves in the atmosphere with hydrometeors: Doctor of physics-math. sciences thesis. Moscow: IRE Academy of Sciences of the USSR, 1988. 351 p.
74. Zuev V. E. Distribution of visible and infrared waves in the atmosphere. Moscow: Sov. Radio, 1970. 496 p.
75. Kalinovsky A. B., Pinus N. Z. Aerology. Leningrad: Gidrometeoizdat, 1961. 345 p.
76. Zhukov B. V., Kabanov V. A., Mytsenko I. M., Sinytskyi V. B., Khomenko S. I., Khlopov G. I. Diagnostics of VHF propagation conditions in the troposphere. Ed. by G. I. Khlopov. Kyiv: Naukova dumka, 2010. 263 p.
77. Isimaru I. Spreading and scattering of waves in randomly inhomogeneous environment. Moscow: Mir, 1981. Vol. 2. 317 p.
78. Kabanov V. A. The relationship between the radio brightness temperature at sliding angles and the conditions of radio wave propagation over the sea. *Radiophysics and Electronics*. Kharkiv. 2006. Vol. 11. No. 2. P. 234—239.
79. Brown E.H., Hall F.F. Jr. Advances in atmospheric acoustics. *Rev. Geophys. and Space Phys*. 1978. Vol. 16. No. 1. P. 47—100.
80. Little K.G. Acoustic methods of remote sensing of the lower atmosphere. *PIIER*. 1969. Vol. 57. No. 4. P. 222—230.
81. Hall F.F., Wescott J.W., Simmons W.R. Acoustic echo sounding of atmosphere thermal and wind structure. *Seventh International Symposium on Remote Sensing of the Environment: Conf. Proc*. Univ. of Michigan, 1971. Vol. I. P. 1715—1732.

82. Oltersten H., Hurtig M., Stilke G. et al. Shipborne sodar measurements during Jonswap 2. J. *Geoph. Research*. 1974. Vol. 79. No. 36. P. 5573—5584.
83. Tatarsky V. I. To the theory of propagation of sound waves in a turbulent flow. *JETP*. 1953. Vol. 25. P. 74.
84. Bergmann P. G. Propagation of radiation in a medium with random inhomogeneities. *Phys. Rev*. 1946. Vol. 70. P. 456.
85. Bradley S. Atmospheric Acoustic Remote Sensing. Boca Raton, FL, USA: CRC Press, 2008. 302 p.
86. Kallystratova M.A., Kon A.M. Radioacoustic sounding of the atmosphere. Moscow: Nauka, 1985. 198 p.
87. Krasnenko N. P. Acoustic sounding of the atmosphere. Novosibirsk: Nauka, 1986. 167 p.
88. Matuura N., Masuda Y., Inuki H. et al. Radio acoustic measurement of temperature profile in the troposphere and stratosphere. *Nature*. 1986. Vol. 323. Iss. 6087. P. 426—428. DOI: 10.1038/323426a0
89. Kartashov V. M. Models and signal processing methods of radioacoustic and acoustic atmospheric sounding systems: Monograph. Kharkiv: KhNURE, 2011. 230 p.
90. Kolomiets S.M. Measuring the speed of a transparent liquid methods of acousto-optics. *Izv. RAS. Physics of the Atmosphere and Ocean*. 2000. Vol. 36, No. 6. P. 847—852.
91. Kolomiets S.M. Method for determining the speed of sound. Patent 2221224 RF. Iss. January 10, 2004.
92. Kolomiets S.M. Interference method for determining refractive index of medium or speed of sound in this medium. *Physics of Vibration*. 2002. Vol. 10. No. 4. P. 222—227.
93. Kolomiets S.M. Sounding of ocean and atmosphere using Doppler effect in inhomogeneous media. *Physics of Wave Phenomena*. 2003. Vol. 11. No. 3. P. 159—167.
94. Carsewell A.I. LIDAR measurements of the atmosphere. *Can. J. Phys*. 1982. Vol. 61. P. 378—393.
95. Argall P.S., Sica R.J. LIDAR. In Encyclopedia of Imaging Science and Technology; Ed. Hornak J.P. New York. USA: John Wiley & Sons, 2002. DOI: 10.1002/0471443395.img061
96. Wandinger U. Introduction to Lidar. In Lidar: Range-Resolved Optical Remote Sensing of the Atmosphere; Ed. Weitkamp C. New York. USA: Springer, 2005. P. 6—11.
97. Menut L., Flamant C., Pelon J., Flamant P.H. Urban boundary layer height determination from lidar measurements over the Paris area. *Appl. Opt*. 1999. Iss. 38. P. 945—954.
98. Murayama T., Okamoto H., Kaneyasu N., Kamataki H., Miura K. Application of lidar depolarization measurement in the atmospheric boundary layer: Effects of dust and sea-salt particles. *J. Geophys. Res*. 1999. Iss. 104. P. 31781—31792.
99. Stephens G.L. Remote Sensing of the Lower Troposphere: An Introduction. New York. USA: Oxford University Press, 1994. 427 p.
100. Markyna N. N., Naumov A. P., Sumyn M. I. Determination of height profiles of atmospheric refraction coefficient in optical and microwave wave ranges by its thermal radiation. *Radiophysics and Quantum Electronics*. 1987. Vol. 30. No. 8. P. 951—960.
101. Gurvych A.S., Ershov A.T. On radiothermal radiation of the atmosphere during wave propagation. *Izv. Academy of Sciences of the USSR. Physics of the Atmosphere and Ocean*. 1979. Vol. 15 No. 2. P. 218—221.
102. Shchukin H. G., Melnyk Yu. A., Halperin S. M., Ilyin Y. K., Mykhaylov N. F., Ryzhkov A. V. Evaluation of the conditions of propagation of radio waves over the sea by radiometric

method. Papers of Geophys. *Observatories, methods of active and passive radar in radiometeorology*. 1982. Iss. 451. P. 65—68.
103. Mykhaylov N.F., Ryzhkov A.V., Shchukin G.G.Radiometeorological studies on the sea. Leningrad: Gidrometizdat, 1990. 208 p.
104. Kabanov V. A. Estimation of radio wave propagation conditions over the sea according to radiometric measurements in the area of sliding angles. *Radiophysics and Electronics.* 2006. Vol. 11. No. 3. P. 400—403.
105. Voytovych O.A., Linkova A.M., Khlopov G.I. Two-frequency profiling of rain parameters. *Radiophysics and Electronics*. 2011. Vol. 2(16). No. 3. P. 51—60.
106. Belov E.N., Voytovych O.A., Linkova A.M., Rudnev G.A., Khlopov G.I., Khomenko S.I. Dual-frequency sounding of liquid sediments using the MRL-1 meteor radar. *Radiophysics and Electronics*. 2012. Vol. 3(17). No. 1. P. 49—59.
107. Zhukov B.V. et. al. Diagnostics of VHF propagation conditions in the troposphere. Ed. G. I. Khlopov. Kyiv: Naukova dumka, 2010. 263 p.
108. Kabanov V.A. The structure of the atmospheric refraction coefficient and diagnostics of VHF propagation conditions over the sea: Candidate of phys. and math. sciences thesis. Kharkiv. 1996. 161 p.
109. Dorfman N.A., Kabanov V.A., Kyvva F.V., Turgenev I.S. Statistical characteristics of the refractive index in the above the see layer of the atmosphere. *Izv. of Academy of Sciences of the USSR*. 1978. Vol. 14. No. 5. P. 549—552.
110. Zamaraev V.B., Sinytskyi V.B. Determination of the characteristics of tropospheric refraction in the shadow zone by radiation from a distant source. Part 1. Model. *Radiophysics and Electronics*. 2014. Vol. 5(19). No. 3. P. 41—48.
111. Kabanov V.A., Morgun H.M., Sinytskii V.B., Turgenev I.S. Determination of the characteristics of tropospheric refraction in the shadow zone by radiation from a remote source. Part 2. Experiment. *Radiophysics and Electronics*. 2014. Vol. 5(19). No. 4. P. 56—62.
112. Khomenko S.I., Khlopov G.I., Halameida D.D. Investigation of refraction properties of the troposphere using a radio interferometer. *Radiophysics and Electronics*. 2012. Vol. 3(17). No. 2. P. 50—53.
113. Ivanov V.K., Levadny Yu.V., Shalyapin V.N. Distribution of radio waves of the millimeter range in the coastal zone. *Radiophysics and Electronics*. 2011. Vol. 2(16) No. 4. P. 46—52.
114. Smirnova A.A. Objective analysis of cloudiness and dangerous weather phenomena according to radar and station observed data: Candidate of geographical sciences thesis. Perm: Perm. University, 2005. 20 p.
115. Solonin A.S. Status and prospects for the development of meteorological radars. 3rd International Radio Electronic Forum (IREF-2008). Modern and promising systems of radar, radio astronomy and satellite navigation (MRRSN-2008). Oct. 22—24, 2008: *Conf. Proc*. Kharkiv. 2008. Part 1. P. 9—13.
116. Veselovska G.B. Backscattering of electromagnetic waves by a polydisperse medium of non-spherical drops in two-frequency remote sensing problems: Candidate of phys. and math. sciences thesis. National Academy of Sciences of Ukraine. O.Ya. Usikov Institute for Radiophysics and Electronics. Kharkiv. 2014. 147 p.
117. Linkova A.M. Combined method of two-frequency sounding of dispersed media in the atmosphere: Candidate of phys. and math. sciences thesis. National Academy of Sciences of Ukraine. O.Ya. Usikov Institute for Radiophysics and Electronics. Kharkiv. 2012. 168 p.

118. Lutsenko V.I., Lutsenko I.V., Anh N.X. The use of Doppler radars for studying the turbulence of air masses in clouds. *Radioelectronics and Communications Systems*. 2010. Vol. 53. No. 6. P. 3—12. DOI: 10.3103/S0735272710060014
119. Marchuk V.V., Ostrovsky Y.P., Mazura I.V., Yanovsky F.J. Methods of Turbulence Detection by Analyzing Precipitation Behaviour. *2nd Microvave & Radar Week in Poland, International Radar Symposium (IRS-2006), 24—26 May 2006. Krakov, Poland: Conf. Proc*. Krakov. 2006. P. 161—164.
120. Khlopov G.I., Lutsenko V.I., Popov I.V. Millimeter Wave Radar for Study of Polarization — Spectrum Features of Signals Scattered by Hydrometeors. *2nd Microvave & Radar Week in Poland, International Radar Symposium (IRS-2006), 24—26 May 2006. Krakov, Poland: Conf. Proc*. Krakov. 2006. P. 275—278.
121. Khlopov G.I. The Spectra of Coherent Millimeter Wave Signals, Reflected from Hydrometeors. *Telecommunications and Radio Engineering*. 1997. Vol. 51. No. 1. P. 17—24.
122. Kozlov A.I., Logvin A.I. Development of radio polarimetry in Russia. Foreign Radio Electronics. *Successes of Modern Radio Electronics*. 1999. No. 7. P. 62—71.
123. Zagorin G.K., Kozhevnikov N.I., Shchupyatskyi A.B. Determination of the microstructure of crystalline and mixed clouds by polarization characteristics of a radar signal. *Methods and Means of Atmospheric Sensing: Proceedings of Central Aerological Observatory*. 1990. Iss. 168. P. 82—93.
124. Ostrovsky Y.P., Yanovsky F.J., Rohling H. Turbulence and Precipitation Classification based on Doppler- Polarimetric Radar Data. *2nd Microvave & Radar Week in Poland, International Radar Symposium (IRS-2006). 24—26 May 2006, Krakov, Poland: Conf. Proc*. Krakov. 2006. P. 275—278.
125. Gorelyk A.G., Sterlyadkin V.V. Influence of the vibration of raindrops on the polarization characteristics of radio echo. *Proceedings of Academy of Sciences of the USSR, Physics of the Atmosphere and Ocean*. 1989. Vol. 25. No. 9. P. 960—968.
126. Kravchenko V.F., Kravchenko O.V., Lutsenko V.I., Lutsenko I.V., Popov D.O. Usage of Global Navigation Systems for Detection of the Dangerous Meteorological Phenomena. *Journal of Measurement Science & Instrumentation*. Mar. 2015. Vol. 6. Iss. 1. P. 68—74.
127. Gudkov V.N., Lutsenko V.I., Lutsenko I.V., Anh N.X. Diagnosing refraction properties of troposphere over land using global navigation systems. *Radioelectronics and Communications Systems*. 2010. Vol. 53. No. 7. P. 3—12. DOI: 10.3103/S0735272710070010
128. Laush A.G., Lutsenko V.I., Lutsenko I.V. Use of global navigation satellite systems radiation for solving of radar problems. *Radioelectronics and Communications Systems*. 2015. Vol. 58. No. 11. P. 14—27. DOI: 10.3103/S0735272715110023
129. Lutsenko V.I., Popov D.O., Lutsenko I.V. Investigation of the underlying surface with the help of radiation from the global navigation satellite system. *Radiophysics and Electronics*. 2016. Vol. 7(21). No. 1. P. 31—39. URL: http://dspace.nbuv.gov.ua/ handle/123456789/106285
130. Lusignan B., Modrell G., Morrison A., Pomalaza J., Ungar S. G. Sensing the Earth's atmosphere with occultation sattellites. *Procceed. IEEE*. April 1969. Vol. 57. No. 4. P. 438—467.
131. Anderson K.D. Inference of refractivity profiles by satellite–to–ground RF measurements. *Radio Sci*. 1982. Vol. 17. No. 3. P. 653 — 663.
132. U.S. Patent 4 093 918. Means for determining the refractive index profile of the atmosphere / Herbert W. Hitney June 6, 1978.

133. Armand N. A., Andrianov V. A., Smirnov V. M. Restoring the profile of the refraction coefficient of the troposphere by measurements of the frequency of radio frequency signals. *Journal of Communications Technology and Electronics*. 1987. Vol. 32. Iss. 4. P. 673—680.
134. Lutsenko V.I., Popov D.O., Lutsenko I.V. Research on the underlying surface by radiation of global navigation satellite system. *Telecommunication and Radio Engineering*. 2016. Vol. 75. No. 10. P. 909—922. DOI: 10.1615/TelecomRadEng. v75.i10.50
135. Lutsenko I.V., Popov D.O. Diagnostics of the atmosphere and underlying surface using emitted global navigation satellite systems. *14th Ukrainian Conference on Space Research. Sep. 8—12, 2014. Uzhhorod: Conf. Proc*. 2014. P. 33.
136. Levchenko S. A., Lutsenko V. I., Lutsenko I. V., Popov D. O. Monitoring of the atmosphere and ocean surface with the help of GPS, GLONASS global satellite navigation system receivers / S.A. Levchenko, I.V. Lutsenko, D.O. Popov Science and technology as a basis of modernization for future sustainable development. *SSF—2014: Proceed. of International Humboldt Conference (18—21 Sep. 2014, Minsk)*. Ed. by S. Levchenko, A. Kuzei. Minsk, 2014. P. 26—30.
137. Lutsenko I.V., Sytnyk O.V., Anh N.X., Gudkov V.N. Prediction of the Refraction Coefficient in Arbitrary Points of Space Using Results of Measurements of Meteorological Parameters in Base Stations. *Radiophysics and Electronics*. Kharkiv. 2012. Vol. 3(17). No. 4. P. 54—63. URL: http://dspace.nbuv.gov.ua/handle/ 123456789 /105921
138. Lutsenko V.I., Lutsenko I.V., Kryvenko E.V., Popov D.O. Detection of dangerous meteorological phenomena using global navigation satellite systems. *1st Ukrainian Conf. Electronic Methods of Research of the Surrounding Space. Sep. 25—27, 2012: Conf. Proc*. Kharkiv. 2012. P. 253—255.
139. Lutsenko I.V., Popov I.V., Krivenko E.V., Gudkov V.N., Lukianenko N.V., Anh N.X. Detection of Dangerous Meteorological Phenomena with Usage of GPS Signals. *The 9th European Radar Conference (EuRAD-2012). 31 Oct — 2 Nov 2012. Amsterdam: Conf. Proc*. Amsterdam. 2012. P. 353—356.
140. Lutsenko V. I., Lutsenko I.V., Popov D. O. Weather-induced influence on the change of coordinates of consumers in GNSS. *24th Int. Crimean Conference "Microwave & Telecommunication Technology" (CriMiCo'2014). 7—13 Sep. 2014*. Sevastopol. Crimea. Ukraine: Conf. Proc. 2014. P. 1125—1126.
141. Lutsenko V. I., Lutsenko I. V., Popov D. O. Detection of meteorological formations using a global navigation system. *5th Int. Radio Electronic Forum (IREF-2014)*. Applied radio Electronics. Status and Prospects of Development. Oct. 14—17, 2014: Proc. of the IREF. Vol. 1. Integrated Information Radio-Electronic Systems and Technologies. Kharkiv. 2014. P. 207—210.
142. Kravchenko V.F., Kravchenko O.V., Lutsenko V.I., Lutsenko I.V., Popov D.O. Usage of global navigation systems for detection of dangerous meteorological phenomena. *JMSI Journal of Measurement Science and Instrumentation*. 2015. Vol. 6. No. 1. P. 68—74.
143. Lutsenko V.I., Lutsenko I.V., Popov D.O. Investigation of the underlying surface with the help of GNSS. *5th Int. Scient. and Pract. Conf. Signal Processing and Non-Gaussian Processes. In memory of Professor Yu.P. Kunchenko for the 55th anniversary of ChDTU.* May 20—22, 2015. Cherkasy. Ukraine: Conf. Proc. Cherkasy. 2015. P. 113—115.
144. Lutsenko V.I., Popov D.O., Lutsenko I.V. Investigation of the underlying surface using the radiation of the global navigation and satellite system. *Radiophysics and electronics*. 2016. Vol. 7 (21). No. 1. P. 31—39.

145. Anh Nguyen Xuan, Lutsenko V. I., Popov D.O., Cong Pham Chi, Trung Tran Hoai. Remote Sensing Of Atmosphere And Underlying Surface Using Radiation Of Global Navigation Satellite Systems. *Journal of Marine Science and Technology*. 2017. Vol. 17. No. 4B. P. 1—7. DOI: 10.15625/1859-3097/17/4B/12985
146. Nguyen Xuan Anh, Popov D.O., Lutsenko V.I., Lutsenko I.V., Cong Pham Chi. Remote sensing of atmosphere and underlying surface using signals of global navigation satellite systems. *The Int. of Research Development and Cooperation in Geophysics (VIET-Geophys 2017)*. 18—22 Oct. 2017. Hanoi. Vietnam: Book of Abstract. Hanoi. 2017.
147. Lutsenko V. I., Popov D. O., Lutsenko I. V., Anh Nguyen Xuan. Remote sensing of the underlying surface using global satellite navigation systems. *European Microwave Conference in Central Europe (EuMCE-2019). 13-15 May 2019. Prague. Czech Republic.: Conf. Proc*. Prague. 2019. P. 350—353.
148. Laush A.G., Lutsenko I.V., Popov D.O. The use of emission of the global navigation satellite systems to solve the problems of radar and remote sensing. *24th Int. Crimean Conference "Microwave & Telecommunication Technology" (CriMiCo'2014). 7—13 Sep. 2014, Sevastopol, Crimea, Ukraine: Conf. Proc*. Sevastopol. 2014. P. 1149—1150.
149. Laush A.G., Lutsenko I.V., Popov D.O. Illumination of the air and surface environment with the use of emitted global navigation satellite systems. *5th Int. Radio Electronic Forum (IREF-2014). Applied radio Electronics. Status and Prospects of Development. Oct. 14—17, 2014: Proc. of the IREF. Vol. 1. Integrated Information Radio-Electronic Systems and Technologies*. Kharkiv. 2014. P. 45—48.
150. Ivanov V.A., Shumaev V.V., Kurkin V.I., Nosov V.E., Uryadov V.P. Chirp ionosonde and its application in the ionospheric research. *Radiophysics and Quantum Electronics*. 2003. T. 46. No. 11. P. 821—851.
151. Gardner F.F., Pawsey J.L. Study of the ionospheric D-region using partial reflections. *J. Atmos. Terr. Phys*. 1953. Vol. 3. No. 8. P. 321—324.
152. Ivanov V.A. Investigation of the D-region of the ionosphere by the method of particle reflections. Yoshkar-Ola: VYNITY, 1985. 196 p.
153. Gokov A.M., Tyrnov O.F., Chernogor L.F. Experimental study of the reaction of the mid-latitude D-region of the ionosphere to X-ray and optical flares. *Space Science and Technology*. 2005. Vol. 11. No. 3/4. P. 56—67.
154. Gokov A.M., Chernogor L.F. Variations of the electron concentration in the midlatitude D-region of the ionosphere during magnetic storms. *Space Science and Technology*. 2005. Vol. 11. No. 5/6. P. 12—21.
155. Manson A.H., Meek C.E., Hall G., McMurray R. Winds and waves from the Canadian prairies (CNSR) triple-MF radar system. *Geophys. Res. Lett*. 1993. Vol. 20. No. 13. P. 1375—1378.
156. Namboothiri S.P., Manson A.H., Meek C.E. Variations of mean winds and tides in the upper middle atmosphere over a solar cycle, Saskatoon, Canada, 52°N, 107°W. *J. Atmos. Terr. Phys*. 1993. Vol. 55. No. 10. P. 1325—1334.
157. Panasenko S.V., Rozumenko V.T., Tyrnov O.F., Chernogor L.F. Results of studies of dynamic processes in the mesosphere with the help of radar of particle reflections. *Advances in Modern Radio Electronics*. 2005. No. 3. P. 36—54.
158. Panasenko S.V., Chernogor L.F. Radar observations of quasi-periodic processes in the mesosphere. Part 1. Theoretical foundations and results of computer modeling. *Radio Physics and Radio Astronomy*. 2004. Vol. 9. No. 4. P. 404—416.

159. Panasenko S.V., Chernogor L.F. Radar observation methods of quasi-periodic processes in the mesosphere. Part 2. Methodology and observation results. *Radio Physics and Radio Astronomy*. 2005. Vol. 10. No. 1. P. 38—49.
160. Panasenko S.V., Chernogor L. F. Detection of disturbed waves in the mesosphere with the help of a medium-high frequency radar. *Geomagnetism and Aeronomy*. 2006. Vol. 46. No. 4. P. 525—535.
161. Chernogor L.F. Large-scale disturbances in the lower ionosphere caused by the influence of powerful non-stationary radio radiation. *Radio Physics and Radio Astronomy*. 2013. Vol. 18. No. 1. P. 49—64.
162. Pakhomova O.V., Chernogor L.F. Study by the method of vertical sounding of the reaction of the ionosphere to the impact of powerful radio radiation. *Bulletin of Karazin Kharkov National University. Ser. Radiophysics and Electronics*. 1988. No. 318. P. 29—30.
163. Harmash K.P., Chernogor L.F., Schwartzburg A.B. Emergence of large-scale perturbations in the ionosphere initiated by powerful non-stationary radio radiation. *Computer optics*. 1989. Iss. 6. P. 62—71.
164. Chernogor L.F., Domnyn I.F., Panasenko S.V., Uryadov V.P. Aperiodic large-scale disturbances in the E-region of the ionosphere stimulated by powerful radio radiation. *Radiophysics and Quantum Electronics*. 2012. Vol. 55. No. 3. 173—185.
165. Guo Q., Zheng Y., Chernogor L.F., Garmash K.P., Rozumenko V.T. Ionospheric processes observed with the passive oblique-incidence HF Doppler radar. *Bulletin of Karazin Kharkov National University. Ser. Radiophysics and Electronics*. 2019. Vol. 31. P. 3—15.
166. Chernogor L.F., Garmash K.P., Guo Qiang, Rozumenko V. T., Zheng Yu. Passive Radar for Oblique-Incidence Ionospheric Sounding: Observations of Ionospheric Storms. IEEE Ukrainian Microwave Week (UkrMW). *6th Int. Symposium on Microwaves, Radar and Remote Sensing (MRRS). Sept. 21—25. 2020. Kharkiv. Ukraine: Conf. Proc*. Kharkiv. 2020. Vol. 2. P. 253—258.
167. Konovalenko A.A. I.S. Shklovsky and low-frequency radio astronomy. *Radio Physics and Radio Astronomy*. 2017. Vol. 22. No. 1. P. 7—30. DOI.org/10.15407/rpra22.01.007.
168. Braude S.Ya., Men A.V., Sodin L.G. UTR-2 decameter wave radio telescope. Antennas. Moscow: Svyaz, 1978. Vol. 26. P. 3—14.
169. Konovalenko A., Sodin L., Zakharenko V. et al. The modern radio astronomy network in Ukraine: UTR-2, URAN and GURT. *Exp. Astron*. 2016. Vol. 42. Iss. 1. P. 11—48. DOI: 10.1007/s10686-016-9498-x
170. Men A.V., Braude S.Ya., Rashkovsky S.L., Sharykin N.K., Shepelev V.A., Inyutyn G.A. et al. System of decameter radio interferometers of URAN. Part 1. Basic principles. Overview. *Radio Physics and Radio Astronomy*. 1997. Vol. 2. No. 4. P. 385—401.
171. van Haarlem M.P., Wise M.W., Gunst A.W. et al. LOFAR: The LOw-Frequency ARray. *Astronomy & Astrophysics*. 2013. Iss. A2. P. 556. DOI: 10.1051/0004-6361/201220873
172. Long Wavelength Array. Project website. URL: http://lwa.unm.edu
173. Ellingson S.W. Antennas for the Next Generation of Low Frequency Radio Telescopes. *IEEE Transactions on Antennas and Propagation*. Aug. 2005. Vol. 53. No. 8. P. 2480—2489. DOI: 10.1109/TAP.2005.852281
174. NIST Framework and Roadmap for Smart Grid Interoperability Standards, Release 2.0. NIST (National Institute of Standards and Technology, USA) Special Publication 1108R2. State Department of Commerce, USA. February 2012. URL: https://www.nist.gov/system/files/documents/smartgrid/NIST_Framework_Release_2-0_corr.pdf

175. European SmartGrids Technology Platform. Vision and Strategy for Europe's Electricity Networks of the Future. Luxembourg: Office for Official Publications of the European Communities. 2006. URL: http://www.oe.energy.gov/smartgrid.htm
176. Cruiser anti-ship missile P-700 Granit (3M-45). Information and News System. Rocket technology. URL: http://rbase.new-factoria.ru/missile/wobb/granit/ granit.shtml
177. Yakhont (Onyx) anti-ship missile. Information and News System. Rocket technology. URL: http://rbase.new-factoria.ru/missile/wobb/jakhont/jakhont.shtml
178. Tank T-14 "Armata" or T-99 "Prioritet". News of the Armed Forces. URL: http://vpk.name/library/f/armata.html
179. Biryukov I.Yu., Busyak Yu.M., Shulga A.V. Analysis of the priorities of ground reconnaissance systems for the detection of weapons and military equipment objects. *Engineering, Technical, Software Tools, Complexes and Systems. National Academy of the National Guard of Ukraine*. 2015. Iss. 2 (26). P. 81—87.
180. Lutsenko V.I., Lutsenko I.V., Sobolyak A.V. Range of action of acoustic reconnaissance systems. *Applied Radio Electronics*. 2015. Vol. 14. No. 2. P. 125—136.
181. Kravchenko V.F., Lutsenko V.I., Lutsenko I.V., Sobolyak A.V. Estimation Method of the Acoustic Noise Level of Objects on the Terrain. *Acoustooptic and Radar Methods for Information Measurements and Processing: Conf. Proc. 8th Int. Conf., 20—23 Sept., 2015*. Suzdal: A.S. Popov RNTORES, 2015. P. 220—225.
182. Lutsenko V.I., Lutsenko I.V., Sobolyak O.V. The use of acoustic reconnaissance systems to increase the survivability of ground equipment objects. *IV Int. Scientific and Practical Conf. Problems of Coordination of Military-Technical and Defense-Industrial Policy in Ukraine.* Prospects for the development of weapons and military equipment. Oct. 12—13, 2016. Kyiv. Ukraine: Conf. Proc. Kyiv. 2016. P. 139—141.
183. Lutsenko V.I., Lutsenko I.V., Popov I.V., Sobolyak A.V. Optimal Reception of Signals Propagating in Media with Absorption and Dispersion. *2016 9th International Kharkiv Symposium on Physics and Engineering of Microwaves, Millimeter and Submillimeter Waves (MSMW)*. Kharkiv. Ukraine. 2016. P. 1—4. DOI: 10.1109/MSMW.2016.7538172
184. Acoustic weapons. URL: http://alexsnews.com/ploxoe/2012/01/akusticheskoe-oruzhie/
185. Veretennikov A.I., Rasskazov I.I., Sidorov K.V., Reshetylo E.I. Kharkiv Morozov Machine Building Design Bureau. Ed. by M.D. Borysyuk. Kharkiv: KhMDB, 2007. 188 p.
186. Noise attenuation of sound when spreading on the ground. Part 2. General method of calculation. Interstate standard, GOST 31295.2-2005 (ISO 9613-2:1996). Moscow: Standartinform, 2006. 42 p.
187. Noise. Calculation model User's guide. LLC "ECOcenter". 2012. 19 p.
188. Kyrychenko V.A., Lutsenko V.I. Experimental determination of informative signs for radar recognition of ground and surface objects. *Technique of Millimeter and Submillimeter Radio Waves*. Kharkiv. 1993. P. 5—18.
189. Isaakovich M.A. General acousticz. Study guide. Main Editorial Office of Physical and Mathematical Literature. Moscow: Nauka, 1973. 495 p.
190. Brekhovskikh L.M., Godin O.A. Acoustics of layered media. Main Editorial Office of Physical and Mathematical Literature. Moscow: Nauka, 1989. 416 p.
191. Barton D., Ward G. Handbook of radar measurements. Transl. with English. Ed. by M.M. Weisbern. Moscow: Sov. Radio, 1976. 392 p.
192. Radar reference book. Ed. by M. Skolnyk. Moscow: Sov. Radio, 1976. Vol. 1. 455 p.

193. Valeev F.Ya., Zheleznyak G.V., Kirichenko V.O., Lutsenko V.I., Kukla S.A. Peculiarities of backscattering of radio waves by vegetation at small slip angles. *Ukr. Symp. Physics and Technology of Millimeter and Submillimeter Radio Waves. Oct. 15—18, 1991.* Kharkiv: Conf. Proc. Kharkiv. 1991. Part 2. P. 66—67.
194. Lutsenko V.I. Detection of signals against the background of non-Gaussian noise from the underlying surface. *Electromagnetic Waves and Electronic Systems, Mathematical Modeling of Physical Processes*. 2007. No. 12 P. 41—57.
195. Lutsenko V.I., Khomenko S.I., Roenko A.N. Backscattering Spectral and Polarization Features of the Surface Targets in Centimeter and Millimeter Waves Ranges. *Physics and Engineering of Millimeter and Sub — Millimeter Waves (MSMW'2001) June 4—9, 2001.* Kharkiv. Ukraine: Symp. Proc. Kharkiv. 2001.Vol. 1. P. 405—407.
196. Lutsenko V.I., Lutsenko I.V., Popov I.V., Sobolyak A.V. Signatures of Acousto-Electromagnetic Portraits of Aerodynamic and Terrestrial Mechanical Objects. *2016 9th International Kharkiv Symposium on Physics and Engineering of Microwaves, Millimeter and Submillimeter Waves (MSMW)*. Kharkiv. Ukraine. 2016. P. 1—4. DOI: 10.1109/MSMW.2016.7538146
197. Lutsenko V.I., Lutsenko I.V., Sobolyak O.V. Acoustic-electromagnetic portraits of objects of ground and air technology. *IV International Scientific and Practical Conference. Problems of Coordination of Military-Technical and Defense-Industrial Policy in Ukraine. Prospects for the development of weapons and military equipment*. Oct.12—13, 2016: Conf. Proc. Kyiv. 2016. P. 137—138.
198. Lutsenko V., Lutsenko I., Sobolyak A., Luo Y., Guo Q., Zheng Y. The Acousto-Electromagnetic Portrait Signatures for The Aerodynamic and Ground Technology Objects. *Telecommunication and Radio Engineering*. 2018. Vol. 77. No. 11. P. 971—993.
199. Lutsenko V.I., Khlopov G.I., Popov I.V. Informative characters in spectral – polarization images of backscattering from surface objects. *2nd Microvave & Radar Week in Poland, International Radar Symposium (IRS 2006). 24—26 May 2006. Krakov. Poland.: Conf. Proc*. Krakov. 2006. P. 271—274.
200. Lutsenko V. I., Khomenko S. I. Frequency dependences of RCS objects in the decameter range. *Radiophysics and Electronics*. Kharkiv. 1998. T. 3. No. 2. P. 33—37.
201. Lutsenko V. I., Tolstel S. Y. Frequency Dependences of Scattering Matrices in the Resonance Domain. *Telecommunication and Radio Engineering*. 2001. Vol. 55. No. 4. P. 33—39.
202. Shirman Y.D., Losev Y.I., Minervin N.N., Moskvityn S.V., Gorshkov S.A., Lekhovytskyi D.I. et al. Radio electronic systems: construction principles and theory. Handbook. Ed. by Y. D. Shirman. Moscow: ZAO "MAKVIS". 1998, 828 p.
203. Nebabyn V.G., Sergeev V.V. Methods and techniques of radar recognition. Moscow: Radio and Communication, 1984. 152 p.
204. Detection and recognition of radar objects. Collective monograph. Ed. by A.V. Sokolova. Moscow: Radiotechnique, 2006. 176 p.
205. Geister S.R., Kurlovych V.I., Shalyapin S.V. Experimental studies of spectral portraits of propeller and turbojet aircraft in survey radar with a CW sounding signal. *Radiolocation and Radiometry*. 2000. Iss. 3. P. 90—96.
206. Chernykh M.M., Vasiliev O.V., Bogbanov A.V., Savelev A.N., Makaev V.E. Experimental studies of information properties of coherent radar signals. *Radio Engineering*. 2000. No. 3. P. 45—54.

207. Helicopters. URL: http://www.ukamina.com/books/vertoleti.html
208. Kobak V.O. Radar reflectors. Moscow: Sovetskoe Radio, 1975. 348 p.
209. Emelyanov E.V., Dorofeeva G.A. Dielectric permeability of composite materials based on multi-walled carbon nanotubes, measured by the open quasi-optical resonator method. *Electronics, Measuring Technology, Radio Technology and Communication, TUSUR Reports*. December 2010. No. 2 (22). Part 2. P. 38—40.
210. Kanareykin D. B., Pavlov N. F., Potekhin V. A. Polarization of radar signals. Moscow: Sov. Radio, 1966. 439 p.
211. Bogert B.P., Healy M.J.R., Tukey J.W. The Quefrency Alanysis of Time Series for Echoes: Cepstrum, Pseudo Autocovariance, Cross-Cepstrum and Saphe Cracking. *Proc. of the Symposium on Time Series Analysis*. Ed. by M. Rosenblatt. New York: Wiley, 1963. Chapter 15. P. 209—243.
212. Oppenheim A.V., Shafer R.V. Digital signal processing. Transl. in Engl. Ed. by S.Ya. Shatsa. Moscow: Svyaz, 1979. 416 p.
213. Jeong J. Kepstrum Analysis and Real-Time Application to Noise Cancellation. *8th WSEAS International Conference on Signal Processing, Robotics and Automation. Mathematics and Computers in Science and Engineering. World Scientific and Engineering Acad and Soc.: Conf. Proc.* Athens. Grece. 2009. P. 149—154.
214. Schafer R.W. Echo removal by discrete generalized linear filtering. *Res. Lab. Electron. MIT. Tech. Rep*. 1969. No. 466. 142 p.
215. Oppenheim A.V., Schafer R.W. Homomorphic analysis of speech. *IEEE Trans. Audio Electroacoust. AU-16*. 1968. P. 221—226.
216. Silvia M.T., Robinson E.A. Use of the kepstrum in signal analysis. *Geoexploration*. 1978. Iss. 16. P. 55—73.
217. Kolmogorov A.N. Stationary sequences in Hilbert space. *Bulletin of Moscow State University. Math*. 1941. Vol. 2. No. 6. P. 3—40.
218. Lutsenko V. I., Lutsenko I.V., Popov D.O., Popov I.V. Remote sensing of the environment using the radiation of existing ground and space radio systems. Kyiv: Акademperiodyka. 2020. 345p. DOI: 10.15407/akademperiodyka.429.345
219. Lutsenko V.I., Lutsenko I.V., Popov I.V., Luo Yiyang, Anh Nguyen Xuan, Guo Qiang et al. GNSS Signal Use for Sea Waves Monitoring. *IEEE Ukrainian Microwave Week (UkrMW)*. Kharkiv. Ukraine. 2020. P. 768—771. DOI: 10.1109/UkrMW49653.2020.9252723
220. Popov I.V., Lutsenko V.I., Lutsenko I.V. Illumination of Air Environment Using Radiation of SB Broadcast Station. *International Radar Symposium (IRS 2006). 2nd Microvave & Radar Week in Poland. 24—26 May 2006: Conf. Proc*. 2006. P. 233—236.
221. Popov I.V., Lutsenko V.I., Lutsenko I.V. Illumination of the air envxironment with the use of radiation from broadcasting stations in the HF range. Sovremennye Problemy Radioelektroniki. Ed. by Gromyko A.I., Sarafanova A.V. Moscow: Radio and Communication, 2006. P. 25—28.
222. Popov I.V., Lutsenko V.I., Lutsenko V.I. Bistatic radars illuminated by ionospheric signals from communication stations in the short-wave range. *Radiophysics and Electronics*. 2007. Vol. 12. No. 1. P. 199—203.
223. Anh N. X., Khuong P. L., Kabanov V. A., Lutsenko V. I., Lutsenko I. V., Sinitsky V. B. Estimation of Atmospheric Parameters Using Radio Occultation Method. *J. Geology. Series B*. 2008. No. 31—32. P. 60—66.

224. Lutsenko V.I., Popov I.V. Illumination of Air Environment Using Radiation of SW Broadcasting stations. *The 5th European Radar Conference. 30—31 Oct. 2008. Amsterdam. The Netherlands: Conf. Proc*. Amsterdam. 2008. P. 396—399.
225. Kravchenko V.F., Lutsenko V.I., Lo Iyan, Popov I.V. Non-equidistant two-dimensional antenna arrays based on Latin squares. *Physical Foundations of Instrumentation*. 2018. Vol. 7. No. 1(27). P. 4—23.
226. Lutsenko V.I., Lutsenko I.V., Soboliak A.V., Popov I.V., Anh N.X. Use of Radiation of Broadcast Stations of HF Range for Detection of Air Objects. *IEEE Ukrainian Microwave Week (UkrMW). 2020 IEEE 6th International Symposium on Microwaves, Radar and Remote Sensing (MRRS). Sept. 21—25, 2020*. Kharkiv. Ukraine: Conf. Proc. Kharkiv, 2020. Vol. 2. P. 267—271.
227. Lutsenko I. V., Lutsenko V. I., Popov I.V., Sinitsky V. B., Tarnavsky E. V., Anh N.X. Usage of Electromagnetic Fields of Antropogenic Irradiation Sources for Remote Sensing of Atmosphere. *The 6th European Radar Conference (EuRAD-2009). 28 Sept — 2 Oct 2009. Rome. Italy*: Conf. Proc. Rome. 2009. P. 545—548.
228. Gudkov V.N., Lutsenko V.I., Lutsenko I.V, Anh N.X., Popov I.V, Sinitskiy V.B. Using Signals of the Global Navigation Satellites for Diagnostics of Above Land Troposphere Refraction. *The 7th European Radar Conference (EuRAD-2010). 30 Sept — 1 Oct 2010. Paris. France: Conf. Proc*. Paris. 2010. P. 495—498.
229. Kryvenko O.V., Laush A.G., Lutsenko V.I., Lutsenko I.V., Popov D.O., Popov I.V. et al. The use of radiation from artificial Earth satellites and television centers for the study of atmospheric processes. *Space science and technology*. 2015. Vol. 21. No. 3. P. 83—90.
230. Kalinin A.I. To calculate the field strength in the shadow and penumbra zones during the propagation of ultrashort waves along the smooth spherical surface of the earth. *Radiotehnika*. 1956. Vol. 11. No. 6. P. 43—49.
231. Kalinin A.I. Propagation of radio waves on terrestrial and space radio lines. Moscow: Svyaz, 1976. 296 p.
232. Lvovsky E.N. Statistical methods of constructing empirical formulas: Educational manual. Moscow: Vysshaya Schola. 1982. 224 p.
233. Belov Ye.N., Lutsenko V.I., Lutsenko I.V., Khomenko S.I. Estimation of tropospheric refraction by the attenuation coefficient of radio waves when spreading on Over the Horizon routes. *Radiophysics and Electronics*. Kharkiv. 2004. Vol. 9. No. 1. P. 248—258.
234. Belov Ye.N., Lutsenko I.V., Lutsenko V.I., Khomenko S.I. The Troposphere Refraction Estimation by Attenuation Factor of Radiowave Beyond-the-Horizon Propagation. *Telecommunication and Radio Engineering*. 2003. V. 60. No. 10, 11&12. P. 1—14.
235. Lutsenko V.I., Belov E.N., Lutsenko I.V., Khomenko S.I. Diagnosis of refraction of the troposphere by the field attenuation factor of meter waves in the shadow zone. *Bulletin of V. N. Karazin Kharkiv National University, Ser. Radiophysics and Electronics*. 2002. No. 570. P. 208—209.
236. Kulemin, G.P., Tarnavskyi E.V. Modeling of interference maps from the earth's surface for MMD radar at small slip angles. *Radioelectronic and Computer Systems*. 2004. No. 1. P. 5—12. URL: http://nbuv.gov.ua/UJRN/recs_2004_1_3
237. Anh Nguyen Xuan, Lutsenko V.I., Lutsenko I.V., Popov I.V., Soboliak A.V., Cong Pham Chi et al. Determination Of The Characteristics Of Inversion Reflecting Layers In The Troposphere On Changes In The Signal Intensity On The Near-Earth Over-The-Horizon

Routes In The Middle Latitudes. *Journal of Military Science and Technology*. 2021. Special Iss. No. 72A, 5. P. 13—21.
238. Bogaturov A.N., Gaikovich K.P., Gurevich A.S., Ivanov V.K., Kashkarov S.S., Krivonozhkin S.N. et. al. On the possibility of determining reflective layers in the troposphere above the sea by variations in the levels of ISS signals. *RAS USSR. Geophysics series*. 1990. Vol. 315. No. 4. P. 830—834.
239. Lutsenko V.I., Lutsenko I.V., Belov E.N., Khomenko S.I. On the possibility of determining the characteristics of reflective layers in the troposphere above land based on variations in the levels of VHF signals on over-the-horizon tracks. *Bulletin of V. N. Karazin Kharkiv National University, Series Radiophysics and Electronics*. 2002. No. 570. P. 203—204.
240. Popov I.V., Lutsenko I.V., Lutsenko V.I. Use of detection-measurement methods for the analysis of the characteristics of multi-beam channels. *Radiophysics and Electronics*. Kharkiv. 2006. Vol. 11. No. 2. P. 305—308.
241. Arenberg A.G. Propagation of decimeter and centimeter waves. Moscow: Soviet Radio, 1957. 303 p.
242. Lutsenko I.V., Popov I.V., Lutsenko V.I. Spectral methods for estimating the characteristics of secondary sources in multibeam channels. *Radiophysics and Electronics*. Kharkiv. 2006. Vol. 11. No. 1. P. 144—148.
243. Kivva F.V., Kortunov V.A., Strelnikov Yu.M. On the effect of refraction on the propagation of meter radio waves near the diffraction horizon. *Radio Engineering and Electronics*. 1990. Vol. 35. No. 4. P. 730—733.
244. Sedyshev Y.N., Sedyshev P.Yu., Tyutyunnik V.A. Bistatic noise radars with coherent spatial and temporal processing of echo signals and active interference. *Applied Radio Electronics. Kharkiv National University of Radio Electronics (KHNURE)*. 2002. Vol. 1. No. 2. P. 189—194.
245. Katsko S.V., Chernogor L.F. Estimation of the influence of ionospheric storms on ionospheric channels of radio wave propagation according to observation data on the Kharkov incoherent scattering radar. *Bulletin of the National Technical University "KhPI". Series: Radiophysics and ionosphere*. 2015. No. 37. P. 36—40.
246. Khlopov G.I., Khomenko S.I. Development of scientific research in the department of physical foundations of radar IRE of the National Academy of Sciences of Ukraine. *Radiophysics and Electronics*. 2008. Vol. 13. Sp. Iss. P. 321—332.
247. Lutsenko V.I., Lutsenko I.V., Khlopov G.I. Spectral model of backscattering of microwave and microwave radio waves by biological objects. *Electromagnetic Waves and Electronic Systems*. 2007. Vol. 12. No. 3. P. 9—21.
248. Lutsenko V.I., Popov I.V., Khlopov G.I., Khomenko S.I. Polarization — Spectrum Signatures of Above — Water and Surface Targets. *16th International Conference on Microwaves, Radar and Wireless Communications. May 22—24, 2006. Krakow, Poland*: Conf. Proc. Krakow. 2006. P. 1192—1195.
249. Braude S.Ya., Men A.V., Shulga V.F. Radiooceanographic studies of sea waves. Ed. by Braude S.Ya. Kyiv: Institute of the Academy of Sciences of the Ukrainian SSR. 1962. P. 26—48.
250. Braude S.Ya., Men A.V., Poplavko Y.V., Turgenev I.S., Shulga V.F. Radiooceanographic studies of sea waves. Ed. by Braude S.Ya. Kyiv: Institute of the Academy of Sciences of the Ukrainian SSR. 1962. P. 49—78.

251. Lobochko S.E. Building a detection system using VHF radiation and TV transmitters. *International Scientific Conference. Radiation and Scattering of Electromagnetic Waves (RSEMW-2003). Taganrog: Conf. Proc.* Taganrog. 2003. P. 287—290.
252. Stepanov Yu.G. Anti-radio-location masking. Moscow: Sov. Radio, 1968. 145 p.
253. Lutsenko V. I., Turgenev I. S., Khomenko S. I. On the effects that can lead to the increase of RCS of small-sized objects in the decameter range. *Radiophysics and Electronics*. Kharkiv. 1997. Vol. 2. No. 1. P. 60—63.
254. Popov I.V., Lutsenko I.V., Lutsenko V.I. Detection and measurement of the parameters of an unknown number of signals in the conditions of non-Gaussian interference. *Applied Radio Electronics. ANPRE*. Kharkiv. 2006. Vol. 5. No. 3. P. 378—382.
255. Sinytskyi V. B. On the possibility of using GPS satellite radiation for marine wave diagnostics. *Radiophysics of Electronics*. 2010. Vol. 1(15). No. 3. P. 58—64.
256. Lutsenko V. I., Popov D. O., Lutsenko I. V. Investigation of the underlying surface with the help of radiation from the global navigation satellite system. *Radiophysics and electronics*. 2016. Vol. 7(21). No. 1. P. 31—39.
257. Mendes V. B. Modeling the neutral-atmosphere propagation delay in radiometric space techniques: Ph.D. thesis. New Brunswick. Canada. 1999. 353 p.
258. Anh N.X., Laush A.G., Khomenko Yu., Lutsenko V.I., Lutsenko I.V., Popov I.V. Testing of GNSS Receivers of Space Objects in Earth Conditions and the Implementation of Spoofing using Simulator of GNSS Signals. *Telecommunications and Radio Engineering*. 2020. Vol. 79. Iss. 20. P. 1773—1784.
259. Barton D., Ward G. Guide to radar measurements. Moscow: Sov Radio. 1976. 392 p.
260. Lutsenko V., Lutsenko I., Popov I., Soboliak A., Anh Nguyen Xuan, Babakov M. Active-Passive Radar Systems Using Radiation Of HF Band Broadcasting Stations For Airborne Objects Detection. Eds by Nechyporuk M., Pavlikov V., Kritskiy D. Integrated Computer Technologies in Mechanical Engineering — 2020. ICTM 2020. *Lecture Notes in Networks and Systems*. Springer, Cham. 2021. Vol. 188. P. 620—632. DOI: 10.1007/978-3-030-66717-7_53
261. Lutsenko V.I., Lutsenko I.V., Babakov M.F., Luo Y., Sobolyak A.V. The use of semi-markov nested processes for the description of non-stationary acoustic noise. *Telecommunication and Radioengineering*. 2019. Vol. 78. No 11. P. 1015—1025. DOI: 10.1615/TelecomRadEng.v78.i11.80
262. Lutsenko V.I., Lutsenko I.V., Sobolyak A.V., Popov I.V. Optimum detection of signals against a background of stationary non-Gaussian noise. *VI International Science and Practice Conf. Signal processing and non-Gaussian processes (OSNP-17) in memory of Professor Yu.P. Kunchenko. May 24—26, 2017. Cherkasy. Ukraine: Conf. Proc*. Cherkasy. 2017. P. 121—123.
263. Lutsenko V.I., Lutsenko I.V., Sobolyak A.V., Popov I.V. Resolution — detection — measurement of signal parameters in non-Gaussian noises. *VI International Science and Practice Conf. Signal processing and non-Gaussian processes (OSNP-17) in memory of Professor Yu.P. Kunchenko. May 24—26, 2017. Cherkasy. Ukraine*: Conf. Proc. Cherkasy. 2017. P. 118—120.
264. Lutsenko V.I., Lutsenko I.V., Soboliak A.V., Popov I.V., Anh N.X., Luo Y. Interference to Active-Passive Radar Systems Created by Emissions from HF and VHF Broadcasting Stations. *Telecommunications and Radio Engineering*. 2020. Vol. 79. Iss. 10. P. 829—845. DOI: 10.1615/TelecomRadEng.v79.i10.10

265. Lutsenko V.I., Lutsenko I.V., Soboliak A.V., Popov I.V., Anh Nguyen, Luo Yiyang. Characteristics of Interference to Active-Passive Radar Systems from Emissions of HF and VHF Broadcasting Stations. *IEEE Ukrainian Microwave Week (UkrMW-2020). IEEE 6th International Symposium on Microwaves, Radar and Remote Sensing (MRRS). Sept. 21—25, 2020. Kharkiv. Ukraine:* Conf. Porc. Kharkiv. 2020. Vol. 2. P. 259—262.
266. Michel H. Sea echoes with radar, models and experimental results. *L'Onde Electrique*. 1971. 51. No 8. P. 704—713.
267. Trunk, G.V. Radar properties of non-Rayleigh sea clutter. *Trans AES-8*. Mar 72 1975. No 2. P. 196—204.
268. Trunk G. V., George S. F. Detection of targets in non-Gaussian sea clutter. *IEEE Trans*. 1970. AES-6. P. 620—628.
269. Kulemin G. P. Millimeter-Wave Radar Targets and Clutter; Tech. Ed. David K. Barton. Boston. London: Artech House, 2003. 417 p.
270. Kulemin H.P., Goroshko E.A., Tarnavsky E.V. Spatial-temporal characteristics of backscattering from the earth's surface. *Successes of modern radio electronics*. 2004. No. 12. P. 60—70.
271. Valeev V.G., Sosulin Yu.G. Detection of weak coherent signals in correlated non-Gaussian noise. *Radio Technology and Electronics*. 1969. No 2. P. 230—238.
272. Chabdarov Sh.M., Trofimov A.T. Polygaussian representation of arbitrary interference and reception of discrete signals. *Radio Technology and Electronics*. 1975. Vol. 20. No. 4. P. 734—745.
273. Chabdarov Sh.M., Nadev A.F., Faizullin R.R., Senyushin A.V., Falin A.V., Egorov A.E. New classes of polygaussian models in the statistical theory of signal reception of modern radio electronic radio systems. *Applied Radio Electronics*. Kharkiv. 2002. Vol. 1. No. 2. P. 171—180.
274. Lutsenko V. I. Simulation model of the backscatter signal from the sea surface. *Successes of modern radio electronics*. 2008. No. 4. P. 59—73.
275. Lutsenko V.I., Lutsenko I.V., Khomenko S.I., Zatserklyany A.Ye. Simulation Statistical Model of Reflection from the "Clear-Sky". *Telecommunications and Radio Engineering*. 2005. Vol. 63. No. 5. P. 371—380.
276. Kravchenko V.F., Lutsenko V.I., Masalov S.A., Academician Pustovoit V.I. Analysis of non-stationary signals and fields using embedded semi-Markov processes. *Proceedings of the Academy of Sciences*. 2013. Vol. 453. No. 2. P. 1—4.
277. Kravchenko V.F., Lutsenko V.I., Lutsenko I.V., Popov D.O. Description and analysis of non-stationary signals by nested semi-Markov processes. *Journal of Measurement Science and Instrumentation*. 2014. Vol. 5. No. 3. (Sept. 2014, Sum No. 19). P. 25—32.
278. Kravchenko V. F., Kravchenko O. V., Lutsenko V. I., Lutsenko I. V., Churikov D. V. Restoration of information parameters of natural environments using atomic and WA-system functions. Overview of Part I. Application of the theory of semi-Markov fields and finite functions for the description of non-stationary processes. *Physical Engineering Principles*. 2014. Vol. 3. No. 2. P. 3—17.
279. Lutsenko V.I., Lutsenko I.V., Masalov S.A., Khomenko S.I. Using nested semi-Markov processes for nonstationary signals and fields. *Radiophysics and Electronics*. Kharkiv. 2012. Vol. 3 (17). P. 57—64. URL: http://dspace.nbuv.gov.ua/handle/123456789/105896

280. Ivanov V.K., Pashchenko R.E., Stadnyk A.M., Yatsevich S.E. The application of fractal analysis in the processing of agricultural applications. *Successes of Modern Radio Electronics*. 2007. No. 5. P. 48—55.
281. Ivanov V.K., Pashchenko R.E., Stadnyk A.M., Yatsevich S.E. Methods of multi-frequency radar remote sensing of forests. *Successes of Modern Radio Electronics*. 2005. No. 7. P. 57—72.
282. Kalinkevich A.A., Kutuza B.G., Plyushchev V.A., Druchinin S.V. Possibilities of using multi-frequency RSA for layer-by-layer probing of the underlying surface. *Successes of Modern Radio Electronics*. 2001. No. 311. P. 31—39.
283. Kulemin G.P., Yatsevich S.E. The relationship between the backscattering of microwave radio waves and the parameters of vegetation cover and open soils in remote sensing methods. *Successes of modern radio electronics*. 2004. No. 3. P. 24—34.
284. Tikhonov V. I., Mironov M. A. Markov processes. Moscow: Sov. Radio, 1977. 488 p.
285. Koroliuk V.S., Turbine A.F. Semi-Markov processes and their applications. Kyiv: Naukova dumka, 1976. 184 p.
286. Davydan I.M., Lopatukhin L.I., Rozhkov V.A. Wind waves as probabilistic hydrodynamic progress. Leningrad: Gidrometeoizdat, 1978. 286 p.
287. Kozlov B.A., Ushakov I.A. Reference book for calculating the reliability of radio electronics and automation equipment. Moscow: Sov. Radio, 1975. 472 p.
288. Kravchenko V.F., Lutsenko V.I., Lutsenko I.V. Scattering of radio waves by the sea and the detection of objects on its background. Moscow: Fizmatlit, 2015. 448 p.
289. Roenko A.N., Zamaraev B.D., Kostyna V.L., Tymoshenko V.F. Scattering of millimeter radio waves by plant cover. *Radiophysics and Electronics*. 2002. Vol. 7. No. 2. P. 335—341.
290. Zamaraev B.D., Kolesnikov V.G. Specific RCS of some landscapes in the millimeter range of waves. Propagation and diffraction of radio waves in the millimeter and submillimeter bands. Kyiv: Naukova dumka, 1985. P. 44—49.
291. Volosyuk V.K., Kravchenko V.F. Statistical theory of radio engineering systems of remote sensing and radar; Ed. by V.F. Kravchenko. Moscow: Fizmatlyt, 2008. 704 p.
292. Kopytova L.D. The influence of free water content on the functional activity of common pine needles in the Cisbaikalia region [Irkutsk]. *Natural and Anthropogenic Dynamics of Terrestrial Ecosystems. Oct. 11—15. 2005. Irkutsk:* Conf. Proc. Irkutsk. 2005. P. 116—119.
293. Stasova V.V., Chebakova N.M., Parfenova E.I., Bugaenko T.N., Cherednikova Yu.S. Structure and functioning of terrestrial ecosystems, their biodiversity. Seasonal dynamics of chlorophyll content in the vegetation of the steppes of southern Siberia. *Natural and Anthropogenic Dynamics of Terrestrial Ecosystems. Oct. 11—15, 2005. Irkutsk:* Conf. Proc. Irkutsk. 2005. P. 72—74.
294. Kravchenko V.F., Labunko O.S., Lerer A.M., Sinyavsky H.P. Computational methods in modern radio physics; Ed. by V.F. Kravchenko. Moscow: Fizmatlyt, 2009. 464 p.
295. Kulemin H.P., Narrative V.B. Scattering of millimeter radio waves by the Earth's surface under small ridges. Kyiv: Naukova dumka, 1986. 229 p.
296. Kivva F.V., Roenko A.N., Vasilyev Yu.F., Zamaraev B.D.Correlation Between Backscattering Coefficient a Vegetation Water Content. *Turkish Journal of Physics*. 1995. Vol. 19. No. 10. P. 1339—1345.
297. Shostak A.S., Zagoskin V.V., Lukyanov S.P., Karaush A.S. On the possibility of determining the dielectric permittivity of the upper layers of the underlying media based on the measured reflection coefficients during oblique probing by plane waves of vertical

and horizontal polarization in the microwave range. *Journal of Radio Electronics*. 1999. No. 11. URL: http://jre.cplire.ru/alt/nov99/4/text.html
298. Popov I.V., Lutsenko V.I., Lutsenko I.V. Illumination of the air environment with the use of radiation from broadcasting stations in the HF range. Sovremennye Problemy Radioelektroniki. Ed. by Gromyko A.I., Sarafanova A.V. Moscow: Radio and Communication, 2006. P. 25—28.
299. Popov I.V., Lutsenko V.I., Lutsenko I.V. Bistatic Radars with Illumination by Ionospheric Signals of High-Frequency Communication Stations. *Telecommunications and Radio Engineering*. 2008. Vol. 67. No 4. P. 285—292.
300. Kravchenko V.F., Lutsenko V.I., Lutsenko I.V., Popov D.O. Statistical Model Of The Refractive Index Of The Troposphere. *Universal Journal Physics' and Applied (UJPA)*. 2014. Vol. 2(4). P. 206—212.
301. Kovadlo P.H., Shikhovtsev A.Yu. Energy structure of optical atmospheric turbulence under different air flow parameters. *Irkutsk State University. Ser. Earth Sciences*. 2014. Vol. 8. P. 42—55.
302. Theoretical foundations of radar. Ed. by Ya.D. Shirman's textbook for universities. Moscow: Sov. Radio, 1970. 560 p.
303. Shirman Y.D., Losev Y.I., Minervin N.N., Moskvityn S.V., Lekhovytskyi D.I., Levchenko L.S. Radio electronic systems: basic construction and theory. Reference book; Ed. by Ya.D. Shirman. Moscow: ZAO "MAKVIS", 1998. 828 p.
304. Levin B.R. Theoretical foundations of statistical radio engineering. In three books. Book. 2nd Ed., Revised and supplemented. Moscow: Sov. Radio, 1975. 392 p.
305. Tikhonov V.I. Statistical radio engineering. 2nd Ed., Revised and Add. Moscow: Radio and Communication, 1982. 624 p.
306. Kravchenko V.F., Kravchenko O.V., Pustovoit V.I., Churikov D.V. Application of families of atomic, WA-systems and R-functions in modern problems of radiophysics. Part I. *Radio Engineering and Electronics*. 2014. Vol. 59. No. 10. P. 949—978.
307. Kravchenko V.F., Kravchenko O.V., Pustovoit V.I., Churikov D.V., Yurin A.V. Application of families of atomic, WA-systems and R-functions in modern problems of radiophysics. Part II. *Radio Engineering and Electronics*. 2014. Vol. 60. No. 2. P. 109—148.
308. Kravchenko V.F., Kravchenko O.V., Konovalov Y.Yu., Pustovoit V.I., Churikov D.V. Application of families of atomic, WA-systems and R-functions in modern problems of radiophysics. Part III. *Radio Engineering and Electronics*. 2015. Vol. 60. No. 7. P. 663—694.
309. Kravchenko V.F., Kravchenko O.V., Pustovoit V.I., Churikov D.V., Yurin A.V. Application of atomic families, Wa_systems and R_functions in modern problems of radiophysics. Part IV. *Radio engineering and electronics*. 2015. Vol. 60. No. 11. P. 1113—1152.
310. Vishnivetsky O.V., Lazorenko O.V., Chernogor L.F. Analysis of Non-Linear Wave Processes Using Wigner Transform. *Russian Radio Physics and Radio Astronomy*. 2007. Vol. 12. Iss. 9. P. 295.
311. Chernogor L.F., Kravchenko S.G., Lazorenko O.V. System spectral analysis of the fractal ultra-wideband signals. *Nuclear Science and Technology Issues*. 2015. No. 4. P. 244—247.
312. Kravchenko V.F., Lazorenko O.V., Pustovoit V.I. Transformation of Kravchenko Vignera into non-linear digital signal processing. *Reports of the Academy of Sciences*. 2007. Vol. 416. No. 6. P. 754—758.
313. Lazorenko O.V., Chernohor L.F. UWB signals and processes. Kharkiv: V. N. Karazin Kharkiv National University. 2009. 576 p.

314. Yuman M. Molniya. Moscow: Mir, 1972. 327 p.
315. Interstate standard, GOST 31295.2-2005 (ISO 9613-2:1996). Moscow: Standartinform, 2006. 42 p.
316. Lutsenko V.I., Lutsenko I.V., Popov I. V. Detection against the background of non-Gaussian clutter from underlying surface. *European Radar Conference (EuRAD): Conf. Proc.* 2010. P. 411—414.
317. Lutsenko V.I., Lutsenko I.V., Popov I.V. Usage of Spectral — Polarization Features of Backscattering from Objects for Determination of its Movement Direction. *International Radar Symposium (IRS 2009). 09—11 Sept. 2009. Hamburg. Germany*: Conf. Proc. Hamburg. 2009. P. 557—562.
318. Lutsenko V.I., Lutsenko I. V., Sobolyak A. V., Popov I. V. Optimum detection of signals against a background of stationary non-Gaussian noise. *VI International. science and practice conf. Signal Processing and Non-Gaussian Processes (OSNP-17) in memory of Professor Y.P. Kunchenko. May 24—26, 2017. Cherkasy. Ukraine*: Conf. Proc. Cherkasy. 2017. P. 121—123.
319. Kravchenko V.F., Lutsenko V.I., Lutsenko I.V., Popov I. V., Luo Yiyang Description of nonstationary non-Gaussian processes using finite atomic functions. *Journal of Measurement Science and Instrumentation*. 2017. Vol. 8. No 1. P. 37—45.
320. Kravchenko V.F., Luo Yiyang, Lutsenko V.I., Lutsenko I.V., Popov I.V. Description of nonstationary non-Gaussian processes using finite atomic functions. *9th International Kharkiv Symposium on Physics and Engineering of Microwaves, Millimeter and Submillimeter Waves (MSMW)*. Kharkiv. 2016. P. 1—4. DOI: 10.1109/MSMW.2016.7538171
321. Kravchenko V.F., Kravchenko O.V., Safyn A.R. Atomic functions in the theory of probabilities and random processes. *Advances in Modern Radio Electronics*. 2009. No. 5. P. 23—37.
322. Lutsenko V.I., Lutsenko I.V., Popov I.V., Sobolyak A.V., Luo Yiyang. Usage Of Magic Squares Properties For Aperture Synthesis. *Acoustooptic and Radar Methods for Information Measurements and Processing: Conf. Proc. 8th Int. Conf., 20—23 Sept., 2015*. Suzdal: A.S. Popov RNTORES, 2015. P. 215—219.
323. Lutsenko V.I., Popov I.V., Lutsenko I.V., Luo Yiyang, Mazurenko A.V Nonequidistant Two-Dimensional Antenna Arrays are Based on Magic Squares. *2016 9th International Kharkiv Symposium on Physics and Engineering of Microwaves, Millimeter and Submillimeter Waves (MSMW)*. Kharkiv. 2016. P. 1—4. DOI: 10.1109/MSMW.2016.7538080
324. Kravchenko V.F., Lutsenko V. I., Lutsenko I.V., Popov I.V., Luo Yi-Yang, Mazurenko A.V. Nonequidistant Two-Dimensional Antenna Arrays Based On Magic Squares. *Journal of Measurement Science and Instrumentation*. 2017. Vol. 8. No 3. Sum No 20. P. 244—253.
325. Anh Nguyen Xuan, Lutsenko V.I., Yiyang Luo, Popov I.V. Nonequidistant two-dimensional antenna arrays are based on latin squares for registration of cosmic, atmospheric and lithospheric radiation. *The International Conference on Research Development and Cooperation in Geophysics (VIET-Geophys 2017), 18—22 Oct. 2017 Hanoi. Vietnam: Book of Abstract*. Hanoi, 2017.
326. Melyanovsky P.A., Popov I.V. Short spiral doublet. *12th International Conference Microwave and Telecommunication Technology*. Sevastopol, 2002. P 343—344. DOI: 10.1109/CRMICO.2002.1137264
327. Melyanovsky P.A., Popov I.V. Spiral antenna with transverse radiation. *Radiophysics and Electronics*. Kharkiv, 2003. Vol. 9. No. 3. P. 438—441.

328. Melyanovsky P.A., Popov I.V. Compact active Doppler calibrator. *2004 14th International Crimean Conference Microwave and Telecommunication Technology*. Sevastopol. 2004. P. 701—702. DOI: 10.1109/CRMICO.2004.183404
329. Kopylovych L. E., Sodin L. E. One-dimensional and two-dimensional non-equidistant array antennas with a low level of side lobes. Preprint No. 293: Institute of Radiophysics and Electronics. Kharkiv, 1986. 38p.
330. Sachson M.B., Merkulov V.V. Non-equidistant antenna arrays with randomly arranged elements. *Radio Technology and Electronics*. 1965. Vol. 10. No. 1. P. 7—13.
331. Shifrin Y.S. Questions of the statistical theory of antennas. Moscow: Sov. Radio. 1970. 383 p.
332. Sodin L.G. Statistical analysis of non-equidistant linear antenna arrays. *Radio Engineering and Electronics*. 1966. Vol. 11. No. 11. P. 1063—1959.
333. Leeper D.C. Thinned aperiodic antenna arrays with improved peak side lobe level control. Patent USA No 4071848, 31/01 1978.
334. Kopylovych L.E., Sodin L.G. Combinatory methods in radio physics, astronomy and radio astronomy. *Radio Physics and Radio Astronomy*. 1996. Vol. 1. No. 1. P. 61—70.
335. Kopilovich Lazarus E., Sodin Leonid G. Linear Non-Equidistant Antenna Arrays. Multielement System Design in Astronomy and Radio Science. *Astrophysics and Space Science Library*. 2001. Vol. 268. P. 77—96.
336. Kopylovych L.E. Non-excessive configurations of elements on square and hexagonal lattices of large sizes. *Radiophysics and Electronics*. 2014. Vol. 5(19). No. 1. P. 80—84.
337. Kopylovych L.E. Empirical estimation of the maximum number of elements of a non-redundant configuration on a square antenna array. *Radio Physics and Radio Astronomy*. 2009. Vol. 14. No. 2. P. 183—188.
338. Kopylovych L.E. Redundant configurations of antennas on the two-dimensional aperture of the interferometer, giving full coverage of the central regions in the plane of spatial frequencies. *Radio Physics and Radio Astronomy*. 2012. Vol. 17. No. 2. P. 176—182.
339. Kopilovich Lazarus E., Sodin Leonid G. Multielement System Design In Astronomy And Radio Science. Netherlands: Springer, 2001. 268 p.
340. Anh Nguyen Xuan, Lutsenko V.I., Luo Yiyang, Popov I.V. Non-equidistant two-dimensional antenna arrays are based on Latin squares for registration of cosmic, atmospheric and lithospheric radiation. *Journal of Marine Science and Technology*. 2017. Vol. 17. No 4B. P. 14—20.
341. Makarova N.V. Magical world of magic squares. Saratov, 2010. 180 p.
342. Pchelnikov Y.N. Features of delayed waves and the possibilities of their non-traditional application. *Radio Engineering and Electronics*. 2003. Vol. 48. No. 4. P. 494—507.
343. Fradin A.Z. Antennas of ultrahigh frequencies. Moscow: Sov. Radio, 1957. 647 p.
344. George Ploussios. An Electronically tuned HF/VHF helical antenna. *Microwave Journal*. 1991. 34, No. 5. P. 223—224, 227—228, 231, 233—234, 237, 239—240.
345. Computational methods in electrodynamics. Ed. by R. Mitra. Moscow: MIR, 1977. 243 p.
346. Harrington R. F. Electromagnetic scattering by antennas. *IEEE Trans. Antennas Propag.* Sep. 1963. Vol. 11. No. 5. P. 595—596.
347. Lutsenko V.I., Tolstel S. Yu. Frequency dependences of scattering matrices of objects in the resonant region. *Radiophysics and Electronics*. Kharkiv. 2000. Vol. 5. No 1. P. 77—82.
348. Kobak V.O. Radar reflectors. Moscow: Sov. Radio, 1975. 248 p.
349. Lutsenko V.I., Lutsenko I.V., Sobolyak A.V. The use of smart grid technologies to increase the efficiency of the use of ground equipment objects. *Applied Radio Electronics*. 2017. Vol. 16. No. 3, 4. P. 134—145.

350. Kryvenko O.V., Laush A.G., Lutsenko V.I., Lutsenko I.V., Popov D.O., Popov I.V. et al. The use of radiation from artificial Earth satellites and television centers for the study of atmospheric processes. *Space science and technology*. 2015. Vol. 21. No. 3. P. 83—90.
351. Patent Ukraine No. 111262, IPC H03B 7/14 (2006.01), H03B 7/06 (2006.01) Open radiating system. O.V. Kryvenko, V.I. Lutsenko, O.V. Sobolyak. Applicant and owner O.Ya. Usikov Institute for Radiophysics and Electronics of the National Academy of Sciences of Ukraine. No. a 2014 08410, app. 27.04.2014, publ. application data 21.05.2016, Bull. No. 2, publ. data on the patent 11.04.2016, Bull. No. 7.
352. Lutsenko V.I., Lutsenko I.V., Sobolyak O.V. The use of smart grid technologies to increase the efficiency of the use of ground equipment objects. *IV International Scientific and Practical Conference. Problems of Coordination of Military-Technical and Defense-Industrial Policy in Ukraine. Prospects for the development of weapons and military equipment. Oct. 12—13, 2016: Conf. Proc*. Kyiv. 2016. P.141—143.
353. Kryvenko E.V., Lutsenko V.I., Sobolyak A.V. Smart antenna for small-sized radio systems of the millimeter wave range. *VIII Armandov Lectures. IX Scientific and practical Seminar. Applied problems of signal formation and processing in radar, communication and acoustics. 26—28 Jun 2018. Murom*: Conf. Proc. Moscow: Izd. Poligraphic Center of the University of Volgograd, 2018. P. 19—21.
354. Kravchenko V.F., Kryvenko E.V., Levchenko S.A., Lutsenko V.I., Plyuta S.V. Smart grid technology — the basis of modernization of the water supply system. *Journal of the National Academy of Sciences of Belarus. Technical Sciences*. 2015. Vol. 59. No. 3. P. 102—108.
355. Kravchenko V.F., Kryvenko E.V., Levchenko S.A., Lutsenko V.I., Plyuta S.V. Application of smart grid technologies for sustainable development and modernization of water supply systems. *Journal of the National Academy of Sciences of Belarus Series of Physical and Technical Sciences*. 2015. No. 4. P. 67—79.
356. Kravchenko V.F., Kryvenko E.V., Levchenko S.A., Lutsenko V.I. Smart grid technology — the basis of the modernization of the water supply system for future sustainable development of society. *Physical Foundations of Instrumentation*. 2015. Vol. 4. No. 1. P. 12—29.
357. Kravchenko V.F., Kryvenko E.V., Levchenko SA, Lutsenko V.I., Plyuta S.V. Mathematical modeling of smart grid technologies for sustainable development and modernization of water supply systems. *National Academy of Sciences of Belarus A.V. Luikov Heat and Mass Transfer Institute*. Minsk, 2016. P. 269—277.
358. Complex BrahMos/PJ-10. URL: http://militaryrussia.ru/blog/topic-397.html
359. Prospective projects of BrahMos family rockets. Military review. URL: https://topwar.ru/70301-perspektivnye-proekty-raket-semeystva-brahmos.html
360. Lutsenko I.V. The use of electromagnetic fields of sources of civilian use for the diagnosis of the troposphere and the illumination of the air situation. *3rd International Radio Electronic Forum "Applied Radio Electronics. State and prospects of development" (IREF 2008). Int. Conf. Modern perspective systems of radar, radio astronomy and satellite navigation (SRRSN-2008) Oct. 22—24, 2008. Kharkiv*: Conf. Proc. Kharkiv, 2008. Vol. 1. Part 2. P. 184—188.
361. Theoretical foundations of radar. Ed. by Y.D. Shirman. Moscow: Sov. Radio, 1970. 559 p.
362. Portable VHF radio station R-030 U. URL: https://ru.uos.ua/produktsiya/svyaz-i-asu/186-vozimaya-ukv-radiostantsiya-r-030-u
363. Radio station R-163-50K (Arbalet-50K). URL: http://www.cqham.ru/review/showproduct.php?product=290

В монографії розглянуто вирішення проблеми використання власних акустичних та вторинних електромагнітних випромінювань об'єктів антропогенного походження у системах активно-пасивного моніторингу. Запропоновано методики оцінки дальності виявлення джерел акустичного випромінювання, спосіб визначення радіолокаційних сигнатур об'єктів за оптичними та акустичними портретами та виділення корисного сигналу на фоні завад, методики дистанційної діагностики стану поверхні моря, тропосфери Землі за випромінюванням телевізійних та радіомовних станцій і ШСЗ систем глобальної навігації, модель нестаціонарних завад. Розглянуто нові методи опису нестаціонарних процесів і сигналів з використання функцій розподілу Кравченка—Рвачова та вкладених напівмарковських процесів.

Книга призначена для науковців та фахівців, що займаються розробкою методів і технологій дистанційного зондування. Буде корисна для студентів і викладачів навчальних закладів радіофізичного профілю.

Наукове видання

НАЦІОНАЛЬНА АКАДЕМІЯ НАУК УКРАЇНИ
ІНСТИТУТ РАДІОФІЗИКИ ТА ЕЛЕКТРОНІКИ
ім. О.Я. УСИКОВА НАН УКРАЇНИ

ЛУЦЕНКО Владислав Іванович
ЛУЦЕНКО Ірина Владиславівна
ПОПОВ Ігор Володимирович
СОБОЛЯК Олександр Васильович

МОНІТОРИНГ ДОВКІЛЛЯ З ВИКОРИСТАННЯМ ЕЛЕКТРОМАГНІТНИХ І АКУСТИЧНИХ ВИПРОМІНЮВАНЬ ОБ'ЄКТІВ, ІСНУЮЧИХ НАЗЕМНИХ ТА КОСМІЧНИХ РАДІОСИСТЕМ

Англійською мовою

Редактор-коректор *О.В. Нікітченко*

Художнє оформлення *Є.О. Ільницького*

Технічне редагування *Т.М. Шендерович*

Виготовлення ілюстрацій *О.В. Нікітченка*

Комп'ютерна верстка *Н.М. Коваленко*

Підп. до друку 02.12.2024. Формат 70 × 100/16. Гарн. Minion Pro.
Ум. друк. арк. 21,61. Обл.-вид. арк. 19,83. Тираж 100 прим. Зам. № 7538.

Видавець і виготовлювач Видавничий дім "Академперіодика" НАН України
01024, Київ, вул. Терещенківська, 4

Свідоцтво про внесення до Державного реєстру суб'єктів
видавничої справи серії ДК № 544 від 27.07.2001 р.